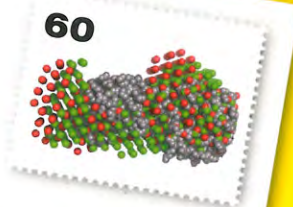
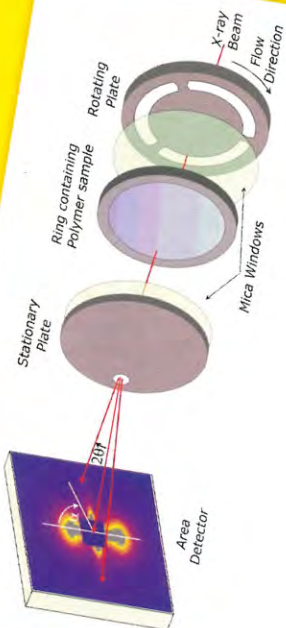




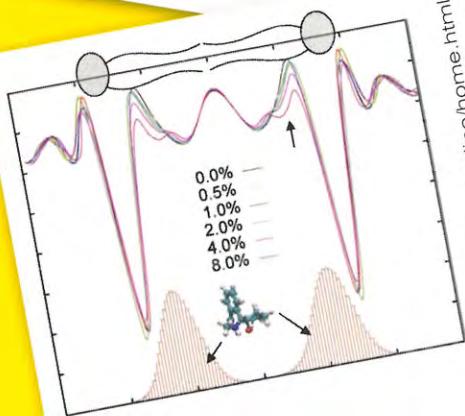
OAW
Austrian Academy
of Sciences

IBn
INSTITUTE OF BIOPHYSICS AND
NANOSYSTEMS RESEARCH

ANNUAL REPORT 2009



Austrian SAXS Beamline
e/o Sinerotrone Trieste
Strada Statale 14, km 163.5
I-34149 Basovizza



More infos under www.ibn.oew.ac.at/beamline/home.html



Austrian SAXS Beamline
e/o Sinerotrone Trieste
Strada Statale 14, km 163.5
I-34149 Basovizza

Best regards and greetings
from the user community!

AUSTRIAN SAXS BEAMLINE AT



Austrian Small Angle X-ray Scattering (SAXS) Beamline at ELETTRA

Annual Report 2009

Compiled by the SAXS-Group:

- for IBN: H. Amenitsch, M. Rappolt & B. Sartori
- for ELETTRA: S. Bernstorff

Table of Contents

› Preface	
› The SAXS-Group	3
› The SAXS-Beamline in General	4
› Application for Beamtime at ELETTRA	8
› List of Users and Institutes in 2009	10
› List of Performed Experiments	18
› User Statistics	23
› Experimental Possibilities at the SAXS-beamline	
1. Accessible SAXS and WAXS ranges	27
2. Calibration of the s-axis and flat field correction	28
3. Site laboratories	30
4. Available sample manipulation stages	31
› User Contributions	
1. Materials Science	39
2. Life Sciences	79
3. Chemistry	108
› Publications	131
› Author Index	147

Preface



Peter Laggner
Director
Institute of Biophysics and Nanosystems Research
Austrian Academy of Sciences

In its 13th year of operation, the Austrian SAXS station has again proven to be one of the most successful facilities of its kind worldwide, despite the increased number of stations at other synchrotrons. Apart from the technical quality and flexibility in the choice of sample environment, which is a decision factor for SAXS, the attractiveness of the station to users results primarily from the competence and dedication of the local support team. Without such a team, even the most brilliant X-ray beam would be of little use.

What are the expectations for the future? Where will synchrotron SAXS be in, say, 2015? As I already mentioned last year, the integration and combination with other spectroscopic, thermodynamic or microscopic techniques will certainly continue to be an important trend, as well as the focus on surface structure analysis, as evident from the increasing number of GISAX contributions documented here.

Another kind of integration seems to be medium-term programmed on the part of systems to be studied: the combination of nanomaterials with bio-inspired functionality. Together with deep X-ray lithography as patterning technique, this has very attractive potential for realising old dreams of nanotechnology.

These perspectives are fascinating but also demanding. Such targets in the first place require a broad team-work between the scientists who know the systems involved and the different experimental specialists. This means to establish a “nano-foundry” at the beam-line, which obviously requires additional resources. However, with their experience and talents in improvisation, our team appears to be very well prepared for these steps.

To ensure the future, we must continue to take risks and be adventurous in our concepts. I am convinced that this is the only way to positively inspire also those who control the budgets.



Alfonso Franciosi
Chief Executive Officer
Sincrotrone Trieste S.C.p.A.

We are pleased to introduce the 2009 Annual Report of the SAXS Beamline of the Austrian Academy of Sciences. The notable scientific production and constantly high demand by the user community continues to make the SAXS Beamline an example of what a successful scientific partnership can achieve.

The strategies that Sincrotrone Trieste and its partners have implemented in 2009 have been aimed at assuring the renewed and extended competitiveness of the Elettra Laboratory as a whole, responding to the competition generated by the completion of various third generation synchrotron radiation laboratories, such as Diamond in the UK and Soleil in France. The introduction of a new full-energy injector capable of bringing Elettra to function in top-up mode, i.e., running at constant current, and the actions taken to upgrade the existing beamlines currently underway, are keeping Elettra up to par with the most advanced competition. At the time of this writing Elettra has become one of the only four synchrotron radiation sources of the third generation in the world to operate in top-up mode, and the one and only machine in the world that was not designed as such, but has been successfully converted to operate in top-up mode.

As we are entering the commissioning phase of the new fourth generation source FERMI@Elettra, the first and, at present, only free electron laser (FEL) source worldwide designed as a seeded source from the start, we are relaunching our international presence and attracting a number of new highly qualified international partners. More than twentyfive international institutions take part in the scientific programs currently under development at FERMI, in the three areas *Low Density Matter (LDM)*, *Elastic and Inelastic Scattering (EIS)* and *Diffraction and Projection Imaging (DiProI)*.

The beginning of the commissioning phase was celebrated with a ceremony on November 30, 2009 when the FERMI photoinjector was inaugurated by the Italian Minister of Instruction, University and Research, the honorable Mariastella Gelmini. These developments have been made possible by financial contributions from the Italian Government, the European Commission and the Regional government of Friuli Venezia Giulia, as well as by a 80 million euro loan from the European Investment Bank (EIB), which recognized the importance of our project on a pan-European level. This also permitted us to strengthen the trend towards an internationalization of Sincrotrone Trieste with the perspective of institutional ties with long-term European programs.

We now have at our disposal all necessary resources to complete our project and progressively open up the new installations to international users in 2010-2012. The beginning of the next European Framework Program in 2013 and the perspective of transforming our laboratory into an European Research Infrastructure Consortium (ERIC), are important targets not to be missed. In this three-year transition period Sincrotrone Trieste shall take full advantage of the available opportunities: the prospective for future development will depend crucially on how our organization can adapt itself to new conditions.

We emphasize that FERMI is already part of the roadmap of the European Strategy Forum for Research Infrastructure (ESFRI) through the EuroFEL initiative (once IRUVX-FEL, from infrared, ultraviolet, X-ray Free Electron Laser). The Elettra Laboratory has a proven track record on both the European and international level in the development of high quality research and technological innovation, as we have seen the successful fulfillment of common initiatives with partner institutions in Austria, the Czech Republic, Slovenia, Croatia, India, France, Germany and other EU and non-EU countries. The transformation of Sincrotrone Trieste, for the moment a shareholders company with the participation of the Italian government, into an ERIC is a realistic possibility that will require the participation of nearby countries. We must therefore strive to reinforce and expand our network of partners in Italy and Europe, with particular attention paid to the new Member States of the European Union. In this our long-standing relation with the Austrian Academy of Sciences will be the model to follow.

We take this opportunity to thank our Austrian partners for their professionalism and steady dedication over the years. We at Elettra look forward to expanding the scope and depth of our collaboration and exploring together the frontiers that the new upgraded Elettra and FERMI will open for all of us.

The SAXS Group

HEAD OF PROJECT: Peter Laggner ¹⁾
e-mail: peter.laggner@oeaw.ac.at

SCIENTISTS: Heinz Amenitsch ^{1), 3)}
e-mail: amenitsch@elettra.trieste.it

Sigrid Bernstorff ²⁾
e-mail: bernstorff@elettra.trieste.it

Michael Rappolt ^{1), 3)}
e-mail: michael.rappolt@elettra.trieste.it

POST DOCS: Fernando Cacho ^{1), 3)}
e-mail: fernando.cacho@elettra.trieste.it

Shyjumon Ibrahimkutty ^{1, 3)} (until May 2009)
e-mail: shyju.ibrahimkutty@elettra.trieste.it

Karin Jungnikl ^{1, 3)} (from May 2009)
e-mail: karin.jungnikl@elettra.trieste.it

Benedetta Marmioli ^{1, 3)}
e-mail: benedetta.marmioli@elettra.trieste.it

SCIENTIFIC ASSISTANT: Barbara Sartori ^{1, 3)}
e-mail: barbara.sartori@elettra.trieste.it

TECHNICIAN: Christian Morello ²⁾
e-mail: christian.morello@elettra.trieste.it

1) Institute for Biophysics and Nanosystems Research, Austrian Academy of Sciences, Schmiedlstraße 6, 8042 Graz, Austria.

Tel 0043-316-4120 302

Fax 0043-316-4120 390

2) Sincrotrone Trieste, Strada Statale 14, km 163.5, 34012 Basovizza (TS), Italy.

Tel 0039-040-375 81

Fax 0039-040-938 0902

3) Institute for Biophysics and Nanosystems Research, Austrian Academy of Sciences
c/o Sincrotrone Trieste

The SAXS-Beamline in General

Small Angle X-ray Scattering has become a well known standard method to study the structure of various objects in the spatial range from 1 to 1000 Å, and therefore instruments capable to perform such experiments are installed at most of the synchrotron research centers. The high-flux SAXS beamline at ELETTRA is mainly intended for time-resolved studies on fast structural transitions in the sub-millisecond time region in solutions and partly ordered systems with a SAXS-resolution of 10 to 1400 Å in real-space.

The photon source is the 57-pole wiggler whose beam is shared and used simultaneously with a Macromolecular Crystallography beamline. The wiggler delivers a very intense radiation between 4 and 25 keV of which the SAXS-Beamline accepts 3 discrete energies, namely 5.4, 8 and 16 keV. The beamline optics consists of a flat double crystal monochromator and a double focusing toroidal mirror.

A versatile SAXS experimental station has been set-up, and an additional wide-angle X-ray scattering (WAXS) detector monitors simultaneously diffraction patterns in the range from 1 to 9 Å. The sample station is mounted move-able onto an optical table for optimising the sample detector distance with respect to SAXS resolution and sample size.

Besides the foreseen sample surrounding the users have the possibility to install their own specialised sample equipment. In the design phase, besides technical boundary conditions, user friendliness and reliability have been considered as important criteria.

The optimisation of the beamline with respect to high-flux and consequently high flux density, allows to perform the following experiments:

- Low Contrast Solution Scattering
- Grazing Incidence Surface Diffraction
- Micro-Spot Scanning
- X-ray Fluorescence Analysis
- Time-Resolved Studies $\geq 11 \mu\text{s}$
- Simultaneously Performed Small- and Wide-Angle Measurements (SWAXS) on:
 - Gels
 - Liquid Crystals
 - (Bio) Polymers
 - Amorphous Materials
 - Muscles

Furthermore, using 5.4 and 16 keV energies, the beamline is widely applicable also to very thin, e.g. single muscle fibers, and optically thick (high Z) specimen, as often used in e.g., material science and solid state physics.

THE INSERTION DEVICE

The wiggler for the SAXS beamline consists of three 1.5 m long segments, each having 19 poles. The device can work with a minimum gap of 20 mm, which corresponds to $K=20$ at 2 GeV. The main parameters of the wiggler are:

- Critical Energy 4.1 keV
- Radiation Power 8.6 kW
- Flux 3.5×10^{14} ph/s/mrad/0.1%BW (at 400 mA)

The wiggler radiation cone has a horizontal width of 9 mrad. From this the SAXS-beamline accepts vertically 0.3 mrad, and horizontally +/-0.5 mrad at a 1.25 mrad off-axis position. The resulting source size for 8 keV photons is $3.9 \times 0.26 \text{ mm}^2$ (horiz. x vert.).

THE OPTICS

The optics common with the diffraction beamline consists of:

- C-Filter and Beryllium window assembly to reduce the power load on the first optical elements by a factor of 2 and to separate the beamline vacuum from the storage ring.
- Beam defining slit chamber which allows to define the SAXS beam on three sides before the monochromator in order to reduce the straylight in the downstream beamline sections.

The SAXS beamline optics consists of:

- A double-crystal monochromator consisting of four individual chambers, in which three interchangeable asymmetric Si(111) crystal pairs are used to select one of three fixed energies. Each of the crystal pairs is optimised for the corresponding energy to accomplish a grazing angle of 2° . The energy resolution $\Delta E/E$ of the monochromator is in the range of $0.7 - 2.5 \cdot 10^{-3}$.
- A baffle chamber after the monochromator is used as an adjustable straylight fenditure.
- A segmented toroidal mirror focuses the light in horizontal and vertical direction with a $1/2.5$ magnification onto the SAXS-detector.
- An aperture slit reduces the straylight after the monochromator and the toroidal mirror.
- A guard slit defines the illuminated region around the focal spot. The spot size on the detector is 1.6 mm horizontally and 0.6 mm vertically. The calculated flux at the sample is in the order of 10^{13} ph/s at 400 mA. For a maximum sample size of $5.4 \times 1.8 \text{ mm}^2$ correspondingly a flux density of 10^{12} ph/s/ mm^2 has been calculated.

SAMPLE STAGE

The multipurpose sample stage allows to perform fast time-resolved relaxation studies based on temperature- or pressure-jumps as well as stopped flow experiments. Shear jump relaxation experiments are planned. Specifically, T-jumps can be induced by an infra-red light pulse (2 ms) from an Erbium-Glass laser, raising the temperature about 20°C in an aqueous sample volume of $10 \mu\text{l}$. A hydrostatic pressure cell with a maximal accessible angular range of 30° for simultaneous SAXS and WAXS measurements is available. P-jumps are realised by switching fast valves between a low and a high pressure reservoir, increasing or decreasing the hydrostatic pressure in the range from 1 bar to 2.5 kbar within a few ms. A Differential Scanning Calorimeter (DSC) allows for DSC-scans simultaneously to SWAXS measurements. In an overview, the following sample manipulations are possible (further details, see page 31-35):

- Temperature Manipulations: Ramps, Jumps and Gradient Scans
- Pressure Manipulation: Scan and Jumps
- Stopped Flow Experiments
- SWAXS Measurements Applying Mechanical Stress
- Calorimetric measurements

Scientific Applications	<p>Low Contrast Solution Scattering, Grazing Incidence Surface Diffraction, Micro-Spot Scanning, X-ray Fluorescence Analysis, Time-Resolved Studies $\geq 11 \mu\text{s}$ and Simultaneously Performed Small- and Wide-Angle Measurements (SWAXS) on:</p> <p style="text-align: center;">Gels Liquid Crystals (Bio) Polymers Amorphous Materials Muscles</p>																											
Source characteristics	<p><u>Wiggler (NdFeB Hybrid):</u></p> <table border="0" style="width: 100%;"> <tr> <td style="width: 60%;">Period</td> <td style="text-align: right;">140 mm</td> </tr> <tr> <td>No. full poles</td> <td style="text-align: right;">57</td> </tr> <tr> <td>Gap</td> <td style="text-align: right;">20 mm</td> </tr> <tr> <td>B_{max}</td> <td style="text-align: right;">1.607 T</td> </tr> <tr> <td>Critical Energy ϵ_c</td> <td style="text-align: right;">4.27 keV</td> </tr> <tr> <td>Power (9 mrad)</td> <td style="text-align: right;">8.6 kW</td> </tr> <tr> <td>Effective source size FWHM</td> <td style="text-align: right;">$3.9 \times 0.26 \text{ mm}^2(\text{h} \times \text{v})$</td> </tr> </table>	Period	140 mm	No. full poles	57	Gap	20 mm	B_{max}	1.607 T	Critical Energy ϵ_c	4.27 keV	Power (9 mrad)	8.6 kW	Effective source size FWHM	$3.9 \times 0.26 \text{ mm}^2(\text{h} \times \text{v})$													
Period	140 mm																											
No. full poles	57																											
Gap	20 mm																											
B_{max}	1.607 T																											
Critical Energy ϵ_c	4.27 keV																											
Power (9 mrad)	8.6 kW																											
Effective source size FWHM	$3.9 \times 0.26 \text{ mm}^2(\text{h} \times \text{v})$																											
Optics	<table border="0" style="width: 100%;"> <tr> <td style="width: 30%;"><u>Optical elements:</u></td> <td style="width: 35%;"><i>Double crystal monochromator:</i></td> <td style="width: 35%;"><i>Mirror:</i></td> </tr> <tr> <td></td> <td>Si (111) asym. cut, water cooled.</td> <td>two-segment, toroidal, Pt coated.</td> </tr> <tr> <td><u>Distance from source:</u></td> <td>18.4 m</td> <td>26.5 m</td> </tr> <tr> <td>Acceptance</td> <td colspan="2">1 mrad/0.3 mrad (h x v)</td> </tr> <tr> <td>Energy (3 selectable)</td> <td colspan="2">5.4, 8, 16 keV (0.77, 1.54, 2.3 Å)</td> </tr> <tr> <td>Energy resolution $\Delta E/E$</td> <td colspan="2">$0.7\text{-}2.5 \times 10^{-3}$</td> </tr> <tr> <td>Focal spot size FWHM</td> <td colspan="2">$1.2 \times 0.6 \text{ mm}^2(\text{h} \times \text{v})$</td> </tr> <tr> <td>Spot at Sample FWHM</td> <td colspan="2">$5.4 \times 1.8 \text{ mm}^2(\text{h} \times \text{v})$</td> </tr> <tr> <td>Flux at sample</td> <td colspan="2">$5 \times 10^{12} \text{ ph s}^{-1}(2 \text{ GeV}, 200 \text{ mA}, 8 \text{ keV})$</td> </tr> </table>	<u>Optical elements:</u>	<i>Double crystal monochromator:</i>	<i>Mirror:</i>		Si (111) asym. cut, water cooled.	two-segment, toroidal, Pt coated.	<u>Distance from source:</u>	18.4 m	26.5 m	Acceptance	1 mrad/0.3 mrad (h x v)		Energy (3 selectable)	5.4, 8, 16 keV (0.77, 1.54, 2.3 Å)		Energy resolution $\Delta E/E$	$0.7\text{-}2.5 \times 10^{-3}$		Focal spot size FWHM	$1.2 \times 0.6 \text{ mm}^2(\text{h} \times \text{v})$		Spot at Sample FWHM	$5.4 \times 1.8 \text{ mm}^2(\text{h} \times \text{v})$		Flux at sample	$5 \times 10^{12} \text{ ph s}^{-1}(2 \text{ GeV}, 200 \text{ mA}, 8 \text{ keV})$	
<u>Optical elements:</u>	<i>Double crystal monochromator:</i>	<i>Mirror:</i>																										
	Si (111) asym. cut, water cooled.	two-segment, toroidal, Pt coated.																										
<u>Distance from source:</u>	18.4 m	26.5 m																										
Acceptance	1 mrad/0.3 mrad (h x v)																											
Energy (3 selectable)	5.4, 8, 16 keV (0.77, 1.54, 2.3 Å)																											
Energy resolution $\Delta E/E$	$0.7\text{-}2.5 \times 10^{-3}$																											
Focal spot size FWHM	$1.2 \times 0.6 \text{ mm}^2(\text{h} \times \text{v})$																											
Spot at Sample FWHM	$5.4 \times 1.8 \text{ mm}^2(\text{h} \times \text{v})$																											
Flux at sample	$5 \times 10^{12} \text{ ph s}^{-1}(2 \text{ GeV}, 200 \text{ mA}, 8 \text{ keV})$																											
Experimental apparatus	<p><u>Resolution in real space:</u> 10-1400 Å (small-angle), 1- 9 Å (wide-angle)</p> <p><u>Sample stage:</u> temperature manipulations: ramps, jumps and gradient scans, pressure manipulation: scan and jumps, stop flow experiments, SWAXS measurements applying mechanical stress, SWAXS measurements applying magnetic fields. In-line calorimetric measurements simultaneously with SWAXS.</p> <p><u>Detectors:</u> 1D gas-filled detectors for simultaneous small- and wide-angle (Gabriel type), 2D CCD (Photonic Science) and Mar300 Image Plate for small-angle, Vantec-1D (Bruker AXS), Pilatus 2D detector.</p>																											
Experiment control	<p><u>Beamline control:</u> Program-units written in LabView for Windows</p> <p><u>1 D detector control:</u> PC-card and software from Hecus X-ray Systems GmbH, Graz.</p> <p><u>2 D detector control:</u> Software from corresponding detector system.</p>																											

CURRENT STATUS

The beamline has been built by the Institute for Biophysics and Nanosystems Research (IBN), Austrian Academy of Science in collaboration with staff members from Sincrotrone Trieste, and is in user operation since September 1996. The set-up of the beamline started at the beginning of January 1995 with the installation of the support structure. Until the end of 1995, the 8 keV single energy system had been realised. The upgrade to the full three energy system was finished in spring 1998. Time resolved experiments require fast X-ray detectors and data acquisition hard- and software. Depending on the desired resolution in time and in reciprocal space, on isotropic or anisotropic scattering of the sample, one-dimensional position sensitive (delay-line type) or two-dimensional CCD detectors are employed.

In August 2002 our new chemistry and X-ray laboratory went into operation. The chemistry unit serves mainly for sample preparation and analysis for both, in house research and external user groups, whereas the X-ray laboratory allows on-site testing of samples before moving on to the SR beamline (see page 30).

In May 2008 we extended about 3 m also our experimental hutch. It is now possible to increase the sample to detector distance and therefore improve our minimum SAXS resolution or maximise the flux density at sample position for certain experiments.

In conclusion, due to wide versatility of the beamline and the highly flexible sample stage, there are nearly no limits for the realisation of an experiment, and you are welcome by our team to propose any interesting and highlighting investigation for the benefit of material and life sciences.

Application for Beamtime at ELETTRA

1. Beamtime Policy at SAXS beamline

According to the agreement from March 2001 regarding the co-operation between the Austrian Academy of Sciences and Sincrotrone Trieste, at the Austrian SAXS-beamline the available beamtime of about 5000 hours/year is distributed as follows:

- 35% for Austrian Users, type: "CRG" (Collaborating Research Group)
- 35% for Users of Sincrotrone Trieste (General Users (GU))
- 30% is reserved for beamline maintenance and in-house research

In both user beamtime contingents also any industrial, proprietary and confidential research can be performed according to the "General User Policy" of Sincrotrone Trieste.

To apply for CRG and GU user beamtime proposals must be submitted according to the rules of Sincrotrone Trieste. The international review committee at ELETTRA will rank the proposals according to their scientific merit assessment. Based on this decision beamtime will be allocated according to the specific quotes for the beamtimes (CRG/GU) either for the following semester ("normal application") or for the next two years ("long term application"). However, at the moment no more than a maximum of 10% of the beamtime will be assigned to "long term" projects.

2. How to apply for beamtime

There are two deadlines each year for proposals, namely August 31st and February 28th. Accepted proposals will receive beamtime either in the then following first or second half year period, respectively. The Application Form must be completed on-line according to the following instructions.

ELETTRA USERS OFFICE

Strada Statale 14 - km 163.5

34012 Basovizza (Trieste), ITALY

Tel: +39 040 375 8628 / 8538- fax: + 39 040 375 8565

e-mail: useroffice@elettra.trieste.it

INSTRUCTIONS GIVEN BY THE USERS OFFICE

(see also <http://www.elettra.trieste.it/UserOffice/>)

1. Read carefully the General Guidelines.
2. Connect to the Virtual Unified Office: <https://vuo.elettra.trieste.it/pls/vuo/guest.startup> using your favorite browser with JavaScript enabled.
3. Select the Virtual Unified Office link.

4. When prompted, insert your ID and password. If you are a new user fill in the registration form with your data and choose your institution with the search button; in case your institution does not appear in the list, please contact useroffice@elettra.trieste.it giving all the details about it. When registered, you will receive an acknowledgment with your ID and password. You can change your password, if you wish. In case you forget your password, please don't register again but contact useroffice@elettra.trieste.it. At any moment you can select the help button and view more detailed instructions. By inserting your ID and password you will be able to continue.
5. Select the proposals button in the User functions group.
6. Select add and fill in on-line the proposal form. Please, type your proposal in English. Repeat this procedure for each proposal you intend to submit.
7. In case of continuation proposal: a) attach the experimental report of previous measurements; b) give your previous proposal number.
8. When finished, submit the proposal electronically, selecting the save button.
9. Print the proposal form together with each related safety form.
10. Sign the safety form(s).
11. Mail all signed safety form(s) as printed copy to the Users Office.

NOTE:

For technical questions related to proposals submission or other practical issues, contact useroffice@elettra.trieste.it

For scientific questions related to the possibility of performing a given experiment, contact bernstorff@elettra.trieste.it or amenitsch@elettra.trieste.it

Users and institutes performing experiments in 2009

Australia

CSIRO, Division of Materials Science & Engineering, Clayton
FALCARO Paolo

Monash University, Victorian College of Pharmacy, Dept.of Pharmaceutics, Parkville
VIC

BOYD Ben J.
DONG Yao-Da
TILLEY Adam

Austria

Austrian Academy of Science, Institute of Biophysics and Nano-systems Research,
Graz

AMENITSCH Heinz
BERTONI Ambra
BOULGAROPOULOS Beate
CACHO-NERIN Fernando
IBRAHIMKUTTY Shyjumon
KRIECHBAUM Manfred
JUNGNIKL Karin
LAGGNER Peter
MARMIROLI Benedetta
PABST Georg
RAPPOLT Michael
SARTORI Barbara

Austrian Institute of Technology, Department of Health & Environment, Seibersdorf
JERABEK H.

Medical University of Vienna, Department of Medical Chemistry, and Austrian Institute
of Technology, Department of Health & Environment, Seibersdorf
STOCKNER T.

Graz University of Technology, Institute for Chemistry and Technology of Organic
Materials, Graz
LARISSEGGER Sonja

Graz University of Technology, Institute for Chemistry and Technology of Materials,
Graz, and Christian Doppler Laboratory for Nanocomposite Solar Cells
EDLER Michael
FISCHEREDER Achim
PEIN Andreas
RATH Thomas
TRIMMEL Gregor

Graz University of Technology, Institute for Electron Microscopy and Fine Structure
Research, Graz, and Christian Doppler Laboratory for Nanocomposite Solar Cells
HAAS Wernfried

University of Vienna, Faculty of Physics, Dep. Physics of Nanostructured Materials
KERBER Michael B.
SCHAFLER Erhard
SCHUSTER Roman
SPIECKERMANN Florian
ZEHETBAUER Michael J.

Canada

Université du Québec, INRS, Varennes, Québec
BROWN Cameron P.

Croatia

Institute of Physics, Zagreb
KREGAR Z.
KRSTULOVIĆ N.
MILAT Ognjen
MILOŠEVIĆ S.
SALAMON Krešimir

"Ruder Bošković" Institute, Zagreb
BOGDANOVIĆ-RADOVIĆ I.
BULJAN Maya
DESNICA Uroš
DUBČEK Pavo
GAJOVIĆ Andreja
GRACIN, Davor
JERČINOVIĆ Marko
JURAIĆ Krunoslav
KARLUŠIĆ M.
LONČARIĆ Martin
PIVAC Branko
RADIĆ Nikola
SANCHO-PARRAMON Jordi
TURKOVIC Aleksandra
ZORC Hrvoje
ZORIC Nedeljko

University of Split, Faculty of Chemistry and Technology, Split
JOZIC Drazen
LUCIC LAVCEVIC Magdy

University of Zagreb, Faculty of Science, Department of Physics
DJERDJ Igor

Czech Republic

Charles University, Faculty of Mathematics and Physics, Prague
HOLY Vaclav

University of Pardubice, Department of Physics, Pardubice, and Academy of Sciences
of the Czech Republic, Institute of Macro-molecular Chemistry, Prague
STEINHART Milos

France

Université de Paris-sud, Laboratoire de Physico-Chimie des Systèmes Polyphasés,
UMR CNRS, Chatênay-Malabry
FAIVRE Vincent

Université Paris 6, Chimie de la Matière Condensée, Paris
FAUSTINI Marco
GROSSO David

Université d'Orléans, Centre de Recherche sur la Matière Divisée
SINTUREL Christophe
VAYER Marylène

Germany

Forschungszentrum Borstel, Borstel
BRANDENBURG Klaus
GUTSMANN T.
HOWE Joerg
KACONIS K.Y.

Max-Planck-Institute for Coal Research, Mülheim / Ruhr
SCHMIDT Wolfgang

University of Bremen, Institute for Applied and Physical Chemistry
BäUMER Marcus
RöHE Sarah

University of Bremen, Institute of Solid State Physics
FALTA Jens
SCHMIDT Thomas Jr.
ZARGHAM Ardalan

University Erlangen-Nuremberg, Institute of Crystallography and Structural Physics,
Erlangen
MAGERL Andreas

University of Munich, Department of Chemistry and Biochemistry and Center for NanoScience

BEIN T.
DöBLINGER Markus
KEILBACH Andreas
KöHN Ralf
LI Yan
LOTSCH Bettina V.
MANDLMEIER Benjamin
SCHUSTER Joerg
SZEIFERT Johann Martin

Greece

University of Athens, Chemistry Department
CHATZIGEORGIOU Petros
MAVROMOUSTAKOS Thomas

India

Indian Association for the Cultivation of Science, Department of Materials Science, Jadavpur, Kolkata

ACHARYA Somabrata
SENGUPTA Sucheta

Indian Institute of Science, Solid State and Structural Chemistry Unit, Bangalore

DATAR S.S.
SANTRA Pralay Kanti
SAPRA Sameer
SARMA Dipankar Das
VISWANATHA Ranjani

Israel

The Hebrew University of Jerusalem, Institute of Chemistry

RAVIV Uri
SELA Or
SZEKELY Pablo

Italy

C.N.R. - Istituto di Biofisica (I.B.F.), Unita' di Genova

MORAN Oscar

CNR - Istituto di Biofisica (I.B.F.), Unita' di Palermo

MARTORANA Vincenzo

CNR, Istituto di Chimica e Tecnologia dei Polimeri, Pozzuoli

DURACCIO Donatella

CNR - ISMN, Bologna
GRECO Pierpaolo

C.N.R. - IMM, Bologna
LISCIO Fabiola
MILITA Silvia

CNR - Institute of Material Structure, Monterotondo, Rome
MARI Alessandra
SUBER Lorenza

CNR - Institute of Crystallography, Monterotondo, Rome
CAMPI Gaetano
PIFFERI Augusto

INFN - CNR National Laboratorio, TASC, Trieste
GRENCI Gianluca

Maxun s.r.l., Trieste
ANTONIOLLI Francesca
RADIVO Andrea

Sincrotrone Trieste, Trieste
BERNSTORFF Sigrid
MORELLO Christian

SISSA-ELETTRA NanoInnovation Lab, SISSA-ISAS, Trieste
CASALIS Loredana
SCOLES Giacinto

SISSA-ISAS (International School of Advanced Studies), Laboratory of Prion Biology,
Neurobiology Sector, Basovizza/Trieste
BENETTI Federico

S.I.S.S.A.-I.S.A.S. Unit, Italian Institute of Technology, Trieste
LEGNAME Giuseppe

Università di Cagliari, Dip. di Scienze Chimiche, Monserrato
CASULA Maria Francesca

Università di Padova, Dep. of Organic Chemistry, Padova
CARRARO Mauro

University of Padova, Department of Chemical Sciences, and ITM-CNR, Padova
SARTOREL Andrea
CARRARO Mauro
SCORRANO G.
BONCHIO Marcella

Università Politecnica delle Marche, Depart. SAIFET, Physical Science Section,
Ancona

BALDASSARRI Enrico
BURATTINI Danilo
MARIANI Paolo
MAZZONI Serena
SPINOZZI Francesco

University of Rome II, Science Department, Rome
VITTORINI ORGEAS Alessandra

University of Rome “La Sapienza”, Department of Chemistry
CARACCILO Giulio
POZZI Daniela

Università di Roma “La Sapienza”, Dip. di Fisica
COPPOLA Stefano

Università di Sassari, Laboratorio di Scienza dei Materiali e Nanotecnologie, CR-
INSTM, D.A.P., Alghero

INNOCENZI Plinio
MALFATTI Luca
MARONGIU Daniela

University of Trieste, Center of Excellence for Nanostructured Materials (CENMAT),
INSTM and Department of Pharmaceutical Sciences, Trieste

Da ROS Tatiana
PRATO Maurizio
TOMA Francesca Maria

University of Trieste, Department of Materials and Natural Resources

BATTISTON M.
COZZARINI Luca
LUGHI Vanni

Portugal

University of Lisbon, Physics Department, and ICEMS, Lisbon
CONDE O.

Universidade do Minho, Centro de Física, Braga

GOMES Maria.J.M.
LEVICHEV Sergey
PINTO Sara R. C.
ROLO Anabela G.
VIEIRA Eliana M. F.

Russia

Institute of Solid State Chemistry, Ural Branch of the Russian Academy of Sciences,
Ekaterinburg

REMPEL Andrey

Slovenia

Josef Stefan Institute, Ljubljana

ČEH M.

DRAŽIĆ G.

University of Ljubljana, Faculty of Electrical Engineering, Laboratory of Biophysics

IGLIC Aleš

PERUTKOVÁ Šárka

Spain

Consejo Superior de Investigaciones Científicas - Centro de Investigación y Desarrollo,
Barcelona

AUBERY Carolina

Sweden

Life Science and Chemical Industries Section YKI,

Ytkemiska Institute AB (YKI, Institute for Surface Chemistry), Stockholm,

KALNIN Daniel

University of Lund, Institute for Physical Chemistry 1

DAHLENBORG Hanna

United Kingdom

University of Edinburgh, Royal (Dick) School of Veterinary Studies

BRADSHAW Jeremy P.

KE Li Jing

SA'ADEDIN Farid

University of Manchester, School of Chemical Engineering and Analytical Science

MASTERS Andrew

SINTYUREVA Marina

TIDDY G.J.T.

DUTTON Helen

University of Newcastle, Medical School, Institute for Cell and Molecular Biosciences,
Newcastle-upon-Tyne

JOHNSON Christopher

LAKEY Jeremy H.

RIDLEY Helen

SOLOVYOVA Alexandra

University of Reading, Polymer Science Centre, Whiteknights, Reading

DAVIS Fred J.

MITCHELL Geoffrey R.

OLLEY Robert H.

List of Performed Experiments

2009 (first half year)

Proposal	Proposer	Institution	Country	Title	Research Area
20085077	CARACCIOLO Giulio	Uni of Rome "La Sapienza", Chemistry Department	Italy	Cytoskeletal involvement in the lipid-mediated intracellular trafficking of plasmid DNA	Life Sciences
20085091	BRADSHAW Jeremy	Uni. of Edinburgh, Dept. Preclinical Veterinary Sciences	United Kingdom	Temperature-sensitive liposomes	Life Science
20085134	TRIMMEL Gregor	Technical Uni Graz, Inst. for Chem. and Technology of Organic Materials	Austria	Formation of metal chalcogenides nanoparticles in solution studied in-situ by TR- SWAXS	Chemistry
20085145	TURKOVIC Aleksandra	Ruder Bošković Institute, Zagreb	Croatia	Study of Polymer Electrolyte for Zn Rechargeable Nanostructured Galvanic Cells via Combined in- situ SAXS/DSC/WAXD Measurements	Materials Science
20085150	BOULGARO- POULOS Beate	Austrian Academy of Sciences, Inst. of Biophysics and X-Ray Structure Research (AAS, IBR), Graz	Austria	Effect of Sphingomyelinase on Sphingomyelin containing Lipid Model Membranes	Life Sciences
20085170	DESNICA Uros	Ruder Bošković Institute, Zagreb	Croatia	Optimization of growth of three- dimensional superlattices from Ge quantum dots	Materials Science
20085173	MORAN Oscar	C.N.R., Institute for Biophysics, Genoa	Italy	Structural features of the nucleotide binding domain to the CFTR by small angle x ray scattering	Life Sciences
20085184	BOYD Ben	Monash Univ. , Dept. of Pharmaceutics, Parkville, Victoria	Australia	Properties and structure of adsorbed liquid crystalline particles and thin liquid crystalline particle films.	Life Science
20085194	SCHAFLER Erhard	Uni Vienna, Inst. for Material Physics	Austria	In-situ thermal treatment of ultrafine-grained metals produced by sever plastic deformation	Materials Science

20085211	MARMIROLI Benedetta	AAS, IBR, Graz	Austria	Study of Ultrafast Nucleation and Growth of Calcium Carbonate in Presence of a Polyelectrolyte Additive by SAXS	Materials Science
20085240	TRIMMEL Gregor	Technical Uni Graz, Inst. for Chem. & Technology of Organic Materials	Austria	Thermal formation of thin layers of metal sulfide nanoparticles and metal sulfide nanoparticle/polymer composites: a time resolved X-ray scattering study	Chemistry
20085247	CACHO NERIN Fernando	AAS, IBR, Graz	Austria	Assessment of nonaffine kinematics for the main arterial layers	Life Sciences
20085285	DUBCEK Pavo	Ruder Bošković Institute, Zagreb	Croatia	Ge quantum dots internal strain study by GID/GISAXS	Materials Science
20085316	IBRAHIM- KUTTY Shyjumon	AAS, IBR, Graz	Austria	Study of Evaporation controlled mesophases of Silica using in situ SAXS	Materials Science
20085326	TOMA Francesca Maria	SISSA, Trieste	Italy	Structural evolution of new catalysts and materials for artificial photosynthesis studied with in situ TRSAXS	Chemistry
20085346	MARIANI Paolo	Polytechnical Univ. delle Marche, Ancona	Italy	Analysis of mechanical properties of guanosine-guanine nanowires in aqueous solution by high-pressure X-ray diffraction	Life Sciences
20085365	SCHMIDT Thomas Jr.	Uni Bremen, Institute of Solid State Physics	Germany	Ordering of CoPt ₃ nanoparticles on organic self-assembled monolayers	Materials Science
20085366	CAMPI Gaetano	CNR, Inst. of Crystallography, Monterotondo (Rome)	Italy	Liquid crystal template for silver nanoparticle superstructures	Chemistry
20085423	GRACIN Davor	Ruder Bošković Institute, Zagreb	Croatia	Origins of quantum confinement effects in thin film solar cells materials	Materials Science
20085470	LUGHI Vanni	Uni Trieste, Department of Chemistry	Italy	Self-assembly of II-VI nanocrystals into 3D superlattices: characterization of different experimental protocols by means of SWAXS studies	Materials Science
Inhouse research	AMENITSCH Heinz & BENETTI Federico	AAS, IBR, Graz & SISSA, Section of Neurobiology, Trieste	Austria & Italy	SAXS analysis of Syrian hamsters PrP ²⁷⁻³⁰ fibers	Life Sciences
Inhouse research	AMENITSCH Heinz & SCHUSTER Joerg	AAS, IBR, Graz & Uni-versity of Munich, Dept. of Chemistry & Biochemistry	Austria & Germany	In situ 2D-SAXS characterization of the mesostructure formation for spin-coated carbon thin films with variable nitrogen content.	Chemistry

Inhouse research	BERNSTORFF Sigrid & PAVLOVIC Mladen	Sincrotrone & Ruder Bošković Institute, Zagreb	Italy & Croatia	Morphology study of metal islands films via simultaneous GISAXS, GIWAXD and GIXR techniques	Materials Science
Inhouse research	BERNSTORFF Sigrid & PIVAC Branko	Sincrotrone & Ruder Bošković Institute, Zagreb	Italy & Croatia	Si quantum dots production in silicon nitride/Si rich silicon nitride multilayers: process characterization & optimization	Materials Science
Inhouse research	BERNSTORFF Sigrid & LUCIC-LAVCEVIC Magdy	Sincrotrone & Uni Split, Faculty of Chemical Technology	Italy & Croatia	Analysis of nanostructures in metal oxide thin films by simultaneous application of the GISAXS and GIXRD techniques	Materials Science

2009 (second half year)

Proposal	Proposer	Institution	Country	Title	Research Area
20090037	INNOCENZI Plinio	Uni Sassari	Italy	In situ study of self-assembled titania films with tunable multimodal porosity	Chemistry
20090044	KALNIN Daniel	C.N.R.S., Uni Paris Sud	Sweden	Structuring through Lipid Self-Assembly and Processing	Life Sciences
20090086	PIVAC Branko	Ruder Bošković Institute, Zagreb	Croatia	Si QD production in silicon nitride/Si rich silicon nitride multilayers: process characterization and optimization	Materials Science
20090087	MITCHELL Geoffrey	University of Reading, Dept. of Physics	United Kingdom	Dispersion and Crystallisation in Polymer Nanocomposites	Materials Science
20090099	JUNGNIKL Karin	AAS, IBR, Graz	Austria	Study of the initial stages of evaporation controlled mesophase formation of Silica using in-situ SAXS	Life Sciences
20090107	SOLOVYOVA Alexandra	Inst. for Cell & Molecular Bio-sciences, Uni of New-castle upon Tyne	United Kingdom	Conformational Reorganisation of a Bacterial Signalling Protein Following Photo activation	Life Sciences
20090109	MITCHELL Geoffrey	University of Reading, Dept. of Physics	United Kingdom	Directing the crystal morphology of polymers using xylitol derivatives	Materials Science
20090117	SZEIFERT Johann	University of Munich, Dept. of Chemistry & Biochemistry	Germany	In situ 2D SAXS characterization of anatase nanocrystal growth in amorphous walls of bricks and mortar mesoporous thin films	Chemistry

20090125	SCHUSTER Joerg	University of Munich, Dept. of Chemistry and Biochemistry	Germany	In situ 2D-SAXS characterization of the mesostructure formation of ordered mesoporous carbon within the vertical channels of anodic alumina membranes	Chemistry
20090129	MASTERS Andrew	University of Manchester	United Kingdom	Novel Structures in Chromonic Liquid Crystals. (EPSRC EP/19404/1, EP19412/1, EP19420/1)	Chemistry
20090171	PABST Georg	AAS, IBR, Graz	Austria	Effects of a Cholesterol Metabolic Precursor on Physical Properties of Biomimetic Membranes	Life Sciences
20090182	BROWN Cameron	Uni of Rome "Tor Vergata", Dep. of Sciences and Chemical Tecnologies	Italy	Transient stress processing in spider silk - SAXS	Life Sciences
20090206	MARMIROLI Benedetta	AAS, IBR, Graz	Austria	Study of Fast Nucleation and Growth of Calcium Carbonate in Presence of Additives by SAXS	Materials Science
20090235	BENETTI Federico	SISSA / ISAS, Section of Neurobiology, Trieste	Italy	A SAXS study of recombinant prion protein oligomers	Life Sciences
20090237	MILITA Silvia	CNR, Institute IMM, Bologna	Italy	In-situ study of amyloid peptide self-assembly process in micro- confined environments	Life Sciences
20090353	REMPEL Andrey	Uni Erlangen- Nürnberg, Dep. for Crystallography and Physics of Structures	Germany	The birth and growth of nanoparticles in solution observed by small angle scattering	Materials Sciences
20090398	SARMA Dipankar Das	Indian Institute of Science, Bangalore	India	In-situ SAXS studies of chemically programmed ordered two dimensional semiconductor superlattice arrays	Chemistry
20090410	RAVIV Uri	Hebrew University, Inst. of Chemistry, Jerusalem	Israel	Following the time-dependent structural changes during the self-assembly process of SV40 virus	Life Sciences
20090434	LUCIC- LAVCEVIC Magdy	Uni Split, Faculty of Chemical Technology, Dept. of Physics	Croatia	Analysis of nanostructures in metal oxide thin films by simultaneous application of the GISAXS and GIXRD techniques	Materials Science

20090465	GRACIN Davor	Ruder Bošković Institute, Zagreb	Croatia	Origins of quantum confinement effects in thin film solar cells materials – extension the experiment	Materials Science
20090483	SCHMIDT Wolfgang	Max Planck Institute for Coal Research, Mülheim / Ruhr	Germany	Gas adsorption on CMK-n type carbon investigated by in-situ SAXS	Materials Science
Inhouse research	BERNSTORFF Sigrid & DUBCEK Pavo	Sincrotrone & Ruder Bošković Institute, Zagreb	Italy & Croatia	Structural study of pulsed laser deposited GaAs	Materials Sciences
Inhouse research	BERNSTORFF Sigrid & GOMES Maria	Sincrotrone & Uni. of Minho, Dep. of Physics, Braga	Italy & Portugal	GID and GISAXS investigations of flash memory structures based on semiconductor nanocrystals	Materials Sciences
Inhouse research	BERNSTORFF Sigrid & KHODOROV Anatoli	Sincrotrone & Uni. of Minho, Dep. of Physics, Braga	Italy & Portugal	GISAXS and GIXRD study of Mn doped ZnO ferromagnetic nanostructures	Materials Science
Inhouse research	RAPPOLT Michael & MAVROMOUSTAKOS Thomas	AAS, IBR, Graz & Uni of Athens, Dept. of Chemistry	Austria & Greece	The examination of the possible relation between the extent of interdigitation and antihypertensive activity	Life Sciences
Inhouse research	RAPPOLT Michael & BRADSHAW Jeremy	AAS, IBR, Graz & University of Edinburgh, Dept. Preclinical Veterinary Sciences	Austria & United Kingdom	Mechanism of Anti-influenza Virus Activity of Traditional Chinese Medicines	Life Sciences
Inhouse research	RAPPOLT Michael & BRANDENBURG Klaus	AAS, IBR, Graz & Research Center Borstel	Austria & Germany	Conformational studies on bacterial virulence factors and interaction with binding proteins and antimicrobial peptides	Life Sciences
Inhouse research	BERNSTORFF Sigrid & LUGHI Vanni	Sincrotrone & Uni Trieste, Dep. Chemistry of Materials and Applied Chemistry	Italy	Characterization of 3D close-packed semiconductor nanocrystal assemblies and of multiphase nanostructured materials by means of static and time-resolved SWAXS	Materials Science
Inhouse research	AMENITSCH Heinz & GROSSO David	AAS, IBR, Graz & Uni Paris 6, Chemistry of Condensed Matter	Austria & France	Structural characterization of flexible thin films of Nanoporous Metal-Organic Frameworks	Chemistry
Inhouse research	BERNSTORFF Sigrid & ZORC Hrvoje	Sincrotrone & Ruder Bošković Institute, Zagreb	Italy & Croatia	GISAXS study of gold nanoparticles on BK7 glass and predeposited oxides	Materials Science

User Statistics

1. Number of submitted proposals and assigned shifts from 1995 until December 2010

The Austrian SAXS-beamline at ELETTRA opened to users in September 1996. Since then many experiments have been performed related to the fields of life science, materials science, physics, biophysics, chemistry, medical science, technology and instrumentation.

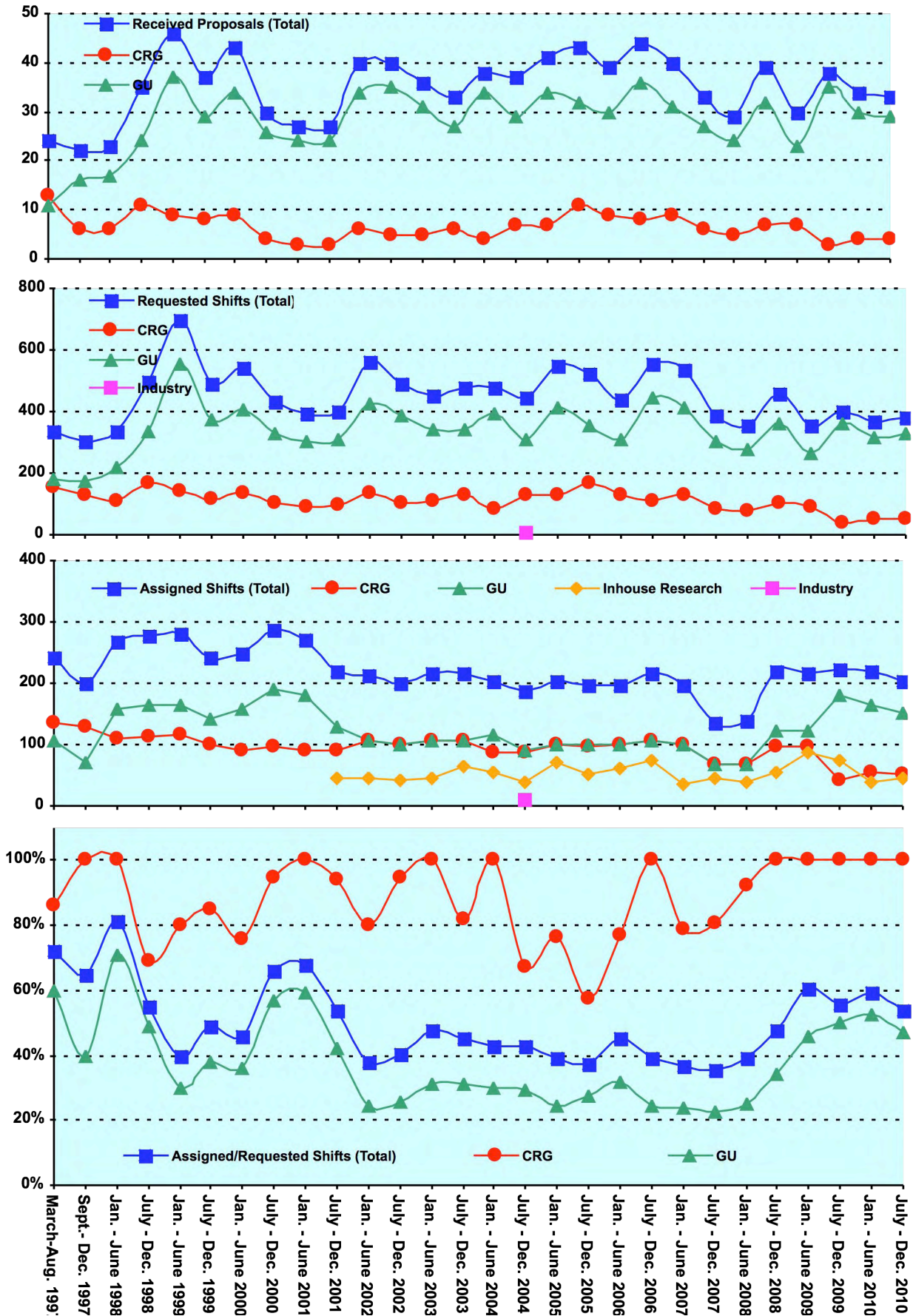
The assignment of beamtime at this beamline is done separately for the group of "General Users" (GU) and the "Collaborating Research Group" (CRG), i.e., the Austrian users. Beamtime was assigned to the proposals of each group in the order of the rating received by the Scientific Committee, and up to the maximum number of shifts available to each group according to the contract between "The Austrian Academy of Sciences" and the "Sincrotrone Trieste". Until December 1997 up to 30 % of the beamtime was given to CRG, up to 55 % to GU, and 15% was reserved for maintenance purposes. From January 98 to June 2001 the quota for beamtime was up to 35 % for CRG, up to 50 % for GU, and again 15% reserved for maintenance purposes. From July 2001 on the two contingents for user proposals from CRG and GU receive up to 35% of the beamtime each. The remaining 30 % of beamtime are used for inhouse research projects as well as for maintenance purposes.

Figure 1 gives an overview of the numbers of received proposals, the numbers of requested and assigned shifts, as well as the percentage between assigned and requested shifts during the last years. As can be seen in Fig.1, the request for beamtime at the SAXS-beamline increased strongly until the first half year of 1999. Then, probably due to the high rejection rates, the number of submitted proposals decreased somewhat during 2001, which resulted in a better ratio of accepted / rejected proposals. This oscillating behaviour of beamtime request can also be seen for the period 2002 – 2010 where after higher numbers of submitted proposals slightly reduced request periods follow. The numbers for the second semester of 2007 and first of 2008 reflect also that, due to the long shut-down from 1.10.2007 to 3.03.2008 (for the booster installation) less proposals were submitted, and less beamtime was available.

In 2009, in total 68 proposals (10 from CRG, and 58 from GU) were submitted. From these 13 proposals (1 from CRG and 12 from GU) were submitted by "new" usergroups, i.e. groups which so far had never beamtime at the SAXS beamline. From these, 1 CRG and 8 GU proposals were accepted by the review committee.

Figure 1 (Next page). The statistical information about the beamtime periods since end of 1995 are given for the groups "CRG", and "GU" separately, as well as for both together ("Total"). Shown are, for all beamtime periods (from top to bottom):

- Number of received proposals, ● Number of requested shifts,
- Number of assigned shifts, and ● Relation between assigned and requested shifts



2. Provenience of users

During 2009, 165 users from 63 institutes in 17 countries have performed experiments at the SAXS beamline. In Fig. 2 are shown both the provenience of these users, and of their respective institutes. Each user or institute was counted only once, even though many users performed experiments in both beamtime periods of 2009.

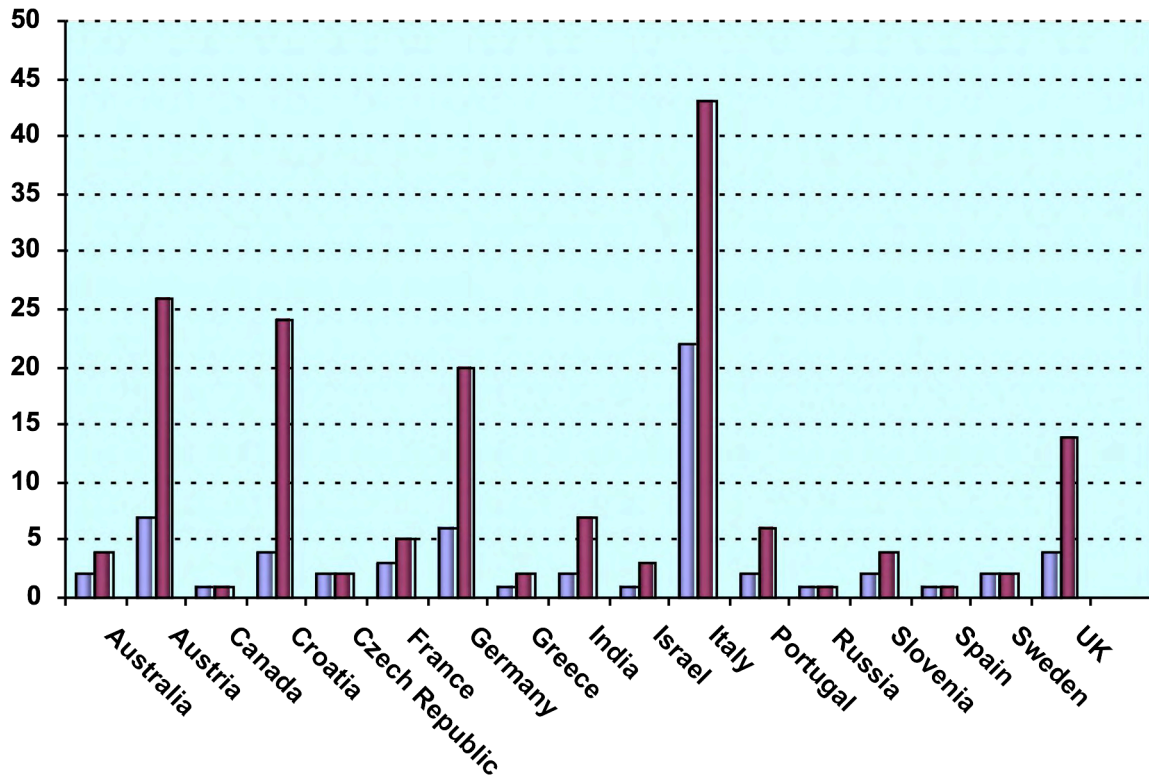


Figure 2. Nationality of the Austrian SAXS beamline users in the year 2009. The number of users (red) and the corresponding number of institutes (blue) are shown for each country.

3. Documentation of experimental results

As could be expected, with the start of user-operation at the SAXS-beamline the number of contributions to conferences started to increase strongly. With a delay of one year - the average time needed for paper publications - also the number of publications increased accordingly, as can be seen in Fig. 3.

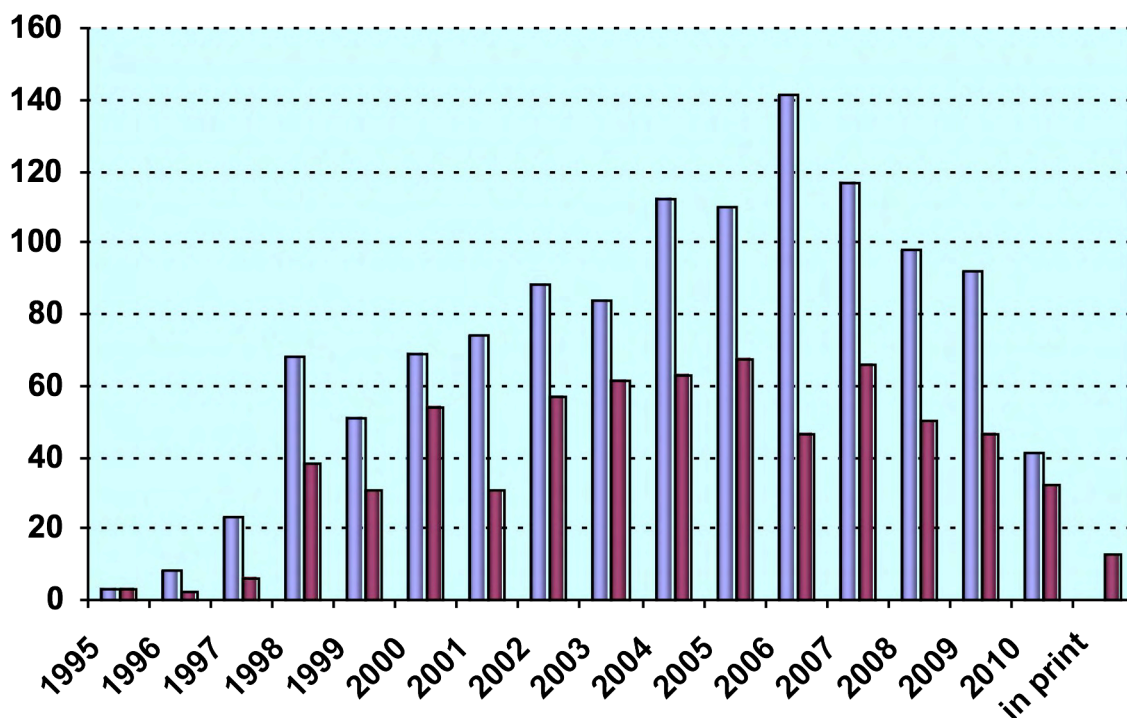


Figure 3. Number of conference contributions (blue) and of refereed paper publications (red) for the years 1995-2009. Also contributions, which have been published until June 2010 as well as those in print at that time are included.

In addition, from 1995 until June 2010, the following documentations based on instrumentation of the SAXS-beamline, or on data taken with it, have been produced:

Unrefereed publications:

Technical Reports on Instrumentation: 5

Contributions to Elettra Newsletters: 15

Contributions to Elettra Highlights: 33

Habil Thesis: 4

PhD Thesis: 79

Master Thesis: 39

Experimental Possibilities at the SAXS-beamline

1. ACCESSIBLE SAXS AND WAXS RANGES

Simultaneous SAXS- and WAXS-measurements can be performed using a linear sensitive gas detector (Gabriel type, windows size 8 x 100 mm, active length 86.1 mm with a resolution of 0.135 mm/channel) for the WAXS-range, and either a second linear Gabriel type detector (windows size 10 x 150 mm, active length 134 mm with a resolution of 0.159 mm/channel), or the 2D CCD-system for the SAXS-range. A specially designed vacuum chamber (SWAXS-nose, see Annual Report of 1996/97, p. 32) allows to use both scattering areas below (for SAXS) and above (for WAXS) the direct beam, respectively.

Depending on the photon energy maximum SAXS resolutions of 2000 Å (5.4 keV), 1400 Å (8 keV) or 630 Å (16 keV) are available. The available possible WAXS-ranges are summarised in Table 1. The overall length of the SWAXS-nose in the horizontal direction, measured from the sample position, is 512 mm and the fixed sample to WAXS-detector distance is 324 mm. At the shortest SAXS camera-length an overlap in the d-spacings covered by the SAXS- and WAXS-detectors, respectively, is possible: then, the common regime lies around 9 Å.

Range	2θ [deg]	d-spacing (Å)		
		8 keV	5.4 keV	16 keV
1	9.4	<i>9.40</i>	14.03	4.27
	27.6	3.23	4.82	1.47
2	27.4	3.25	4.86	1.48
	45.6	1.99	2.97	0.90
3	45.4	2.00	2.98	0.91
	63.6	1.46	2.18	0.66
4	63.4	1.47	2.19	0.67
	81.6	1.18	1.76	0.54

Table 1. Possible d-spacing ranges in the WAXS-regime at the SAXS-beamline at ELETTRA. Since the WAXS-detector can be mounted at four different fixed positions on the SWAXS-nose (range 1-4), with the three possible energy choices (5.4, 8 and 16 keV) this results in 12 different d-spacing regimes. In italic the most common choice (8 keV, range 1) is highlighted. This range is suited for experiments, e.g., on lipid-systems and (bio)polymers.

2. CALIBRATION OF THE S-AXIS AND FLAT FIELD CORRECTION

At the SAXS beamline various standards are used for the angular (s-scale) calibration of the different detectors:

- Rat tail tendon for the SAXS detector - high resolution (rtt*.dat)
- Silver behenate for the SAXS detector – medium and low resolution (agbeh*.dat)
- Para-bromo benzoic acid for the WAXS detector – WAXS range 1 and 2 (pbromo*.dat)
- Combination of Cu, Al foils and Si powder for the WAXS detector – WAXS range 2 and higher

In Figure 1 a typical diffraction pattern of rat tail tendon is shown, depicting the diffraction orders (from the first to the 14th order) measured with a "high" resolution set-up (2.3 m) and the delay-line gas detector. The d-spacing is assumed to be 650 Å, but this value can vary depending on humidity up to 3%. Thus, the rat tail tendon is often used only to determine the position of the direct beam (zero order), while the absolute calibration is performed using the diffraction pattern of Silver behenate powder. Fig. 2 depicts a diffraction pattern of Silver behenate measured with "medium" resolution set-up (1.0 m) from the first to the 4th order (repeat spacing 58.4 Å) [1].

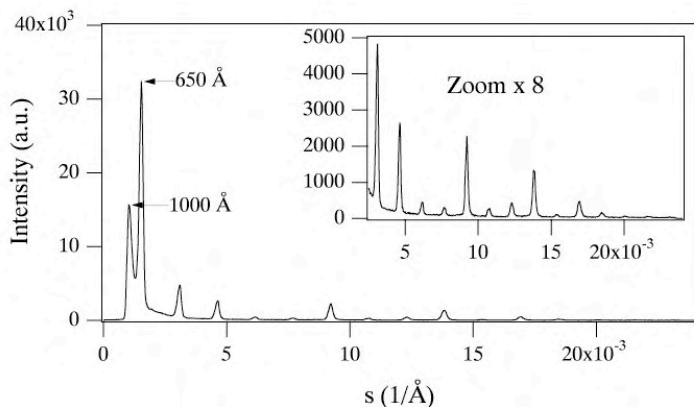


Figure 1. SAXS diffraction pattern of the collagen structure of rat tail tendon fibre at a distance of 2.3 m

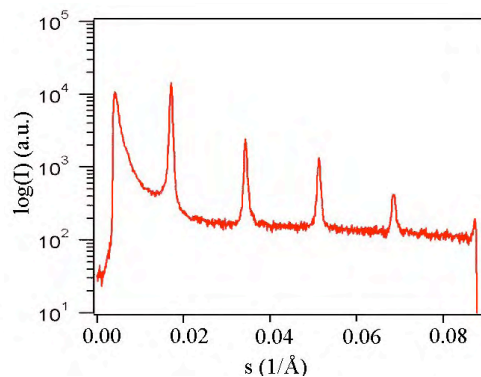


Figure 2. SAXS diffraction pattern of Ag behenate powder at a distance of 1.0 m

In Figure 3 a typical WAXS pattern of p-bromo benzoic acid is shown. The diffraction peaks are indexed according to the values given in Table 2, taken from [2].

d-spacing/Å	rel. intensity	d-spacing/Å	rel. intensity
14.72	18000	4.25	490
7.36	1200	3.96	2380
6.02	330	3.84	10300
5.67	980	3.74	26530
5.21	6550	3.68	1740
4.72	26000	3.47	760

Table 2. d-spacings and relative intensities of p-bromo benzoic acid according to [2].

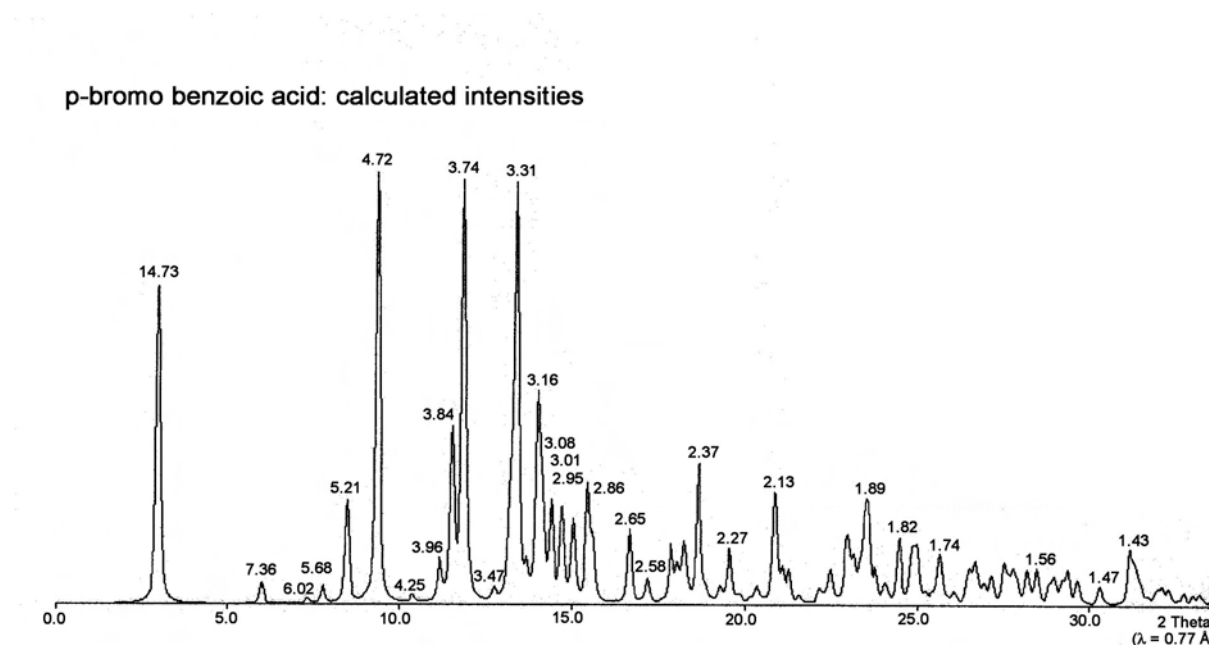


Figure 3. Calculated diffraction pattern of p-bromo benzoic acid. d-spacings are given in Å.

The s-scale for both, the SAXS and the WAXS range, can be obtained by linear regression, i.e., the linear relation between the known s-values of the calibrant versus the measured peak positions has to be found.

A further correction is regarding the flat field response (efficiency) of the detectors. For this correction, the fluorescence light of various foils are used to illuminate the detectors rather homogeneously:

At 8 keV: iron foil (100 µm thick), fluorescence energy: 6.4 keV K_{α} , 7.1 keV K_{β} (effic*.dat)

At 16 keV: copper foil (> 100 µm thick), fluorescence energy: 8.028 keV $K_{\alpha 2}$, 8.048 keV $K_{\alpha 1}$, 8.905 keV K_{β} (effic*.dat)

The measured scattering pattern are corrected for the detector efficiency simply by dividing them by the fluorescence pattern. Note: The average of the detector efficiency data should be set to unity and a small threshold should be applied to avoid any division by zero.

[1] T.N. Blanton et. al., Powder Diffraction 10, (1995), 91

[2] K. Ohura, S. Kashino, M. Haisa, J. Bull. Chem. Soc. Jpn. 45, (1972), 2651

3. SITE LABORATORIES

In August 2002 our new chemistry and X-ray laboratory went into operation. The 70 m² big laboratory is divided in two parts, in which the bigger share of 43 m² is occupied by the chemistry lab. This unit serves mainly for sample preparation and analysis for both, in house research and external SAXS user groups. In the X-ray laboratory the set-up of a SWAX camera for simultaneous small and wide angle scattering has been completed (Hecus X-ray Systems, Graz, Austria: www.hecus.at), which allows on-site testing of samples before moving on to the SR beamline. The chemistry lab is meanwhile equipped with:

- micro centrifuge (max. 13200 rpm; model 5415D from Eppendorf , Hamburg, Germany)
- Chemical fume hood, equipped with a carbon filter for general organic solvents (model GS8000 from Strola, Italy)
- vacuum drying oven (min. pressure 1 mbar; max. T: 200 °C, precision +/- 0.4°C; Binder WTB, Tuttlingen. Germany)
- balance (min.-max.: 0.001 - 220g; model 770 from Kern & Sohn, Balingen, Germany)
- Magnetic stirrer with heating plate and thermometer, temp max 260°C
- vortex for microtubes (model MR 3001 and REAX; both from Heidolph, Schwabach, Germany)
- two water baths :
 - Unistat CC, freely programmable in the range from -30 to 100°C (Huber, Offenburg, Germany);
 - Lauda M3, available for heating only (Lauda-Könighofen, Germany)
- ultrasonic bath with water heater (VWR International, Milano, Italy)
- Ultrasonic processor equipped with a 3 mm probe (Sonics VCX130, SY-LAB Geräte GmbH, Germany)
- HPLC pump, Pharmacia LKB; working range, 0,01-9,99 ml/min, 0,1-40MPa
- HPLC pump, Gilson 307; working range, 0,01- 5 ml/min, 0,1-60MPa
- three syringe pumps, low pressure; flow rate range, 1µl/hr – 2120 ml/hr
- four syringe pumps, high pressure: P max ~ 60 bar
- three high pressure infusion modules: P max ~ 690 bar

Further, four working benches (one with a water sink), two fridges (+ 4°C) and a separate freezer (- 20 °C), standard glassware, syringes and needles of different sizes, µ-pipettes (p10 - p100 - p200 - p1000), as well as some standard chemical reagents (e.g., chloroform, ethanol, methanol); deionized water (milli-RO and ultrapure milli-Q water) is available.



Figure 4. View of the Chemistry laboratory (left) and X-Ray laboratory (right).

4. AVAILABLE SAMPLE MANIPULATIONS STAGES

1. General

Usually the sample is mounted onto the sample alignment stage which allows the user to place the sample into the beam with a precision of $5\mu\text{m}$ (resolution: $1\mu\text{m}$). In Fig. 5 the ranges for vertical and horizontal alignment as well as the maximum dimensions of the sample holders are given. The maximum weight on the sample stage is limited to 10 kg. In case the envelope dimensions of a sophisticated sample station provided by the users are slightly larger than those given in Fig. 5, the user can ask the beamline responsible for a check up of his space requirements. If it does not fit at all to these specifications, user equipment can also be mounted directly onto the optical table, which allows much larger spatial dimensions.

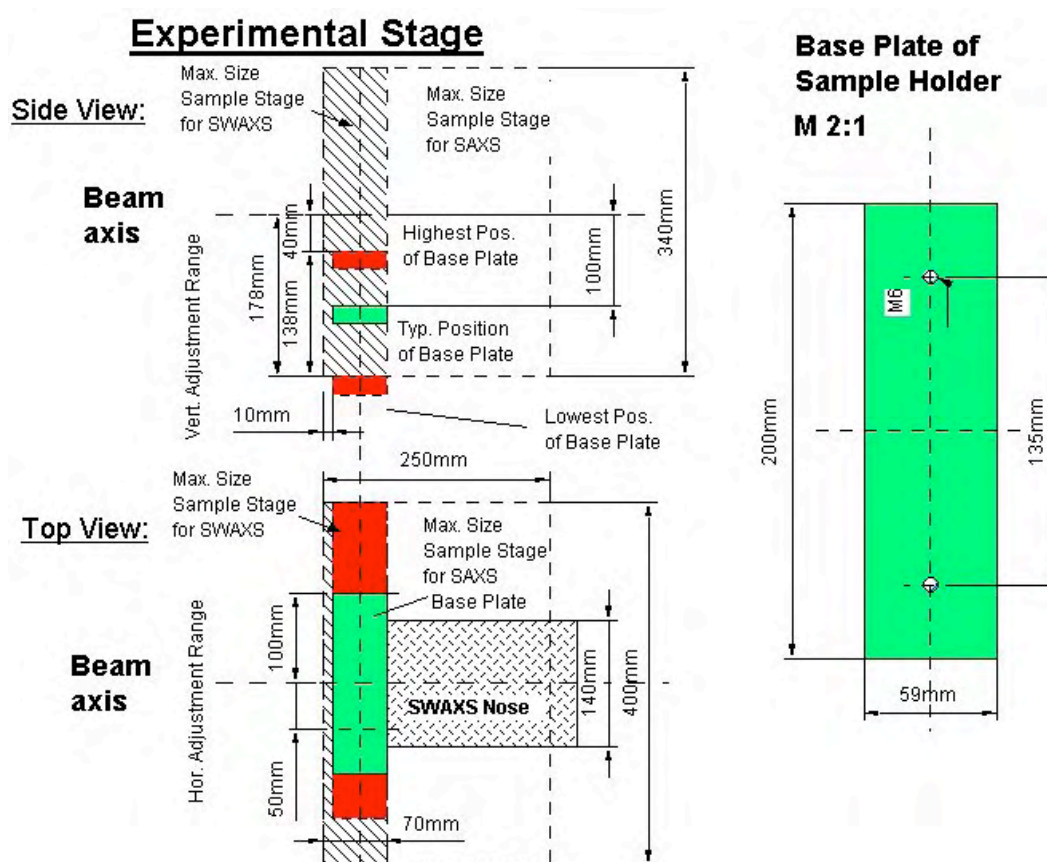


Figure 5. Maximum dimensions and alignment range of the sample holder to be mounted via a base-plate onto the standard alignment stage (left), and dimensions of the base-plate (right).

2. Sample Holders

As standard equipment for liquid samples Paar capillaries (diameter: 1 and 2 mm) are used thermostated with the KPR (Peltier heating/cooling) sample holders (Anton Paar, Graz, Austria). For use in these sample holders flow through capillaries and Gel holders are standard equipment. Temperature scans can be performed with KPR (-30 – 70 °C). Typically the precision and the stability of this systems is 0.1 °C. Additionally thermostats for temperature control or cooling proposes can be used at the beamline (-40 – 200 °C). Helium and Nitrogen gas bottles are available at the beamline, for other gases please contact the beamline responsible.

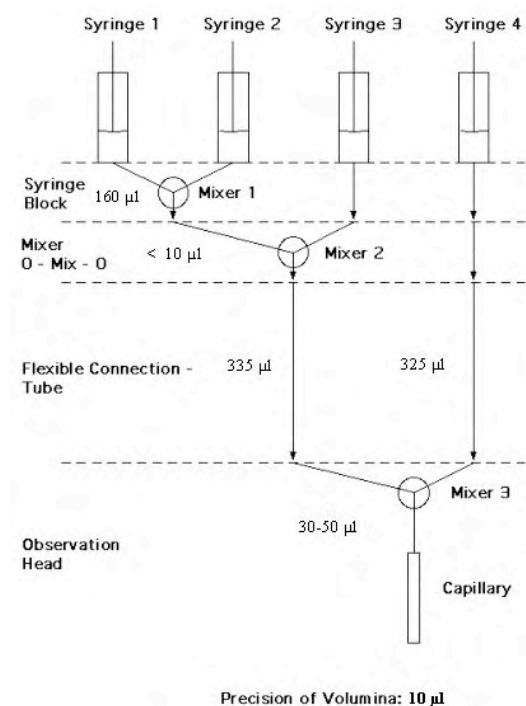
Multiple-sample holders can be mounted onto the standard sample manipulator. At present holders are available for measuring in automatic mode up to 30 solid samples at ambient temperature or up to 4 liquid or gel samples in the temperature range 0 – 95 °C.

3. Online Exhaust System

At the experimental station is available a custom-built fume cover and chemical exhaust system for toxic gases. Thus it is possible to e.g. study in-situ chemical reactions, during which toxic gases might develop.

4. Stopped Flow Apparatus

A commercial stopped flow apparatus (manufactured by Bio-Logic, Paris, France), especially designed for Synchrotron Radiation SAXS investigations of conformation changes of proteins, nucleic acids and macromolecules, is available. The instrument consists of a 4-syringe cell with 3 mixer modules manufactured by Bio-Logic. Each syringe is driven independently from the others by an individual stepping-motor, which allows a high versatility of the mixing sequence (flow-rate, flow duration, sequential mixing). For example, injection sequences using one or up to 4 syringes, unequal filling of syringes, variable mixing ratio, reaction intermediate ageing in three- or four-syringe mode etc.. The solution flow can be entirely software-controlled via stepping motors, and can stop in a fraction of a millisecond.



The software allows the set-up of the shot volumes of each of the 4 syringes in a certain time interval. Up to 20 mixing protocols can be programmed. Additionally macros for the repeated execution of individual frames can be defined. Furthermore, the input and output trigger accessible for user operation can be programmed. In the usual operation modus the start of rapid mixing sequence is triggered from our X-ray data-acquisition system (input trigger).

After the liquids have been rapidly mixed, they are filled within few ms into a 1 mm quartz capillary - situated in the X-ray beam- , which is thermostated with a water bath. Depending on the diffraction power of the sample time resolutions of up to 10 ms can be obtained.

Figure 6. Sketch of the stop flow system.

The main parameter of the system are:

- Thermostated quartz capillary (1 mm)
- Temperature stability 0.1 °C
- Total sample used per mixing cycle (shot volume): 100 µl
- Maximum 2θ angle of 45°
- Total Volume 8 ml
- Dead volume 550 µl
- Flow rate: 0.045 – 6 ml/s
- Duration of flow 1 ms to 9999 ms/Phase
- Dead time: 1 ms
- Reservoir volume: 10 ml each

Further information can be found at the webpage: <http://www.bio-logic.fr/>

5. Grazing Incidence Small Angle X-ray Scattering

Grazing incidence studies on solid samples, thin film samples or Langmuir-Blodgett-films can be performed using a specially designed sample holder, which can be rotated around 2 axes transversal to the beam. Furthermore the sample can be aligned by translating it in both directions transversal to the beam. The precisions are 0.001 deg for the rotations and 5 µm for the translations. Usually the system is set to reflect the beam in the vertical direction. According to the required protocol and the actual assembly of the rotation stages ω , θ , 2θ and φ scans can be performed.

6. Temperature Gradient Cell

A temperature gradient cell for X-ray scattering investigations on the thermal behaviour of soft matter manybody-systems, such as in gels, dispersions and solutions, has been developed. Depending on the adjustment of the temperature gradient in the sample, on the focus size of the X-ray beam and on the translational scanning precision an averaged thermal resolution of a few thousands of a degree can be achieved.

7. Flow-through Cell

The flow through cell works in a simple manner: Special quartz capillaries (Glas Technik & Konstruktion, Schönwalde/Berlin) of 1.5 mm diameter and wide openings of about 3 mm at each end, can be inserted into the standard Anton Paar sample holder, which allows various temperature treatments (T-range 25-300 or -30-70 °C, respectively). Thin tubes are connected directly to the capillary ends and a constant flow is achieved by a peristaltic pump.

8. IR-Laser T-Jump System for Time-Resolved X-ray Scattering on Aqueous Solutions and Dispersions

The Erbium-Glass Laser available at the SAXS-beamline (Dr. Rapp Optoelektronik, Hamburg, Germany) delivers a maximum of 4 J per 2ms pulse with a wavelength of $1.54 \mu\text{m}$ onto the sample. The laser-beam is guided by one prism onto the sample, which is filled in a glass capillary (1 or 2 mm in diameter) and Peltier or electronically thermostated in a metal sample holder (A. Paar, Graz, Austria). With a laser spotsize of maximal 7 mm in diameter a sample-volume of maximal $5.5 \mu\text{l}$ or $22 \mu\text{l}$, respectively, is exposed to the laser-radiation. In a water-solutions/dispersions with an absorption coefficient of $A = 6.5 \text{ cm}^{-1}$ T-jumps up to 20°C are possible.

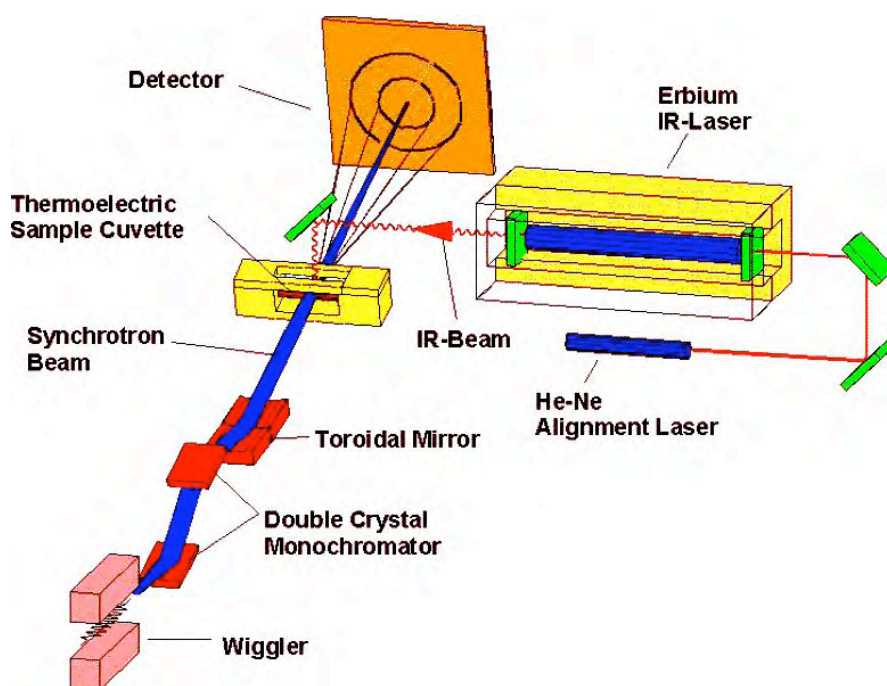


Figure 7. Sketch of the T-jump set-up.

9. High Pressure Cell System

SWAXS measurements of samples under pressure can be performed from 1 to 2500 bar, from 0 to 80°C in the scattering angle region up to 30 degrees, both in the static or time-resolved mode, e.g. p-jump or p-scan, with a time-resolution down to the ms range. Precise pressure scans of any speed within a broad range (e.g. ca. 1.0 bar/s - 50 bar/s in the case of water as pressurising medium, and a typical sample volume) can be performed. Alternatively, dynamic processes can be studied in pressure-jump relaxation experiments with jump amplitudes up to $2.5 \text{ kbar}/10\text{ms}$ in both directions (pressurising and depressurising jumps).

In most applications diamond windows of 0.75 mm thickness (each) are used. The transmission of one pair (entrance and exit window) is 0.1 at 8 keV , i.e. lower than 0.3, the value for the originally used 1.5 mm thick Be-windows. However the loss in intensity is more than compensated for by the considerably lower background scattering of diamond thus leading to higher q-resolution in the experiments.

The sample thickness can be $0.6\text{-}4.0 \text{ mm}$, with a volume of approximately $0.5\text{-}3 \text{ mm}^3$ completely irradiated by pin-hole collimated ($< 1.0 \text{ mm}$ diameter) X-rays.

The pressure cell system is flexible and can be built according to the needs of the particular experiment. Normally, a liquid (water, ethanol or octanol) is used as pressurising medium. But in principle, also gaseous media can be employed as well. N₂ has been successfully tested, and measurements in supercritical CO₂ became frequent.

Beside bulk measurements on samples in transmission set-up, also grazing incidence experiments using silicon wafer with highly aligned samples on its surface inserted in the high-pressure cell have been carried out successfully.

10. Oxford Cryostream Cooler

The Cryostream cooler creates a cold environment only a few millimeters from the nozzle position. The temperature and the flow of the nitrogen gas stream is controlled and regulated by a Programmable Temperature Controller based on an 'in stream' heater and a thermo-sensor before it passes out over the sample.

The system has been especially developed for X-ray crystallography to perform diffraction experiments on e.g. shock frozen bio-crystals. However, the programmable temperature controller allows further implication for SAXS-experiments, e.g., rapid temperature drops in solvents. The design of the Cryostream Cooler facilitates:

- Nitrogen stream temperatures from -190 to 100 °C
- Stability of 0.1 °C,
- Refill without any disturbance of the temperature at the sample
- Temperature ramps can easily be carried out remotely controlled with scan rates up to 6 °C/min
- Individual temperature protocols can be cycled
- T-jumps in both directions can be performed by rapid transfer of the sample in a pre-cooled or -heated capillary using a fast syringe driver reaching a minimum temperature of -80 °C. Here, typical scan rates are about 15 °C/sec with a total process time in the order of 10 sec.

Further information can be found at the webpage: <http://www.oxfordcryosystems.co.uk/>

11. In-line Differential Scanning Calorimeter (DSC)

The in-line micro-calorimeter built by the group of Michel Ollivon (CNRS, Paris, France) allows to take simultaneously time-resolved synchrotron X-ray Diffraction as a function of the Temperature (XRDT) and high sensitivity DSC from the same sample.

The microcalorimetry and XRDT scans can be performed at any heating rate comprised between 0.1 and 10 °C/min with a 0.01 °C temperature resolution in the range -30/+130 °C. However, maximum cooling rates are T dependent and 10°C/min rates cannot be sustained below 30°C since cooling efficiency is a temperature dependent process. Microcalorimetry scans can be recorded independently, and also simultaneously, of X-ray patterns. The microcalorimeter head can also be used as a temperature controlled sample-holder for X-ray measurements while not recording a microcalorimetry signal. Isothermal microcalorimetry is also possible when a time dependent thermal event such as meta-stable state relaxation or self-evolving reaction, is expected. The sample capillaries have a diameter of 1.5 mm and are filled over a length of 10 mm.

12. 2D Detectors: Image Plate & CCD-Camera System

The Mar300 Image Plate detector with a circular active area of 300mm in diameter is the largest-area detector available to users of the beamline, with a spatial resolution (pixel size) of 150 μ m. This detector has two modes of operation (180mm or 300mm), depending on the desired active area, which result in image sizes of 1200x1200 and 2000x2000, respectively. They are stored in the mar image format (16 bit for compactness, with higher precision extensions for values out of range), and can be processed and converted using the Fit2D program [1]. Typical applications are those that need a large Q-range with high dynamic range (typical values of 10^5), i.e. solution scattering from proteins and nanoparticles, temperature-step scans, slow processes like nanoparticle formation, mesophase formation, etc. The exposure time for the Image Plate is given in seconds, with typical values between 1 and 60. Readout time depends on the chosen active area (for 180mm mode, about 130 seconds; for 300mm mode, about 210 seconds), and therefore it is not suitable for samples where high time resolution is needed. Exposure information, number of images in the series and other information is automatically written to a summary file after each image.

So far the detector cannot be triggered by an external trigger input. Controlling an additional (external) device or experiment can only be done by hardware wiring of the TTL shutter signal.

The CCD has a 115 mm diameter input phosphor screen coupled by means of a fiber optic to the image intensifier, which itself is coupled with an additional taper to the CCD (charged coupled device). The spatial resolution of a pixel is 79 μ m. The number of pixels is 1024 x 1024 and they can be pinned down to 2 x 2 and 4 x 4. The dynamic range of the CCD is 12 bit. The dark current of the CCD is in the order of 100 ADU (off-set) and the readout noise (read out speed: 10 MHz) is in the order of 6 ADU. (The CCD is cooled by multistage Peltier element for reducing the dark noise.) The intensifier gain is adjustable between 200 and 20000 photons full dynamic range. Typical readout times and exposure times are 150 ms and 100 ms, respectively. The readout times can be reduced down to 100 ms by using the pinning mode of the CCD. Between the frames additional wait times can be programmed e.g. for reducing the radiation damage in the sample or to extend the time for measuring long time processes. For the external control a TTL trigger signal is provided (active low, when the CCD is accumulating an image), which is used to control the electromagnetic fast shutter of the beamline on one hand. On the other hand this signal can be used also to trigger processes as requested by the user.

The CCD is controlled by Image Pro+, which also includes some simple data treatment capabilities:

- flat fielding/background corrections
- enhanced filters and FFT
- calibration utilities (spatial and intensity)
- segmentation and thresholding
- arithmetic logic operations
- various measurements, like surface, intensity, counts, profiles
- advanced macro management

The data are stored in 12 bit – TIFF format and can be directly processed with FIT2D [1]

[1] A.P. Hammersley, "Fit2D: an introduction and overview", ESRF Internal Report, ESRF97HA02T, 1997

[2] <http://www.esrf.eu/computing/scientific/FIT2D/>

13. Vantec Detector

The one-dimensional high count rate capable Vantec-1 Detector from BrukerAXS Inc. has an active area of 50 x 16 mm and reaches a spatial resolution of about 50 μm , which is smaller than the resolution obtained by the presently used Gabriel Type Gas detectors. Moreover its new gas amplification principle based on the Microgap technology [1] allows much higher count rates compared to the old system. Now the main limitation is the data acquisition system with its maximum integral count rate of about 1 MHz. In the present data acquisition system HCI (Hecus X-ray Systems, Graz, Austria) the detector has the following performance:

- Minimal time resolution: 11 μs
- Maximum No. of frames: 512 (depending on the no. of channels)
- Maximum integral count rate: 1 MHz

14. Tension Cell

Together with the external user group Schulze-Bauer/Holzapfel the research team constructed a general-purpose tension cell. This particular cell was designed for *in-situ* tensile testing with the particular feature that the sample could be completely immersed in a solvent (e.g. physiological solution), which is of particular interest for the blood vessel or collagen fiber testing. The sample container can be attached to a thermal bath to control the temperature in the range from 5 to 95 $^{\circ}\text{C}$. A screw with an appropriate opening for the passage of the X-ray beam can adjust the optical thickness of the sample container continuously and optimize the set-up for different sample geometries.

The fully remote controlled system allows to control not only the fiber extension from 0 to 50 mm, but also it records simultaneously the force signal in the range from 0 to 25 N and as an option the optically determined Video extensometer signal to measure the transversal contraction of the sample.

15. Larger experimental hutch

After the prolongation of the experimental hutch by about 3m we have now the possibility to e.g. permanently install a diffractometer (roll on/roll off), or a micro focus set-up, which delivers focal spot sizes down to 10 μm and thus will allow for micro spot scanning SWAXS experiments with a new X-Y scanning stage.

On the other hand we can increase the sample to detector distance and therefore improve our minimum SAXS resolution or maximise the flux density at the sample position for certain experiments. Nevertheless this prolongation of the experimental hutch will ensure the sustainable development of the beamline also in the future by giving us the opportunity to realize new optical concepts, e.g. new mirrors, Fresnel or refractive lenses.

User Contributions

Material Science

SELF-ASSEMBLY OF II-VI NANOCRYSTALS INTO 3D SUPERLATTICES: CHARACTERIZATION OF DIFFERENT EXPERIMENTAL PROTOCOLS

F. Antonioli¹, S. Bernstorff², L. Cozzarini³, A. Radivo¹, M. Battiston³ and V. Lughi³

1) Maxun s.r.l., Trieste, Italy

2) Sincrotrone Trieste, Basovizza/Trieste, Italy

3) Department of Materials and Natural Resources – University of Trieste, Italy

Introduction

We performed static and dynamic GISAXS and GIWAXS measurements on semiconductor nanocrystals (NCs), assembled as 3D closed-packed films. The main objectives of these studies were to:

- (i) determine of the size and shape of different kinds of NCs;
- (ii) evaluate the average interparticle distance on series of assemblies obtained under different experimental conditions;
- (iii) perform preliminary experiments to study the diffusion and growing processes governing the densification mechanism.

These studies are part of a broader research project at the University of Trieste devoted to the development of a novel class of multiphase nanostructured materials, which represent an excellent platform for the fabrication of novel and performing optoelectronic devices, LEDs, solar cells.

Experimental set-up

Experiments were carried out by using X-ray photons at 8 keV; the GISAXS scattering patterns were collected with a 2D CCD detector (1024 x 1024 pixels) positioned perpendicular to the incident beam at a distance of 1.81 m from the sample. In order to block the intense reflected beam, a beam stopper was inserted, allowing better sensitivity for the weak diffuse scattering at larger q . Our measurements can be classified under three main categories:

- (i) static GISAXS measurements on semiconductor nanocrystals assembled as 3D-close-packed films, analyzed under different grazing angles to enable in-depth profiling. The samples were previously prepared in our laboratories at the University of Trieste by evaporation, flocculation and electrophoresis deposition. Films of ZnSe NCs and core-shell NCs (CdSe core and ZnSe shell), obtained under different experimental conditions – i.e. varying deposition temperature, voltage and current, NCs concentration – were analyzed.
- (ii) in-situ time-resolved GISAXS measurements on self-assembling of nanocrystals starting from different colloidal suspensions (ethanol, methanol and pyridine were used as solvent).
- (iii) in-situ time-resolved GISAXS and GIWAXS measurements at high temperature (up to 500 °C) to observe the densification mechanism of NC assemblies, by using a heating stage.

Results

The 2D GISAXS scattering patterns were analyzed by taking vertical ($q_y = -0.1 \text{ nm}^{-1}$) and horizontal ($q_z = 0.7 \text{ nm}^{-1}$) sections. For the analysis we considered the simple particle scattering model (Guiner approximation). The average NCs radius R was obtained from the radius of gyration R_g computed from the slope of the linear region of the $\ln I(q)$ versus q^2 dependence. The average distance among nanocrystals was determined from the position of the interference peak. Comparative 2D GISAXS patterns are depicted in Fig. 1a for a series of samples of ZnSe NCs thin films obtained through electrophoresis of colloidal solutions at

increasing operating currents (ZnSe1: 30 A, ZnSe2: 60 A, ZnSe3: 90 A; ZnSe4: 120 A). The interference peak in the $I(q)$ vs q graph (fig. 1b) varies slightly among the four scans, assuming that the deposition current does not affect the average distance among nanocrystals. The radius of gyration computed from the slope of the linear region determined in the $\ln I(q)$ vs q^2 graph (fig. 1c) indicates larger particle dimensions at increasing deposition currents (analogous results were obtained at increasing deposition voltages and temperatures). Two different radii, R_v and R_h , were computed from the vertical and the horizontal scans (see table in Fig. 1), assuming an almost spheroid shape of the ZnSe nanocrystals, with the main axes oriented perpendicularly to the sample stage. These results were verified and supported by numerical simulations performed with the IsGISAXS software. In-depth profiles were also analyzed, showing that the NCs' size increases going from the surface to the deeper layers of the assembly and indicating that, for a given current, there is preferential deposition of larger NCs.

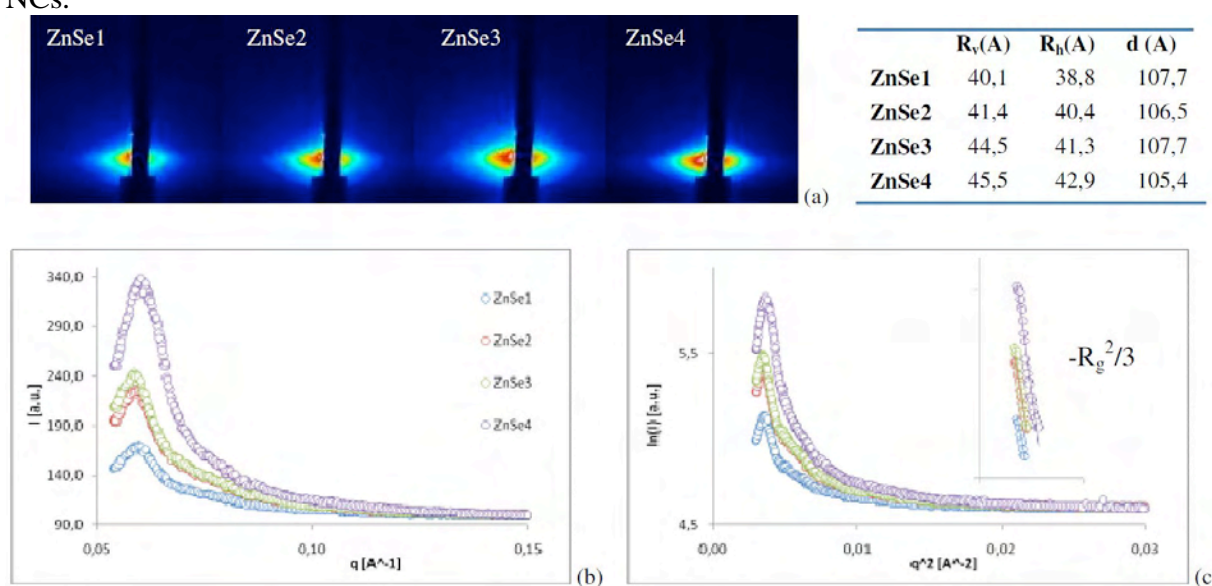


Figure 1. GISAXS measurements on assemblies of ZnSe NCs obtained increasing the deposition currents.

Concerning the in-situ time-resolved GISAXS measurements on self-assembling of nanocrystals starting from different colloidal suspensions, we observed that the solvent plays an important role in the assembling mechanism, that there are a number of stages at which different structures form at the nanoscale, corresponding to the various stages of solvent evaporation. Methanol is a particularly promising solvent for obtaining ordered nanostructures (data not shown). The in-situ time-resolved GISAXS and GIWAXS measurements at high temperature showed very interesting preliminary data about the densification dynamics of NCs assemblies. The 2D GISAXS patterns depicted in Fig. 2a refer to a sintering experiment performed on a core-shell nanocrystals film (CdSe core and ZnSe shell) maintained at a temperature of 500°C for 30 minutes (CS1: 0'; CS2: 5'; CS3: 10'; CS4: 15'; CS5: 20'; CS6: 25'). We observed an initial increase of the nanoparticles dimensions due to the atomic diffusion at the NCs superficial interface (increasing slope in the linear region of the $\ln I(q)$ vs q^2 graph in Fig. 2b). Unfortunately the oxidation process rapidly prevails on the diffusion process and causes the complete oxidation of the NCs shell. This phenomenon is evident observing the GIWAXS 1D scans depicted in the graph in Fig. 2c. The peaks attributable to the core-shell structure (25.3 and 43.2 2-theta degrees) are subjected to a shift toward lower diffraction angles, meaning a gradual disappearing of the ZnSe shell; after 20 minutes only the CdSe peaks at 24.4 and 42.4 remain. At the same time, the increase of the

ZnO peaks at 32.5, 34 and 36 2-theta degrees is attributable to the oxidation of the ZnSe shell to zinc oxide.

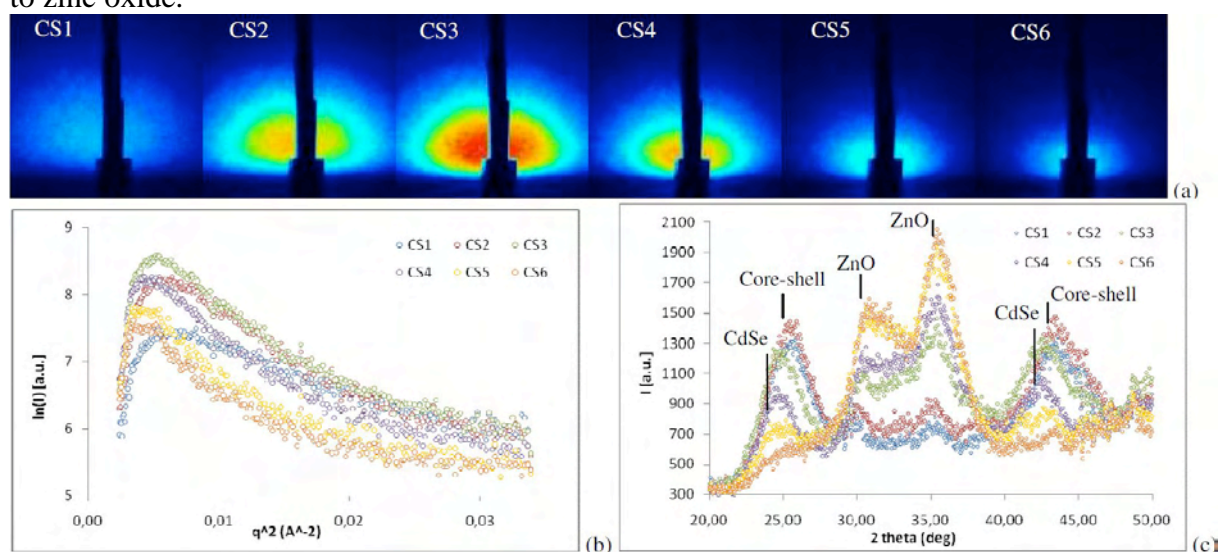


Figure 2. In situ time-resolved GISAXS and GIWAXS measurements at high temperature on a core-shell NCs assembly.

Conclusions

In this first beamtime slot we performed a large number of experiments aimed to explore the correlations between processing and morphology, both for the NCs and the assemblies, for a broad process parameter space. We also tested the feasibility of two different time-resolved in-situ experiments in air. Performing high temperature time-resolved experiments in inert atmosphere will be the next challenge – as well as the aim of future experiments – in order to obtain insight into the complex mechanisms governing diffusion and growing processes at the nanoscale, which currently represent an almost unexplored field.

PRODUCTION OF REGULARLY ORDERED QUANTUM DOT LATTICES

M. Buljan¹, U. Desnica¹, N. Radić¹, I. Bogdanović-Radović¹, K. Salamon², M. Karlušić¹, P. Dubček¹, G. Dražić³, S. Bernstorff⁴ and V. Holy⁵

- 1.) Ruđer Bošković Institute, Bijenička cesta 54, 10000 Zagreb Croatia
- 2.) Institute of Physics, Bijenička cesta 46, 10000 Zagreb, Croatia
- 3.) Jožef Stefan Institute, Jamova 39, 1000 Ljubljana, Slovenia
- 4.) Sincrotrone Trieste, Basovizza 34012, Italy
- 5.) Charles University in Prague, Faculty of Mathematics and Physics, Czech Republic

Semiconductor quantum dots (QDs) are subject of extensive studies because of their unique physical properties and for numerous technology applications [1-3]. One of the most important parameters for possible applications of Ge QD is the uniformity of the QD sizes and their arrangement in the matrix. In crystalline multilayers it is possible to induce a self-ordered growth of QDs by the strain fields which appear due to the mismatch of the lattice parameters of the dot and the matrix materials. However, this mechanism is not active in amorphous systems, where a regular ordering and size uniformity of the dots is more difficult to achieve. Last year we have shown the possibility of the self-ordering growth of QDs in amorphous systems [4,5]: the morphology of the growing surface supports the self-ordering even if the matrix is amorphous.

We continued our investigation, and have now developed a new method for the production of ordered QD systems. The method consists in ion beam irradiation of a fully amorphous multilayer followed by thermal annealing [6,7]. We have shown that nuclei of QDs form during the irradiation, which triggers the formation of Ge clusters ordered along the irradiation direction. Figure 1 shows transmission electron micrographs (TEM) of non-irradiated and irradiated Ge+SiO₂/SiO₂ multilayers before and after annealing: (a) and (b) depict the multilayer before and after irradiation, respectively. It is evident that the film is fully amorphous before irradiation without formation of Ge clusters, while Ge clusters are visible after irradiation. The annealing causes the formation of crystalline and spherical Ge QDs (Figs. 1(c) and (d)) which are ordered along the irradiation direction. The ordering follows also from the Fourier transformation of the TEM cross-section shown in the inset of panel 1(d).

Grazing-incidence small-angle x-ray scattering (GISAXS) is a very suitable method for the analysis of the morphology of these composite systems. GISAXS pattern of the as-deposited and irradiated samples are shown in Fig. 2. For the as-deposited film (shown in 2a) standard Bragg sheets parallel to the q_y axis are well visible. These sheets are due to the periodicity of the multilayer stack in the growth direction and to the correlation of the shapes of different interfaces. It is very interesting that the sheets appear completely inclined for the irradiated films (2c) in which the azimuthal direction of the primary x-ray beam was perpendicular to the azimuthal direction of the irradiating ions. The inclination of the sheets is perpendicular to the irradiation direction. From this fact follows that both the Ge clusters and the interface roughness are spatially correlated in the direction of irradiation and it is easy to determine the correlation angle of the QDs from the corresponding GISAXS pattern. The samples after ion irradiation therefore contain Ge QDs ordered along the lines parallel to the irradiation direction. In the lateral direction the QD chains are ordered in a 2D hexagonal lattice parallel to the substrate.

After thermal annealing the dominant contribution to the GISAXS intensity comes from the Ge QDs (Figs. 2 (e), (f)). For the annealed films, the Bragg sheets are much weaker, but the inclination angle remains the same. This shows that the initial Ge cluster arrangement induced

by irradiation is preserved after annealing. We have simulated the measured GISAXS data using the model developed for this system [7]. The simulated GISAXS patterns are shown in Figs 2(d), (f). From the simulation follows that the in-plane distance of the QDs is 21.6 ± 0.4 nm, while the vertical multilayer period is 14.8 ± 0.2 nm. The in-plane QD distance in the irradiated multilayer is larger than in the non-irradiated one, where the lateral distance is found to be 14.5 ± 0.6 nm. The average size of QDs is also larger in the irradiated multilayer $R_{\text{irr}} = 4.1 \pm 0.1$ nm, while $R_{\text{non-irr}} = 3.2 \pm 0.2$ nm.

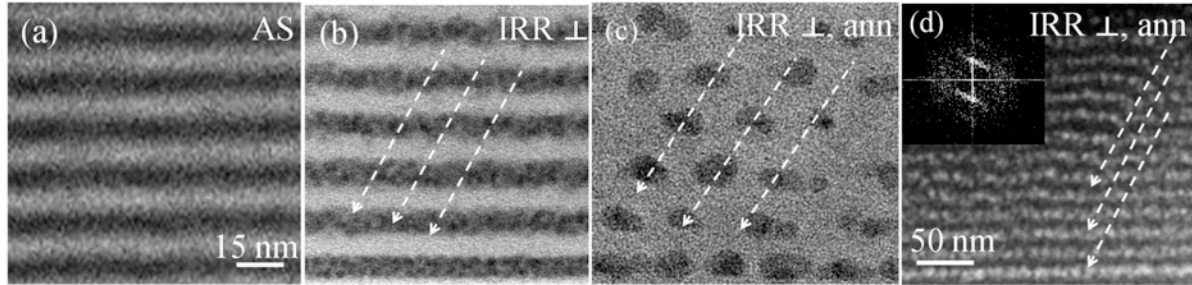


Figure 1. TEM cross-section of the (a) as-deposited film, (b) irradiated multilayer before annealing, (c) and (d) TEM cross-sections after annealing showing two different magnifications

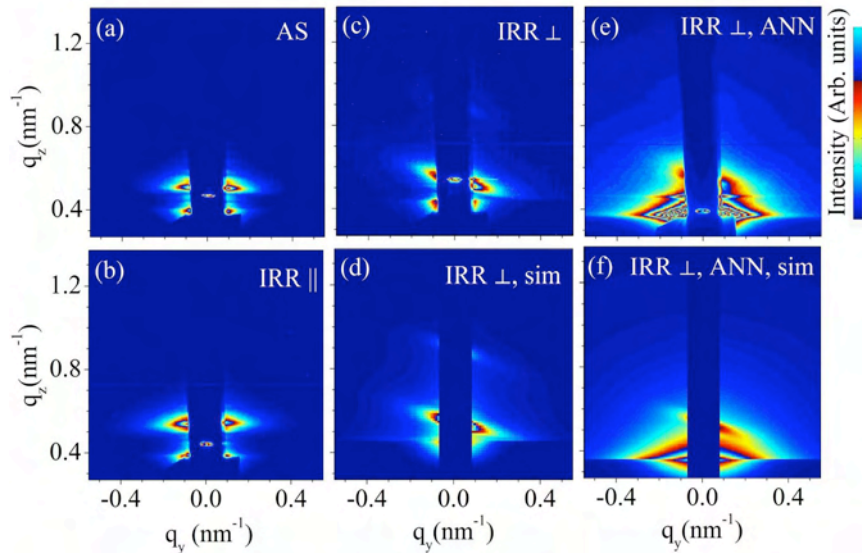


Figure 2. GISAXS pattern measured on (a) as-deposited film, (b),(c) irradiated (IRR) multilayer in || and \perp configurations respectively. (d) Simulation (sim) of the GISAXS map shown in (c). Measured (e) and simulated (f) map of the film after annealing

References:

- [1] A. P. Alivisatos; Semiconductor Clusters, Nanocrystals, and Quantum Dots; Science 271, 933-937 (1996)
- [2] A. L. Goodwin; Nanomaterials: The ins and outs of thermal expansion; Nature Nanotechnology 12, 710-711 (2008)
- [3] P. Michler, A Kiraz, C. Becher, W.V. Schoenfeld, P. M. Petroff, Lidong Zhang, E. Hu, A. Imamolu; A Quantum Dot Single-Photon Turnstile Device; Science 290; 2282-2285 (2000)
- [4] M. Buljan, U.V. Desnica, G. Dražić, M. Ivanda, N. Radić, P. Dubček, K. Salamon, S. Bernstorff, V. Holý; The influence of deposition temperature on the correlation of Ge quantum dots positions in amorphous silica matrix; Nanotechnology 20, 085612 (2009)
- [5] M. Buljan, U.V. Desnica, G. Dražić, M. Ivanda, N. Radić, P. Dubček, K. Salamon, S. Bernstorff, V. Holý; Formation of three-dimensional quantum dot superlattices in amorphous systems: Experiments and Monte Carlo simulations; Phys. Rev. B 70, 035310 (2009)
- [6] M. Buljan, I. Bogdanović-Radović, M. Karlušić, U.V. Desnica, G. Dražić, N. Radić, P. Dubček, K. Salamon, S. Bernstorff, V. Holý; Formation of long range ordered quantum dots arrays in amorphous matrix by ion beam irradiation; Appl. Phys. Lett. 95, 063104 (2009)
- [7] M. Buljan, I. Bogdanović-Radović, M. Karlušić, U.V. Desnica, N. Radić, N. Skukan, G. Dražić, M. Ivanda, Z. Matej, V. Valeš, J. Grenzer, T. Cornelius, H. T. Metzger, V. Holý; Generation of an ordered Ge quantum dot array in an amorphous silica matrix by ion beam irradiation: Modeling and structural characterization; Phys. Rev. B 81, 085321 (2010)

PULSED LASER ABLATION OF GaAs USING NANO PULSE LENGTH

P. Dubček¹, B. Pivac¹, S. Milošević², N. Krstulović², Z. Kregar², S. Bernstorff³

- 1.) R. Boskovic Institute, Bijenicka 54, Zagreb, Croatia
- 2.) Institute for physics, Bijenicka 46, Zagreb, Croatia
- 3.) Sincrotrone Trieste, SS 14, km 163.5, Basovizza (TS), Italy

Processes in solids exposed to pulsed laser irradiation are important for several rapidly developing laser-assisted techniques, pulsed laser deposition (PLD) being one of them.

Gallium arsenide, already important in the electronic and opto-electronic industries, has even greater potential if quantum confinement effects could be used to tune its material properties. Therefore, it is the scope of this work to explore the effects of the PLD deposition parameters on the structural properties of GaAs nanoparticles deposited on Si substrate.

GISAXS data for Ar assisted PLD of GaAs on monocrystalline silicon are shown in fig.1. The incident angle was set to the critical angle value for GaAs. This way the scattering from the film was enhanced, since the X-ray beam within the sample was concentrated near the surface and the penetration depth was less than 20 nm. The left side of each of the three images represents the measured intensity, while the right side shows the result of the fit, which will be discussed further down.

The shape of this intensity distribution is changing gradually as the number of pulses is increased. Still, the difference between sample a and b is less pronounced, while the scattering distribution of sample c is standing out. Our own software, that calculates the scattering from a distribution of particles, located on top of the substrate, was applied in the numerical data fitting. A model of either cylinders or domes, varying in diameter as well as in height according to the normal size distribution was attempted in the numerical reproduction of the measured intensities.

It turned out that the shape of the scattering particles could be reproduced properly for the measured intensity patterns only when different particle shapes were applied for the fitting. The final results shown in fig.1. are obtained by applying a cylindrical shape for sample a) and b), while domes resulted in a better reproduction of the pattern measured for sample c).

The results of the fit are summed in table 1. There is a trend of size reduction as the number of pulses is increased: the radius decreases from 10 nm down to 4 nm, while the height has changed from 7 nm to 6 nm. Also, note a rather broad size distribution for all the samples. For sample b) the halfwidth equals the average size both for radius and height. This is apparently an extreme and enhances the difference as compared to the other two samples. Since the particles shape is different in sample c) we can conclude that the 500 pulses applied in sample b) are close to a limiting value when different particles begin to form.

We suspect that in sample c) a homogeneous film has been formed, and the modeled size distribution is describing the surface topology/roughness of this film. Although the shape of the scattering pattern appears similar to the one of sample a), the extreme value of the size distribution width obtained for sample b) indicates that the change of the particle shapes begins already at 500 pulses.

The scattering from sample a) and b) contains a rather strong contribution from the substrate surface, but this is mostly restricted to the specular plain and partly hidden below the semitransparent vertical absorber, and has been ignored in the analysis.

Both the SAXS and AFM results confirm a relatively large size distribution of the nanoparticles formed by PLD. Both methods point to the 500 pulses sample having the broadest particle size distribution width. Also, both methods indicate a particle radius reduction with increasing number of laser pulses.

A less good agreement regards the vertical particle size (perpendicular to the film surface): The SAXS data fitting resulted in a similar height in all the samples, where only the height

distribution width in sample b) stands out as being equal to the average height value, and the AFM roughness values are more than two times smaller.

Keeping in mind the differences between the two methods, e.g. the used wavelength of 1.54 nm for SAXS compared to the ~15nm tip radius of AFM, and the probed area in GISAXS of about 50 μm^2 while it is square micrometers in AFM, we can conclude that the correspondence is fair.

We have found that the PLD GaAs nanoparticle sizes and size distributions can be controlled partly by the number of laser pulses applied in their production. A further investigation into the growth mechanism under influence of different working gas and pulsing regimes is planned.

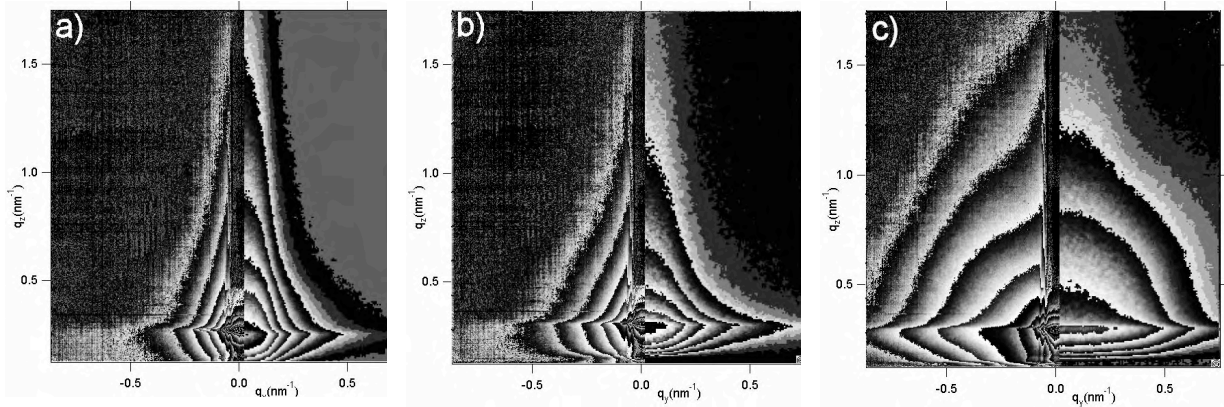


Figure 1. GISAXS intensities for Ar assisted PLD of GaAs for different pulse numbers, i.e. a) 100, b) 500 and c) 1000. The left side of each of the images represents the measured intensity, while right side is the result of a numerical fitting calculus.

Table 1. The fit parameters obtained for the SAXS pattern shown in fig. 1a), 1b) and 1c). The last line gives the values obtained from AFM data.

Number of pulses	a) 100	b) 500	c) 1000
shape of particles	cylinder	cylinder	dome
Radius and halfwidth	10 +/- 9 nm	6 +/- 6 nm	4 +/- 3 nm
height and halfwidth	7 +/- 5 nm	7 +/- 7 nm	6 +/- 3 nm
AFM radius and halfwidth	12 +/- 5 nm	10 +/- 18 nm	6 +/- 4 nm

He ASSISTED PULSED LASER ABLATION OF Ge

P. Dubček¹, B. Pivac¹, S. Milošević², N. Krstulović², Z. Kregar², S. Bernstorff³

1.) R. Boskovic Institute, Bijenicka 54, Zagreb, Croatia
2.) Institute for physics, Bijenicka 46, Zagreb, Croatia
3.) Sincrotrone Trieste, SS 14, km 163.5, Basovizza (TS), Italy

The pulsed laser deposition (PLD) technique, that proved to be valuable for the growth of multiple component oxides, is a promising technique also for high-quality crystalline thin films. We applied it to grow germanium, which was very important in the early days of electronic and opto-electronic, and is now regaining its role and has even greater potential if quantum confinement effects could be used to tailor its properties. It is the scope of this work to explore the effects of the pulsed laser deposition (PLD) parameters on the structural properties of Ge nanoparticles deposited on Si substrate.

GISAXS data for He assisted PLD of Ge on monocrystalline silicon are shown in fig.1. In order to enhance the scattering from the film, the incident angle was set to the critical angle value for Ge where the penetration depth was less than 20 nm. The left half of each of the images represents the measured intensity in contour like false color plot, while the right side shows the result of the fit.

As the number of pulses is increased, so does the coverage of the substrate surface: for very low number of the pulses, localized nanoparticles are expected to form on the surface, while the coverage is complete for large number of laser pulses, i.e. full grown film is formed. Therefore, the shape of the SAXS intensity distribution is changing gradually with the number of pulses. A model of either cylinders or domes, varying in diameter as well as in height according to the normal size distribution was used in the numerical reproduction of the measured intensities.

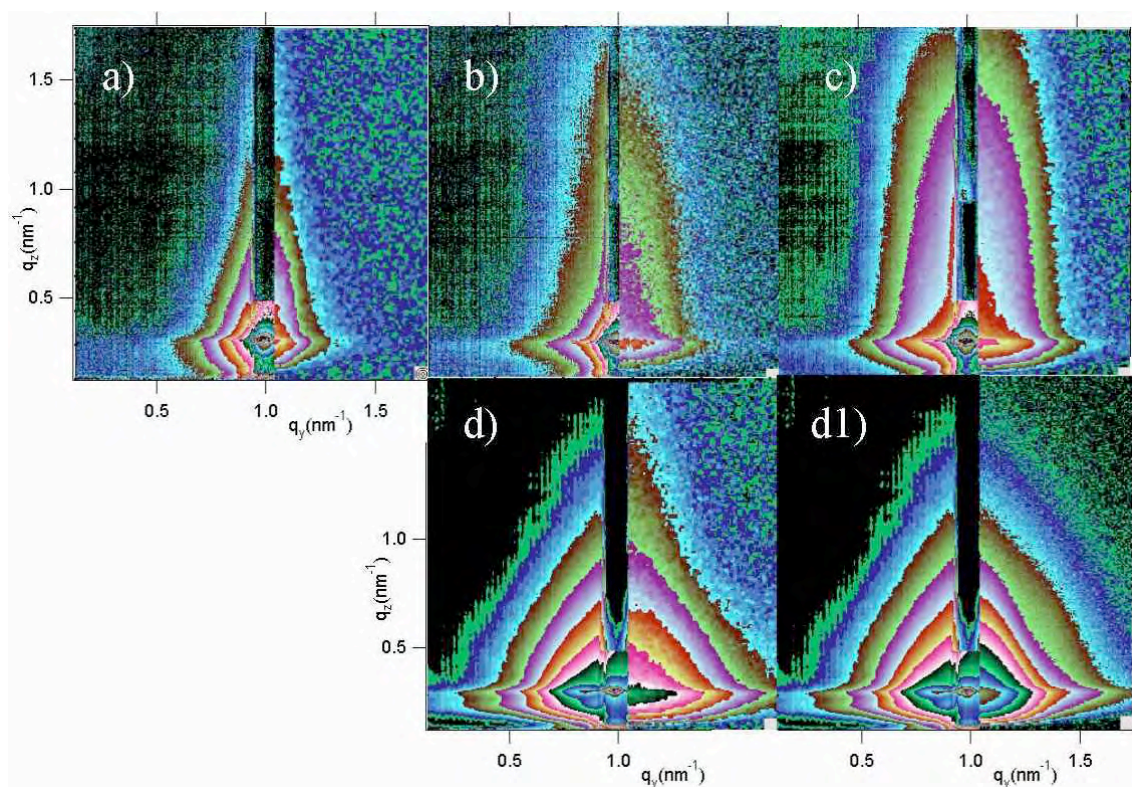


Figure 1. GISAXS intensities for He assisted PLD of Ge for different number of pulses, i.e. a) 100, b) 500, c) 1000 and d) 5000. The left half of each of the images represents the measured intensity, while the right side is the result of a numerical fitting calculus.

The final results shown in fig.1. are obtained applying cylindrical shape for sample a), b) and c), while domes and even ellipsoid shapes had to be applied to sample d).

The results of the fit are summed in fig 2. The average size of cylinders is minimum in sample b) and are slightly increased again for sample c). On the other hand, the size distribution widths are roughly halved going from a) to b), and are further reduced for c), especially in the vertical direction, where they are reduced for another factor of two.

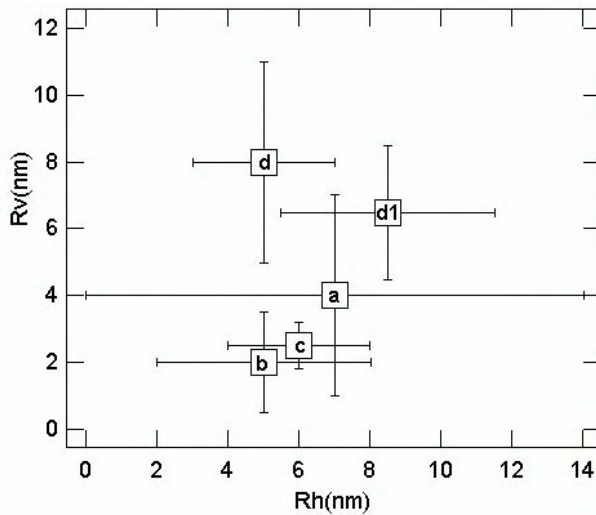


Figure 2. Nanoparticles sizes obtained by data fitting. The error bars represent the distribution halfwidths in horizontal and vertical direction

We suspect that in sample d) a homogeneous film has been formed, and the modeled size distribution cannot be described by the surface topology/roughness of this film. The latter has been attempted by dome fitting and the result is displayed in fig 1.d). In order to obtain a better fit we had to assume an ellipsoidal shape of the scattering particles, as displayed in fig. 1.d1). This can be ascribed to the presence of voids in the film. Namely, we suppose that isolated cylindrical particles are present on the surface up to 1000 laser pulses, and after that a film is formed. The growth is relatively fast compared to the surface movement of the atoms being deposited from the plasma, therefore rather irregular voids are left in the film. The wide size distribution of the ellipsoids is a good approximation for such voids. Note the rather large size distribution for both dome and ellipsoid fit results in both cases. Also, the distribution widths in vertical and horizontal direction are similar to each other, while the horizontal distribution size is always bigger in the first three samples.

The scattering from sample a) and b) contains a rather strong contribution from the substrate surface, but this is mostly restricted to the specular plain and partly hidden below the central, partly transparent absorber, and has been ignored in the analysis.

We have found that the PLD Ge nanoparticle sizes and size distributions can be controlled partly by the number of laser pulses applied in their production. However, for the applied pulse rate a film with voids is formed after a sufficient number of pulses. A further investigation into the growth mechanism under the influence of different working gases and pulsing regimes is planned.

STRUCTURAL AND OPTICAL PROPERTIES OF AMORPHOUS-NANOCRYSTALLINE SILICON THIN FILMS

D. Gracin¹, K. Juračić¹, A. Gajović¹, P. Dubček¹, S. Bernstorff² and M. Čeh³

1.) Ruđer Bošković Institute, Bijenička c. 54, 10000 Zagreb, Croatia

2.) Sincrotrone Trieste, SS 14 km 163.5, 34012 Basovizza (TS), Italy

3.) Jožef Stefan Institute, Jamova 39, 1000 Ljubljana, Slovenia

Nano-crystalline thin films are a promising candidate for producing high efficiency solar cells and hence electric power ("solar electricity") with the price competitive with conventional sources (oil, hydropower, etc) but without emission of "greenhouse gasses" (CO₂). Those high expectations are based on using quantum confinement effects connected with nano-meter sized objects in the form of ordered 3D domains, quantum dots, QD, called also nano-crystals. The optical, electrical and vibrational properties of QD in thin films are not fully explained, among others due to the substantial influence of the matrix effect. Therefore, the establishment of a firm correlation between the volume fraction and size distribution of nano-crystals with the deposition parameters and - in a next step - with the optical and opto-electrical properties is of key importance for wider application.

In this work we studied the properties of amorphous–nano-crystalline silicon (a-nc-Si:H) thin films having a Raman volume fraction of the crystalline phase close to 35% as described earlier [1, 2]. High-resolution transmission electron microscopy, HRTEM, was used for examining the nanostructure that corresponds to the surface in the μ -meter range while GISAXS and SAXS was used for studying the average nanostructure over a 5 orders larger area. The basic units in our samples, as shown in Fig 1, are nano-meter sized ordered grains in the 5 nm range embedded in an amorphous silicon matrix.

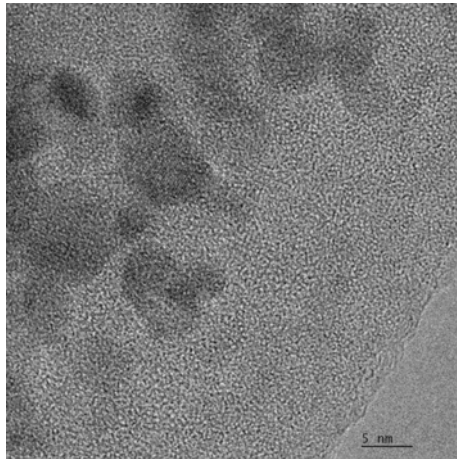


Figure 1. High-resolution transmission electron microscopy (HRTEM) image of a-nc-Si:H

Measurements of the optical properties using standard methods [3] showed that the absorption coefficient is similar or slightly lower than for pure amorphous silicon in the visible part of the spectrum and showed a square dependence on the photon energy (Tauc gap). As a result of the quantum confinement effect related to the small size of the silicon nano-crystals the optical energy gap is shifted to higher energy ($E_g > 2$ eV) compared to amorphous silicon ($E_g = 1.7$ eV) and crystalline silicon ($E_g = 1.1$ eV).

Grazing Incidence Small Angle X-ray Scattering (GISAXS) measurements were performed at 8 keV, using a two dimensional position sensitive charge-coupled device (CCD) detector at a detector-to-sample distance $L = 2$ m. Grazing Incidence Wide Angle X-ray Scattering (GIWAXS) spectra were recorded simultaneously during the GISAXS experiment. The

measurements were performed for various grazing incidence beam angles, starting from the critical angle and continued for angles slightly above which allowed in depth structural analysis.

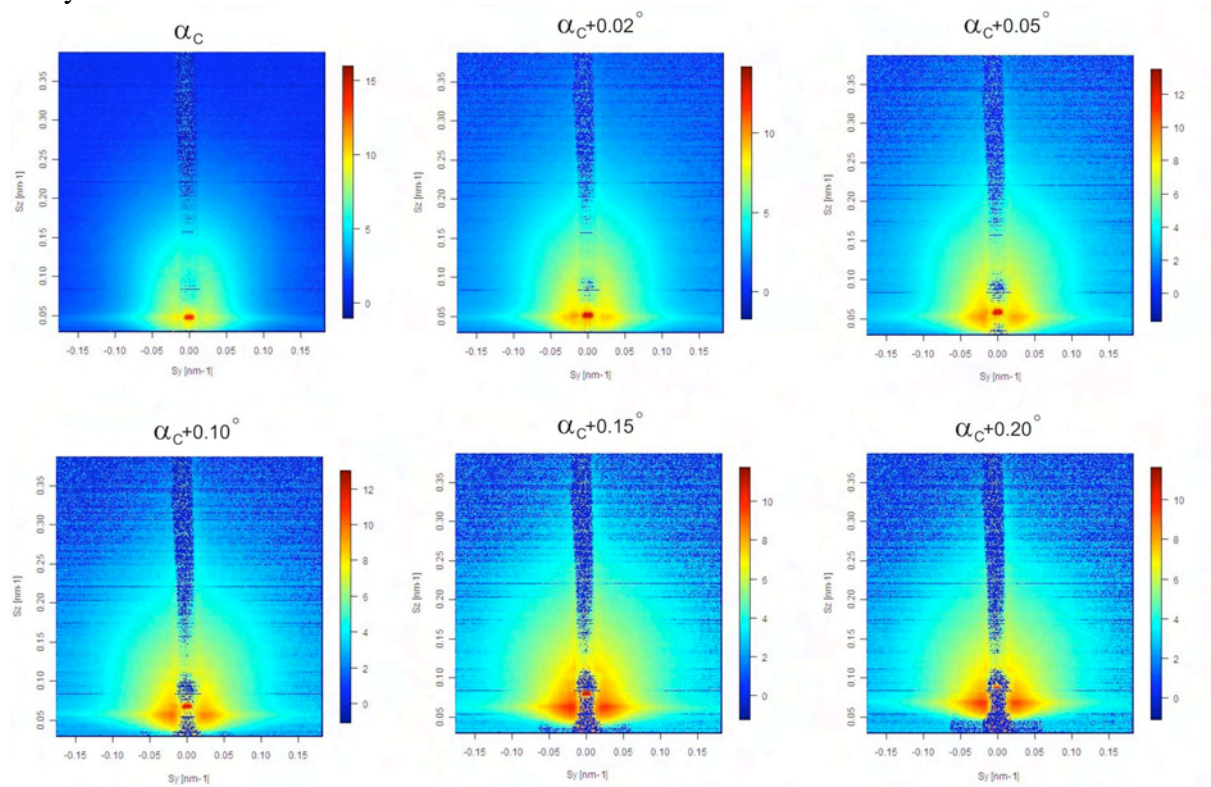


Figure 2. 2D GISAXS patterns of a-nc-Si:H thin films as a function of the angle of incidence which was increased from the critical angle α_c for crystalline silicon (first image) up to $\alpha_c + 0.20^\circ$ (last image)

The analysis of two dimensional GISAXS pattern (Figure 2) showed that the object sizes were in the range of several nano-meters while the intensity distribution shape was close to spherical.

The average sizes of the nano-particles were estimated from 1D vertical (Figure 3) and horizontal (Figure 4) cuts using the simple Guinier approximation [4]. The in-depth size distribution of the nano-crystals was found either uniform across the sample, or the crystals were slightly larger when located closer to the surface.

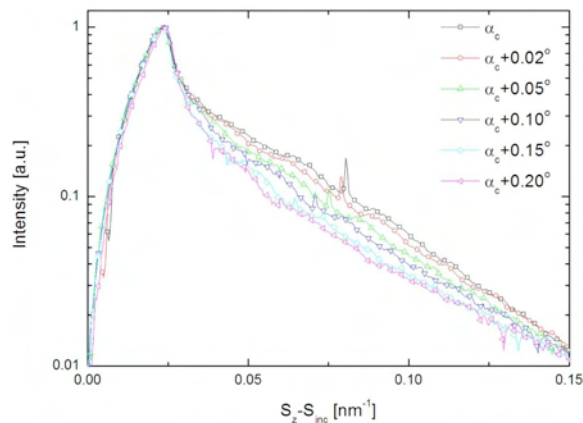


Figure 3. 1D vertical cuts taken from the 2D GISAXS images (Figure 2) near the beam-stop area for different values of angle of incidence

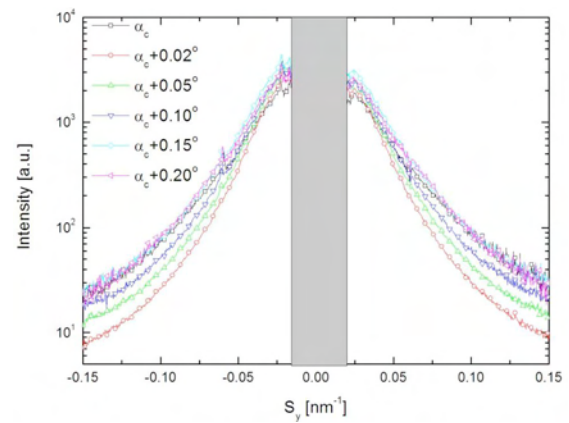


Figure 4. 1D horizontal cuts taken from the 2D GISAXS images (Figure 2) just above the Yoneda maximum for different value of angle of incidence

The GIWAXS spectra confirmed that the objects seen by GISAXS are well ordered nano-sized Si domains while the line broadening of the characteristic diffraction lines corresponds to few nano-meters large crystals [5]. Comparing the HRTEM, GISAXS and GIWAXS results, there are strong indications that the structural units shown in Fig.1 are good representatives of the nano-structure of the deposited films.

A possible application of the examined a-nc-Si:H layers structure as active part in solar cells was tested by integration in a typical p-i-n solar cell structure. The most important property, beside high absorption, reflects itself in the possibility of changing the spectral distribution of the opto-electrical response (Quantum efficiency, QE) by changing the crystals size in the thin film. In Fig. 5 are compared the QEs of a-Si, a-nc-Si:H and μ c-Si solar cells. As can be seen, the QE of the solar cell with nano-crystals has a “blue shift” comparing to the amorphous and the microcrystalline cells which enables the use this kind of material in multigap-multilayer solar cells. In this kind of device each of the individual cells covers a part of the solar spectrum, and thus stacked together an increase of the total efficiency of the photovoltaic conversion can be obtained.

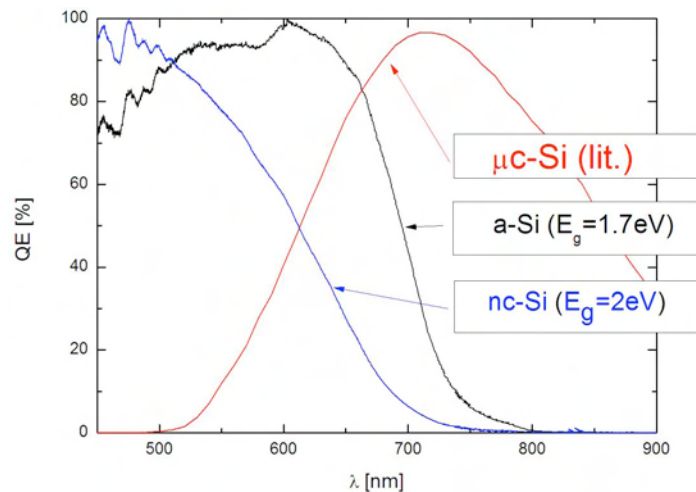


Figure 5. Quantum efficiency of solar cells with a-nc-Si:H, a-Si:H and μ c-Si thin film as active material

References:

- [1] D. Gracin, K. Juraic, P. Dubcek, A. Gajovic, S. Bernstorff, Applied Surface Science, 252 (2006) 5598
- [2] A. Gajovic, D. Gracin, K. Juraic, J. Sancho-Parramon, M. Ceh, Thin Solid Films 517 (2009) 5453
- [3] D. Gracin, J. Sancho-Paramon, K. Juraic, A. Gajovic, M. Ceh, Micron, 40 (2009) 56
- [4] O.Glatte, O.Kratky, Small Angle x-Ray Scattering, Academic Press, London, 1982, 272
- [5] K.Williamson, W.H.Hall, Acta Metall. 1 (1953) 22

TIME RESOLVED IN-SITU STUDIES OF AGEING OF (CTAB/TEOS) SILICA PRECURSOR SOLUTIONS

K. Jungnikl¹ and H. Amenitsch¹

1.) Institute of Biophysics and Nanosystems Research (IBN), Austrian Academy of Sciences, Graz, 8042 Austria

Evaporation induced self assembly (EISA) provides an attractive process for the synthesis of mesostructured materials. A large variety of mesostructures is produced from precursor solutions consisting of a soluble silica precursor, solvent(s) (mostly alcohols and/or water), surfactant(s) and acidic or alkaline components to adjust pH and ion concentration. The final mesostructures are controlled by adjusting the ratio of those components, by the process conditions during solvent evaporation and by the degree of precursor solution ageing. Two basic chemical processes can be distinguished: 1) hydrolysis of the silica precursor and subsequent silica condensation and 2) change of the solvent concentration and composition (EtOH content) due to evaporation during the process. Mesophase formation (surfactant curvature) and silica condensation are dependent on the solvent properties [1]. Aim of the experiment was a systematic assessment of the structural effects of ethanol released during TEOS (silica precursor) hydrolysis and of the subsequent silica condensation on the micellar structure in the precursor solution. This was achieved by *in-situ* measurements with a flow-through capillary through which the solution was carried by a peristaltic pump [2]. For a sketch of the experimental setup see Figure 1.

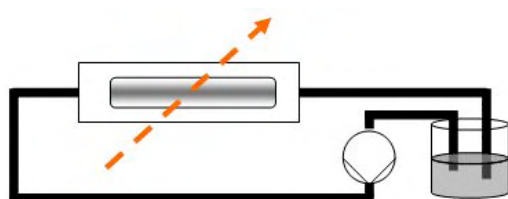


Figure 1. Sketch of the experimental setup. The preparation of the precursor solution and the subsequent chemical reaction took place in a glass container located beside the beamline. This way it was possible to start the measurement within less than one minute after adding TEOS to the solution. The arrow symbolises the X-ray beam path.

The structural evolution of a TEOS/CTAB/H₂O/HCl precursor solution during hydrolysis (a process that is happening within a relatively short timeframe of several minutes) and subsequent silica condensation was followed by *in-situ* ageing experiments over several hours. In order to enable the systematic assessment, we measured also solutions of CTAB/TEOS/HCl/(H₂O) and alcohols of different molecular weight (methanol, ethanol, isopropanol), which is known to have an effect on the micelle curvature [1, 3] (Figure 2).

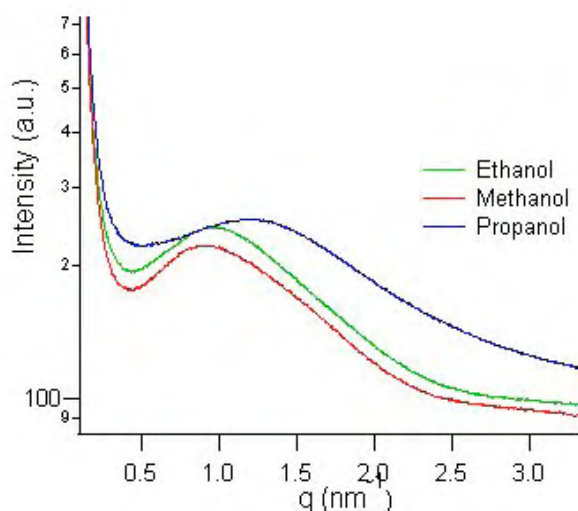


Figure 2. CTAB/TEOS Precursor solution measurements with alcohols of different molecular weight.

In contrast to previous *in-situ* material formation studies on comparable systems [4, 5], we inhibited solvent evaporation by closing the solution container. This way it was possible to separate the quantifiable and time dependent chemical changes due to hydrolysis and condensation from structural changes due to solvent evaporation.

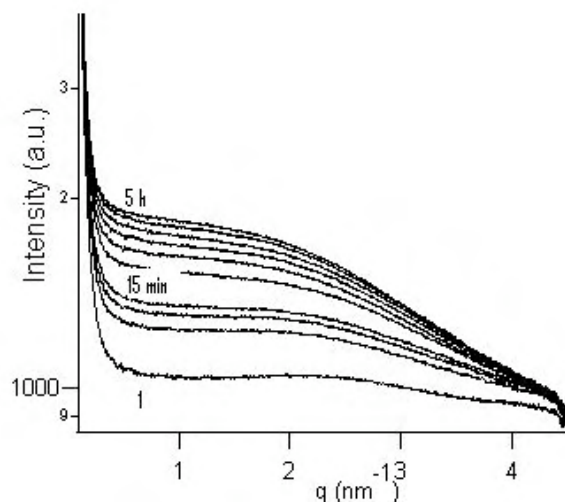


Figure 3. X-ray measurements during ageing of a TEOS/CTAB/Ethanol solution. The increase of intensity during ageing is due to progressive silica condensation. Patterns were collected every 5 min.: Curve (1) after complete TEOS dissolution, the three subsequent curves in 5 min steps, the patterns from the subsequent 5 hours are shown in time steps of 50min (for clarity).

References:

- [1] M. Tomšič, M. Bešter-Rogač, A. Jamnik, W. Kunz, D. Touraud, A. Bergmann and O. Glatter; Ternary systems of nonionic surfactant Brij 35, water and various simple alcohols: Structural investigations by small-angle X-ray scattering and dynamic light scattering. *J. Coll. Interf. Sci.* 294, 194-211 (2006)
- [2] P. Ågren, M. Lindén, J.B. Rosenholm, R. Schwarzenbacher, M. Kriechbaum, H. Amenitsch, P. Laggner, J. Blanchard and F. Schüth; Kinetics of Cosurfactant-Surfactant-Silicate Phase Behavior. 1. Short-Chain Alcohols. *J. Phys. Chem. B* 103, 5943-5948 (1999)
- [3] F. Venditti, R. Angelico, G. Palazzo, G. Colafemmina, A. Ceglie and F. Lopez; Preparation of nanosize silica in reverse micelles: Ethanol produced during hydrolysis affects the microemulsion structure. *Langmuir* 23, 10063-10068 (2007)
- [4] L. Bollmann, V.N. Urade and H.W. Hillhouse; Controlling Interfacial Curvature in Nanoporous Silica Films Formed by Evaporation-Induced Self-Assembly from Nonionic Surfactants. I. Evolution of Nanoscale Structures in Coating Solutions. *Langmuir* 23, 4257-4267 (2007)
- [5] V. Luca, W. K. Bertram, G. D. Sizgek, B. Yang and D. Cookson; Delineating the First Few Seconds of Supramolecular Self-Assembly of Mesoporous Titanium Oxide Thin Films through Time-Resolved Small Angle X-ray Scattering. *Langmuir* 24, 10737-10745 (2008)

GISAXS STUDY OF GOLD NANOPARTICLES ON BK7 GLASS AND PREDEPOSITED OXYDES

M. Lončarić¹, H. Zorc¹, J. Sancho-Parramon¹, P. Dubček¹ and S. Bernstorff²

1.) Rudjer Boskovic Institute, Bijenicka c. 54, 10002 Zagreb, Croatia

2.) Sincrotrone Trieste, SS 14, km 163.5, Basovizza (TS), Italy

The scope of this project was to study the morphology of evaporated gold nanoparticles on BK7 glass substrates as well as on predeposited dielectric films (SiO_2 and TiO_2). It was a continuation of the previous project with Elettra where silver films on amorphous substrates (glass) have been studied [1]. We have prepared a set of samples evaporated in high vacuum. Gold films of different mass thicknesses have been prepared at different substrate temperatures. According to the Volmer-Weber mechanism of growth, supported nanoparticles of gold were formed. Their structural properties were analyzed using GISAXS with the aim of determining the correlation with optical properties known from spectroscopic ellipsometry studies [2] and to complement the information obtained with AFM measurements. For data analysis the program IsGISAXS has been used [3]. The scattering calculations were done in the Distorted Wave Born Approximation (DWBA) on gradient layer. The calculation of the particle-particle correlations was done in the framework of the Local Monodisperse Approximation (LMA). For the model particle shapes, truncated spherical particles were chosen. In Figure 1, an example of measured GISAXS scattering is presented. Corresponding q_y and q_z cuts (1D cuts of experimental GISAXS pattern parallel and perpendicular to the sample surface at the position of the intensity maximum, respectively) together with fitting results are shown in Figure 2. The morphological information obtained from the GISAXS analysis of all the samples, as illustrated for one sample in Figure 2, was used to correlate the structural and optical properties [2] of gold island films prepared with different fabrication parameters.

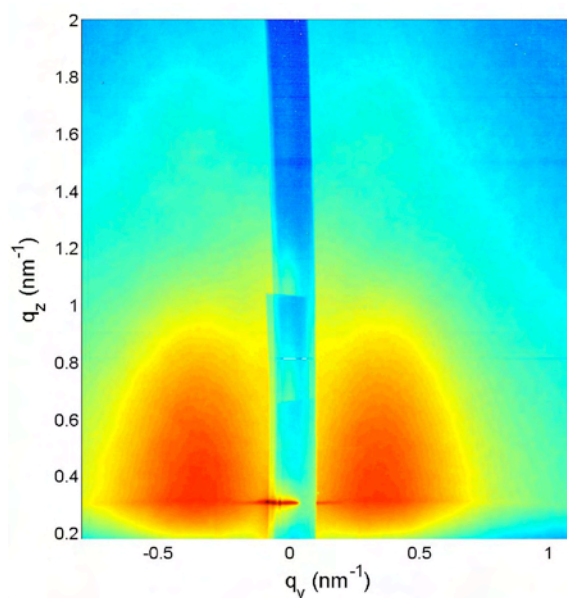


Figure1. 2D GISAXS scattering pattern of 3 nm mass thickness Au film on BK7 substrate.

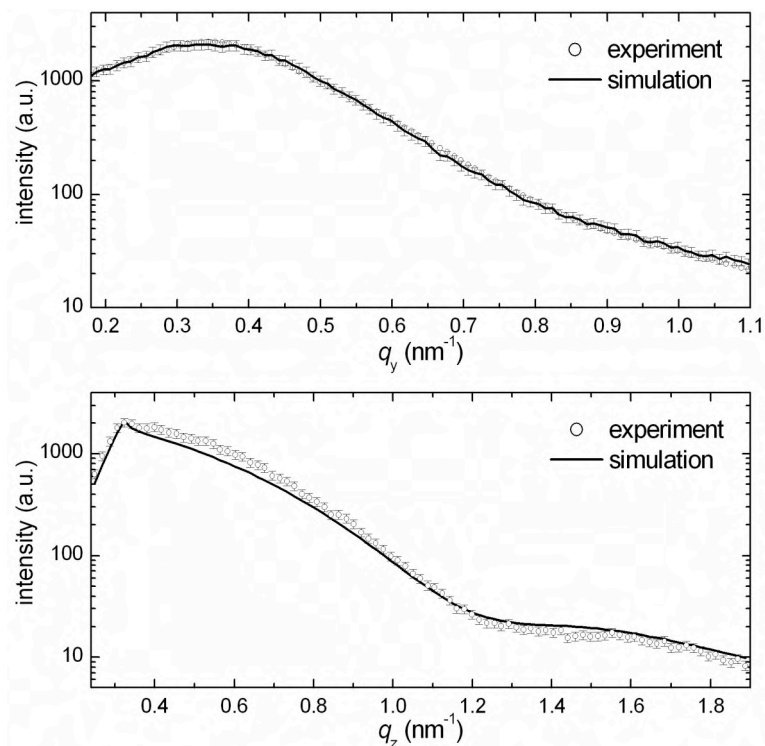


Figure 2. 1D cuts of experimental GISAXS pattern parallel and perpendicular to the sample surface at the position of the intensity maximum, respectively, together with fitting results. The resulting values for average truncated spherical particle radius, height and interparticle distances with dispersions of these values are: $R = (5 \pm 1)$ nm, $\sigma_R = (2 \pm 2)$ nm, $H = (7 \pm 2)$ nm, $\sigma_H = (0.5 \pm 0.3)$ nm, $D = (14 \pm 7)$ nm, $\sigma_D = (6 \pm 3)$ nm.

References:

- [1] M. Lončarić et al; Optical and structural characterization of silver islands films on glass substrates; Vacuum 84, 188-192 (2009)
- [2] M. Lončarić, J. Sancho-Parramon and H. Zorc; Dispersion Models for Spectroscopic Ellipsometry Characterization of Gold Island Films, submitted to Thin Solid Films
- [3] R. Lazzari; IsGISAXS: a program for grazing-incidence small-angle X-ray scattering analysis of supported islands; Journal of Applied Crystallography 35, 406-421 (2002)

THE INFLUENCE OF SYNTHESIS TYPE AND CONDITIONS ON THE MORPHOLOGY OF NANOSTRUCTURED ZnO THIN FILMS

M. Lucic Lavcevic¹, S. Bernstorff², P. Dubcek³ and D. Jozic¹

1.) Faculty of Chemistry and Technology, University of Split, Teslina 10, 21000 Split, Croatia

2.) Sincrotrone Trieste, SS 14 km 163.5, 34012 Basovizza (TS), Italy

3.) Rudjer Boskovic Institute, Bijenicka 54, 10000 Zagreb, Croatia

Introduction

At the SAXS beamline, we performed simultaneous GISAXS/GIXRD measurements on samples of ZnO, prepared by several deposition routes on a variety of substrates, followed by post-preparation treatments. These measurements are the continuation of the measurements performed in the frame of the previous project, which was focused on the analysis of the morphology of metal oxide films, the preparation of which was carried out using low temperature hydrothermal processes, without templates or surfactants. In new measurements, we were focused on samples derived by preparation routes which included hydrothermal synthesis assisted by capping organic molecules, modified Pechini and sol-gel process. More complex preparation routes allowed the generation of anisotropic and oriented building blocks of various length scales on different substrates, i.e., the design of novel morphologies, which are in better adequacy with the application of films in electronics and optoelectronics.

Experimental

In the preparation procedures, zinc nitrate, sulfate, acetate, chloride and powder were exploited as precursors. As capping species, we used citric acid, eosin, sodium dodecyl sulfate, phenolphthalein, and ethylene diamine tetraacetic acid. Films were deposited on glass, Si(100) and Si(111) wafers, ITO substrates and ZnO thin films derived by e-beam evaporation.

In GISAXS measurements, the critical angle was determined for each sample, and the scattered photons were measured for five different, larger grazing angles, using a two dimensional detector. The scattering was measured in the wave vector range from 0.02 nm^{-1} to 0.31 nm^{-1} .

Simultaneous GIXRD measurements were performed in the reflectivity plain, in the broad angular range, from around 20 to 80 degrees ($/2 \text{ theta}/$). Additionally, diffraction patterns were scanned at higher incident angles, for the analysis of crystal orientations.

Results

The objective was to analyze the correlations between parameters that define the preparation conditions and parameters that describe details of the film morphology, which determinates the film properties in applications. The results of the GISAXS/GIXRD measurements show the dependence of the degree of film crystallinity and the appearance of the crystal phases, as well as of the dimension, size, alignment and correlation of the nanosized units (nanocrystals and nanopores), on the preparation conditions (type and concentration of precursors, type and concentration of assistant species, temperature and pH of reaction, type and pre-treatment of substrate, annealing temperature, etc.). In addition, scattering and diffraction patterns, recorded on samples at different deposition time, show that the growth of nanostructures can be generally divided in distinct, fast and slow steps. The comparison of morphological characteristics (as seen by GISAXS and GIXRD) showed similarities of some samples, which were obtained by significantly different synthesis procedures (these similarities are also confirmed by scanning electron microscopy), indicating favorable conditions for preferential growth.

As an example of the dependence of the morphology on the synthesis conditions, in Fig. 1 and 2 are shown the change of the GISAXS and GIXRD patterns of ZnO films, grown in supersaturated aqueous solutions on seeded glasses, at various concentrations of capping, additive species. The hydrated form of zinc salt was used as the source of zinc ions and phenolphthalein was added for their coordination under basic conditions. Concentrations (C1 = 0.4, C2 = 0.5 and C3 = 0.6), of phenolphthalein are expressed as molar ratios to zinc ions. The scattering and diffraction patterns suggest that a change of concentration affects the way of the adsorption of capping molecules on the crystal planes. Therefore, the GIXRD peak in Fig. 1. a, representing the reflection from the (002) plane, shows the preferred orientation of nanograins deposited by nonselective adsorption of phenolphthalein, at concentration C1.

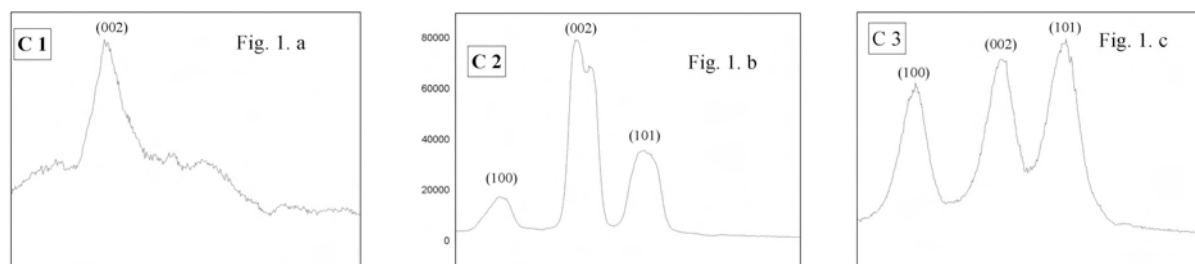


Figure 1. GIXRD patterns of ZnO nanocrystals in films, prepared at different concentrations of capping species: a) C1, b) C2 and c) C3.

According to the isotropic GISAXS pattern of the same sample (Fig. 2. a), we assume that such grains form a porous film, with either spherical or randomly oriented pores. Selective adsorption at concentrations C2 and C3 leads to a planarizing effect in the crystal growth: the appearance of additional peaks in GIXRD (Fig. 1. b and c), for reflections from the (100) and (101) planes, indicates the formation of oriented plates. Corresponding GISAXS anisotropic patterns (Fig. 2. b and c), produced by scattering on elongated pores, allow the size description of the nanoporous structure throughout the film depth.

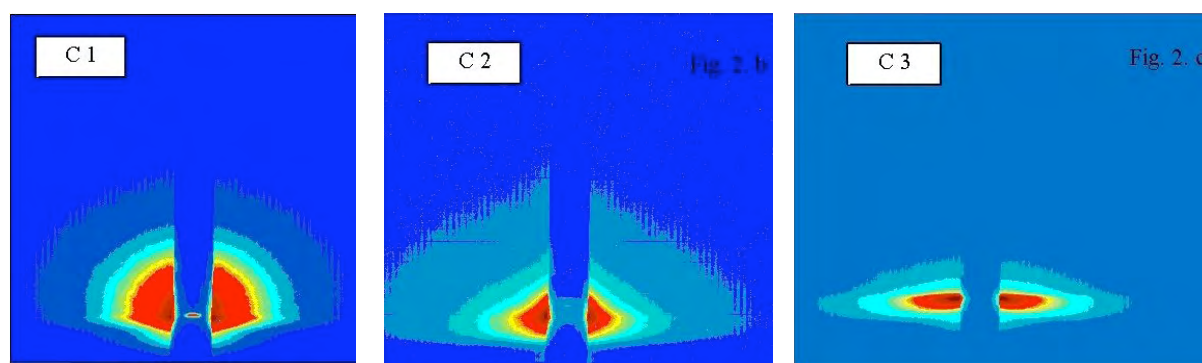


Figure 2. GISAXS patterns, attributed to scattering from pores in ZnO films, prepared at different concentrations of capping species: a) C1, b) C2 and c) C3.

Acknowledgments

Our work at ELETTRA has been supported by the European Project ELISA- 226716.

SUB 100 μ S TIME RESOLVED SAXS STUDIES OF NANOPARTICLES FORMATION USING A FREE-JET MICROMIXER

B. Marmiroli¹, G. Greci², F. Cacho- Nerin¹, B. Sartori¹, P. Laggner¹ and H. Amenitsch¹

1.) Institute of Biophysics and Nanosystem Research, Austrian Academy of Sciences, Schmiedlstraße 6, Graz, Austria

2.) IOM-CNR at Elettra Synchrotron, S.S. 14 km 163.5, Trieste, Italy

Knowledge of crystallization is important both from the technological point of view and for natural processes (i. e. biomineralization and geosciences). Fundamental characteristics of nanoparticles like lattice type, dimension, size distribution, and the effect that additives exert on these, are already defined in the early stages of the reaction. Therefore, many studies have lately been conducted on the first stages of nanoparticle formation, focusing in particular on calcium carbonate, which presents many interesting features: (i) polymorphism that can be regulated by additives, (ii) it is the most abundant biomaterial, and (iii) it has industrial relevance due to its low cost and physicochemical properties [1-3]. Recently, we have combined the state of the art in terms of synchrotron SAXS measurements, rapid mixing through microfluidics and free micro jets in air to push the limits of time resolved measurements of fast chemical reactions. We designed, fabricated and tested a micromixer based on laminar flow and producing a free jet. We achieved a mixing time $< 40 \mu\text{s}$ and a time of first accessible measurement of $75 \mu\text{s}$, to our knowledge the fastest obtained up to now for SAXS measurements following up mixing processes [4]. We have now implemented a method to estimate whether a given chemical or biological reaction can be investigated with the micromixer, and optimized the beam size for the measurement at the chosen SAXS beamline. Moreover, we have found two methods to align the jet with the X-ray beam. One is a system based on stereoscopic imaging which allows the alignment of the liquid jet with the x-ray beam with a precision of $20 \mu\text{m}$ [5]. The second is based on the WAXS signal of the microfluidic jet that can be clearly detected also when the jet is only composed of water. We have then used this second method to study the evolution of the chemical reaction of formation of calcium carbonate from sodium carbonate and calcium chloride in the time range $100\text{-}600\mu\text{s}$. We were also able to perform WAXS measurements, which seem to indicate that the early stages of Calcium Carbonate are amorphous. By employing a new detector (Dectris Pilatus 100k), which is more sensitive, we found out an unexpected behaviour while measuring the water jet background before the chemical reaction. The water signal is not negligible with respect to the air background. This effect is currently under investigation, as we want to confirm that it is not creating interference with the measurements of the chemical reactions.

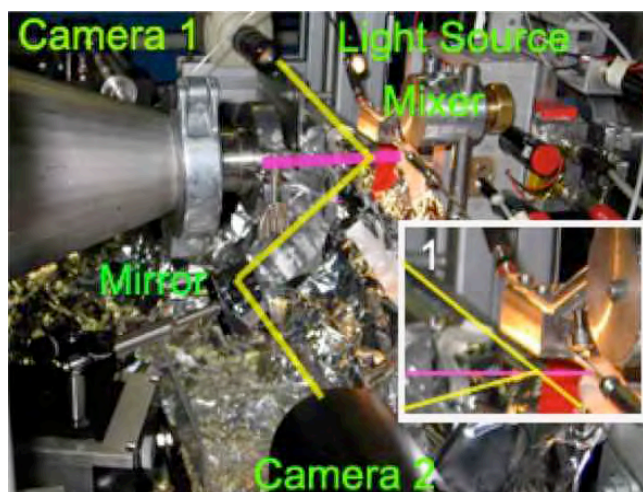


Figure 1. Alignment set-up of the free jet micromixer with the x-ray beam at the Austrian SAXS beamline at Elettra. In inset 1 a detail of the mixer sample holder is shown

Acknowledgements:

We would like to thank M. Rappolt for useful discussion, A. Bertoni, C. Morello and A. Allemandi for the precious technical support.

References:

- [1] F. C. Meldrum, and R. P. Sear ; Now you see them ; Science 322 1802 (2008)
- [2] D. Gebauer, A. Völkel, and H. Cölfen, , Stable prenucleation calcium carbonate clusters ; Science 322 1819 (2008)
- [3] E. M. Pouget , P. H. H. Bomans, J. A. C. M. Goos, P. M. Frederik, G. de With, and N. A. J. M. Sommerdijk; The Initial Stages of Template-Controlled CaCO₃ formation Revealed by Cryo-TEM; Science 323 1455 (2009)
- [4] B. Marmiroli, G. Greci, F. Cacho- Nerin, B. Sartori, P. Laggner, E. Ferrari, L. Businaro and H. Amenitsch; Free jet micromixer to study fast chemical reactions by small angle X-ray scattering, Lab Chip, 9 2063-2069 (2009)
- [5] B. Marmiroli, G. Greci, F. Cacho- Nerin, B. Sartori, P. Laggner, L. Businaro and H. Amenitsch Experimental set-up for time resolved small angle X-ray scattering studies of nanoparticles formation using a free -jet micromixer , Nucl. Instrum. Meth. B, 268 329-333 (2010)

DISPERSION AND CRYSTALLISATION IN POLYMER NANOCOMPOSITES

Geoffrey R. Mitchell¹, Donatella Duraccio², Marilena Pezzuto², Clara Silvestre² and Sigrid Bernstorff³

- 1.) University of Reading, Polymer Science Centre, Whiteknights, Reading RG6 6AF UK
- 2.) CNR - Istituto di Chimica e Tecnologia dei Polimeri, Pozzuoli, Italy
- 3.) Sincrotrone Trieste, 34012 Basovizza (TS), Italy

The addition of small quantities of nanoparticles to conventional and sustainable thermoplastics leads to property enhancements with considerable potential in a number of areas. Highly dispersed clay platelets are an attractive option with strong potential in food packaging. In such applications the dispersion of the platelets is to generate a highly tortuous pathway for gas diffusion to limit permeability. The inclusion of clay in a crystallisable matrix will also lead to changes in the flow and subsequent crystallization behavior. It is well-established that flow fields can induce a small degree of anisotropy in the polymer melt which can be subsequently greatly amplified upon crystallization. In this work we explore how such processes of nucleation and crystal growth are modified by the presence of small levels of clay particles. To quantify these effects we have exploited the power of synchrotron-based time-resolving x-ray scattering techniques coupled with a shear flow cell which allows a defined temperature and shear profile to be applied to a particular sample and follow the evolution of structure during and subsequent to flow.

We have dispersed montmorillonite by melt mixing in a Brabender-like apparatus. The matrix polymer was isotactic polypropylene (iPP) Moplen S30S having MFI of 1.8 g/10min (230°C), $M_w = 4.7 \times 10^5$ g/mol $M_w/M_n = 5.7$, manufactured by Basell, Ferrara, Italy. The montmorillonite (MMT) used was a commercial product (Laviosa- Italy), modified with dimethyl dehydrogenated tallow ammonium Dellite 67G. Some experiments were also made on the unmodified MMT (Dellite HPS) for comparison.

We have focused our experiments on clays dispersed in isotactic polypropylene. We mounted a shear stage developed at the University of Reading [1] on the SAXS beam line (Figure 1) and obtained quantitative time-resolved SAXS data as well as 1d-WAXS data. We were able to follow the variation in the structure during the shear phase as well as the subsequent crystallisation processes. We use time-resolved small-angle x-ray scattering with a time cycle of 10s to quantitatively follow the behaviour of the clay particles during shear flow and the subsequent directed crystallisation. The simultaneous WAXS capability available on the SAXS beamline at Elettra allows us, after data analysis, to follow the development of crystallinity in the polymer matrix. The 2-d nature of the SAXS data collection allows us, after data analysis, to evaluate the length scales and the level of orientation present before, during and after shear flow.

Figure 2 shows the temperature and shear versus time profile applied to each sample. The shear temperature was varied systematically from 165 to 200°C. We collected SAXS and WAXS data over the complete cycle. Figure 3 shows a SAXS pattern taken towards the end of the processing cycle where crystallization is almost complete. In this case the influence of the shear induced row nuclei has dominated the crystallization and led to a highly anisotropic crystal morphology. The anisotropic scattering from the aligned lamellar crystals is superimposed on a substantial isotropic signal which arises from the clay nanoparticles. In the figure, the shear flow direction is vertical on the page. In other samples and processing conditions, the reverse occurs and the crystallization is defined by the nucleating clay particles. The nature and proportion of compatibiliser also has a marked effect of the

structures and morphologies which develop. We did not observe any significant alignment of the clay particles.

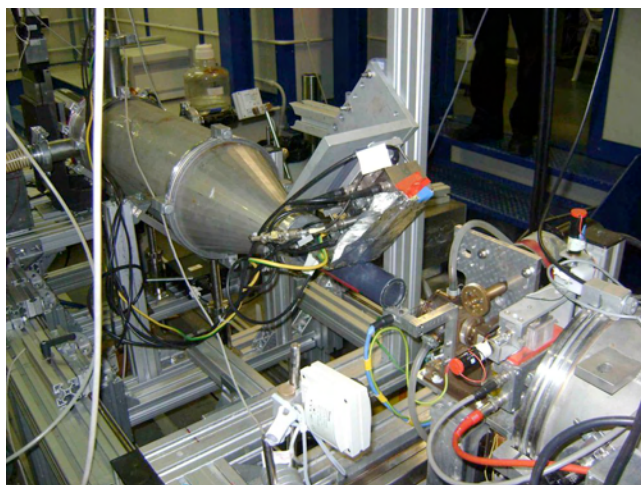


Figure 1. A photograph of the shear cell mounted on the SAXS beam-line. The WAXS detector can be seen mounted above the SAXS vacuum tube

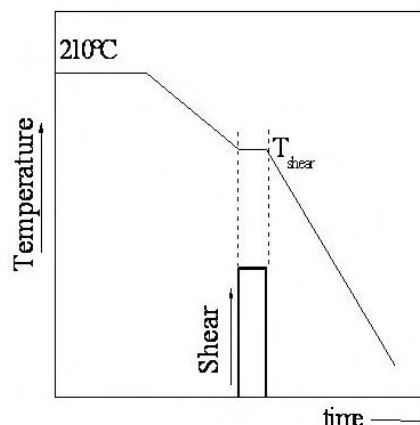


Figure 2. A schematic of the temperature / shear – time profile for each experiment

we have used each frame of the SAXS data to obtain quantitative structural information including orientation and crystallinity. We have calculated an orientation parameter $\langle P_2 \rangle$ which describes the preferential orientation of the crystal lamellae using the scattering which arises from these stacks of lamellae.

$$\langle P_2 \rangle_q = \frac{\int_0^{\pi/2} I_a(q, \alpha) P_2(\cos \alpha) \sin \alpha d\alpha}{\int_0^{\pi/2} I_a(q, \alpha) \sin \alpha d\alpha}$$

Figure 4 shows the values of $\langle P_2 \rangle$ calculated at the end of each thermal programme for a range of shear temperatures. At high shear temperatures, the level of preferred orientation is low as the anisotropy developed in the melt on shearing relaxes before crystallisations takes place. At low temperature crystallisation takes places from an anisotropic melt and hence a high level of orientation is observed. The data shows that the presence of the clay either as modified or unmodified MMT extends the shear temperature at which this cross-over from high orientation to low orientation takes place.

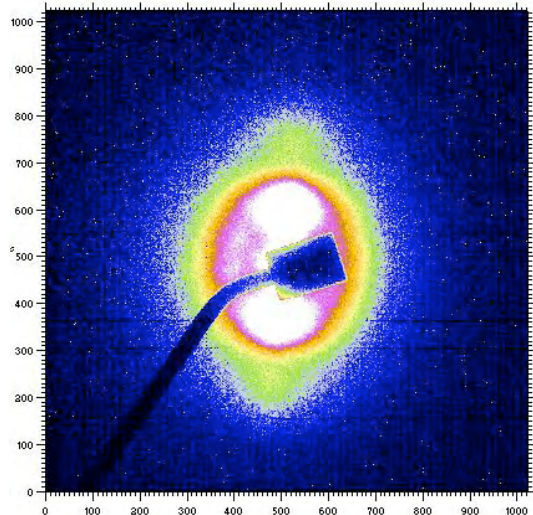


Figure 3. A SAXS pattern of isotactic polypropylene after crystallization from a sheared melt, the shear temperature was 170°C, the pattern was taken at 40°C

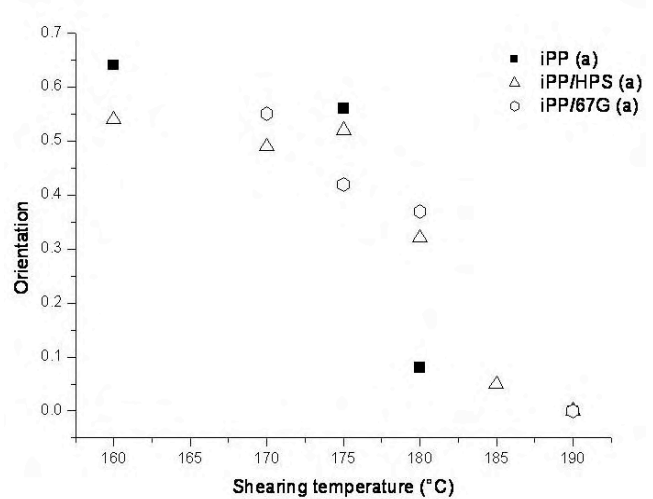


Figure 4. A plot of the value of <P2> evaluated at the end of each experiment plotted as a function of the temperature at which the shear flow was applied.

The crystallization kinetics have been analysed by calculating the invariant Q which is defined below for each frame of the SAXS data during the thermal programme:

$$Q = \int_0^{\infty} I(q)q^2 dq$$

The invariant Q is related to the electron density variation in the sample and can be broadly related to the level of crystallinity. The crystallization temperature was determined by taking the derivative of Q i.e. dQ/dT and using the maximum in the peak in an analogous manner to DSC data. There is a general reduction in the peak crystallisation temperature with increasing shear temperature as the memory of shearing becomes less. As with the orientation plot the differences between the iPP and iPP plus clay are in the cross-over range between the low and high orientation states.

In summary we find that the clay has a significant effect on the level of anisotropy which develops from shear flow at a specific temperature and on the crystallisation kinetics.

The research leading to these results has received support from the European Community's Seventh Framework Programme [FP7/2007-2013] under grant agreements n° 218331 NaPolyNet and n° 226716.

References:

- [1] A. Nogales, S.A. Thornley, G.R. Mitchell, J. Macrom. Sci: Phys. B43 1161-1170 (2004)

DIRECTING THE CRYSTAL MORPHOLOGY OF POLYMERS USING XYLITOL DERIVATIVES

Geoffrey R. Mitchell¹, Robert H. Olley¹, Fred J. Davis¹, Supatra Wangsoub² and Sigrid Bernstorff³

1.) University of Reading, Polymer Science Centre, Whiteknights, Reading RG6 6AF UK

2.) Department of Chemistry, Faculty of Science, Naresuan University, Phitsanulok, 65000 Thailand

3.) Sincrotrone Trieste, 34012 Basovizza (TS), Italy

The properties of semi-crystalline polymers such as polyethylene, polypropylene or poly(ϵ -caprolactone) depend as much on the morphology which develops during processing as they do on the chemical configuration of the polymer. We show in this work that small quantities of dibenzylidene xylitol and related compounds dispersed in poly(ϵ -caprolactone) and polypropylene provide a very effective self-assembling nanoscale framework which, with a flow field, yields extremely high levels of polymer crystal orientation. During modest shear flow of the polymer melt, the additive forms highly extended nano-particles which adopt a preferred alignment with respect to the flow field. On cooling, polymer crystallisation is directed by these particles.

We mounted our special shear stage [1] on the SAXS beam line (Figure 1). This allows us to closely define the flow and temperature environment of the polymer. For both SAXS and WAXS, the incident x-ray beam was normal to the plane of the sample. As a consequence, for the SAXS measurements the scattering vector probing the structure lies more or less in the plane of the sample, while for the WAXS, the scattering vector is tilted out of this plane by an angle, (θ), corresponding to the particular scattering angle, (2θ), of interest. In this work, the maximum scattering angle was $\sim 20^\circ$ and hence the largest value of θ or the tilt was $\sim 10^\circ$. The WAXS detector is set to measure the scattering along the meridional axis, i.e. parallel to the flow field. The shear cell was based on a parallel plate geometry, the shear rate varied across the radius. The radius of the rotating plate in the shear system was 9.5 mm, which coupled to the position of the incident beam meant that the recorded scattering pattern averaged over a range of shear rates $\sim 4\%$. The curved nature of the flow field, essentially tangential to the rotating plate, means that the scattering is also averaged over a range of slightly different orientations between the flow direction and the scattering vector; this variation was limited to $\pm 1^\circ$.

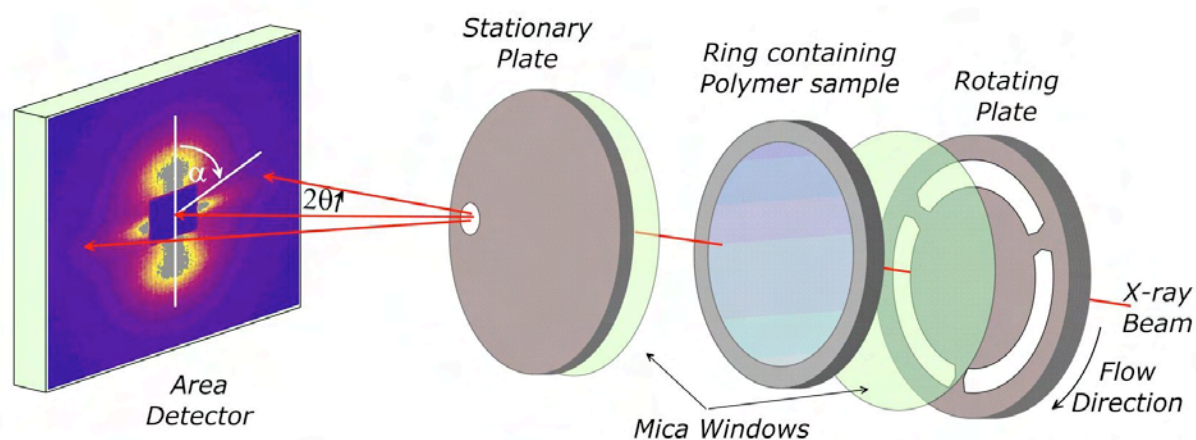


Figure 1. A schematic of the shear cell and the SAXS geometry

This arrangement allowed us to obtain quantitative time-resolved SAXS data with a time-cycle of 10s as well as 1d-WAXS data over a complete cycle of melting, shearing and

crystallization. We were able to follow the crystallisation processes from the very earliest stages which enabled us to identify the orientation of the dominant structures which grew first.

We use time-resolved small-angle x-ray scattering (SAXS) to quantitatively follow the development of the nanoscale fibrils and the subsequent directed crystallisation. The simultaneous WAXS capability available on the SAXS beamline at Elettra allows us, after data analysis, to follow the development of crystallinity in both the nanoscale fibrils and the polymer matrix. The 2-d nature of the SAXS data collection allows us, after data analysis, to evaluate the length scales and the level of orientation present before, during and after shear flow.

We were able to explore the behaviour of both dibenzylidene xylitol and a chloro derivative as the self-assembling additive. In the case of the dibenzylidene xylitol, the high solubility of this in both polypropylene and polycaprolactone (revealed by SAXS) limited its effect. In contrast the chloro derivative was very effective and efficient in directing the crystallisation of the matrix polymer for both polypropylene and polycaprolactone as shown in Figure 2. The horizontal streak arises from the nanofibrils while the two spots on the meridional section arise from a highly aligned system of polymer lamellar crystals. Figure 3 shows schematically the key structural components in terms of the aligned nanofibrils and the subsequent directed crystallization of the matrix polymer.

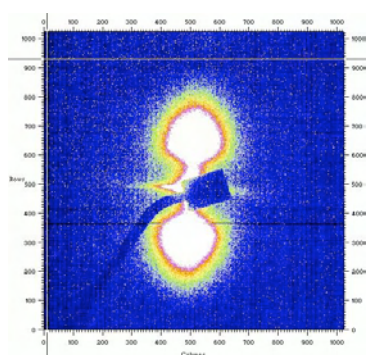


Figure 2. SAXS pattern of a sheared sample of polycaprolactone containing di-para-chloro-benzylidene sorbitol showing the highly aligned lamellar structure and the horizontal streak which arises from the aligned nanofibrils. The flow direction was vertical.

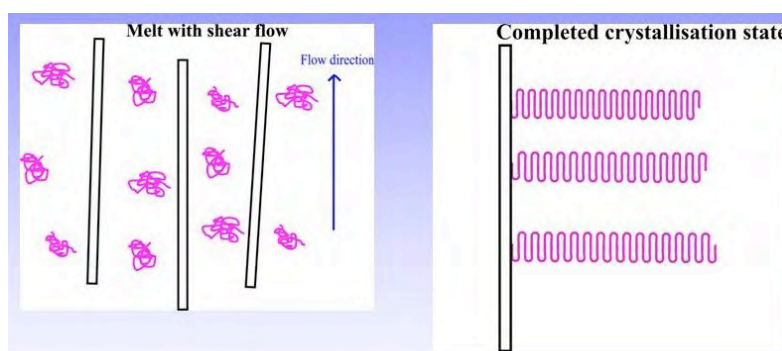


Figure 3. A schematic of the aligned nanofibrils (left) and the directed lamellar crystals (right) which give rise to the pattern shown in Figure 2.

We also were successful in exploring the effectiveness of a systematic series of chloro isomers of dibenzylidene sorbitol. The ortho and para isomers exhibited similar behaviour in directing the crystallisation of the matrix polymer. In contrast the meta isomer was surprisingly more stable at elevated temperatures.

We contrasted the effects of the nanofibrils with extended polymer chains generated by shear flow and there was considerable asymmetry in the effects of residual moieties after melting compared with those developed during shearing in the melt.

References:

- [1] Nogales A., Thornley S.A. Mitchell G.R., J. Macrom. Sci: Phys. B43, 1161-1170 (2004)

GISAXS CHARACTERIZATION OF CARBON/TUNGSTEN MULTILAYERS

N. Radić¹, M. Jerčinović¹, P. Dubček¹, K. Salamon², O. Milat² and S. Bernstorff³

- 1.) Rudjer Bošković Institute, Bijenička 54, Zagreb, Croatia
- 2.) Institute of Physics, Bijenička 46, Zagreb, Croatia
- 3.) Sincrotrone Trieste, Basovizza, Italy

W/C multilayers are frequently examined as a promising material for use as X-ray mirrors. Several physical parameters of the multilayer are critical for its optimal performance in that role: regularity of the stack, bilayer period thickness, layer thickness ratio in a bilayer, interface roughness and interface diffusion/ sharpness. In this work we have deposited a series of W/C multilayers by sequential magnetron sputtering onto various substrates - glass, silica, alumina and mono-Si.

The KJLC CMS-18 sputtering system has been used for deposition of the examined thin films. The circular substrates (diameter 11 mm, at nominally room temperature) were mounted onto a multisite rotating substrate holder in order to prevent preferential stress development in the films. Pure tungsten (99,99%) and pure carbon (99,9%) targets were used for DC and RF sputtering, respectively. Throughout different multilayers series preparation, the carbon has been RF sputtered by 400 W power, with deposition rate of about 0,7 nm/min, while tungsten has been DC sputtered by 20 W power (as a rule), with deposition rate about 1,0 nm/min. Three series of C/W multilayers were designed to examine the effects of three parameters: a) differing carbon layer thickness with constant tungsten layer thickness (≈ 1 nm) and fixed total number of bilayers (20); b) differing tungsten phase (α/β ratio) while keeping fixed the bilayer spacing and total number (20); c) fixed bilayer period for differing total number of bilayers (10-30). The substrate adjacent layer was always carbon, of the thickness repeated throughout the multilayer, while the final layer was always tungsten.

The topography of the surface and morphology of the interfaces have been examined by local (AFM, TEM) and global methods (XRR, GISAXS). Finer details of the surface/ interface morphology (roughness, correlation lengths) can be derived from the GISAXS data. The GISAXS measurements were performed at the Austrian SAXS beamline, with 8 keV ($\lambda = 0.154$ nm) radiation energy. The shape of the incident beam ($h = 0.1$ mm, $w = 2$ mm) was optimized for the best signal to noise ratio and minimum background. The sample was mounted on a stepper-motor-controlled tilting stage with a step resolution of 0.001° . The stage (and the sample surface) was aligned horizontally and parallel to the beam within 0.1° . Measurements were taken at different, fixed grazing angles. The SAXS-pattern were obtained with a 2-dim CCD-detector (X-Ray Hystar 2048 from Photonics Science).

A whole set of obtained data will be analyzed along the lines presented for example in ref. [1]. Measuring of small angle x-ray scattering under grazing incidence angle (GISAXS) with a 2D detector gives insight into the nature of the W/C multilayer growing process. The scattered diffuse intensity is concentrated in the so-called Bragg sheets, which means that the roughness is mostly correlated among different interfaces. The issue of the conformality is quantified from the full width of the Bragg sheets at each value of the lateral (parallel to the surface) scattering momentum. It is found that the high-frequency components of the roughness do not propagate well through the W/C multilayers despite a quite long vertical correlation length for the low-frequency roughness components.

The integral (over 'Brillouin zone') intensity of the Bragg sheet vs. q_{\parallel} gives the self height-height correlation function for all interfaces. The asymptotic properties of the correlation function for small distances are determined from the power law decay of the integrated intensity at high q_{\parallel} .

We found a scaling (power law) behavior in the scattering, which implies that on a small scale the interfaces are self-affine.

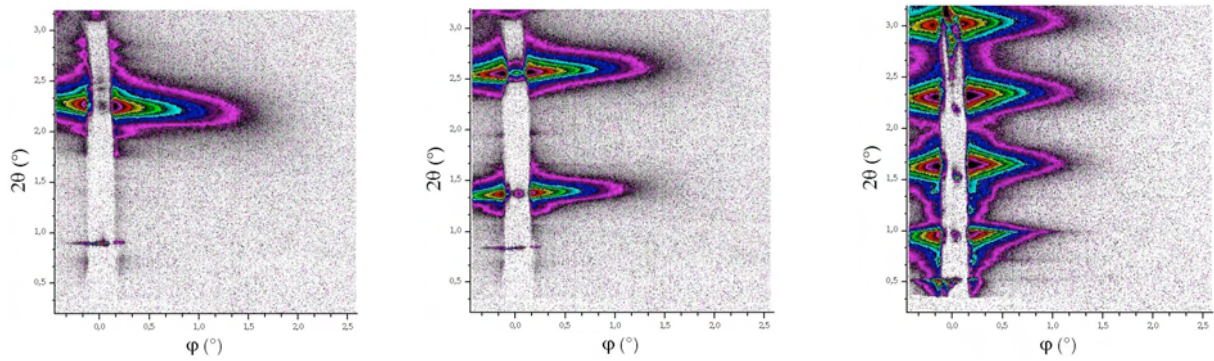


Figure 1. GISAXS intensity patterns for three C/W multilayer samples with constant tungsten layer thickness (≈ 1 nm) and differing carbon layer thickness: ≈ 3 nm, ≈ 6 nm, ≈ 11 nm, respectively, and a fixed total number of bilayers (20).

References:

- [1] R. Paniago, R. Forrest, P.C. Chow, S.C. Moss, S.S.P. Parkin and D. Cookson, Physical Review B, 56 13442-13454 (1997)

THE GROWTH AND COAGULATION OF CdS NANOPARTICLES IN EDTA AQUEOUS SOLUTION OBSERVED BY SMALL ANGLE SCATTERING SAXS

A. A. Rempel¹, A. Magerl² and H. Amenitsch³

1.) Institute of Solid State Chemistry, Ural Branch of the Russian Academy of Sciences, Pervomaiskaya 91, 620990 Ekaterinburg, Russia

2.) Institute of Crystallography and Structural Physics, University Erlangen-Nuremberg, Staudtstr. 3, 91058 Erlangen, Germany

3.) Institute of Biophysics and Nanosystems Research, Schmiedlstr. 6, A-8042 Graz, Austria

The goal of this work was an *in situ* study of nucleation and growth of nanoparticles in supersaturated aqueous solutions. Within this work we focus primarily on the very early stage of the formation of CdS nanoparticles in a chemical bath (order of hundred milliseconds). In addition, significant attention was paid to long term process like coagulation (order of hours). CdS (cadmium sulfide) nanocrystals were chosen for the experiment. This material serve as model systems for a wide range of applications relating e. g. to the ability to adjust the electronic band gap energy through the particle size [1] or for their capacity to increase the conversion coefficient of solar cells [2]. Furthermore nanocrystals of this material are applied for light detectors, lasers [3], catalyst, and as biological labels [4, 5].

High quality synthesis route for CdS nanoprticles has been developed successfully in our labs [6]. In this route we start from two solutions containing (1) complexed Cd²⁺ ions in form of CdY²⁻, where Y⁴⁻ is the complexing ion and (2) dissolved sulfur ions S²⁻ (see Fig. 1). Until these solutions are not mixed all substances remain in solutions in their ionic form. Nucleation according to the chemical reaction $\text{CdY}^{2-} + \text{S}^{2-} = \text{CdS}(\text{solid}) + \text{Y}^{4-}$ sets in immediately after mixing and nanocrystalline CdS particles start to grow. Other ions in the solution have undersaturated concentrations and they will not form solid phases. Although little is known today, we believe that the growth rate at this early stage can be influenced by temperature and it is sensitive to the ionic concentration. This method of synthesis is closely related to chemical bath deposition [1,7], which is highly promising [8] for preparing large quantities of nanomaterials with size-dependent properties. Previously CdS nanoparticles were characterized by TEM, SEM, X-ray diffraction and the coherent particle size was estimated from the Scherrer formula [9, 10].

The SAXS measurements have been conducted at the Austrian SAXS beamline. First, prepared solutions containing (1) dissolved complexed cadmium ions, and (2) sulfur ions were measured with the image plate detector (MAR 300). Subsequently, the two solutions were automatically mixed in the Biologic Stop Flow Module. The kinetics of particle formation and growth was followed during 3 h by means of two VANTECH detectors with minimal frames of 50 ms. During 3 h the solid nanoparticles were grown to about 3 to 20 nm (Fig. 1). The kinetics of particle coagulation was followed during 10 h by means of static measurements with frames of 30 s. During 10 h the coagulates were grown to about 50 to 100 nm. Between single experiments the Stop Flow Module was rinsed by a solution of hydrochloric acid (HCl) with a concentration of about 20-30 mass.%. The q -range of interest in our experiment was from 0.01 to 0.5 Å⁻¹.

The active time for nucleation and growth of CdS nanoparticles was measured to be of about 1 s and 1 min, respectively, depending on initial concentration of the components (between 0.002 and 0.0125 M). The characteristic time for coagulation in heavily concentrated solution (0.0125 M) was measured to be about of 5 hours (Fig. 2).

After evaluation of all measured data we expect to contribute to the development of a kinetical model for the growth of binary materials nanoparticles and to obtain insights into the process of coagulation.

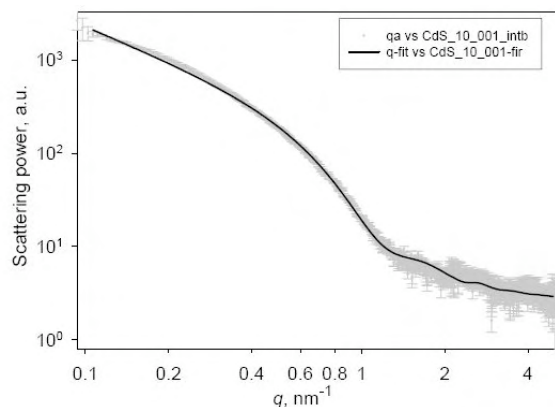


Figure 1. SAXS of diluted (0.00125 M) CdS nanoparticles solution (grey points and error bars) and fit (solid line) using elongated cylinders as model system.

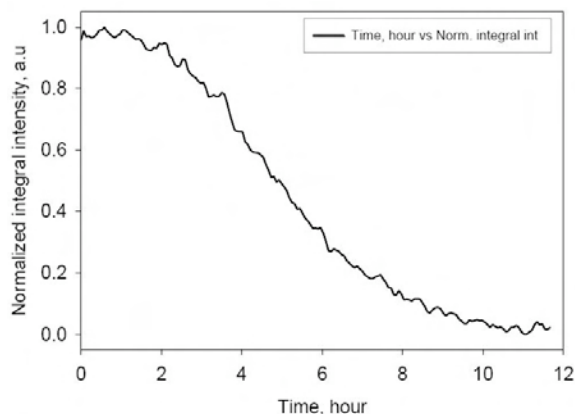


Figure 2. CdS with initial and diluted 1/6 and 1/10 concentrations in compare to water

References:

- [1] L. Katsikas, A. Eychmüller, M. Giersig, H. Weller; Discrete excitonic transitions in quantum-sized CdS particles; *Chem. Phys. Lett.* 172, 201-204 (1990)
- [2] S. Kumazawa, S. Shibutani, T. Nishio, T. Aramoto, H. Higuchi, T. Arita, A. Hanafusa, K. Omura, M. Murozono, H. Takakura; *Sol. Energy Mater. Sol. Cells* 49, 205 (1997)
- [3] V. I. Klimov, A. A. Mikhailovsky, S. Xu, A. Malko, J. A. Hollingsworth, C. A. Leatherdale, H.-J. Eisler, M. G. Bawendi; *Science* 290, 314 (2000)
- [4] M. Jr. Bruchez, M. Moronne, P. Gin, S. Weiss, A.P. Alivisatos; *Science* 281, 2013 (1998)
- [5] W. J. Parak, D. Gerion, T. Pellegrino, D. Zanchet, C. Micheel, S. C. Williams, R. Boudreau, M. A. Le Gros, C. A. Larabell, A. P. Alivisatos; *Nanotechnology* 14, R15 (2003)
- [6] N.S. Kozhevnikov, A.S. Vorokh and A.A. Rempel; Preparation of Stable Colloidal Solution of Cadmium Sulfide CdS Using Ethylenediaminetetraacetic Acid; *Russian Journal of General Chemistry* 80, 391–394 (2010).
- [7] P. O'Brien, J. McAleese, *J. Mater. Chem.* 8 (1998) 2309.
- [8] A.A. Rempel. *Nanotechnologies. Properties and applications of nanostructured materials.* Russian Chemical Reviews. 2007. V.76. No 5. P.435-461.
- [9] A.A. Rempel, N. S. Kozhevnikova, S. Van den Berghe, W. Van Renterghem. Self-organization of cadmium sulfide nanoparticles on the macroscopic scale. *Physica status solidi (b)*. 2005. V.242. No 7. P.R61-R63.
- [10] N.S. Kozhevnikova, A.A. Rempel, F. Hergert, A. Magerl. Structural study of the initial growth of nanocrystalline CdS thin films in a chemical bath. *Thin Solid Films*. 2009. V.517. P. 2586-2589.

EFFECTS OF RELEASING THE HYDROSTATIC PRESSURE ON THE NANOSTRUCTURE AFTER SEVERE PLASTIC DEFORMATION OF Cu

E. Schafler¹, R. Schuster¹, M.B. Kerber¹, F. Spieckermann¹, M. Zehetbauer¹ and S. Bernstorff²

1.) Physics of Nanostructured Materials, Faculty of Physics, University of Vienna, A-1090 Wien

2.) Sincrotrone Trieste, Basovizza, Italy

In [1] first in-situ stress-strain relations determined by torque measurement during high pressure torsion (HPT) deformation were presented and compared to flow-curves obtained from microhardness measurements of the processed HPT-pillet. Due to the big difference between of the two strength measures the effect of hydrostatic pressure became subject of interest. Fig.1 shows the torque-stress of HPT-Cu at 4 GPa compared with the strength after HPT-deformation (microhardness) and during conventional torsion at ambient pressure.

The difference has been explained by considerations on intrinsic parameters affected by the hydrostatic pressure by adapting the large strain work hardening model of Zehetbauer: (i) Young's modulus (ii) flow stress through the extra work which is necessary to generate the excess volume of deformation induced defects against the external hydrostatic pressure p ; and (iii) the enhanced hydrostatic pressure has a contribution to the enthalpy of vacancy migration, which governs the annihilation of dislocation via climb of edges. These first two effects have been estimated to increase the flow stress by 15 % per 1 GPa pressure [1]. Considering the in-situ stress levels $p=0.1$ MPa and 4 GPa in Fig.1, about 60 % of stress increase can be attributed to effects (i) and (ii), while the difference left arises from effect (iii) representing the pressure induced permanent change of microstructure. This difference indeed matches with that between flow stress for 0.1 MPa and the post flow stress left after HPT at 4 GPa (Fig.1)

Thus it is of special interest to analyse the differences in the microstructure of the loaded (under hydrostatic pressure) and unloaded (after pressure release) state. Low temperature is considered to have similar influence on the diffusivity $D=D_0 \exp(-\Delta H_{\text{eff}}/kT)$ as the hydrostatic pressure (see Table 1). So a special experimental setup and procedure has been developed to measure X-ray diffraction profiles of the loaded and unloaded state (see details in [2]). In Fig. 2 the remarkable difference in the peak width confirms all previous suggestions of static recovery/recrystallisation effects upon unloading. While the results from XPA of the unloaded state are equal to previous investigations [3 -5] the loaded state exhibits a substantially higher dislocation density, while the size evolution of the coherently scattering domains indicates that the grain fragmentation is completed under pressure.

The slightly larger sizes d at higher strains were observed also in [3] and indicate the evolution of an equilibrium subgrain structure with minimum internal stresses [3, 4]. The drop of the flow stress curve in the unloaded state (Fig. 1) as well as the decrease of the dislocation arrangement parameter $M = R_e \sqrt{\rho}$ (see Table 1) support this interpretation. Smaller values of M mean increased screening of the dislocation strain field by formation of a polarised dislocation structure i.e. dislocation dipoles [6]. This low-stress arrangement is formed after high strain deformation, but, on the other hand, also upon release of the hydrostatic pressure, and has been found to increase with higher hydrostatic pressure [3]

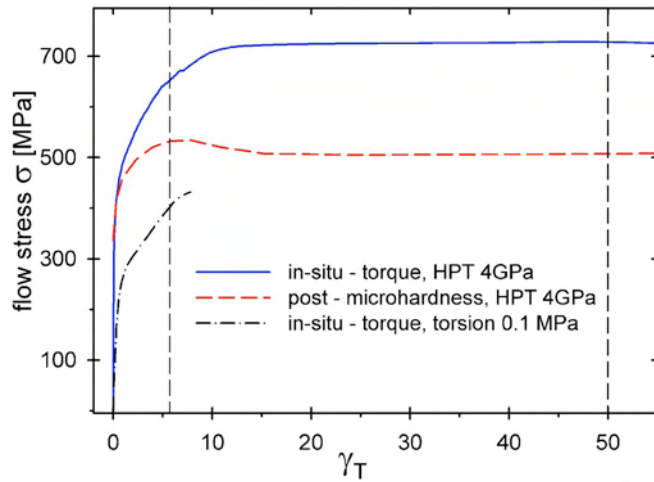


Figure 1. Flow stress as determined by in-situ torque measurement (full) and microhardness indentation (dash) both for HPT at 4 GPa, and for conventional torsion (dash-dot).

Figure 2. Diffraction profiles for $\gamma_T = 50$ in the loaded (full) and unloaded (dash) state.

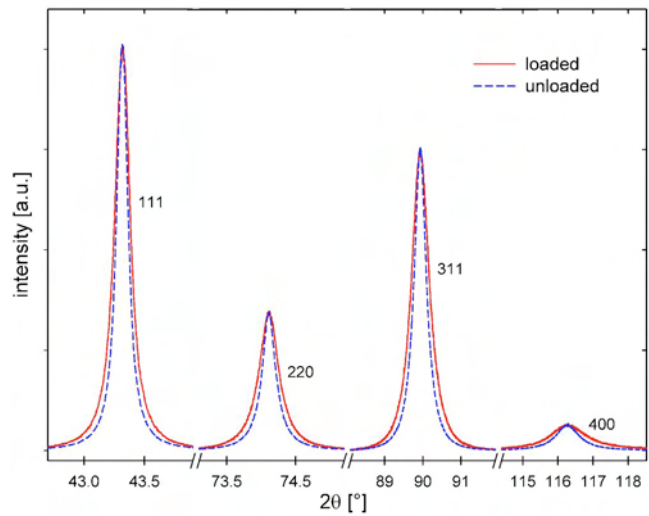


Table 1. Resulting parameters of the X-ray profile analysis, average coherently scattering domain size d , dislocation density ρ and dislocation arrangement parameter M .

	d [nm]	ρ [10^{15}m^{-2}]	M
$\gamma_T = 6$, loaded	56	3.4	1.7
$\gamma_T = 6$, unloaded	60	3.1	1.5
$\gamma_T = 50$, loaded	68	7.9	1.3
$\gamma_T = 50$, unloaded	76	4.4	1

References:

- [1] M. Zehetbauer, H.P. Stüwe, A. Vorhauer, E. Schafner, J. Kohout, Adv.Eng.Mater. 5 (2003) 330
- [2] E. Schafner, Scripta Mater. 62 (2010) 423
- [3] A. Dubravina, M. Zehetbauer, E. Schafner, I. Alexandrov, Mater.Sci.Eng. A 387-389 (2004) 817
- [4] E. Schafner, A. Dubravina, B. Mingler, H.P. Karthaler, M. Zehetbauer, Mater.Sci.Forum 503-504 (2006) 51
- [5] E. Schafner, M. Kerber, Mater.Sci.Eng. A 462 (2007) 139
- [6] M. Zehetbauer, T. Ungar, R. Kral, A. Borbely, E. Schafner, B. Ortner, H. Amenitsch, S. Bernstorff, Acta Mater. 47 (1999) 1053

ORDERING OF CoPt₃ NANOPARTICLES ON ORGANIC SELF-ASSEMBLED MONOLAYERS

Th. Schmidt¹, A. Zargham¹, S. Röhe², S. Bernstorff³, M. Bäumer², and J. Falta¹

1.) Institute of Solid State Physics, University of Bremen, Otto-Hahn-Allee 1, 28359 Bremen, Germany

2.) Institute for Applied and Physical Chemistry, University of Bremen, Loebener-Str. 2, 28359 Bremen, Germany

3.) Sincrotrone Trieste, Strada Statale 14, km 163.5, 34012 Basovizza / Trieste, Italy

Nanoparticles (NPs) establish the link between bulk materials and atomic and molecular structures and thus are of enormous scientific and technological interest. NPs can be synthesized by several chemical and physical methods amongst which colloidal bimetallic NPs offer superior capabilities due to the fact that their physical and chemical properties can be precisely determined by minute tailoring of size, shape, stoichiometry and internal structure [1]. Cobalt, to take an example, is one of the few materials that show catalytic behavior in Fischer-Tropsch processes. Combining Co with a noble metal like Pt into alloy or core-shell NP structures, drastically changes its catalytic properties. Self-assembled ordered monolayers of these particles may then in future be incorporated as active high-surface-area catalysts for a variety of catalytic reactions, resulting in increased selectivity and activity [2,3]. In the present study, the lateral ordering of such CoPt NPs deposited on organic self-assembled monolayers (SAMs) by means of either spin or dip coating have been investigated by grazing-incidence small-angle X-ray scattering (GISAXS). As a model system we used SAMs of hexadecanethiol (HDT) on gold-coated Si wafers as substrates.

The samples discussed here had already undergone investigations by X-ray standing waves in total external reflection (TER-XSW) and scanning electron microscopy (see Fig. 1), which delivered information about the nanoparticle size as well as the surface coverage [4]. Furthermore, the TER-XSW measurements revealed the density distribution in vertical direction and as a result the mean distance between the nanoparticles and the support [4]. In these studies we observed clear dependencies of vertical ordering of the NPs and coverage, i.e., that a higher coverage leads to a better vertical ordering for both preparation methods (spin coating and dip coating).

GISAXS investigations were performed on differently covered NP samples at different incidence angles, below and above the critical angle of the substrate. Figure 2 shows a scattering pattern of one of the samples as an example. Since the scattering contrast scales with the element number, it is evident that the heavy NPs dominate the small-angle scattering while the contribution of the SAM film is negligible. Due to the long camera distance of about 90 cm not all information could have been collected. Therefore, the detector was shifted horizontally, such that $q_{\parallel}=0$ is not positioned in the center, in order to make at least one second-order peak visible. A line through $q_{\perp}=0.6 \text{ nm}^{-1}$ is also visible on the picture which indicates the position, where the exit angle is equal to the critical angle (Yoneda peak). The line profiles of all the investigated samples are extracted at the mentioned position. By fitting Lorentzian shape functions, which was found to yield satisfactory results in our case, the mean particle-particle distance $\langle d \rangle$ can be calculated from the in-plane distance of the two first-order satellite peak positions. Furthermore, the peak width δq provides a measure for the degree of ordering in the film [5]. It turned out that the degree of ordering hardly depends on the deposition technique (spin or dip coating). By keeping the preparation conditions in a range noticed as optimal [6], the substrate surface is covered homogeneously, and a well-defined lateral ordering is found (cf. Fig. 3). We come to the conclusion that contrary to vertical ordering the lateral ordering is hardly a function of coverage. Samples with different coverages (and same in other aspects) show the same lateral distances within the error bar. The distance in lateral direction seems to be governed by ligand-ligand and, possibly, ligand-

SAM interactions. The results presented here are very promising for future experiments. Performing ligand exchange steps, and using different SAM structures, would shed a light on how the ordering of the NPs is affected by the interaction of SAMs and ligands.

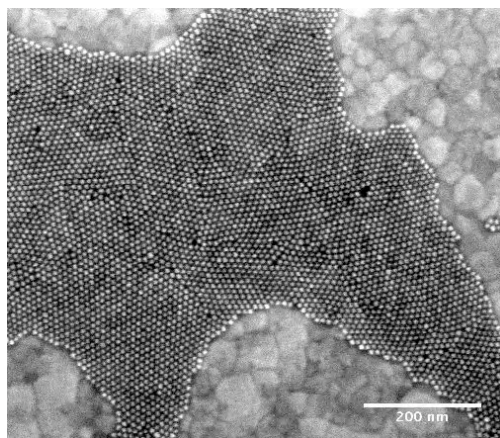


Figure 1. Scanning electron micrograph of CoPt₃ nanoparticles deposited on a functionalized Au substrate. The latter exhibits a grainy structure (bright patches).

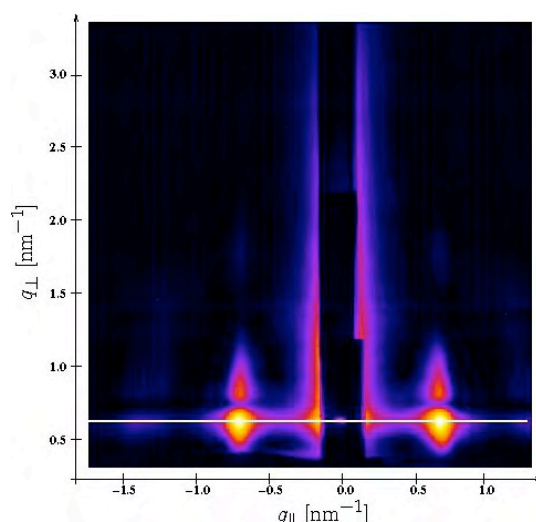


Figure 2. GISAXS pattern of CoPt₃ nanoparticles deposited on a functionalized Au substrate. The vertical stripe indicates the position of the semi-transparent Al absorber. The white line through $q_{\perp}=0.6 \text{ nm}^{-1}$ indicates the line profile extracting position.

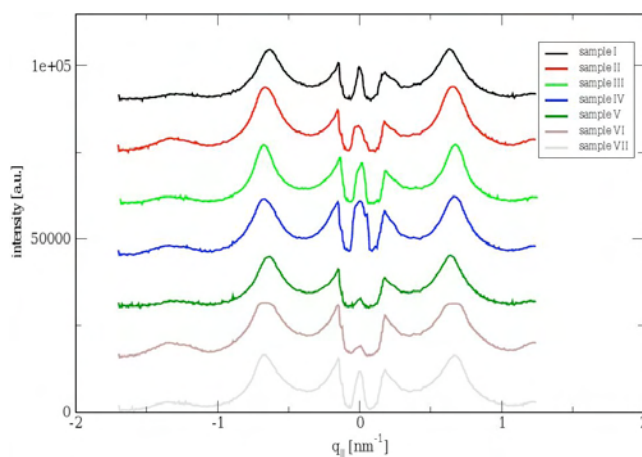


Figure 3. Line profiles along q parallel taken at the line indicated in fig. 2. Independent of sample preparation the average NP spacing (peak position) is nearly identical, and only slight variations in the degree of ordering (peak width) are observed.

References:

- [1] G. Schmid (ed.), Nanoparticles: From Theory to Application (Wiley-VCH, Weinheim, 2004)
- [2] A. F. Carlsson, M. Bäumer, T. Risse, and H.-J. Freund, *J. Chem. Phys.* 119, 10885 (2003)
- [3] N. Toshima and T. Yonezawa, *New J. Chem.* 22, 1179 (1998)
- [4] A. Zargham, T. Schmidt, J. I. Flege, M. Sauerbrey, R. Hildebrand, S. Röhe, M. Bäumer, and J. Falta, *Nucl. Instr. Meth. B* 268, 325 (2010)
- [5] J. I. Flege, Th. Schmidt, V. Aleksandrovic, G. Alexe, T. Clausen, B. Gehl, A. Kornowski, S. Bernstorff, H. Weller, and J. Falta, *Nucl. Instr. Meth. B* 246, 25 (2006)
- [6] A. Zargham, Synchrotron Radiation Based Multi-Scale Structural Characterization of CoPt₃ Colloidal Nanoparticles, Ph.D. thesis, University of Bremen, Germany (2010)

VAPOR ADSORPTION ON CMK-5 MONITORED BY IN SITU XRD EXPERIMENTS

W. Schmidt¹, H. Amenitsch²

1.) Max-Planck-Institut für Kohlenforschung, Mülheim a.d. Ruhr, Germany

2.) Institute of Biophysics and Nanosystems Research, Austrian Academy of Sciences, Graz, Austria

Synthetic CMK-5 – type carbons with ordered arrangement of tubular pores can be synthesized using the mesoporous silica SBA-15 [1,2] as hard template via nanocasting [3-5]. These carbons possess very high surface areas up to $1600 \text{ m}^2\text{g}^{-1}$ and hexagonally ordered pores, the walls of which consist of amorphous carbon. These properties make CMK-5 an interesting adsorbent. However, even though substantial success has been made in the last decade with respect to better understanding gas adsorption processes in porous systems, gas adsorption in CMK-type carbons is still not well understood. Generally, simplified models for gas adsorption are used, considering adsorption only in specific types of pores, with either slit-shaped, cylindrical, or spherical pore geometries. The information about adsorption in mesoporous carbon materials is thus limited to very specific materials. Furthermore, the models (e.g., for DFT or Monte Carlo simulations) are generally over-simplified, e.g., with respect to surface roughness and more complex pore geometries.

CMK-5 carbons exhibit both convex as well as concave surfaces as schematically shown in Figure 1a. Small carbon bridges keeping the carbon tubes together have been omitted for simplicity. Gas adsorption at low loadings generally occurs preferentially either in smaller pores and/or on concave surfaces. In CMK-5 pores with concave curvature and others with convex curvature coexist. Adsorption potentials are supposed to be significantly different for concave and convex pores. Interestingly, the mesopores with convex curvature are somewhat smaller than the ones with concave wall curvature and adsorption potentials are usually also enhanced in smaller pores. Thus, an interesting question arises from this coexistence of small convex pores and larger concave pores. In which type of pores gas molecules would get adsorbed preferentially at low pressures? This question is of fundamental interest for adsorption theory.

A direct insight into the adsorption processes, e.g., by in-situ methods, thus was thought to allow for a much better understanding of the adsorption process on such materials. Theoretical calculations have shown that patterns of CMK-5 materials are very susceptible towards minute variation of electron density variations, e.g., due to changes of wall thicknesses and diameters [6] and/or deposition of adsorbed layers on the pore walls. Vapor adsorption in pores of CMK-5 significantly changes the electron density distribution within such materials and thus is directly detectable in the XRD patterns. The structure of CMK-5 can be described with hexagonal symmetry in two dimensions. Since no translational order exists along c , only (hk0) reflections are observed (see Figure 1b). Low angle XRD investigations have been performed at the SAXS beamline of the Austrian Academy of Sciences (IBN) at the synchrotron radiation source Elettra in Trieste. Vapor adsorption of dichloromethane (DCM) has been monitored by in situ XRD measurements. The sample was placed in a 2mm quartz glass capillary which was attached to a dosing unit consisting of a manifold, pressure gauge, adsorptive reservoir, and a vacuum pump. After activation of the CMK-5 sample at 200°C under vacuum, diffraction patterns were recorded prior to vapor adsorption and successively during dosing DCM vapor to the activated carbon material. Since the adsorption of DCM is a rather slow process, the adsorption could be monitored continuously for which the activated sample has been exposed to a DCM vapor at saturation vapor pressure at 25°C . The recorded XRD patterns are shown in Figure 1b.

Adsorption of DCM resulted in significant changes of the XRD patterns. The positions of the reflections shift during the adsorption process which is caused by changes of the lattice

constant. During the first 45 minutes of adsorption, a decreased of the lattice constant is observed which then increases with successive exposure to the DCM vapor (Figure 2a). From the integrated intensities of the individual reflections, structure factors (F_{hkl}) have been derived which have been used for calculation of electron density maps via inverse Fourier transformation. The respective phases have been calculated from structure models [6]. From the electron density maps, as shown in Figure 2b, it can be seen that in the early stages of adsorption the interstitial pores between the carbon tubes are filled with the adsorbate. This process proceeds along with the decrease of the lattice constant. Obviously, a contraction of the structure occurs during that stage of adsorption. The reason for that is probably a contraction of the structure due to capillary forces which effectively pulls the carbon tubes towards each other. With continuous adsorption of DCM the concave tubular pores are also filled. At that stage of the adsorption the structure obviously expands again which is indicated by the increase of the lattice constant. After about two hours, the adsorption is terminated and no further change in lattice parameter and/or relative peak intensities are observed.

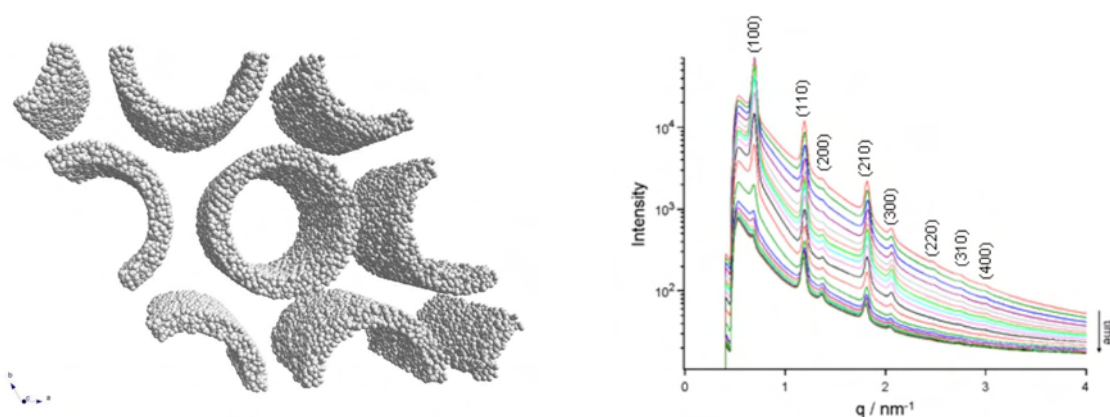


Figure 1. a) Model for CMK-5 showing the two pore systems with convex and concave surfaces, and b) X-ray diffraction patterns successively measured during continuous adsorption of dichloromethane.

The experiments thus have shown that the adsorption of DCM is a dynamic process which goes along with measurable changes of the structure of the mesoporous carbon material. Adsorption in the early stages of the adsorption process takes place preferentially in the smaller convex interstitial pores during which a contraction of the structure. Only upon adsorption of DCM in the larger concave (cylindrical) pores relaxation of the contracted structure takes place.

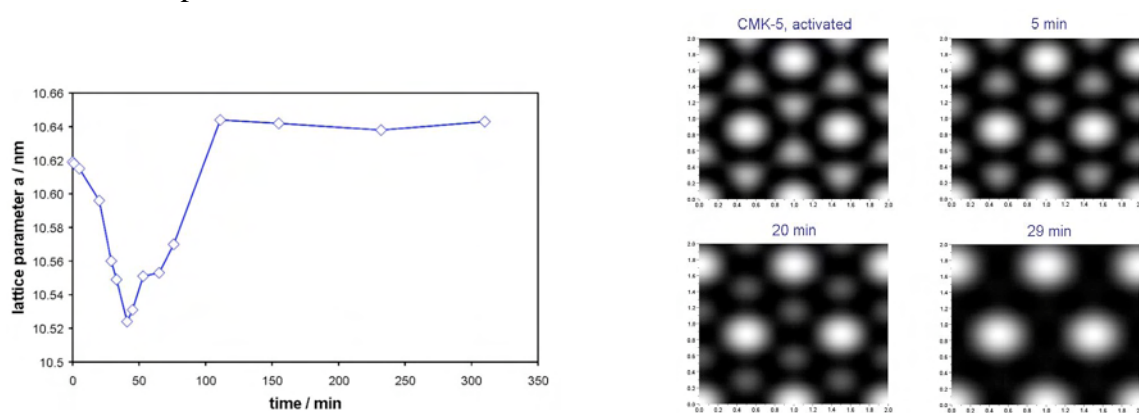


Figure 2. a) Changes of lattice constant a during adsorption of dichloromethane, and b) projections of electron density maps as calculated from integrated intensities of the respective XRD patterns.

References:

- [1] D. Zhao, J. Feng, Q. Huo, N. Melosh, G.H. Frederickson, B.F. Chmelka, G.D. Stucky, *Science* 279, 548-552 (1998)
- [2] D. Zhao, Q. Huo, J. Feng, B.F. Chmelka, G.D. Stucky, *J. Am. Chem. Soc.* 120, 6024-6036 (1998)
- [3] S. Jun, S.H. Joo, R. Ryoo, M. Kruk, M. Jaroniec, Z. Liu, T. Ohsuna, O. Terasaki, *J. Am. Chem. Soc.* 122, 10712-10713 (2000)
- [4] S.H. Joo, S.J. Choi, I. Oh, J. Kwak, Z. Liu, O. Terasaki, R. Ryoo, *Nature* 412, 169-172 (2001)
- [5] S. Che, K. Lund, T. Tatsumi, S. Iijima, S.H. Joo, R. Ryoo, O. Terasaki, *Angew. Chem. Int. Ed.* 42, 2182-2185 (2003)
- [6] W. Schmidt, *Microp. Mesop. Mater.* 117, 372-379 (2009)

STUDY OF POLYMER ELECTROLYTE FOR Zn RECHARGEABLE NANOSTRUCTURED GALVANIC CELLS VIA COMBINED IN SITU SAXS/DSC/WAXD MEASUREMENTS

A. Turković¹, K. Juraić¹, P. Dubček¹ and S. Bernstorff²

1.) R. Bošković Institute, Bijenička 54, Zagreb, Croatia

2.) Sincrotrone Trieste, SS 14, km 163.5, Basovizza (TS), Italy

We have performed SAXS/DSC/WAXD measurements on the superionic phase transition of Zn ions conducting polymer electrolyte, nanocomposite in the temperature range from 20 to 100 °C, this time with a scanning rate of 1/2 °C/min. With this slower rate we have obtained more accurate phase transition temperatures from all three methods and better insight in the crystal morphology in the superionic phase.

Figure 1 shows the results from the SAXS/DSC/WAXD measurements in the temperature range from 20°C to 100°C at the rate of 1/2 C°/min on polymer electrolyte PEO)₈ZnCl₂ irradiated with 309 KGy nanocomposite with TiO₂ nanograins. Previous measurements were done with faster rates of 1 C°/min, 3 C°/min and 5 C°/min [1]. Hysteresis is present in the heating-cooling cycle. SAXS measurements show the change of grain sizes in the range from 4.4 to 2.7 nm. In a lamellar picture of PEO these sizes of grains would correspond to the lamellae LP2 with no integrally folded (NIF) chains [2] combined with salt and TiO₂.

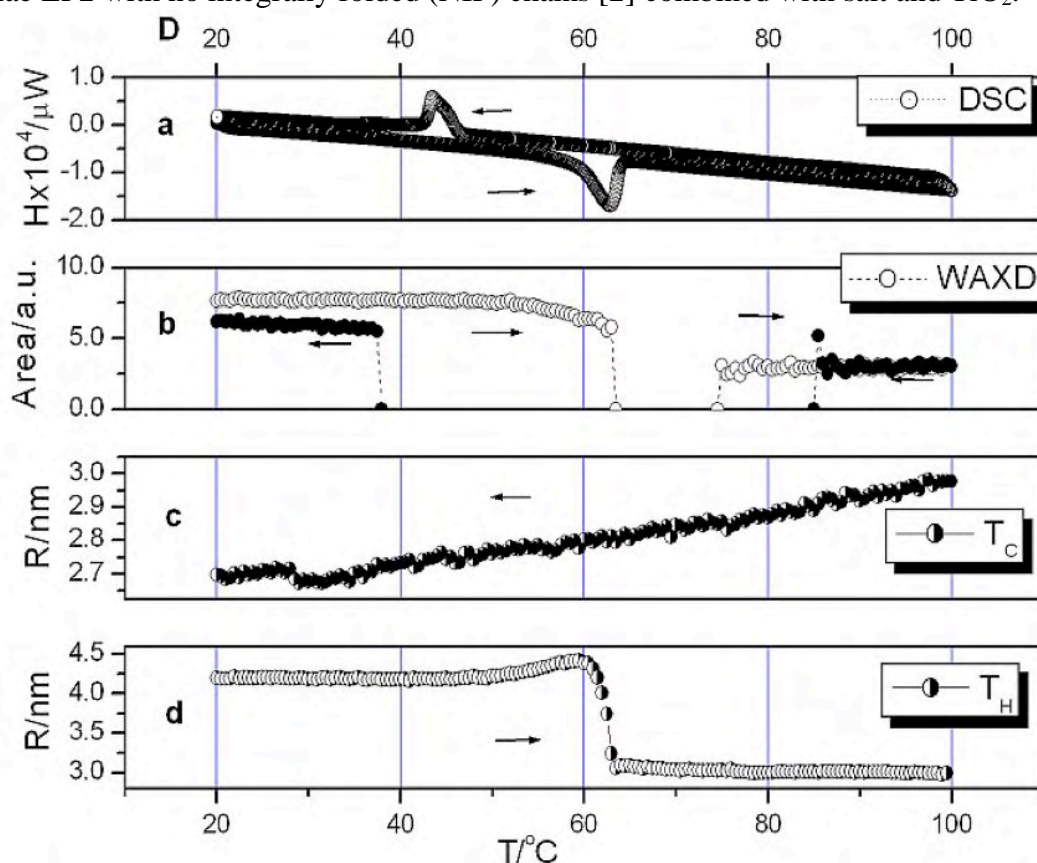


Figure 1. SAXS, WAXD and DSC of PEO)₈ZnCl₂/TiO₂ irradiated with 309 KGy

References:

[1] A. Turković, M. Rakić, P. Dubček, M. Lučić-Lavčević and S. Bernstorff, Vacuum 84/1 68 (2009)

[2] J. Baldrian, M. Horky, A. Sikora, M. Steinhart, P. Vleek, H. Amenitsch and S. Bernstorff, Polymer 40 439 (1999)

STRUCTURAL CHARACTERIZATION OF Si_{1-x}Ge_x NANOCRYSTALS EMBEDDED IN Al₂O₃ MATRIX

E. M. F. Vieira¹, S. Levichev¹, S. R. C. Pinto¹, A. G. Rolo¹, M. Buljan², A. Chahboun^{1, 3}, O. Conde⁴, S. Bernstorff⁵, M.J.M. Gomes¹

- 1.) Centro de Física, Universidade do Minho, 4710-057 Braga, Portugal
- 2.) Rudjer Boskovic Institute, Bijenicka cesta 54, 10000 Zagreb, Croatia
- 3.) LPS, Physics Department, Faculty of Sciences, BP 1796, Fès, Morocco
- 4.) Physics Department, University of Lisbon and ICEMS, 1749-016 Lisboa, Portugal
- 5.) Sincrotrone Trieste, SS 14, km 163.5, Basovizza (TS), Italy

Recently, Si, Ge and SiGe nanocrystals (NCs) embedded in dielectric matrices have been widely investigated due to their potential application in non-volatile memories and optoelectronics [1-4]. Flash memory devices employing NCs have been shown to improve the state of the art of memory devices [1]. For this application, the morphology of NCs layer, namely NCs diameter, uniformity, spatial distribution and density play an important role due to its strong influence on the electrical properties of the devices.

SiO₂ matrix is one of the materials most used and studied as a gate dielectric in flash memory devices. However, the constant shrinking of the thickness of gate dielectrics to below 2-3 nm has started a search for others high dielectric constant (high-*k*) materials. Various high-*k* materials have been suggested to replace silica for future complementary metal-oxide-semiconductor (CMOS) devices. Among other dielectrics, Al₂O₃ has emerged as one potential candidate, since it combines a relatively high dielectric constant (~10), a wide band gap (6.2 eV), as well as a high band offset value of the Al₂O₃/Si barrier height (~2 eV) [2]. SiGe heterostructures are receiving a lot of interests due to their unique properties where the strain modifies the band structures. To the best of our knowledge there are only a few studies reported about SiGe NCs embedded in alumina matrix. In most cases SiGe NCs have been produced in SiO₂ matrix and post annealed at high temperatures (>1000 °C) [3,4].

Si_xGe_{1-x} (x=0 to 1) NCs embedded in Al₂O₃ matrix were grown by RF-magnetron co-sputtering. Different growth and annealing conditions were applied in order to achieve the formation of SiGe NCs embedded in a thin layer of Al₂O₃. XRD and Raman techniques demonstrate the presence of SiGe NCs, as it is illustrated by Figs. 1 and 2.

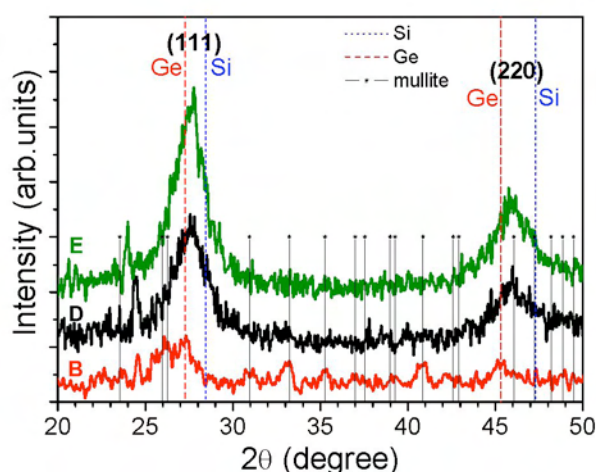


Figure 1. GIXRD patterns of the annealed samples. The position of Si, Ge and mullite diffraction peaks are shown as vertical lines [5]

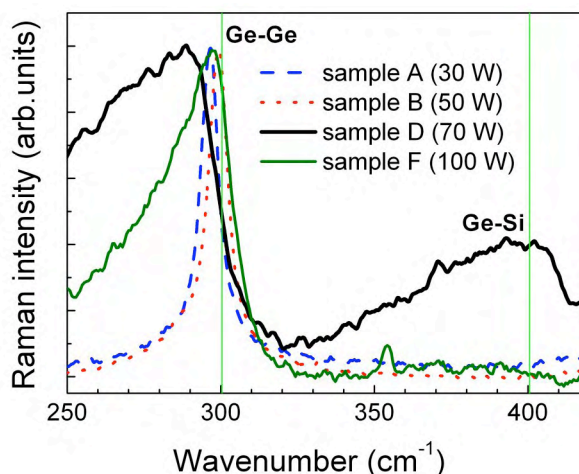


Figure 2. Raman spectra of the studied samples. The positions of Ge-Ge and Ge-Si optical vibration modes are shown as vertical lines [5]

Typical GISAXS maps of the investigated samples are shown in Fig. 3. The intensity distribution in panel (b) shows a ring-like shape which means that NCs are uniformly distributed in the matrix, and can be described well by a gas model [6]. The ring-like distribution of the GISAXS intensity is not so clearly visible in the map shown in panel (a) what is found correlated to the very broad distribution of NC sizes in that film. Two-dimensional maps were fitted using the model described in [6]. The NC sizes obtained by fitting are in good agreement with the ones deduced from XRD and Raman. The simulated intensity distributions are shown in the insets of Fig. 3.

In summary, $\text{Si}_{1-x}\text{Ge}_x$ ($0.8 < x < 1$) NCs in Al_2O_3 matrix were successfully produced by RF magnetron sputtering. Using the combination of GIXRD, GISAXS and Raman techniques the optimum condition to produce $\text{Si}_{1-x}\text{Ge}_x$ NCs were found. All results were consistent, and the obtained NC sizes were in good agreement.

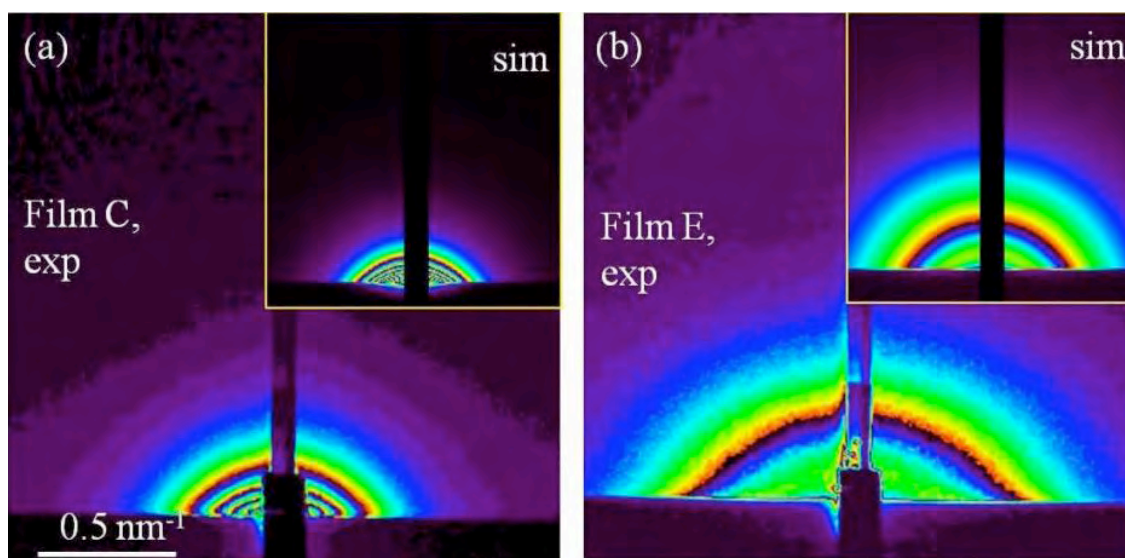


Figure 3. 2D GISAXS maps of sample C shown in (a), and sample E shown in (b) panel. The insets show the corresponding simulated GISAXS maps [5].

References:

- [1] F. Zheng, H. G. Chew, W.K.Choi, J. X. Zhang, and H. L. Seng, *J. Apply. Phys.*101 (2007) 114310
- [2] Yu.N. Novikov, A. V. Vishnyakov, V. A. Gritsenko, K. A. Nasyrov and H. Wong, *Microelectronics Reliability*.50 (2010) 207 - 210
- [3] N. A. P. Mogaddam, A.S. Alagoz, S. Yerci, R. Turan, S. Foss and T. G. Finstad, *J.Appl.Phys.*104 (2008) 124309
- [4] S. Takeoka, K. Toshiakiyo, M. Fujii, S. Hayashi and K.Yamamoto, *Physical Review B*, 61 (2000) 23
- [5] E. M. F. Vieira, S.R.C. Pinto, S. Levichev, A.G. Rolo, A. Chahboun, M. Buljan, S.Bernstorff, O. Conde and M. J. M. Gomes, Submitted to *Microelectronic Engineering*
- [6] M. Buljan, S.R.C Pinto, J. R. Kasthiban, A. G. Rolo, A. Chahboun, U. Bangert, S. Levichev, V. Holy, M. J.M. Gomes; *J. Appl. Phys.* 106 (2009) 084319

Life Sciences

SAXS STUDY OF SYRIAN HAMSTER PRION FIBRILS AND RECOMBINANT TRUNCATED PRION PROTEIN IN THE PRESENCE OF TRANSITION METALS

F. Benetti¹, H. Amenitsch², G. Legname^{1,3,4}

- 1.) Laboratory of Prion Biology; Neurobiology Sector; Scuola Internazionale Superiore di Studi Avanzat—International School of Advanced Studies (SISSA-ISAS); Basovizza (TS), Italy
- 2.) Institute of Biophysics and Nanosystems Research, Austrian Academy of Sciences, Schmiedlstr. 6, Graz, Austria
- 3.) Italian Institute of Technology; S.I.S.S.A.-I.S.A.S. Unit; Trieste, Italy
- 4.) Sincrotrone Trieste S.C.p.A.; Trieste, Italy

Prion diseases or Transmissible Spongiform Encephalopathies (TSEs) are neurological disorders found in humans and animals, which are due to the conversion of the native cellular prion protein (PrP^C) into a pathological PrP^{Sc} conformation. These pathologies are characterized by protein misfolding, neuronal cell loss, and deposition of amyloid fibrils in the brain. While PrP^C is mainly an α -helical protein sensible to protease digestion, PrP^{Sc} displays a high β -sheet content and resistance to protease. TSEs are unique because they can be sporadic, inherited or iatrogenic [1]. Despite numerous efforts, the pathogenesis and molecular bases of neuronal cell death in prion diseases remain still enigmatic [2]. Therefore, the pathological conversion, the early events of aggregation and the mechanisms of fibrillogenesis represent the *hot* topics in the prion field. In order to unravel these questions, we performed two different set of experiments.

In order to describe the quaternary structure of prions, we applied SAXS technique on fibrils extracted from sick Syrian hamster brains. SAXS data (Fig. 1A) were compared with those obtained using cryo-electron and transmission electron microscopies (Fig. 1B-C).

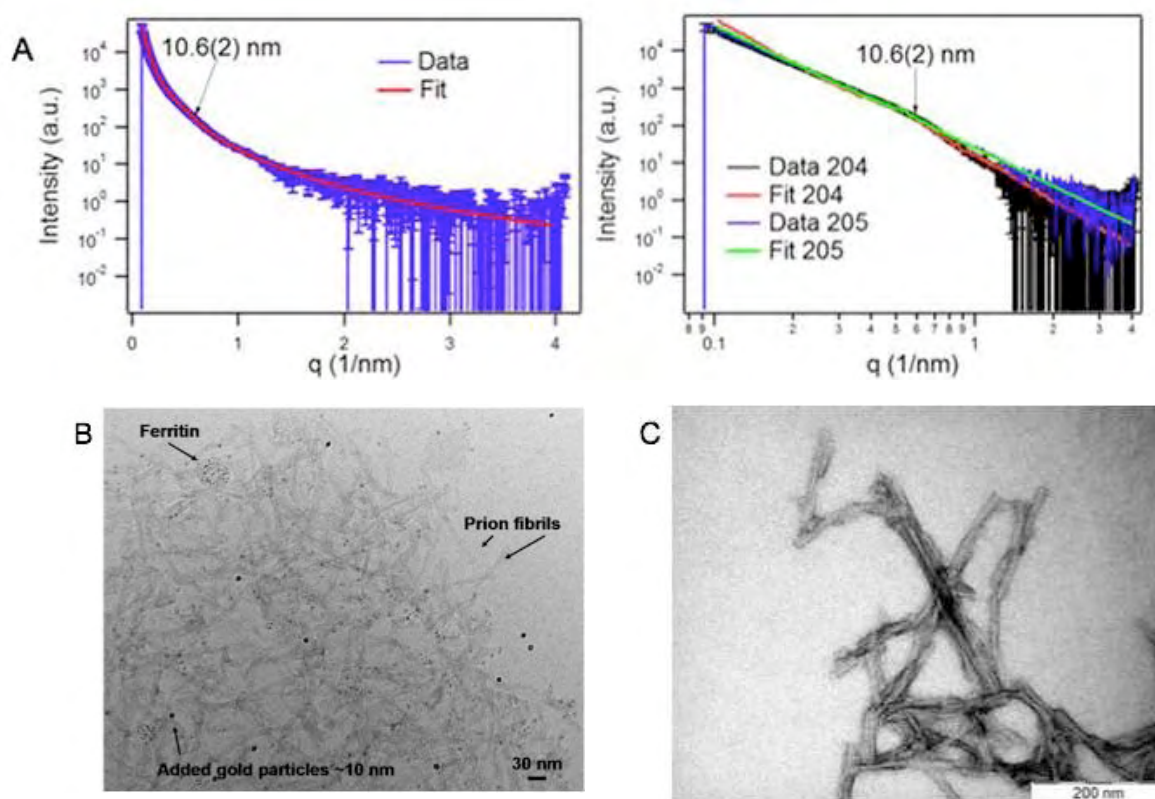


Figure 1. Experimental data (blue) and fit (red) of SAXS data obtained on Syrian hamster fibrils. Data were fitted considering interacting cylinders with interference function (A). Native Syrian hamster fibrils obtained using Cryo-EM (B). Negative stain of Syrian hamster fibrils (C).

Taken together, these results revealed that Syrian hamster fibrils are composed from two intertwined 5 nm wide protofibrils with no regular cross-over distance (Fig. 2).

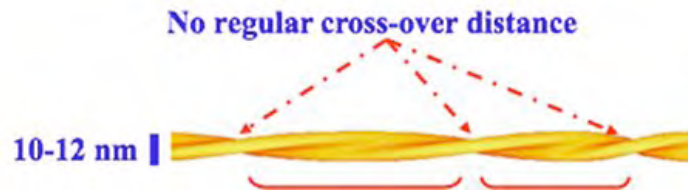


Figure 2. Model of Syrian hamster fibril. It is form from two intertwined proto-filament with a cross-section of 10-12 nm. No regular cross-over-distance seem to be presence along fibril-axis.

PrP^C is composed from an N-terminal unfolding domain and a globular C-terminal domain. Since the C-terminal domain reveals altered physico-chemical properties in the pathological isoform, such as resistance to proteolysis, we focused our attention on this region. Moreover, it has been demonstrated that, under denaturing conditions, recombinant C-terminal domain is able to form synthetic prions [3]. The C-terminal domain contains high affinity metal-binding sites [4, 5]. In the literature, it has been reported that dys-regulation of these metals may favor the conformational conversion. We investigated the effect of different metals - copper and zinc - on the C-terminal domain of murine recombinant prion protein, MoPrP(89-231). Scattering curves of MoPrP(89-231) in the presence of copper showed an higher $I(0)$ than those in the presence of zinc (Fig. 3A). Kratky plot revealed a compact structure for MoPrP(89-231) without metals or in the presence of zinc (Fig. 3B). In the presence of copper, MoPrP(89-231) adopts a fiber-like structure (Fig. 3B). The cross-section of MoPrP(89-231) in the presence of copper and zinc are the same. These preliminary data highlight a different structural rearrangement of MoPrP(89-231) in the presence of various metals. To better define the structures of these states and the effect of metals on MoPrP, further investigations will be necessary.

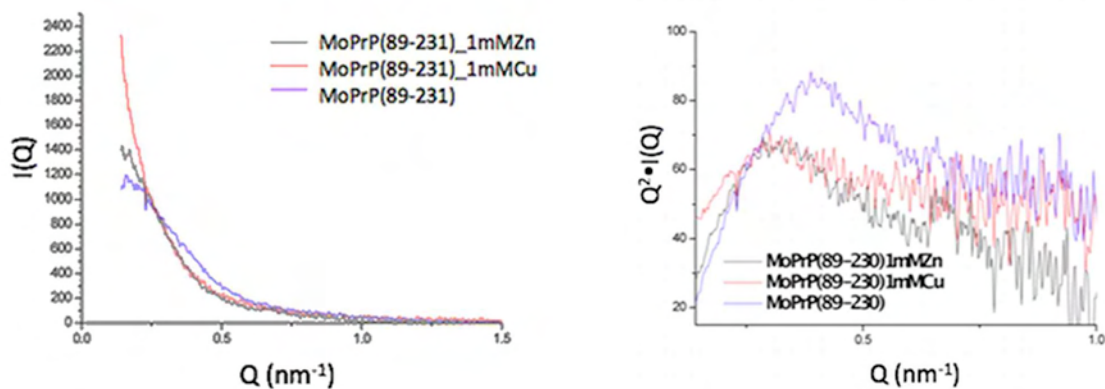


Figure 3. Scattering curves of MoPrP(89-231) either in the absence or in the presence of transition metals (A). Kratky plot of the SAXS experimental curves (B).

References:

- [1] S. B. Prusiner, Prions, *Proc. Natl. Acad. Sci. U.S.A.* 95: 13363-13383 (1998)
- [2] A. Aguzzi, F. Baumann, and J. Bremer, The Prion's Elusive Reason for Being. *Annu. Rev. Neurosci.* 31:439-477 (2008)
- [3] G. Legname, I.V. Baskakov, H.O. Nguyen, D. Riesner, F.E. Cohen, et al., Synthetic mammalian prions. *Science* 305: 673-76 (2004)
- [4] D.R. Brown, et al., The cellular prion protein binds copper in vivo. *Nature*, 390: 684-687 (1997)
- [5] M.W. Brazier, et al., Manganese Binding to the prion protein 9;283(19):12831-9 (2008)

IMPLICATION OF SPHINGOMYELIN/CERAMIDE MOLAR RATIO ON THE BIOLOGICAL ACTIVITY OF SPHINGOMYELINASE

Beate Boulgaropoulos, Heinz Amenitsch, Peter Laggner and Georg Pabst

Institute of Biophysics and Nanosystems Research, Austrian Academy of Sciences, Schmiedlstr. 6, A-8042 Graz, Austria

Sphingolipids are ubiquitously present in all mammalian cells and play an important role in the regulation of diverse cellular functions (1,2). Of particular interest is the enzymatic degradation of sphingomyelin (SM) by sphingomyelinase (SMase) to ceramide (Cer) and phosphocholine and its consequences to the lateral heterogeneity of membranes. Various cellular processes have been related to SMase activity, e.g. apoptosis (programmed cell death) (1-3). Most recently we were able to show that Cer generation might also indirectly affect the activity of non raft proteins (4).

In order to address the membrane dynamical structural changes during the enzyme reaction and their feedback to enzyme activity, we have studied the effect of enzymatically generated Cer in situ on the properties of a well-defined lipid model system, composed of an equimolar mixture of palmitoyl oleoyl phosphatidylcholine (POPC) and SM.

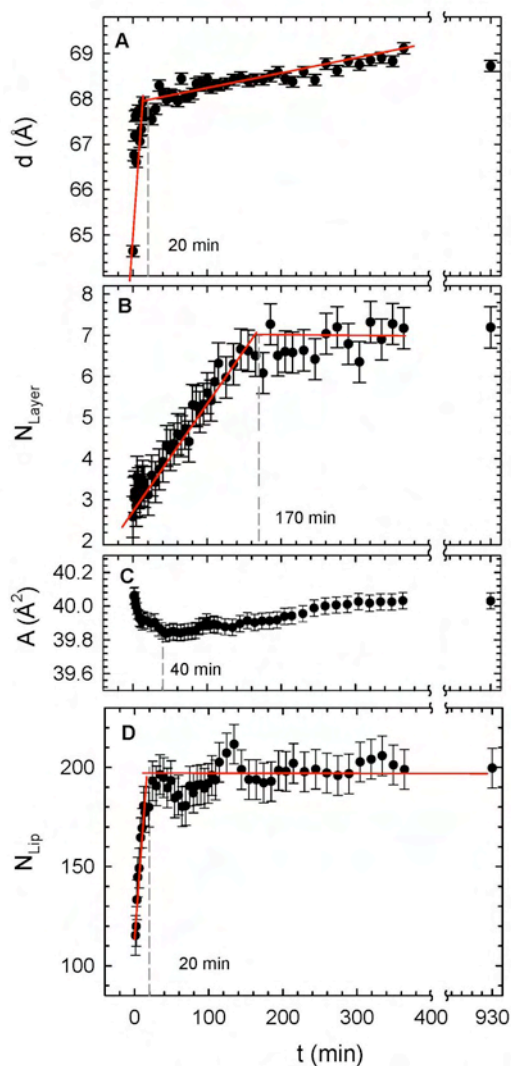


Figure 1. Evolution of lamellar repeat distance (A), average number of positional correlated layers (B), lateral area per lipid in the gel phase (C) and average number of lipids per gel phase domain (D) during the enzyme reaction. Panel A and B show parameters derived from small angle X-ray scattering data and panel C and D those coming from wide angle X-ray scattering data.

We observed that gel phase formation proceeds faster than enzymatic Cer generation as long as each Cer molecule has at least one SM partner. Gel phase domains lead to membrane aggregation because of increased adhesive forces. If Cer levels exceed those of SM, POPC is increasingly incorporated into the gel phase until the reaction stops just below the solubility limit of Cer in membranes (Fig.1). Similar kinetics and SM-saturation levels in cell biology studies suggest that the evolution of apoptosis is influenced to large extent by membrane lipids and their mechanical coupling to SMase activity.

In summary, we found that the SM/Cer molar ratio strongly affects the membrane structural rearrangements through formation of gel phase domains during the action of SMase (Fig. 2).

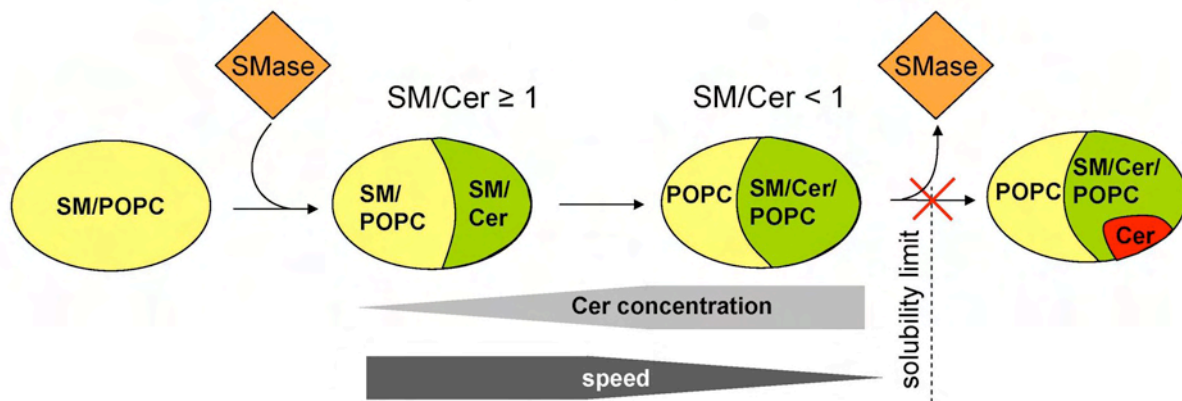


Figure 2. Schematic of SMase activity as a function of the SM/Cer molar ratio. Addition of SMase to SM/POPC vesicles induces a macroscopic phase separation into SM/Cer-rich gel and SM/POPC-rich fluid domains. As long as $SM/Cer \geq 1$, each Cer can pair with at least one SM and progress of gel phase formation is faster than Cer generation. For $SM/Cer < 1$, kinetics slow down, because POPC, which has a lower affinity to Cer, needs to be incorporated into the growing gel domains in order to avoid precipitation of Cer crystallites. The reaction stops just at the solubility limit of Cer within the membrane.

References

- [1] Kolesnick, R N, Goni, F M, Alonso, A (2000) Compartmentalization of ceramide signaling: Physical foundations and biological effects. *J. Cell. Phys.* 184: 285-300
- [2] van Blitterswijk, W J, van der Luit, A H, Veldman, R J, Verheij, M, Borst, J (2003) Ceramide: second messenger or modulator of membrane structure and dynamics? *Biochem. J.* 369: 199-211
- [3] Hannun, Y A, Obeid, L M (2008) Principles of bioactive lipid signalling: lessons from sphingolipids. *Nature Rev.* 9: 139-150
- [4] Pabst, G, Boulgaropoulos, B, Gander, E, Sarangi, B R, Amenitsch, H, Raghunathan, V A, Laggner, P (2009) Effect of ceramide on nonraft proteins. *J Membr. Biol* 231: 125-132

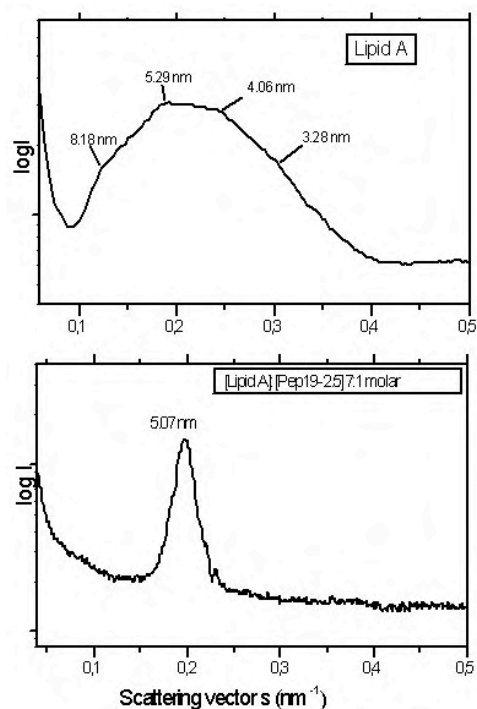
SAXS OF BACTERIAL VIRULENCE FACTORS AND THEIR NEUTRALIZATION

K. Brandenburg¹, J. Howe¹, Y. Kaconis¹, T. Gutschmann¹ and M. Rappolt³

1.) Forschungszentrum Borstel, Parkallee 10, D-23845 Borstel, Germany

2.) Institute of Biophysics and Nanosystems Research, Austrian Academy of Sciences, Graz, Austria

Many bacterial virulence factors are located within bacterial membranes such as lipopolysaccharide (LPS) from Gram-negative bacteria, which is an amphiphilic macromolecule. LPS, which is released by the attack of the immune cells or simply by dividing cells, is able to induce a variety of biological effects such as the secretion of mediators (TNF, interleukins). At low concentrations these mediators are beneficial for the proper functioning of the immune system and its fight against invading microorganisms, at high concentrations, however, these mediators cause toxic effects such irreversible shock, a syndrome from with a very high death-rate (in Germany, each year 60000 cases). We have elucidated in the past for lipid A, the 'endotoxic principle' of LPS, the aggregate structures and molecular conformations and have thus defined an 'endotoxic conformation'¹. For a fight against infection and in particular against Gram-negative sepsis, a new strategy is the development of suitable peptides based on the binding domains of human proteins such as lactoferrin. We have found that general properties of the aggregate structures of these molecules govern their biological effectiveness, and that these characteristics are changed due to binding of antimicrobial agents. In the frame of these investigations, we have stated that a



necessary but not sufficient prerequisite for the inactivation of a given LPS/lipid A due to peptide/protein binding is the conversion of the LPS aggregates into multilamellar structures. A detailed analysis of the kind of multilamellar structure is therefore of high importance. This comprises the number of lamellae, the aggregate (vesicle) size, and the bilayer thicknesses. We have made these experiments with synchrotron SAXS, analysing various LPS chemotypes differing in the length of the sugar chains and their interactions with some model peptides.

Figure 1. X-ray scattering pattern of lipid A in the absence (top) and presence (bottom) an antimicrobial peptide

The experimental results are then compared with theoretical calculations, which should allow to get an estimate of the aggregate fine structures. Furthermore, from these data we will deduce electron density maps of the LPS:peptide multilamellae, which should allow to elucidate the interaction sites of the peptides within the LPS molecules.

References:

- [1] T. Gutschmann, I. Razquin-Olazarán, I. Kowalski, Y. Kaconis, J. Howe, R. Bartels, M. Hornef; T. Schürholz, M. Rössle, S. Sanchez-Gómez, I. Moriyon, G. Martinez de Tejada, K. Brandenburg; New antiseptic peptides to protect from endotoxin-mediated shock, *Antimicrobial Agents Chemother.* 2010 (in press)

THE EFFECT OF HYDRATION ON SPIDER SILK STRUCTURE AND MECHANICS

C.P. Brown^{1,2}, H. Amenitsch³, F. Cacho³, J. MacLeod¹, A. Vittorini Orgeas², E. Traversa², S. Liccocia² and F. Rosei¹

1.) INRS, Université du Québec, 1650 boulevard Lionel-Boulet, Varennes, Québec, Canada

2.) Facoltà di Scienze, Università di Roma II, Via Della Ricerca Scientifica, Roma, Italy

3.) Institute of Biophysics and Nanosystems Research, Austrian Academy of Sciences, Graz, Austria

Spider silk is a remarkable material, with significant potential for use in medicine, military and industry [1, 2]. In addition to biocompatibility and biodegradability, the mechanical properties, which match man-made fibres in terms of strength and outperform them in energy processing capacity, make this material an interesting subject for investigation and an attractive target for application. A number of modellers have attempted to describe the structural origins of these remarkable mechanical properties [eg. 3, 4] but the structure-function relationships, particularly the role of secondary and tertiary structure, remain elusive.

The infiltration of water is generally thought to force some degree of recoverable disorder in spider silk, taking up hydrogen bonds between the molecular chains in the fibre's oriented amorphous domains [5], which are easier to penetrate than the crystalline domains such as β -sheets [6]. This raises some interesting questions; particularly whether the role of water in the disordered domains plays an equal part to that of the proline [7], contributing to the remarkable toughness of spider silk fibres.

A substantial amount of water, which acts as the solvent in the liquid crystalline dope, remains in the fibres after spinning [8]. The higher shear stresses in the outer fibre during extrusion will arguably lead to the formation of more-ordered domains compared to that of the inner regions, similar to the increased order and orientation resulting from the higher stresses during fast extrusion [9]. Concurrently, water would be forced out of the structure in these high-stress regions, and less so from the inner regions.

In a series of AFM indentation studies, we have found that under ambient conditions, the higher amounts of bound water in the inner core will be pushed out under an applied load, allowing this reconfiguration in what is essentially a plastic deformation. Once the load is withdrawn, the now unbound water can retake the hydrogen bonds, allowing recovery. In order to test this theory, a combination of WAXS and SAXS data were captured at different levels of hydration.

Although data analysis is still under way, a number of peaks have been resolved that can provide insight into the structure-function relationships in the material, and the origins of its remarkable mechanical properties. Using the WAXS data, the crystallite orientation in different states was determined from the angular width of the 120 peak, d -spacing $\sim 4.41\text{\AA}$, in arc slices, with the crystallite size measured from equatorial slices (120 peak) [10]. The change in orientation of the β -sheets gives an indication of the tension the disordered domains under different levels of hydration. A change in order may also occur as some of the disordered domains are pulled into an ordered configuration in the dry state. This may be coupled with a decrease in size of the β -sheets. Using the SAXS data, the long spacing (~ 8.3 nm in normal state [11]) and the ratio between 1st and 2nd order lamellar reflections, were measured. The change in long spacing will indicate how much local strain is being taken up by the amorphous domains compared to the bulk strain.

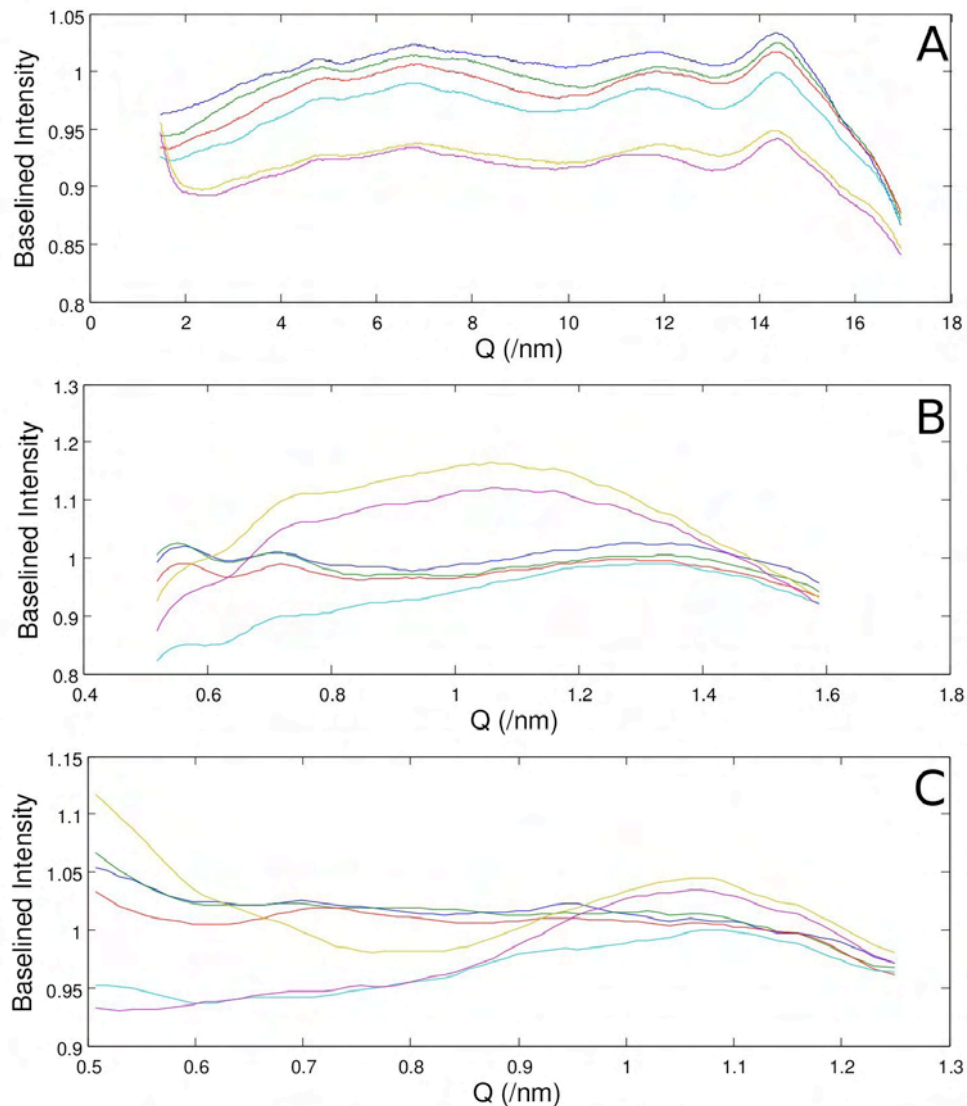


Figure 1: Typical SAXS and WAXS signals from spider silk at different levels of hydration. (A) and (B) show WAXS and SAXS signals respectively across the fibre, with (C) showing SAXS signals along the fibre axis. Blue curves are measured at <1% relative humidity (RH); green at 20%; red at 40%; cyan at 60%; purple at 80% and olive at >99%.

References:

- [1] Altman, D.G. et al., Silk-based biomaterials. *Biomaterials* 24, 401-416 (2003)
- [2] Ball, P., Life's lessons in design. *Nature* 409, 413-416 (2001)
- [3] Porter, D., Vollrath, F., & Shao, Z., Predicting the mechanical properties of spider silk as a model nanostructured polymer. *The European Physical Journal E* 16, 199-206 (2005)
- [4] Termonia, Y., Molecular modelling of spider silk elasticity. *Macromolecules* 27, 7378-7381 (1994)
- [5] Liu, Y., Shao, Z., & Vollrath, F., Relationships between supercontraction and mechanical properties of spider silk. *Nature Materials* 4, 901-905 (2005)
- [6] Simmons, A.H., Michal, C.A., & Jelinski, L.W., Molecular orientation and two-component nature of the crystalline fraction of spider dragline silk. *Science* 271, 84-87 (1996)
- [7] Savage, K.N. & Gosline, J.M., The role of proline in the elastic mechanism of hydrated spider silks. *Journal of Experimental Biology* 211, 1948-1957 (2008)
- [8] Vollrath, F. & Knight, D.P., Liquid crystalline spinning of spider silk. *Nature* 410, 541-548 (2001)
- [9] Du, N. et al., Design of Superior Spider Silk: from Nanostructure to Mechanical Properties. *Biophys. J.* 91, 4528-4535 (2006)
- [10] Gliovi, A., Vehoff, T., Davies, R.J., & Salditt, T., Strain Dependent Structural Changes of Spider Dragline Silk. *Macromolecules* 41, 390-398 (2008)
- [11] Yang, Z., Grubb, D.T., & Jelinski, L.W., Small-Angle X-ray Scattering of Spider Dragline Silk. *Macromolecules* 30, 8254-8261 (1997)

UNIVERSALITY OF DNA ADSORPTION BEHAVIOR ON THE CATIONIC MEMBRANES OF NANOLIPOPLEXES

G. Caracciolo¹, D. Pozzi¹, and H. Amenitsch²

1.) Department of Chemistry, 'Sapienza' University of Rome, P.le Aldo Moro 5, 00185, Rome, Italy

2.) Institute of Biophysics and Nanosystems Research, Austrian Academy of Sciences, Schmiedelstrasse 6, A-8042 Graz, Austria

Cationic liposomes (CLs), when mixed with DNA, spontaneously form stable complexes (lipoplexes) that can deliver DNA into cells by binding electrostatically to their anionic membranes [1,2]. To date, a rational approach for the design of optimal lipoplex formulations has been severely limited by a poor understanding of the physical attributes of cationic membranes regulating the equilibrium structure of lipoplexes. Such an urgent requirement motivated us to investigate the condensation behavior of DNA on cationic membranes.

In this study, we first examined the role of membrane charge density of cationic membranes on the DNA-binding ability of CLs. CLs made of the cationic lipid 1,2-dioleoyl-3-trimethylammonium-propane (DOTAP) and zwitterionic lipid dioleoylphosphocholine (DOPC) were used. CLs with different membrane charge density were prepared by changing the molar fraction of neutral lipid in the bilayer, $\Phi = L_0 / (L_C + L_0)$ (L_0 and L_C indicate the moles of neutral and cationic lipid, respectively). First, we used electrophoresis on agarose gels to determine the DNA-binding ability of CLs. In Figure 1 (panel A), we report the molar fraction of plasmid DNA protected by lipids, X_{DNA} , as a function of the cationic lipid/DNA charge ratio, ρ , for three formulations with different membrane charge densities ($\Phi = 0.3, 0.5, 0.7$). The transfection relevant excess cationic charge regime ($\rho > 1$) was chosen because lipoplexes must be positive to bind electrostatically to mammalian cells. At the isoelectric point ($\rho = 1$), X_{DNA} was found to be lower than 1 for all lipoplex formulations. A first step toward taking into account variations in DNA binding ability between different liposome formulations is to recognize that at fixed ρ complexes with higher Φ have larger lipid surface area. It is natural then to try to factor out the bias induced by the difference in Φ by considering a relative indicator, that is, a dimensionless quantity expressing the ratio between the area of cationic membranes, A_L , and that occupied by DNA molecules, A_D ,

$$\gamma = \frac{A_L}{A_D} = \rho \frac{\left(a_C + a_0 \frac{\Phi}{1 - \Phi} \right)}{2R_D l_D} \quad (1)$$

where $a_C = 62 \text{ \AA}^2$ and $a_0 = 72 \text{ \AA}^2$ denote the cross-sectional area per cationic DOTAP and neutral DOPC (the removal of DOPC phosphate resulting in DOTAP justifies the lower value of a_C with respect to a_0); R_D is the radius of DNA molecules plus a hydration shell; and l_D is the mean distance between two adjacent negative charges projected on the DNA axis, $l_D = 1.7 \text{ \AA}$. This is a very natural choice since, upon formation of lipoplexes, cationic lipid surface becomes the site of a two dimensional (2D) adsorption of DNA chains. Figure 1 (panel B) shows that plotting X_{DNA} versus γ leads to a very good collapse of all curves for different values of Φ onto a single shape demonstrating that γ is a key parameter for 2D DNA condensation on cationic lipid membranes. The distribution then seems to be universal for all formulations considered. Interestingly, the universal curve is fitted by a linear behavior $X_{DNA} = \alpha\gamma$ (with $\alpha = 0.092$) and saturates for $\gamma > \gamma^* \sim 11$ (Figure 1, panel B, dashed line).

The value of correlation coefficient ($R = 0.975$) indicates that a linear fit to the data is good.

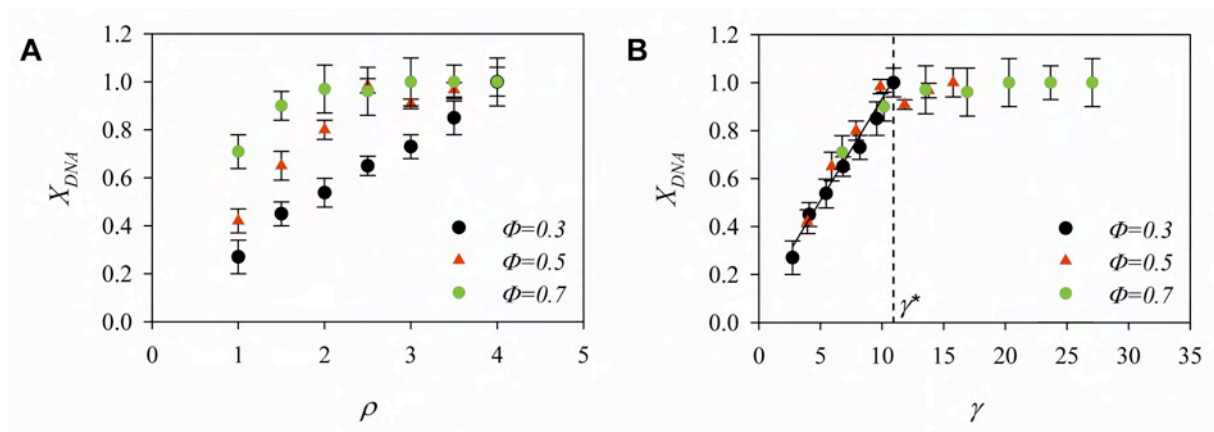


Figure 1. Panel A: molar fraction of plasmid DNA protected by cationic liposomes, X_{DNA} , as a function of the cationic lipid/DNA charge ratio, ρ . Panel B: molar fraction of plasmid DNA protected by CLs, X_{DNA} , as a function of γ . Solid line is the best linear fit to the data. Dashed line indicates the γ value (γ^*) for which complete DNA protection occurs.

The physical meaning of Figure 1 (panel B) seems to be that the DNA-binding ability of cationic liposomes is a linear function of interfacial area of lipid membranes.

Above the transition point ($\gamma > \gamma^*$), we observe that plasmid DNA is completely protected by cationic lipids independently from the cationic to anionic charge ratio, ρ , and the molar fraction of neutral lipid in the bilayer, Φ . As a consequence, complexes with very different membrane charge density (Φ) and charge ratio (ρ) but with similar lipid surface area are expected to exhibit the very same DNA binding capacity. We emphasize that the primary outcome of such a novel data interpretation is that the spatial dimension available plays a key role in the DNA binding ability of lipoplexes. Over the past decade, synchrotron SAXS has been used to elucidate the structure of lipoplexes at the angstrom scale. The DNA intercalated between cationic membranes forms a one-dimensional array of chains which uniformly cover the available lipid area. We therefore collected synchrotron SAXS patterns of a series of DOTAP-DOPC/DNA complexes as a function of ρ and Φ . We observe that, at fixed ρ , an increase in Φ produces the monotonous dilution of the DNA lattice, i.e., the enlargement in the DNA interdistances. We show in Figure 2 (panel A) a set of d_{DNA} curves for DOTAP-DOPC/DNA lipoplexes with different Φ as a function of ρ . All the profiles exhibit a common behavior: the interhelical spacing, d_{DNA} , increases linearly with ρ and saturates for $\rho = \rho^*$. On the other side, we observe that increasing membrane charge density (i.e., decreasing Φ) results in: (i) a marked decrease of the linear slope and (ii) a significant increase in the saturation point values (Figure 2, panel A, dashed line). Figure 2 (panel B) shows that the large variability of DNA packing density, as observed in Figure 2 (panel A), is rescaled away if d_{DNA} is plotted versus γ/X_{DNA} . Remarkably, in rescaling the 1D DNA packing density by γ/X_{DNA} , a universal linear increase of d_{DNA} is found, independent of Φ and ρ .

This finding is most likely to mean that the interhelical DNA-DNA distance is mainly regulated by the interfacial area of lipid membranes that is available to 2D DNA condensation.

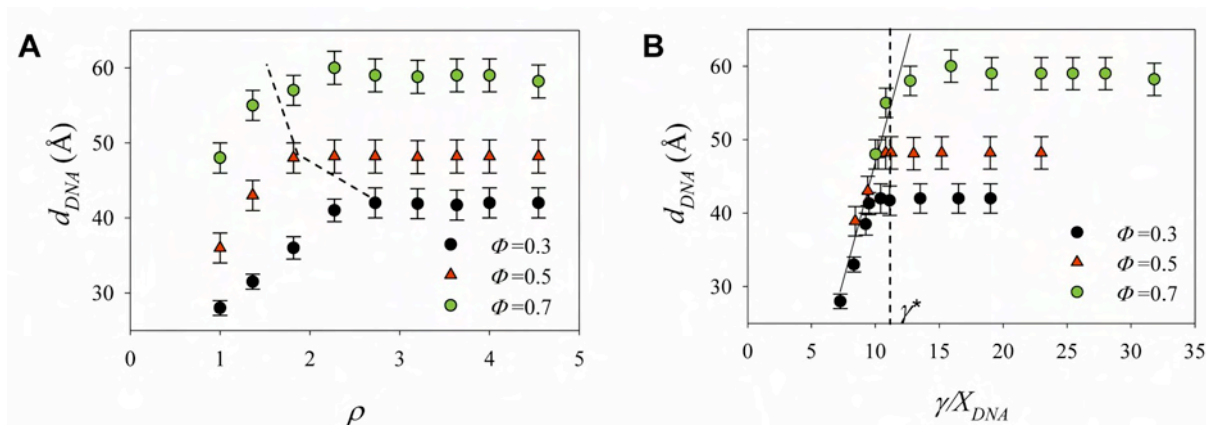


Figure 2. Panel A: $d_{DNA}(\rho)$ curves for DOTAP-DOPC/DNA lipoplexes with different Φ . Panel B: when plotting d_{DNA} against γX_{DNA} , all the data points coalesce onto a single curve. Dashed line is the lowest γ value (γ^*) for which d_{DNA} plateaus.

Remarkably, after rescaling, we observe that adsorption of excess lipid is inversely proportional to Φ with saturation values now appearing to be in reverse order (Figure 2, panel B, dashed line) with respect to when d_{DNA} is plotted against the cationic lipid/DNA charge ratio, ρ (Figure 2, panel A, dashed line). Finally, this result is consistent with the physical expectation that complex affinity for excess cationic lipid is inversely proportional to membrane charge density of lipid membranes. On the whole, the 2D condensation behavior can be regarded as a two-step process. In the first step ($\gamma < \gamma^*$), DNA is not completely protected by lipids, and the spacing between DNA chains is set by the geometrical constraint of the interfacial area of lipid membranes available to DNA condensation and not as a result of a balance of attractive and repulsive forces. For $\gamma > \gamma^*$, the repulsive interaction dependent on the membrane charge density of lipid membranes is the constraint that sets the DNA packing density. It is noteworthy that our analysis identified the interfacial area of lipid membranes as a universal parameter regulating DNA condensation behavior in lamellar cationic liposome/DNA complexes [3].

References:

- [1] P.L. Felgner and G.M. Ringold; Cationic liposome mediated transfection; Nature 331, 461-462 (1989)
- [2] D. Harries, S. May, W.M. Gelbart and A. Ben-Shaul; Structure, Stability and Thermodynamics of Lamellar DNA-Lipid Complexes; Biophys. J. 75, 159-173 (1998)
- [3] G. Caracciolo, D. Pozzi, A. Amici and H. Amenitsch; Universality of DNA Adsorption Behavior on the Cationic Membranes of Nanolipoplexes; J. Phys. Chem. B 114, 2028-2032 (2010)

PHASE DIAGRAM DC-Chol–DOPE/DNA COMPLEXES SUGGESTS STRATEGIES FOR EFFICIENT LIPOPLEX TRANSFECTION

G. Caracciolo¹, D. Pozzi¹, and H. Amenitsch²

1.) Department of Chemistry, 'Sapienza' University of Rome, P.le Aldo Moro 5, 00185, Rome, Italy

2.) Institute of Biophysics and Nanosystems Research, Austrian Academy of Sciences, Schmiedelstrasse 6, A-8042 Graz, Austria

Cationic liposomes (CLs) are self-assembled lipid vesicles currently investigated as possible nonviral carriers of nucleic acids in gene delivery [1]. Nowadays, it is accepted that complete DNA protection is a major step toward rational design of efficient CL/DNA complexes (lipoplexes). Previous investigations aimed at elucidating the interactions determining structure, charge, and thermodynamic stability of lipoplexes, and pointed out the existence of three regions in the phase diagram as a function of the cationic lipid/anionic DNA charge ratio, ρ : complexes are monophasic at the isoelectric point ($\rho = 1$), while they separate into complex plus excess liposomes for $\rho > 1$ and complex plus excess DNA for $\rho < 1$ [2]. As a result, mixing lipid and DNA at the isoelectric point has been long considered sufficient for assuming complete DNA protection within a cationic lipid envelope. However many aspects of the phase diagram of cationic lipid/DNA still remain unclear and need to be further investigated. The aim of this work was to study thoroughly the phase diagram of lipoplexes. We selected the lipoplex formulation made of binary DC-Chol–DOPE CLs and plasmid DNA for two reasons as follows: it has been extensively studied from a biological point of view, and it has recently emerged as a potential candidate for the delivery of the chloride transporter gene to the lungs on the treatment of cystic fibrosis disease. Coexistence of complexes with unbound plasmid DNA was proofed by electrophoresis on agarose gels that provides very precise quantification of free DNA that is not protected by lipids. The nanostructure of complexes was characterized by means of high-resolution synchrotron small angle x-ray scattering (SAXS) that allows to determine the one dimensional (1D) DNA packing density within complexes as well as to reveal the coexistence of complexes with pure liposomes. Binary DC-Chol–DOPE CLs were prepared following standard protocols at molar ratios of neutral lipid to total lipid concentrations of $\Phi = (\text{mol/mol}) = 0, 0.3, 0.5, 0.7, \text{ and } 0.75$. DC-Chol–DOPE/DNA lipoplexes were prepared at 12 cationic lipid/DNA charge ratios $\rho = (\text{mol/base}) = 0.25, 0.33, 0.5, 1, 1.5, 2, 2.5, 3, 3.5, 4, 4.5, \text{ and } 5$. All SAXS measurements were performed at the Austrian SAXS station of the synchrotron light source ELETTRA (Trieste, Italy).

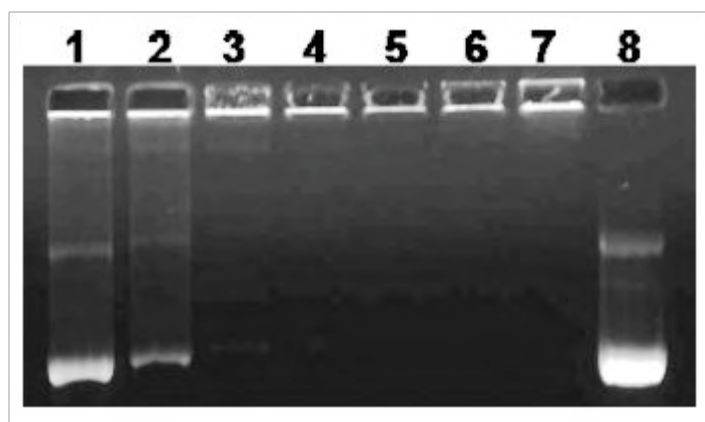


Figure 1. Digital photograph of positively charged DC-Chol–DOPE/DNA lipoplexes ($\Phi = 0.5$) with increasing cationic/anionic charge ratio: $\rho = 1$ (lane 1), $\rho = 1.5$ (lane 2), $\rho = 2$ (lane 3), $\rho = 2.5$ (lane 4), $\rho = 3$ (lane 5), $\rho = 3.5$ (lane 6), $\rho = 4$ (lane 7), and control DNA (lane 8).

Figure 1 shows the digital photograph of DC-Chol–DOPE/DNA ($\Phi = 0.5$) lipoplexes as a function of ρ . Isoelectric DC-Chol–DOPE/DNA complexes ($\rho = 1$) did not protect all the plasmid DNA (Fig. 1, lane 1). Complexes coexisted with free DNA up to $\rho \sim 2$ (Fig. 1, lanes 1–3). As evident, excess cationic charge to protect all the genetic cargo is necessary. As a general rule, such an extra-charge requirement was found to decrease as the molar fraction of neutral lipid in the bilayer increases (i.e., as Φ increases; data not reported for space consideration). Furthermore, the minimum charge ratio from which all plasmid DNA is protected by CLs and complexes start to be monophasic was precisely determined.

Figure 2 shows representative SAXS patterns of DC-Chol–DOPE/($\Phi = 0.5$) lipoplexes as a function of ρ . SAXS experiments revealed that DC-Chol–DOPE/DNA lipoplexes are lamellar even at high DOPE content. The much broader peak marked by arrow is the so-called “DNA peak” arising from the 1D in plane DNA lattice with repeat distance $d_{DNA} = 2\pi/q_{DNA}$. According to literature, the DNA peak is mobile and shifts to lower q with increasing ρ (Fig. 2, from bottom to top). This can be explained considering that increasing ρ results in a growing amount of lipids that enter the complex and separate the DNA strands. At $\rho \sim 4$ (Fig. 2, panel c) the DNA peak is fixed indicating that the 1D DNA lattice cannot be diluted by adding further lipid. Furthermore, the additional peaks at $q \sim 1.25$ and 2.5 nm^{-1} (Fig. 2, panel C, dashed arrows) are consistent with a membrane stack of periodicity $d = 5.03 \text{ nm}$, equal to the periodicity of pure DC-Chol–DOPE bilayers in excess water. This means that starting from $\rho \sim 4$ complexes become biphasic and coexist with excess CLs. SAXS experiments performed on lipoplexes with varying ρ and Φ (data not reported) allowed us to determine the precise charge ratio from which each lipoplex formulation starts to coexist with a pure lipid lamellar phase. Interestingly, a general trend was found: the higher Φ , the lower ρ . This finding is in excellent agreement with electrophoretic data showing that extra-charge requirement decreases with increasing Φ . Combining electrophoresis and SAXS data the phase diagram of DC-Chol–DOPE/DNA lipoplexes was constructed (Fig. 3). Since there are only three relevant chemical components in the system, namely, DNA and the two lipid species, the phase diagram is presented specifying the overall chemical composition of the ternary mixture. Corners of the triangle correspond to 100% molar fraction of DC-Chol, DOPE, and DNA, while black solid line indicates the nominally isoelectric DC-Chol/DNA ratio ($\rho = 1$). Three different phase regions were identified: lamellar complexes coexisting with free plasmid DNA (black points, region A); one-phase complexes (white points, region B); complexes coexisting with excess CLs (gray points, region C). Most remarkable features of the phase diagram reported in Fig. 3 are the following: (i) the extension of region A where the amount of lipid in solution does not suffice to complex all the DNA is much larger than those of regions B and C; (ii) complete association of the lipid and DNA molecules is limited to a very narrow portion of the phase diagram (region B); (iii) region B is not centered around the isoelectric line ($\rho = 1$) as assumed so far. The latter observation is noteworthy since previous studies claimed that stoichiometrically charge-neutral complexes ($\rho = 1$) are monophasic systems with all the DNA and the lipids associated within the complex. Solid lines in the phase diagram of Fig. 3 indicate complexes prepared at the same charge ratio, ρ , with different percentages of neutral lipids in the cationic membranes of lipoplexes. As evident, enriching the cationic membranes with neutral lipid at fixed cationic lipid/anionic DNA charge ratio (moving from the “DC-Chol corner” toward the “DOPE corner”) results in protection of larger amounts of DNA. All these observations are likely to suggest that DNA-binding ability of CLs is mainly regulated by the total lipid membrane area available to DNA condensation [3].

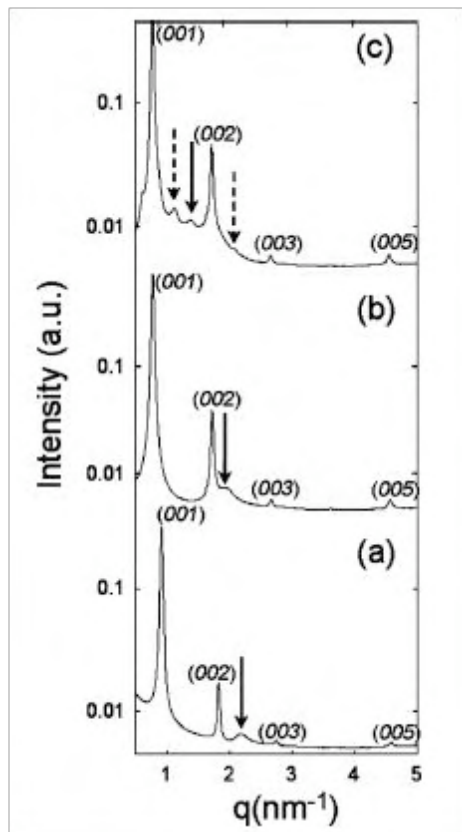


Figure 2. Representative synchrotron SAXS patterns of lipoplexes DC-Chol-DOPE/DNA $\Phi = 0.5$: $\rho=0.5$ (panel a); $\rho = 1$ (panel b); and $\rho = 4$ (panel c).

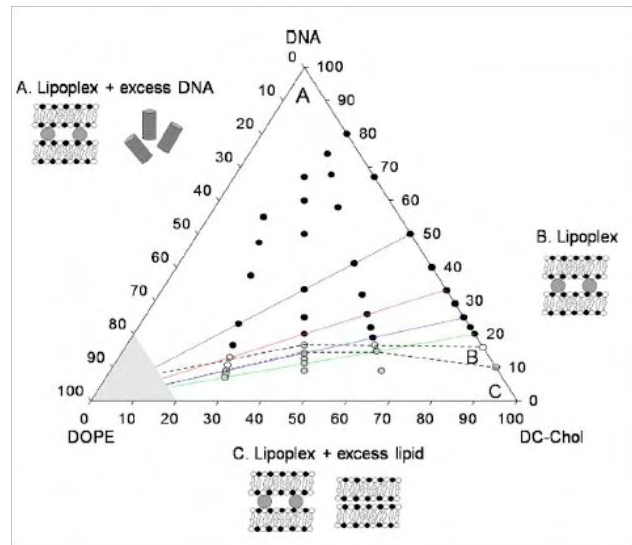


Figure 3. Phase diagram of DC-Chol-DOPE/DNA lipoplexes. Complexes are one phase in the very narrow region B only (white points), while they coexist with excess DNA in region A (black points) and with excess CLs in region C (gray points). Dashed lines give tentative phase boundaries. Lines of equal charge ratio are indicated as: $\rho = 1$ (black solid line); $\rho = 2$ (red solid line); $\rho = 3$ (blue solid line); and $\rho = 4$ (green solid line).

References:

- [1] P.L. Felgner and G.M. Ringold; Cationic liposome mediated transfection; Nature 331, 461-462 (1989)
- [2] A.I. Koltover, T. Salditt, and C.R. Safinya; Phase diagram, stability, and overcharging of lamellar cationic lipid-DNA self-assembled complexes. Biophys. J. 77, 915-924 (1999)
- [3] D. Pozzi, H. Amenitsch, C. Marchini and G. Caracciolo; Phase diagram of DC-Chol-DOPE/DNA complexes suggests strategies for efficient lipoplex transfection; Appl. Phys. Lett. 96, 183703 1-3, 2010

INTERACTIONS OF VINBLASTINE AND CHOLESTEROL WITH DIPALMITOYL-PHOSPHATIDYLCHOLINE BILAYERS

Petros Chatzigeorgiou¹, M. Rappolt² and T. Mavromoustakos¹

1.) University of Athens, Chemistry Department, Panepistimiopolis Zographou 15784, Athens, Greece

2.) Institute of Biophysics and Nanosystems X-ray Research, Austrian Academy of Sciences, c/o Sincrotrone Trieste, Italy

Vinblastine is a mitotic inhibitor isolated from the plant *Catharanthus roseus* G. Don. (Apocynaceae) and it is used clinically in the treatment of leukemia, Hodgkin's disease, breast carcinoma, Wilm's tumor, Ewing's sarcoma and small-cell lung cancer, either alone or in combination with other chemotherapeutic agents [1]. Since it enters into animal cells by diffusion through the plasma membrane its perturbation effects on lipid bilayers have been studied using various biophysical techniques [2,3].

The present study utilizes time resolved simultaneous small angle X-ray (SAXS) and wide angle X-ray scattering (WAXS) on different dipalmitoyl-phosphatidylcholine (DPPC) /vinblastine/cholesterol bilayer systems (Fig. 1). Vinblastine appears to convert MLVs dipalmitoylphosphatidylcholine (DPPC) bilayers to ULVs. This effect may be related to the reported interdigitation that it induces in the fluid phase [2,3]. When cholesterol is present, it induces phase separation, thus increasing the heterogeneity of the lipid bilayers.

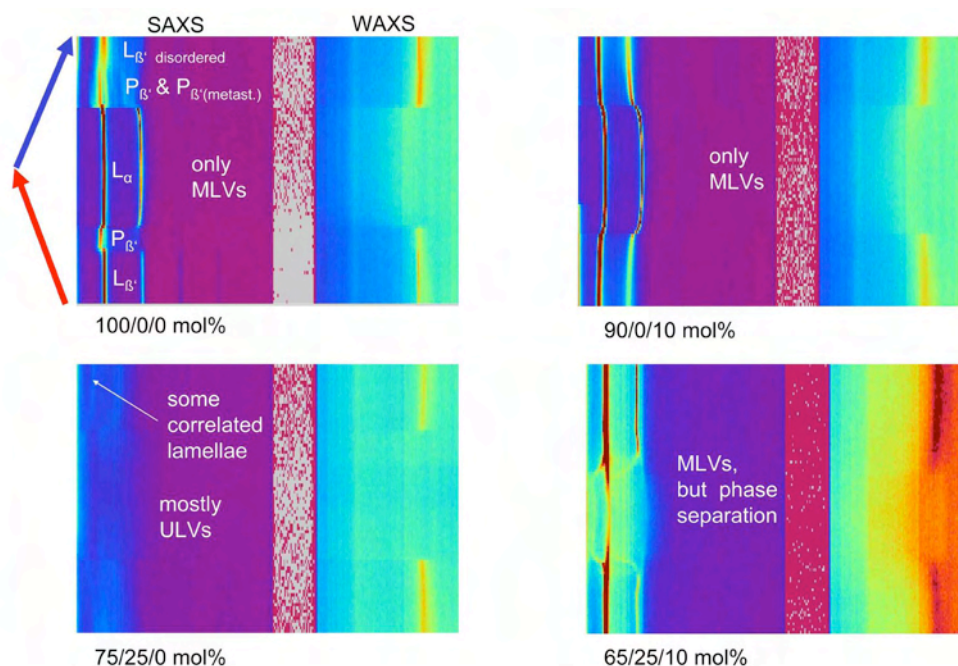


Figure 1. Different DPPC/vinblastine/cholesterol bilayer systems dispersed in excess of water measured by SAXS and WAXS during slow temperature scans from 20 to 60 to 20°C (scan rate 1°C/min).

References:

- [1] I.S. Johnson, J.G. Armstrong, M. Gorman, J.P. Burnett, The vinca alkaloids: a new class of oncolytic agents, *Cancer Res.* 23 1390– 1427 (1963)
- [2] H. Maswadeh, C. Demetzos, I. Daliani, I. Kyrikou, T. Mavromoustakos, A. Tsortos, G. Nounesis. A molecular basis explanation of the dynamic and thermal effects of vinblastine sulfate upon dipalmitoylphosphatidylcholine bilayer membranes. *Biophys Biochim Acta* 1567 49-55 (2002)
- [3] I. Kyrikou, I. Daliani, T. Mavromoustakos, H. Maswadeh, C., Demetzos, S Xatziantoniou, S. Giatrellis, G. Nounesis. The modulation of thermal and dynamic properties of vinblastine by cholesterol in membrane bilayers *Biophys Biochim Acta* 1661, 1-8 (2004)

INTERPARTICLE TRANSFER AND PHASE REORGANIZATION IN SELF-ASSEMBLED SYSTEMS

Yao-Da Dong¹, Adam Tilley¹, Heinz Amenitsch², Michael Rappolt², Ben J Boyd¹

1.) Department of Pharmaceutics, Victoria College of Pharmacy, Monash University, Parkville, VIC 3052, Australia

2.) Institute of Biophysics and Nanosystems Research, Austrian Academy of Sciences, Graz, Austria

Introduction

Certain amphiphilic molecules due to their limited water solubility, only swell to a finite degree when in contact with excess water and forms nanostructured self-assembled systems such as lamellar (L_{α}), inverse cubic (Q_{II}), and inverse hexagonal (H_{II}) lyotropic liquid crystals. In some instances these liquid crystalline structures may be dispersed to form sub-micron particles, termed 'cubosomes' and 'hexosomes' which retain the internal structure of the non-dispersed cubic and hexagonal phase respectively. There is growing recognition of the potential of non-lamellar LC structured systems as vehicles for the encapsulation and delivery of drug and proteins. Using glyceryl monolinoleate (MLO) based cubosomes and hexosomes mixed with octadecane, dodecane and tetradecane microemulsions, Moitzi et al. (2007) demonstrated phase reorganization in self-assembled systems through entropy driven interparticle transfer [1]. The rate of molecular transfer correlated with concentration of the stabilizer F127 present and number of C atoms of the molecule.

In this study we used SAXS to follow interparticle transfer characteristics when using phytantriol (PHYT) to form different particle nanostructures (cubosomes, hexosomes and emulsified microemulsion (L_2) particles).

Results

There were three major new findings arising from these experiments that have consequences for the design and use of these systems in drug delivery applications;

The PHYT based systems showed phase reorganisation during mixing suggesting exchange of material, although the kinetics of interparticle transfer was significantly slower than the MLO systems.

Material exchange is sometimes unidirectional in the PHYT based systems, suggesting compositional ripening

The point of equilibrium for interparticle transfer is not necessarily at the point of homogenous composition, as expected for entropy driven systems

Cubosomes mixed with microemulsions: The equivalent SAXS contour plots in Figure 1 showed phase transition over time when mixing pure PHYT cubosomes with emulsified microemulsion (30% w/w Vitamin E Acetate in PHYT) with equal lipid concentration (10% w/w in water) at volume ratio of 2:1 at 27 °C. This results in a dispersion system containing 10% w/w VitEA to PHYT. In our previous study, dispersion systems formed using pre-mixed VitEA in PHYT at the same ratio showed presence of the HII phase only [2]. The contour plot in Figure 1 showed changes in the relative scattering intensity over time indicating the progressive phase transition from $Q_{II}(Pn3m)$ and L_2 to HII, due to transfer of materials. However, pure HII phase was not observed 3 hr after mixing suggesting a much slower kinetic exchange of material compared to the MLO systems [1]. Furthermore, our previous study showed the lattice size of PHYT-based cubosomes decreases significantly with doping of VitEA and converts to HII phase (hexosomes) with further inclusion. However, only a slight decrease in the lattice size for the cubosomes was observed in the initial 5 min after mixing, after which minimal lattice change was observed for the $Q_{II}(Pn3m)$ phase,

despite progressive decrease in the intensity of the Bragg peaks of the QII(Pn3m) phase. This suggests after the initial 5 min of mixing, further interparticle exchange of materials appeared to be unidirectional, where the PHYT molecules from pure PHYT cubosomes are transferred to the PHYT+VitEA microemulsion droplets whilst minimal VitEA molecules were transferred to the pure PHYT cubosomes. Given the higher lipophilicity of VitEA compared to PHYT molecules, such apparent unidirectional transfer of materials is indicative of entropy driven compositional ripening [3].

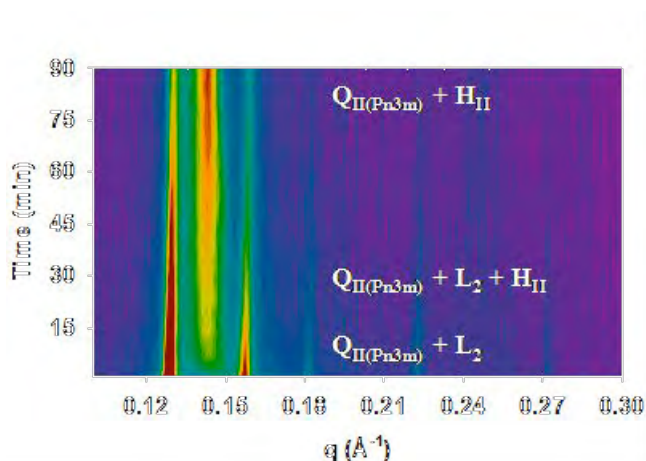


Figure 1. Representative time resolved X-ray diffraction plots after mixing pure PHYT cubosomes with PHYT+30% w/w VitEA microemulsion at volume ratio of 2:1. The relative intensity is represented by rainbow colour where red represents the highest intensity and violet the lowest

Cubosomes mixed with hexosomes: The apparent unidirectional exchange of materials was also evident in Figure 2 when mixing pure PHYT cubosome with hexosomes (10% w/w VitEA in PHYT) at volume ratio of 2.3:1. The final dispersion system contains 3% w/w VitEA in PHYT which in premixed system showed the presence of QII(Pn3m) phase only [2]. Again the pure PHYT cubosomes showed slight decrease in lattice in the initial 5 min after mixing whilst there is a progressive increase in the lattice of the PHYT+VitEA hexosomes over time suggesting the inclusion of PHYT molecules from pure PHYT cubosomes. The presence of cubosomes with smaller lattice than the pure PHYT cubosomes was also detected, with increasing scattering intensity over time. These cubosomes are likely to have originated from the PHYT+10% VitEA hexosomes where the progressive inclusion of PHYT molecules from the pure PHYT cubosomes may have induced the HII to QII phase transition.

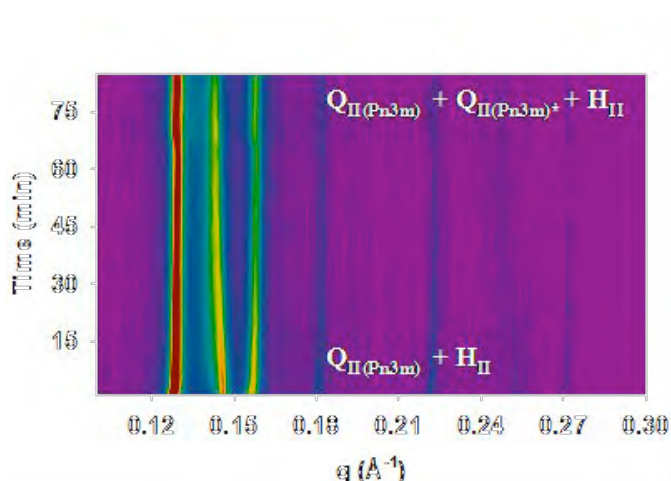


Figure 2. Representative time resolved X-ray diffraction plots after mixing pure PHYT cubosomes with PHYT+10% w/w VitEA hexosomes at volume ratio of 2.3:1. *Formation of QII(Pn3m) with smaller lattice than the original QII(Pn3m) from pure PHYT cubosomes

Cubosomes mixed with cubosomes: Figure 3 showed phase changes over time when mixing equal volume and concentration of pure PHYT cubosomes (QII(Pn3m)) with pure GMO cubosomes (QII(Im3m)). Unlike the PHYT+VitEA systems, the decrease in the lattice size of the GMO cubosomes coincide with the increase in the lattice size for PHYT

cubosomes overtime, suggesting a bidirectional transfer of materials similar to MLO systems. However, the bidirectional transfer appeared to have reached equilibrium prior to reaching mixing homogeneity. 13 min after mixing, no further changes to the Bragg peak positions and intensity was observed, both $Q_{II}(Im3m)$ and $Q_{II}(Pn3m)$ phases were present whilst in our previous internal study, fully pre-mixed GMO+PHYT system showed only the $Q_{II}(Pn3m)$ phase. This finding is significant as it suggests that unlike MLO systems, entropy is unlikely have been the dominant driving force for interparticle transfer between the PHYT and GMO cubosomes.

Conclusion

Despite having similar internal structures, PHYT-based dispersed systems showed very different interparticle transfer characteristics to that of the MLO-based systems. As such, these systems appeared to be non-equivalent and may impact on their potential use as delivery agents. We intend to next examine interparticle transfer in more detail using other self-assembling systems.

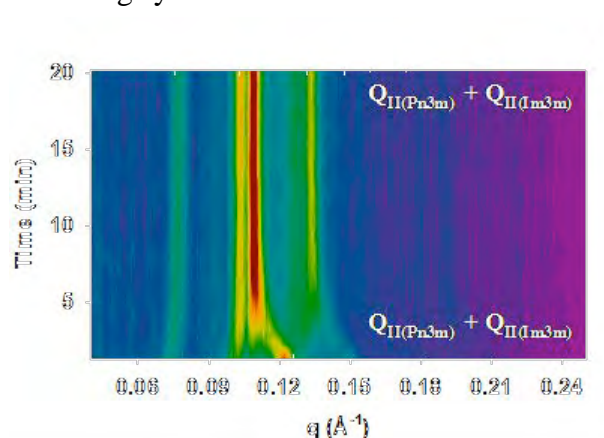


Figure 3. Representative time resolved X-ray diffraction plots after mixing pure PHYT cubosomes with pure GMO cubosomes at volume ratio of 1:1

References:

- [1] Moitzi, C.; S., G. G.; Salentinig, F. S.; Glatter, O., *Adv. Mater.* 2007, 19, (10), 1352-1358
- [2] Dong, Y. D.; Larson, I.; Hanley, T.; Boyd, B. J., *Langmuir* 2006, 22, (23), 9512-9518
- [3] Usui, M.; Harusawa, F.; Sakai, T.; Yamashita, T.; Sakai, H.; Abe, M., *J. Oleo Sci.* 2004, 53, (12), 611-617

SOLUTION STRUCTURE OF THE UNFOLDED DOMAIN OF COLICIN N

Christopher Johnson¹, Alexandra Solovyova¹, Helen Ridley¹, and Jeremy H. Lakey¹

1.) Institute for Cell and Molecular Biosciences, The Medical School, University of Newcastle, Framlington Place, Newcastle-upon-Tyne, NE2 4HH, UK.

Gram negative bacteriocins are a well described group of anti bacterial toxins, known since 1925 when Gratia [1] identified a bactericidal “colicine”. Colicinogenic plasmids enable expansion of their carriers’ numbers by selecting against non-carrier cells, and are thus a microcosm of natural selection [2,3]. Colicins have evolved to invade the cell using complex structures of the bacterial cell envelope. Colicins are thus a unique tool to probe structural and dynamic relationships in the bacterial envelope.

Colicins kill by translocating a 15-25 kDa globular protein domain across the bacterial inner membrane, in one group these are nucleases active in the cytoplasm, in the other major group they are pore-forming toxins. These domains are always at the C-terminus and are preceded by the central receptor binding (R) and N-terminal translocation (T) domains.

The high resolution structure of colN (Figure1) [4] and the three other colicin structures; colE3 (PDB= 1JCH), colIa (1CII) [5, 6] and colB (1RH1) [7], lack data for the unstructured T-domain. It is now clear this is a feature of all colicins. Group A (A, N, E group) colicins bind to periplasmic Tol proteins A or B whereas group B (Ia, B) colicins bind to TonB. Where colE9-T is the best described TolB binding domain [8], ColN-T is the only TolA binding domain which has been fully mapped [9]. The colN-T TolA box comprising residues 40-67, is unfolded in solution but adopts a cooperatively folded structure when bound to TolA [10, 11]. Recently we showed that the T domain binds to the rest of the colicin and that a mutation which affects TolA binding also affects self recognition [12, 13]. Furthermore another mutation K145A on the R-domain also inhibits T-domain self binding. To characterize these structures we used analytical ultracentrifugation and performed SAXS at Elettra.

SAXS revealed for the first time the structure of the complete colicin N molecule and also confirmed the discovery by AUC that the N terminal domain is more disordered in the presence of the Y62A and K145A mutations. This shows the initial unfolding steps that are required for the activity of colicin in vivo.

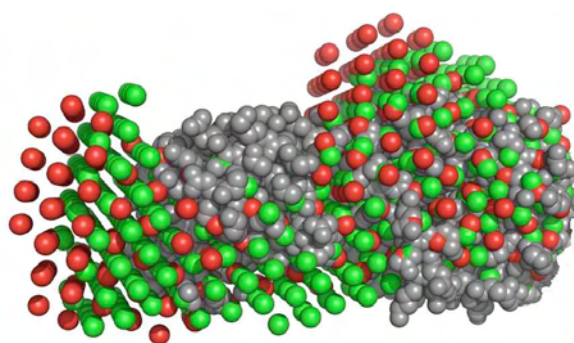


Figure 1. Model of colicin N in solution derived from X-ray scattering data collected at Elettra. X-ray structure of colicin N (1A87) in grey, SAXS model of WT in green showing possible situation of flexible T domain. SAXS model of Y62A mutant in red showing the different distribution of T-domain in this more flexible state.

References:

- [1] Gratia, A. (1925) Sur un remarquable exemple d'antagonisme entre deux souches de colibacille. Comptes Rendus des Seances de la Societe de Biologie et de ses Filiales. 93, 1040-1041
- [2] Lakey, J. H. and Slatin, S. L. (2001) Pore-forming colicins and their relatives. In Pore-Forming Toxins (Van Der Goot, F. G., ed.). pp. 131-161, Springer Verlag, Heidelberg
- [3] James, R., Kleanthous, C. and Moore, G. R. (1996) The biology of E-colicins - paradigms and paradoxes. Microbiology UK. 142, 1569-1580

- [4] Vetter, I. R., Parker, M. W., Tucker, A. D., Lakey, J. H., Pattus, F. and Tsernoglou, D. (1998) Crystal structure of a colicin N fragment suggests a model for toxicity. *Structure*. 6, 863-874
- [5] Soelaiman, S., Jakes, K., Wu, N., Li, C. M. and Shoham, M. (2001) Crystal structure of colicin E3: Implications for cell entry and ribosome inactivation. *Molecular Cell*. 8, 1053-1062
- [6] Wiener, M., Freymann, D., Ghosh, P. and Stroud, R. M. (1997) Crystal structure of colicin Ia. *Nature*. 385, 461-464
- [7] Hilsenbeck, J. L., Park, H., Chen, G., Youn, B., Postle, K. and Kang, C. (2004) Crystal structure of the cytotoxic bacterial protein colicin B at 2.5Å resolution. *Molecular Microbiology*. 51, 711-720
- [8] Collins, E. S., Whittaker, S. B. M., Tozawa, K., MacDonald, C., Boetzel, R., Penfold, C. N., Reilly, A., Clayden, N., Osborne, M. J., Kleanthous, C., James, R. and Moore, G. R. (2002) Structural dynamics of the receptor-binding domain of colicin E9. *J. Mol. Biol.* 122, 145-162
- [9] Gokce, I., Raggett, E. M., Hong, Q., Virden, R., Cooper, A. and Lakey, J. H. (2000) The TolA-recognition Site of Colicin N. ITC, SPR and Stopped-flow Fluorescence Define a Crucial 27-residue Segment. *J. Mol. Biol.* 304, 621-632
- [10] Anderluh, G., Gokce, I. and Lakey, J. H. (2004) A natively unfolded toxin domain uses its receptor as a folding template. *Journal of Biological Chemistry*. 279, 22002-22009
- [11] Anderluh, G., Hong, Q., Boetzel, R., MacDonald, C., Moore, G. R., Virden, R. and Lakey, J. H. (2003) Concerted Folding and Binding of a Flexible Colicin Domain to Its Periplasmic Receptor TolA. *J. Biol. Chem.* 278, 21860-21868
- [12] Hecht, O., Ridley, H., Boetzel, R., Lewin, A., Cull, N., Chalton, D. A., Lakey, J. H. and Moore, G. R. (2008) Self-recognition by an intrinsically disordered protein. *Febs Letters*. 582, 2673-2677
- [13] Hecht, O., Ridley, H., Lakey, J. H. and Moore, G. R. (2009) A Common Interaction for the Entry of Colicin N and Filamentous Phage into *Escherichia coli*. *J. Mol. Biol.* 388, 880-893

EFFECT OF MAILLARD REACTION PRODUCTS (MRPS) ON THE PHASE TRANSITION OF PHOSPHOLIPIDS BILAYERS

L.J. Ke^{1,2}, F. Sa'adedin¹, M. Rappolt³ and J.P. Bradshaw¹

1.) Royal (Dick) School of Veterinary Studies, The University of Edinburgh, Edinburgh, U.K.

2.) Institute of Biotechnology, Fuzhou University, Fuzhou, P.R.China

3.) Institute of Biophysics and Nanosystems Research, Austrian Academy of Sciences, Graz, Austria

In previous studies, we have determined that a group of Maillard reaction products (MRPs) insert between the phospholipids of bilayers and affect the molecular packaging of lipid leaflet. The insertion of MRPs affects the thermal stability of bilayers in a concentration dependent manner. Differential scanning calorimetry has been used to measure the thermodynamic changes, in terms of the phase transition temperature (T) and energy flow (ΔH), of the phase transitions in the presence and absence of MRPs. In order to characterise the structural rearrangements involved in the transition processes, small angle X-ray scattering (SAXS) was used here to investigate the transition from lamellar phase (L_α) to hexagonal phase (H_{II}), with a range of concentrations of MRPs.

A class of hydrophobic peptides, commonly known as membrane fusion peptides, actively participate in fusion events, such as the entry of enveloped viruses into their host cells, or cell-cell fusions induced by viruses. Fusion peptide (GVFVLGFLGFLA) from simian immunodeficiency virus (SIV) glycoprotein gp32 belongs to a family of “oblique-orientated peptides”, and inserts into cellular membranes at an angle of 30° [1]. Its oblique membrane insertion has been directly observed with neutron diffraction on the stacked multi-bilayers of DOPC [2]. SIV fusion peptide associates with lipid in the bilayer at the hydrophobic and hydrophilic interface.

The lipid used in this study, monomethyldioleoylphosphatidylethanolamine (MeDOPE), has two or three phases of lipid behaviour depending on the temperature and the heating rates of the system. Measured by DSC in previous studies, the the lamellar phase (L_α) to hexagonal phase (H_{II}) transition of MeDOPE multilamellar liposome vesicles (MLVs) occurred at $72\sim 73^\circ\text{C}$, whereas the L_α phase to cubic phase (Q) occurred at $\sim 62^\circ\text{C}$. The heating rate of DSC was $40^\circ\text{C}/\text{min}$, at a range from -30°C to 85°C .

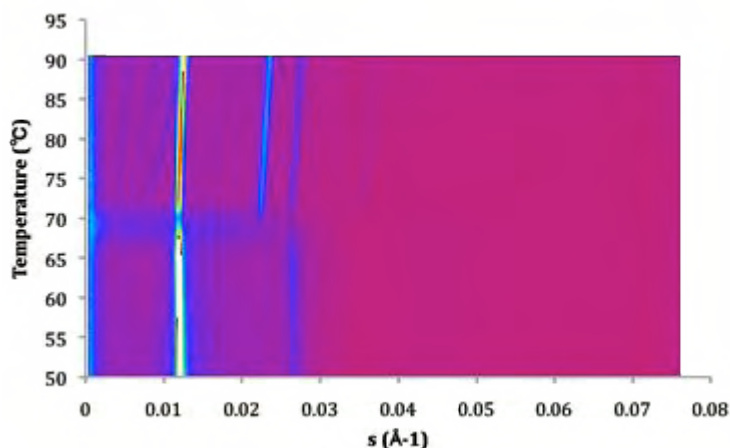


Figure 1. Contour plot of X-ray scattering of MeDOPE MLVs at a temperature scan rate of $1^\circ\text{C}/\text{min}$. The figure shows a L_α to H_{II} phase transition around 70°C and a coexisting of H_{II} phase with Q_{II} phase.

Due to the coexistence of H_{II} with Q_{II} , T_H and T_Q of MeDOPE were the same, 69.8°C (Fig 1). SIV fusion peptide (1 mol%) lowered the T_Q of the cubic phase to 64.3°C, when the T_H was increased to 82.5°C. Theoretically, the fusion peptide disorders the lamellar bilayer and lower the T of non-lamellar vesicle, therefore makes the cubic or hexagonal phase more energy preferable than L_α phase at the high temperature. The T_H was increased here, instead of decreased, by SIV fusion peptide, which is possibly due to the extension of the temperature range of cubic phase. The appearance of a clear cubic phase is generally considered as the initiation of membrane fusion.

The addition of 2 mol% Arg-Glc MRPs, the synthetic MRPs composed of arginine and glucose, to the pure lipid vesicles raised the T of non-lamellar phase to 71.4°C (Figure 2).

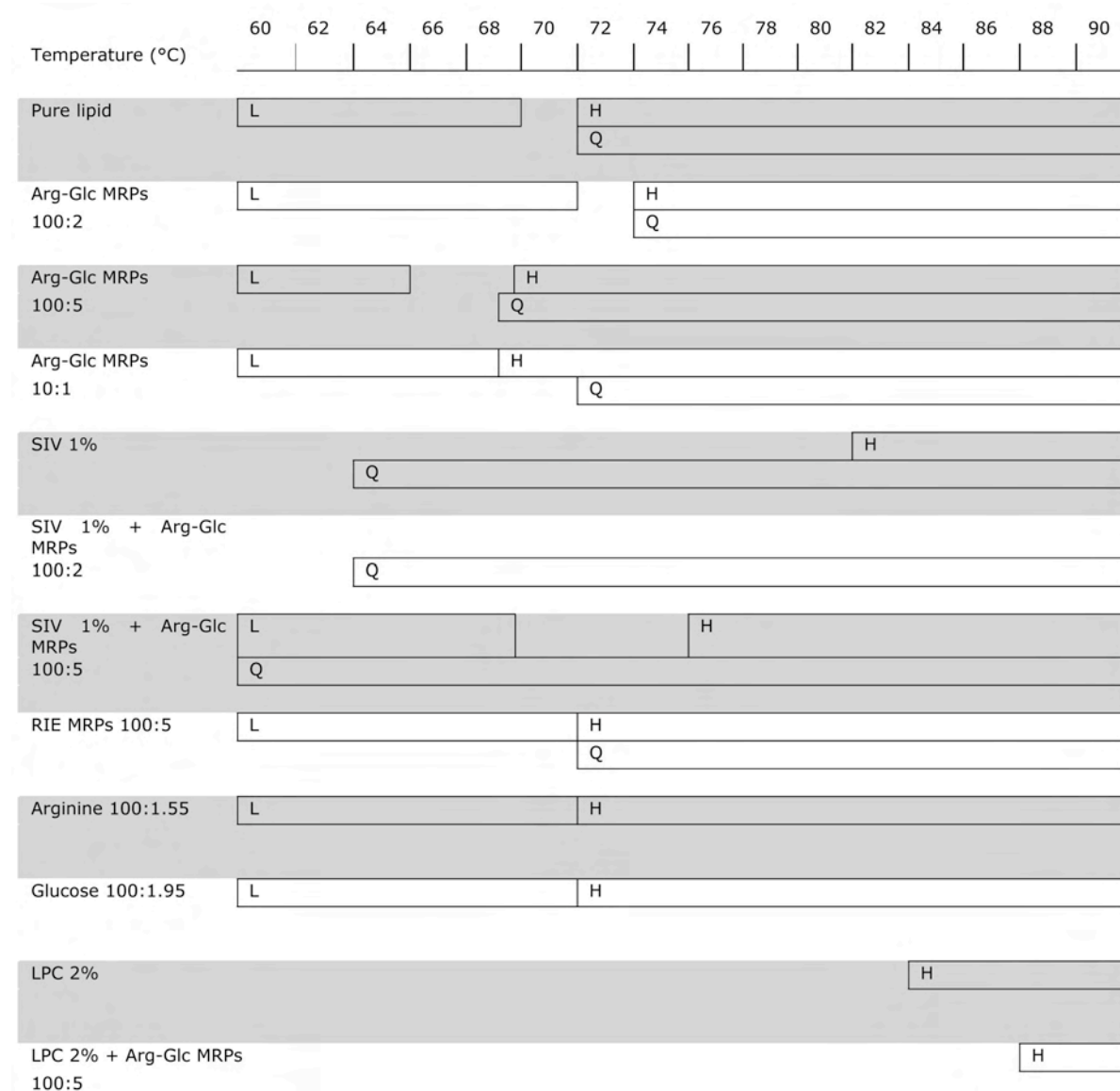


Figure 2. The schematic summary of the phase behaviour of MeDOPE MLVs and the MeDOPE in the presence of Arg-Glc MRPs and/or SIV fusion peptide and fusion inhibitor. The transition temperatures were measured by a temperature scanning at 1°C/min from 30°C to 90°C with the temperature-resolved X-ray diffraction.

However, when the concentration of Arg-Glc MRPs was increased to 5 mol%, the T_Q and T_H decreased to 65.9°C and 66.4°C for hexagonal phase. When the proportion of Arg-Glc MRPs

reached 10 mol%, the T_Q dropped to 68.5°C which was 1.3°C lower than the normal vesicle but 2.6°C higher than the vesicle with 5 mol% Arg-Glc MRPs. This suggests that Arg-Glc MRPs stabilise the lamellar phase at a low concentration (2 mol%), destabilise it at a medium concentration (5 mol%) and high concentration (10 mol%). However, the lipid was less disordered at the high Arg-Glc MRPs concentration than the medium concentration.

As described above, SIV fusion peptide destabilised the lamellar phase when stabilising the cubic phase. The appearance of 2 mol% Arg-Glc MRPs stabilised the cubic phase even more, and raised the T_H to 86°C. 5 mol% Arg-Glc MRPs lowered both T_Q and T_H , which indicates a bilayer destabilising effect.

LPC, lysophosphatidylcholines, is a potent inhibitor to fusion peptide induced membrane fusion, which strongly inhibits the formation of negative curvature. 2 mol% of LPC caused a dramatic increase in the lamellar to hexagonal phase transition temperature, but made the lipid in each phase less ordered. Arg-Glc MRPs enhanced the inhibitory effects caused by LPC, raising the T_H to 87.9°C.

References:

- [1] Robert Brasseur, et al.; Peptides in membranes: tipping the balance of membrane stability; Trends in biochemical sciences 22(5): 167-171 (1997)
- [2] Jeremy Bradshaw, et al.; Oblique Membrane Insertion of Viral Fusion Peptide Probed by Neutron Diffraction; Biochemistry 39 (22): 6581–6585 (2000)

ANALYSIS OF MECHANICAL PROPERTIES OF GUANOSINE-GUANINE NANOWIRES IN AQUEOUS SOLUTION BY HIGH-PRESSURE X-RAY DIFFRACTION

P. Mariani, F. Spinozzi, E. Baldassarri and D. Burattini

Università Politecnica delle Marche, Depart. SAIFET, Physical Science Section, via Ranieri 65, 60131, Ancona, Italy

Of the five nucleotides found in DNA and RNA, only guanosine (G) is able of forming extensive 'self-structures' in solution [1-3]. The common basic building block of such structures is a planar disc-shaped quartet formed by four Hoogsteen hydrogen-bonded guanosine moieties, as schematically represented in Figure 1 (A and B). In water, we demonstrated the presence of an extended lyotropic polymorphism, with the formation of hexagonal and cholesteric phases at low and high hydration, respectively [2]. Both phases are columnar, being formed by columnar helicoidal aggregates of finite length (the so-called G-quadruplex), composed of a stacked array of guanine quartets, piled at the typical distance of 3.4 Å and rotated with respect to each other of about 30°.

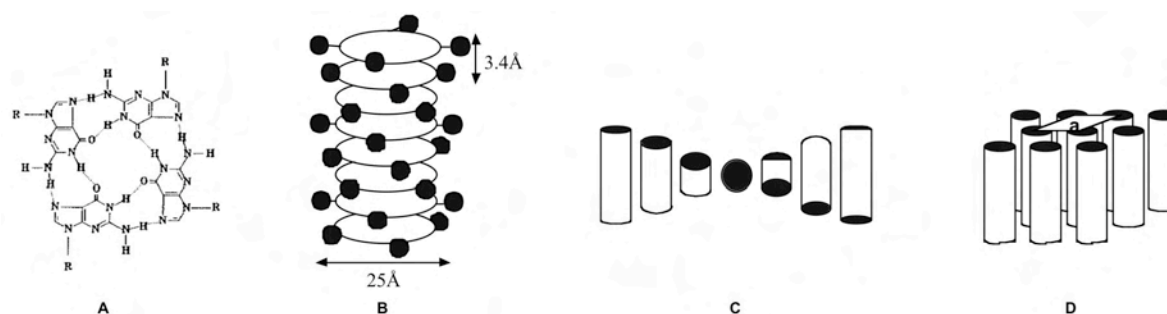


Figure 1. Structural models for guanosine self-assembling. (A) Guanines bonded in a Hoogsteen mode. (B) G-quadruplex: the disk represents a G-quartet, while the dark circle the sugar. The stacking is helical. (C) Cholesteric and (D) hexagonal phase: helices are represented as cylinders.

Besides their biological relevance [1], guanine tetrads have drawn attention in the nanotechnology field. They were in fact proposed as building blocks of molecular nanowires for nanoelectronics [4], as the large number of stacked tetrads provides better conditions for p-overlap compared to the base-pairs of the canonical double-stranded DNA and higher structural rigidity and stability under various conditions. We have developed G-based molecular nanowires of various sorts, using different guanosine derivatives (even lipophilic: see, e.g., [5]) and helical conformations [2]. Most significant, we have improved the control over the structural properties and polymorphism in aqueous solution, by optimizing the experimental condition (pH, temperature, counterion, ionic strength) and protocols. The structural characterization, based on AFM imaging (Figure 2) and spectroscopic and scattering techniques, was an important portion of the whole analysis, dedicated to the demonstration of self-assembling properties and backed up by a strong effort towards physico-chemical understanding. A central finding was the very recently demonstration of a reproducible conductivity on deoxyguanosine 5' monophosphate, d(pG), nanowires (F.Federiconi and K.Kunstelj, to be published).

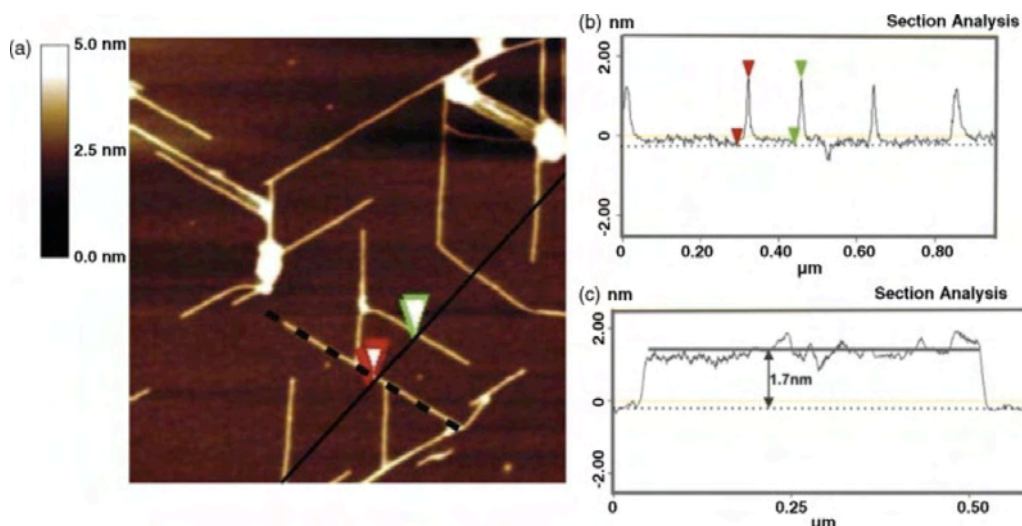


Figure 2. AFM image of d(GMP) based nanowires

An important point concerns the mechanical properties of d(pG) nanowires: the presence of the phosphate charges resulted in relatively soft polymers (as indicated by the axial 1D compressibility recently measured by high-pressure X-ray diffraction [6]) and this drawback limits their application in nanoelectronics.

To reduce the charge effect, and then to improve stiffness and persistence length, we prepared a series of d(pG) samples containing different amount of guanine (the nucleobase in guanosine), which is still able to self-associate in tetrads, but is uncharged, and questions related to the mechanical properties of d(pG)/guanine nanowires and to the roles of preferential hydration and lateral forces on the stability of the systems have been investigated by high-pressure X-ray diffraction measurements. Hydrated samples were prepared by mixing the d(pG), ammonium salt, and guanine (Sigma, 99 % purity) with the required quantities of freshly bidistilled water. Final mixtures (GMP weight fractions c ranging from 0.8 to 0.55) were left for at least two days at 25°C to avoid in-homogeneity. Diffraction experiments were performed at the SAXS beam-line at ELETTRA Synchrotron (Trieste, Italy). The SAXS/WAXS set-up was used to monitor diffraction patterns in the low and high Q -range. Pressure cells with diamond windows, which allow measure diffraction patterns at hydrostatic pressures up to 2 kbar were used. Particular care was taken to check for radiation damage and for equilibrium conditions. Measurements were repeated several times at the same constant pressure to account for stability in position and intensity of Bragg peaks. Accordingly, samples were gently compressed at a rate of 0.5-2 bar/s to ensure the onset of equilibrium conditions. The diffraction patterns were collected at 25°C.

Typical low-angle X-ray diffraction patterns are shown in Figure 3: low angle peaks (from 1 to 3), indexed in a 2D hexagonal lattice, or a broad band, indicating the cholesteric phase, were observed and the unit cell dimension, a , (i.e., the lateral interaxial distance between the helices) derived as a function of pressure (P) and composition. Moreover, a narrow band was observed in the wide-angle region, indicating the columnar nature of the phases. From the position of this peak, d_s , the stacking distance between the G-quartets was obtained.

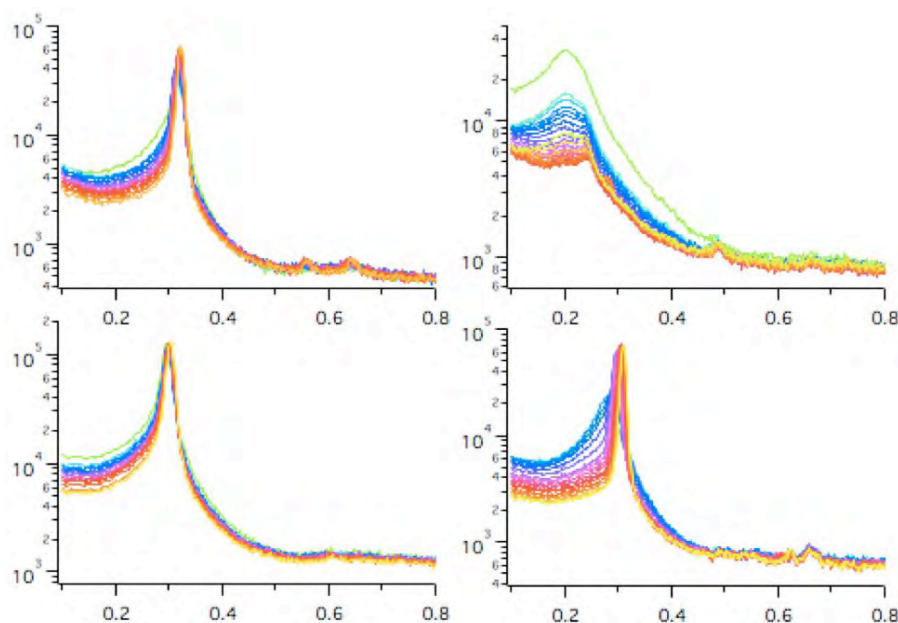


Figure 3. A few SAXS intensity (a.u.) vs. Q (\AA^{-1}) profiles obtained in different experimental conditions at different pressures (from green to red, pressure increases from 1 to 2000 bar).

From structural data, axial (1D) and lateral (2D) compressibilities, $\beta_{1D} = -1/b$ (db/dP) and $\beta_{2D} = -1/\sigma$ ($d\sigma/dP$) (where $\sigma = a^2\sqrt{3}/2$), were calculated. The results deserve two important comments: *first*, lateral compressibilities are positive, and for increasing guanine concentrations strongly increase. *Second*, stacking compressibilities are also positive, but higher than those observed in the absence of guanine [6]. The reduction of charge density along the helix strongly reduces the later repulsive electrostatic inter-columnar forces, but strongly increases the G-quartet stacking energy.

The data analysis is not yet concluded, and then the present report is not exhaustive; however, we are persuaded that the experimental data will help the understanding of the peculiar self-assembling properties of guanosine and will open real possibilities for using G-wires in nano-electronic applications.

References:

- [1] S. Burge et al.; Quadruplex DNA: sequence, topology and structure. *Nucl. Acids Res.*, 34, 5402 (2006)
- [2] P. Mariani et al.; The self-assembly of guanosine derivatives and folic acid. In "Crystallography of Supramolecular Compounds" Tsoucaris & Atwood Ed.s, p. 307, Kluwer Academic Publ. (1996)
- [3] P. Mariani et al.; Small Angle X-ray Scattering Analysis of Deoxyguanosine 5'-Monophosphate Self-Assembling in Solution: Nucleation and Growth of G-Quadruplexes. *J. Phys. Chem. B*, 113, 7934 (2009)
- [4] A.B. Kotlyar et al.; Long, monomolecular guanine-based nanowires. *Adv. Mater.*, 17, 1901 (2005)
- [5] G.P. Spada et al.; Self-assembly of an alkylated guanosine derivative into ordered supramolecular nanoribbons in solution and on solid surfaces. *Chemistry Europ. J.*, 13, 3757 (2007)
- [6] P. Ausili et al.; Pressure effects on columnar lyotropics: anisotropic compressibilities in guanosine monophosphate four-stranded helices. *J. Phys. Chem. B*, 108, 1783 (2004)

MEMBRANE-MEDIATED EFFECT ON ION CHANNELS INDUCED BY THE ANESTHETIC DRUG KETAMINE

G. Pabst¹, H. Jerabek², M. Rappolt¹ and T. Stockner^{2,3}

- 1.) Institute of Biophysics and Nanosystems Research, Austrian Academy of Sciences, Graz, Austria
- 2.) Department of Health & Environment, Austrian Institute of Technology, Seibersdorf, Austria
- 3.) Department of Medical Chemistry, Medical University of Vienna, Vienna, Austria

Anesthetic drugs have been in use for over 160 years in surgery, but their mode of action remains largely unresolved. Thus far, consensus has been reached only in two aspects: (i) general anesthetics act on the central nervous system (brain and spinal cord) and (ii) modulate activity of a large number of ion channels of the neurotransmission system. At present, there are two schools, one favoring specific (direct) interactions of the drugs with the target proteins and a second adhering to nonspecific mechanisms through a modulation of biophysical membrane properties.

We have studied a bilayer-mediated mechanism that was proposed more than 10 years ago [1], but which has never been tested rigorously. In particular, we focused on the effect of R(-)-ketamine on the lateral pressure profile of lipid model membranes composed of palmitoylcholine (POPC) by a combination of X-ray diffraction and all-atom simulations. In agreement with several previous studies, we do not find significant changes to the membrane thickness and lateral area per lipid up to 8 mol % ketamine content (Fig. 1). However, we observed that the insertion of ketamine within the lipid/water interface caused significant changes of lateral pressure and a pressure shift toward the center of the bilayer (Fig. 2A). The changes are predicted to be large enough to affect the opening probability of ion channels as derived for two protein models. Depending on the protein model, we found inhibition values of $IC_{50} = 2$ mol % and 18 mol % ketamine (Fig. 2B), corresponding to approximately 0.08 and 0.9 μ M concentrations in the blood circulation, respectively. This compares remarkably well with clinical applied concentrations. We thus provide evidence for a lateral pressure mediated mode of anesthesia, first proposed more than 10 years ago.

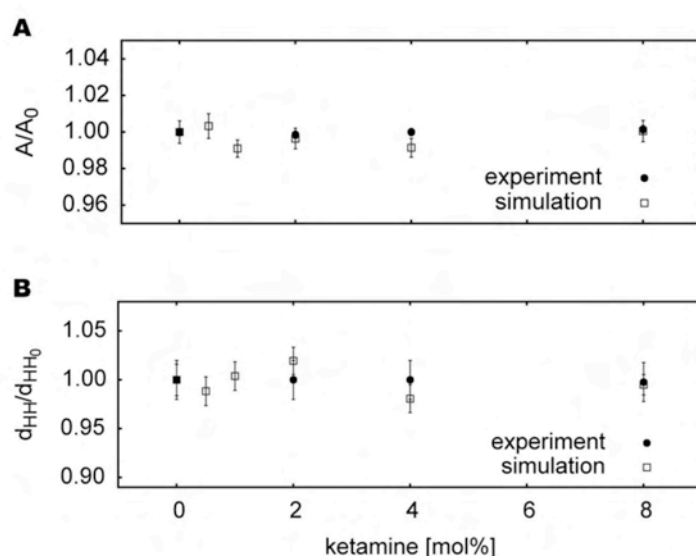


Figure 1. (A) Concentration dependence of the POPC area per lipid relative to the ketamine free membrane A_0 obtained from experiments and simulations. (B) Membrane thickness obtained from experiments and simulations with increasing ketamine concentrations relative to the bilayer free of ketamine d_{HH0} .

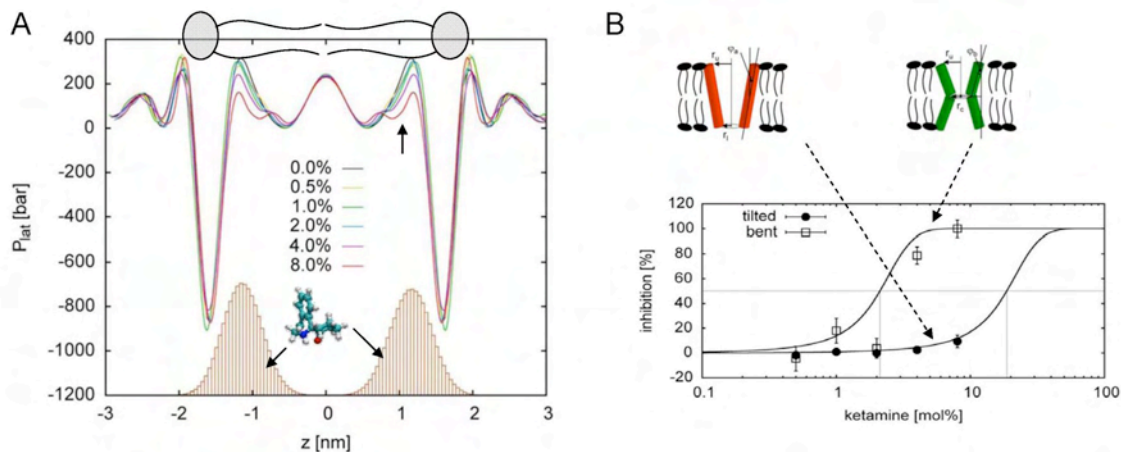


Figure 2. (A) Depth-dependent lateral pressure changes at different ketamine concentrations as determined from simulations. Ketamine distribution functions (histograms) show a preferred location close to the polar/apolar interface. (B) Estimation of the percent inhibition for two channel models (tilted and bent helices, see cartoon) due to changes of lateral pressures. The corresponding IC₅₀ values are indicated by a gray line.

References:

- [1] R.S. Cantor; The lateral pressure profile in membranes: a physical mechanism of general anesthesia; *Biochemistry* 36, 2339-2344 (1997)
- [2] H. Jerabek, G. Pabst, M. Rappolt and T. Stockner; Membrane-mediated effect on ion channels induced by the anesthetic drug ketamine; *J. Am. Chem. Soc.* 132, 7990-7997 (2010)

TUNING THE SPONTANEOUS CURVATURE IN THE INVERSE HEXAGONAL PHASE BY DIFFERENT ADDITIVES

S. Perutkova¹, A. Iglic¹ and M. Rappolt²

1.) Laboratory of Biophysics, Faculty of Electrical Engineering, University of Ljubljana, Slovenia

2.) Institute of Biophysics and Nanosystems X-ray Research, Austrian Academy of Sciences, c/o Sincrotrone Trieste, Italy

The presented small angle X-ray diffraction (SAXD) studies on the inverse hexagonal phase (H_2) of phosphatidylethanolamines (PE) is part of a project that aims to understand the influence of different additives on the spontaneous curvature of the lipid monolayers. Within this framework additives such as vitamin E, different fatty acids as well as binary lipid systems dispersed in excess of water are studied first structurally [1], and then tried to be understood also theoretically [2]. In future simulations on the free energy of such systems the analyzes will take into account both lipid (molecule) packing and membrane bending. When determining the membrane bending, also the lipid anisotropy is accounted for. As can be seen in the figure below the addition of small amounts of saturated PEs (in this case dipalmitoyl-phosphatidylethanolamine – DPPE) to the H_2 phase of palmitoyl-oleoyl-phosphatidylethanolamine (POPE) is sufficient to decrease the spontaneous curvature by about 9%.

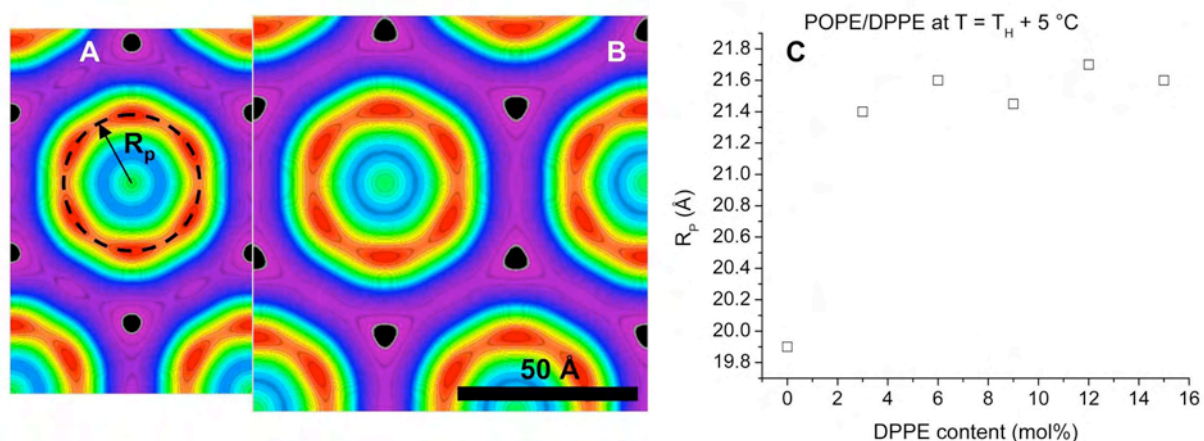


Figure 1. (A) Electron density map of the H_2 phase of POPE/water at 80 °C, and (B) of the POPE/DPPE (5.6 : 1 mol/mol) water system at 91.5 °C. (C) Change of lipid phosphate group position, R_p , with increasing content of DPPE.

References:

- [1] M. Rappolt, A. Hodzic, B. Sartori, M. Ollivon, and P. Laggner. Conformational and hydrational properties during the L_{β} to L_{α} and L_{α} to H_{II} -phase transition in phosphatidylethanolamine. *Chem. Phys. Lipids* 154, 46-55. (2008)
- [2] S. Perutková, M. Daniel, G. Dolinar, M. Rappolt, V. Kralj-Iglič, V., and A. Iglič Stability of the Inverted Hexagonal Phase. In A. Leitmannova Liu and H.T. Tien, editors: *Advances in Planar Lipid Bilayers and Liposomes*, Vol. 9, Burlington: Academic Press, pp. 237-278 (2009)

Chemistry

MONITORING SILVER PARTICLE FORMATION IN A POLYMER SOLUTION BY IN SITU AND TIME RESOLVED SAXS

G. Campi¹, A. Mari², A. Pifferi¹ and L. Suber²

1.) CNR- Istituto di Cristallografia, Via Salaria, Km 29.300, Monterotondo (RM), I-00015, Italy

2.) CNR- Istituto di Struttura della Materia, Via Salaria, Km 29.300, Monterotondo (RM), I-00015, Italy

Noble metals and in particular silver nanoparticles [1] have received considerable attention due to their attractive physicochemical properties. We recently exploited a silver nanoparticle synthesis utilizing silver nitrate as salt, nitric acid to set acidic condition, ascorbic acid as reducing agent and polynaphthalene sulphonate polymer, termed Daxad 19, as stabilizer in aqueous phase at a fixed temperature of 40 °C [2]. In this work we aim to monitor the silver particles formation: we added the reducing agent at a fixed slow rate (0.5 mL/min), in order to control the Ag^+ ions reduction, achieving the formation of the Ag^0 crystalline colloidal dispersion in about 300 seconds; SAXS data have been collected in the $[0.07 < q < 1.7] \text{nm}^{-1}$ range using a CCD device as detector and a batch reactor apparatus allowing time resolution of 0.9 seconds. In this way we could observe different stages in the formation of crystalline silver colloidal dispersion.

SAXS normalized and water-subtracted intensity versus q at different time intervals are shown in the log-log plots of Figure 1. Before the addition of ascorbic acid, for $t < t_0 = 30 \text{s}$, the scattered intensity, due to the Ag salt + polymer background in the aqueous solution, shows power law behaviour (see the SAXS pattern collected at $t = 22.5 \text{s}$ in Fig. 1). As the first micro drop of reduction agent falls in the solution mixture, the scattered intensity starts to gradually increase in the low q region indicating particle nucleation and growth, NG . In the following five minutes we detect *i*) the development of interference oscillations whose maxima and minima progressively shift to smaller q and *ii*) a change in the profile slopes that increase as a function of the time (Fig. 5).

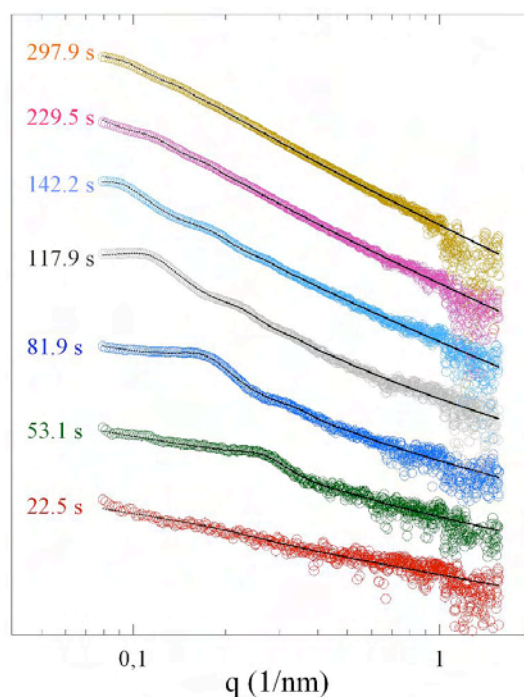


Figure 1. SAXS normalized profiles (open circles) collected at the time intervals indicated; solid lines show the best-fitted curves calculated by eq. 1.

These essential features of our experimental work are captured by assuming a physical system constituted by interacting spherules forming in aqueous solution of Ag salt and polymer, described by

$$I(q) = I_B(q) + I_P(q) \quad (1)$$

where the first power law term

$$I_B(q) = P_C q^{P_E} \quad (2)$$

is due to the polymer and AgNO₃ salt background in the solution, while the second term

$$I_P(q) = CNS(q, R_{HS}, \zeta) \int_0^\infty P(R) [V(R) \tilde{O}(R/R)] dR \quad (3)$$

takes into account the formation of N spherical primary particles with radius R ; C is a constant independent of q and R ; $V(R)$ and \tilde{O} are the volume and the form factor of the single spherical particle, respectively. In order to account for the polydispersity of the particles, the intensity has been integrated over a *log-normal* distribution of R , $P(R)$. Finally, the scattering oscillations have been modelled in the monodisperse approximation of hard spheres with radius R_{HS} and volume fraction calculated with the Percus-Yevick equation.

We used the trust-region-reflective algorithm [3], in order to fit the data and the time dependence of parameters allows us to distinguish two different time regions, highlighted as grey scaled areas in Figure 2.

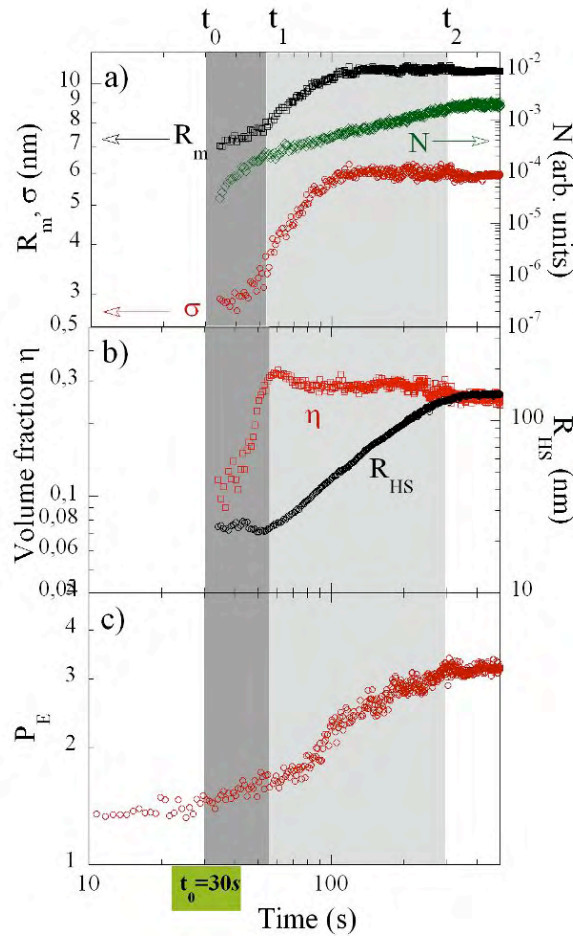


Figure 2. Log-Log time evolution of number density N , mean radius R_m , and dispersivity σ (a), hard sphere radius R_{HS} and volume fraction η in the Percus-Yevick approximation (b), exponent P_E in eq. 2 (c).

As soon as the reduction process by ascorbic acid takes place, Ag-polymer clusters nucleate for $t < t_1 = 54\text{s}$, as indicated (Fig. 2a) by the plot of N as a function of time. In the same time interval, a low-angle diffraction peak arises with q value nearly equal to 0.28 nm^{-1} involving a fraction of about 30% of the total volume of clusters (Fig. 2b).

In the following, for $t_1 < t < t_2$, nucleated clusters grow by slow diffusion, as indicated by the increasing of the mean radius, R_m with its standard deviation, and the number density N (Fig. 2a); remains nearly constant while the interference peaks move towards lower scattering vectors q indicating the development of spatial liquid-like long range correlations, whose lengths are given by the hard sphere radius R_{HS} in the Percus-Yevick approximation.

This could be explained as the formation of core-shell particles, where Ag^0 primary particles are the cores with radius R_m and shells, with radius R_{HS} , are formed by Ag^0 -polymer networks that cover the primary particle, hindering further core growth by Ag^0 diffusion and causing increase of long range liquid-like correlations (*shell expansion*). Figures 2a and 2b well visualize this behaviour: the nucleation of clusters growing up to become primary particles as stable cores in liquid like ordered expanding *shells*.

Subsequently, when $t = t_2$, P_E becomes equal to 3, (Fig. 2c) indicating a mass-surface fractal transition; at the same time *shell* size approaches its maximum value $R_{HS}^* = 120\text{nm}$. We suppose that these two simultaneous events could be due to a Ag-polymer reorganization inducing coalescence of Ag-polymer fragments with primary particles to form final larger Ag particles coated with polymer.

We hope these results could give a contribution to basic chemical physics, dealing with non standard stepwise crystallization from solutions.

References:

- [1] J. H. Lim, J. S. Lee, A statistical design and analysis illustrating the interactions between key experimental factors for the synthesis of silver nanoparticles, *Colloids and Surface A: Physicochem. Eng. Aspects* 322, 155 (2008)
- [2] L. Suber, I. Sondi, E. Matijević and D.V. Goia, L. Suber, I. Sondi, E. Matijević and Dan V. Goia, Preparation and the mechanism of formation of silver particles of different morphologies in homogeneous solutions, *J. Colloid Interface Sci.*, 288, 489-495 (2005)
- [3] T.F. Coleman and Y. Li, An Interior, Trust Region Approach for Nonlinear Minimization Subject to Bounds, *SIAM Journal on Optimization*, 6, 418-445, 1996

BOTTOM-UP APPROACH TOWARDS TITANOSILICATE MESOPOROUS PILLARED PLANAR NANOCHANNELS FOR NANOFLUIDIC APPLICATIONS

M. Faustini¹, B. Marmiroli², M. Vayer³, C. Sinturel³, H. Amenitsch² and D. Grosso^{1*}

- 1.) Laboratoire Chimie de la Matière Condensée de Paris, UPMC, 11 place Marcelin Bertholet, 75231, Paris, France
- 2.) Institute of Biophysics and X-ray Structure Research, Austrian Academy of Sciences, Steyrergasse 17/VI, 8010 Graz, Austria
- 3.) Centre de Recherche sur la Matière Divisée, 1b rue de la Ferrollerie, 45 071, Orleans, France

Nanofluidics transport in lab-on-chip devices requires nanochannels that are difficult to fabricate since they require challenging top-down technological approaches. We present a bottom-up, scalable, low-cost and robust alternative to construct large areas of mesofluidic Pillared Planar Nanochannels (PPNs) [1]. Microscopy images displayed in Figure 1 are representative of the whole system, and show the typical PPN layers made of dense and mesoporous materials organized into vertical nanopillars supporting a continuous roof. Such conformation is homogeneously present all over the coated substrate. They have been obtained upon combining self-assembly of block copolymer [2], nanostructured sol-gel coatings [3] and highly controlled liquid deposition processing [4]. The mesoporous structure contains two types of porosity. The first one is the fully open and accessible inter-pillar porosity with characteristic dimensions adjustable between 20 and 400 nm, which is necessary to allow facile diffusion despite the double layer effect. The second one is present inside the pillars and the roof, and is composed of less than 10 nm pores, which aim at increasing the surface area. Both layer structures have been characterised by Grazing Incidence Small Angle X-ray Scattering. Pillar ordering can be assessed by GI-SAXS analysis as shown in Figure 2a) for F127-templated titanosilicate systems and in Figure 3a) for CTAB-templated silicate systems. In both cases, the intense Bragg diffraction signal at $q_y = 0.14 \text{ nm}^{-1}$, together with its first harmonic at $q_y = 0.28 \text{ nm}^{-1}$, is associated to the both $(01)_p$ and $(02)_p$ diffractions of the highly ordered 2D lateral hexagonal structure formed by the pillar array with a corresponding inter-pillar distance of 51 nm ($d_{(01)} = 44 \text{ nm}$) (see Figure 2b). The latter dimensions can be found on TEM and SEM images whatever the type of inorganic material used for impregnation. The fact that the $(01)_p$ diffraction has a vertical tail (diffraction rod) extending only in the z direction, suggests a high degree of vertical alignment of the pillars. For the F127-templated titanosilicate layers, the GI-SAXS diagram Figure 2a) exhibits, together with the previous $(01)_p$ diffractions of the pillars at low q, the characteristic $(110)_m$, $(101)_m$ and $(1-10)_m$ diffraction points of the $Im\bar{3}m$ mesostructure, revealing that the nanoporous network is composed of contracted body centre cubic arrangement of pores with extended domains having the $[110]$ direction normal to the surface. The lateral periodicity is found to be 14.5 nm, which corresponds to the structure obtained for plain continuous films, for which pores sizes were deduced from ellipsometry porosimetry to be around 6 nm. The high order structure is clearly observed in SEM and TEM corresponding images in Figures 1c)-f). Interestingly, the SEM image c) reveals that the pillars do not have the same texture as the roof. TEM image of Figure 1f) and 1g), shows that the pillars are actually hollow cylinder (tubes) below the roof.

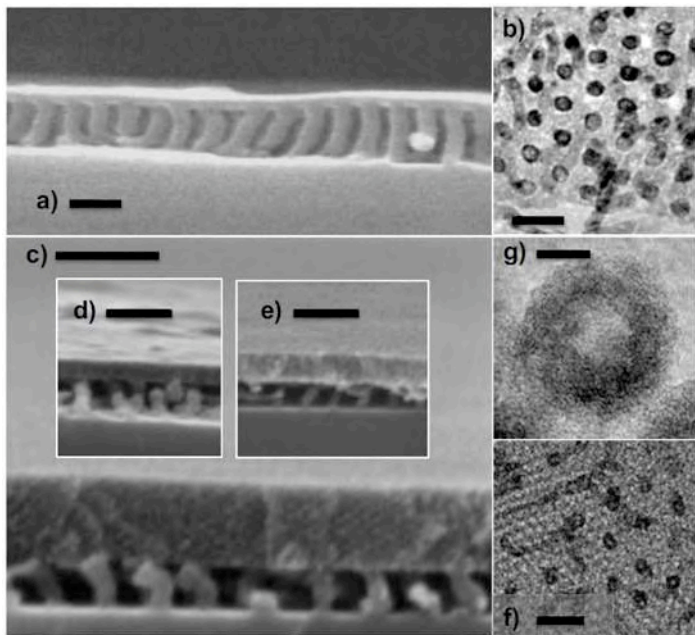


Figure 1. Pillared Planar Nanochannels layers with various chemical compositions, morphologies, and pillar and roof inner structures. a) and b) are SEM (profile cut) and TEM (top view) images respectively of a dense TiO_2 PPN. Images c) to f) were taken from a similar system for which the material is composed of mesoporous 10% SiO_2 -90% TiO_2 . SEM images c) to e) display profile cuts, where one can easily observe the pillars supporting a roof of different thicknesses (obtained with various sol-gel deposition condition), but all bearing the same ordered Im3m mesoporosity induced by the F127. TEM images f) and g) are top views of the layer and reveal a clear emptiness of the pillars. The latter are organised into hexagonal organisation. Scale bars = 50 nm for a), b), and f); 100 nm for c), d), and e); and 5 nm for g)

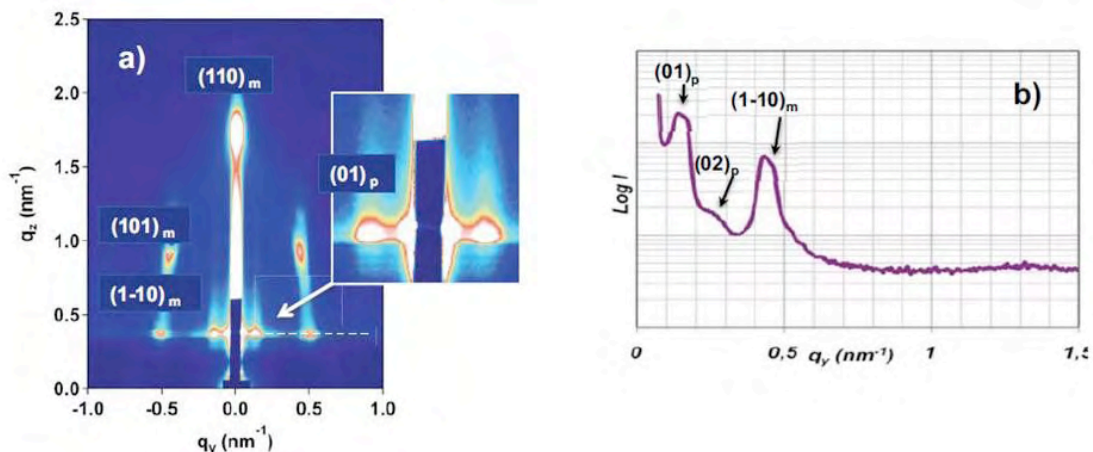


Figure 2. a) GI-SAXS pattern of a Im3m mesoporous (F127 templated) 10% SiO_2 -90% TiO_2 PPN. b) is the plot of the diffused intensity ($\log I$) versus the wave vector in the y direction of the reciprocal space, showing both organisation in the lateral direction.

The GI-SAXS pattern of CTAB-templated silica system displayed in Figure 3a) also reveals the presence of the pillar organisation together with a mesostructure. Indexing of the diffraction points allows to state that the porous network is composed of cylindrical pores organised into a 2D-hexagonal ($p6m$) structure with the $c6$ axis laying horizontally. As expected the periodic distance is found at much higher q values ($d(10) = 2.95$ nm) than for the F127-templated system. Porosities of the latter system were investigated by Ellipsometry Porosimetry [5]. The diagram in Figure 3b) represents the adsorption/desorption isotherms of water inside the pillar underneath layer (orange and red curves) and the roof top layer (light and dark blue curves). The top layer presents the typical adsorption/desorption curves of CTAB-templated films with capillary condensation taking place at 35% RH, which corresponds to pores of diameter below 2 nm. Water desorption takes place at a lower pressure of 25%, suggesting the presence of narrower restrictions between pores. The underneath layer exhibits the same adsorption desorption hysteresis but with a much lower

variation of refractive index, confirming the presence of the same type of porosity inside the pillars. In addition, a significant refractive index increase occurs at higher humidity, which is attributed to inter-pillar porosity with no evident restriction revealed by the lack of hysteresis. At such pressures, pore diameters can be estimated to be over 20 nm in dimension with a fully open geometry. This investigation confirms that mesoporosity is present in both the pillars and the roof materials with the same type of pore distribution, while a much greater porosity is due to the inter-pillar void within the underneath. These Pillared Planar Nanochannel showed the ability to vehicle fluids in the inter-pillars porosity through natural capillary forces, for which the classical Washburn model of diffusion is verified. In addition PPNs are compatible with lithography techniques, such as deep X-ray lithography, for the production of complex designs and thus demonstrating to be ideal candidates for micro/nano fluidic applications.

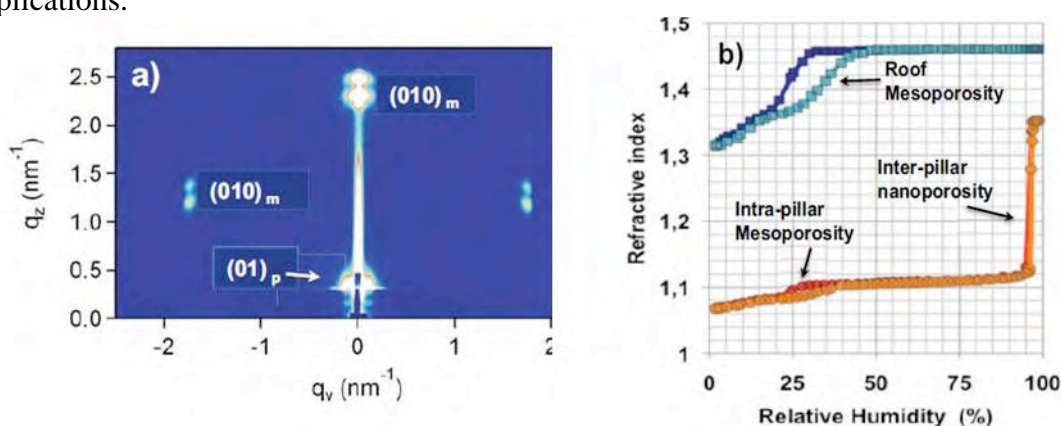


Figure 3. a) GI-SAXS pattern of a p6m mesoporous (CTAB templated) 100% SiO₂ PPN. b) displays the adsorption/desorption isotherms of the p6m mesoporous roof top-layer (blue) and pillared underneath layer (orange) corresponding to the variation of refractive index upon water vapour exposure.

References:

- [1] M. Faustini, M. Vayer, B. Marmiroli, M. Hillmyer, C. Sinturel, H. Amenitsch and D. Grosso; Bottom-up approach towards titanosilicate mesoporous Pillared Planar Nanochannels (PPNs) for nanofluidic applications; Chem. Mater. In press
- [2] M. Vayer, M. A. Hillmyer, M. Dirany, G. Thevenin, R. Erre and C. Sinturel; Perpendicular orientation of cylindrical domains upon solvent annealing thin films of polystyrene-b-poly(lactide); Thin Solid Films 518, 3710–3715 (2010)
- [3] C. Sanchez, C. Boissière, D. Grosso, C. Laberty and L. Nicole; Chem. Mater.; 20 (3), 682–737 (2008).
- [4] M. Faustini, B. Louis, P. A. Albouy, M. Kuemmel and D. Grosso; Preparation of Sol–Gel Films by Dip-Coating in Extreme Conditions; J. Phys. Chem. C, 114 (17), 7637–7645 (2010)
- [5] C. Boissiere, D. Grosso, S. Lepoutre, L. Nicole, A. Brunet Bruneau, and C. Sanchez; Porosity and Mechanical Properties of Mesoporous Thin Films Assessed by Environmental Ellipsometric Porosimetry; Langmuir 21, 12362–12371 (2005)

FORMATION OF THIN $\text{Cu}_2\text{ZnSnS}_4$ LAYERS– A TIME RESOLVED X-RAY SCATTERING STUDY

A. Fischereder^{1,2}, T. Rath^{1,2}, M. Edler^{1,2}, H. Amenitsch³, G. Trimmel^{1,2}

- 1.) Institute for Chemistry and Technology of Materials, Graz University of Technology, Stremayrgasse 9, 8010, Graz, Austria
- 2.) Christian Doppler Laboratory for Nanocomposite Solar Cells
- 3.) Institute of Biophysics and X-ray Structure Research, Austrian Academy of Sciences, Schmiedlstr. 6, A-8042 Graz, Austria

Copper zinc tin sulfide ($\text{Cu}_2\text{ZnSnS}_4$, CZTS) is a very promising alternative to semiconductors based on Ga or In as solar absorber material. CZTS consists of abundant and cheap elements and in addition it displays very beneficial properties like a high optical absorption coefficient [1] and an ideal band gap [2] for photovoltaic applications.

To gain a better insight into the early stages of the formation of CZTS films and to determine the temperature at which the thermally induced precursor decomposition and transformation to CZTS starts, we performed an in situ time- and temperature-resolved synchrotron X-ray analysis.

Therefore, simultaneous 2D grazing incident small angle X-ray scattering (GISAXS) between 0.1 and 3.1 nm^{-1} , and 1D grazing incident wide angle X-ray scattering (GIWAXS) measurements in the angular range 2θ between 21.1° and 41.8° were performed at the Austrian SAXS Beamline 5.2L of the electron storage ring ELETTRA (Italy), using an X-ray energy of 8 keV. The glass/ITO/precursor-substrates were placed in a custom made sample cell with a grazing angle of about 0.18° and were heated from 40 °C up to 180 °C at a heating rate of approx. 8 °C/min in vacuum. During the temperature scan, data were recorded with 5 s and 10 s resolution for GISAXS and GIWAXS, respectively.

GIWAXS patterns collected during the thermally induced conversion of a precursor film containing the metal precursors and the sulfur source are shown in Figure 1. The evolving peak at approx. 28° can be interpreted as the (112) reflection of the kesterite structure of CZTS. This reflection starts to evolve at approximately 105 °C, hence the thermal onset for the formation of CZTS can be assigned to this temperature.

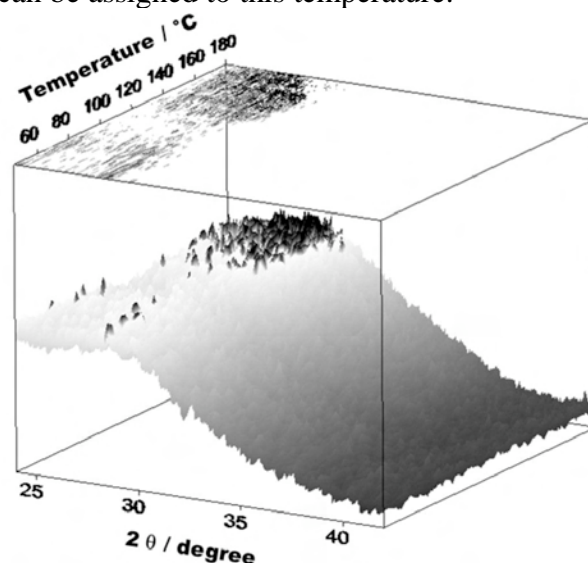


Figure 1. Typical GIWAXS patterns obtained during heating of a precursor film from 40 °C to 180 °C with a heating rate of 8 °C/min showing the (112) reflection of kesterite type CZTS

To probe the internal nanostructure of the films in situ GISAXS patterns were taken simultaneously with the GIWAXS measurements. Typical results are shown in panels a and b in Figure 2 taken at ambient temperature and at 165 °C, respectively.

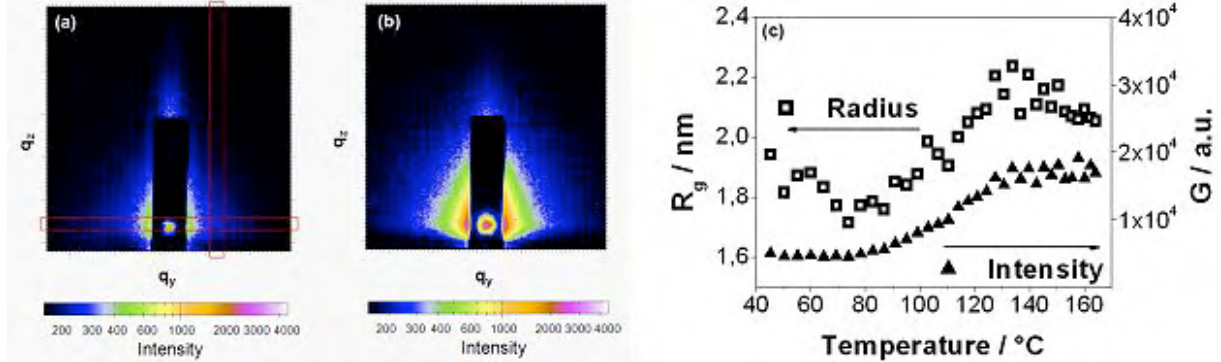


Figure 2. GISAXS patterns at (a) room temperature and (b) at 165 °C. The squares indicate the vertical and horizontal areas for integration (in-plane and out-of-plane scattering). Evolution of the Guinier prefactor G (intensity) and radius of gyration R_g during the heating run (c).

The growth of the nanostructures as well as the increase of surface roughness which occurs in both directions (in-plane and out-of-plane) can be paralleled with the decomposition of TAA and TAA-complexes and the following growth of the CZTS crystallites observed in the GIWAXS data. For quantification, the out-of-plane data have been analyzed in detail, and therefore, have been fitted with a generalized unified Guinier-exponential/power-law function [3] with polymeric constraint, in which additionally a Porod term accounting for the surface roughness and large inhomogeneities was included. The whole equation writes as

$$GISAXS(q_y, q_z) = G \cdot \exp\left(-\left(\frac{q^2 \cdot R_g^2}{3}\right)\right) + \frac{2 \cdot G}{R_g^2} \cdot \left\{ \left[\operatorname{erf}\left(\frac{q \cdot R_g}{\sqrt{6}}\right) \right]^3 / q \right\}^p + \frac{C_{por}}{q^{p_{por}}}$$

in which q stands for the scattering vector calculated with $\sqrt{q_y^2 + q_z^2}$.

The scattering vectors in-plane and out-of-plane are denoted with q_y and q_z , correspondingly. G denotes the Guinier prefactor and R_g the radius of gyration. The parameters C_{por} and P_{por} , determine the power-law contribution of the surface roughness and large inhomogeneities. Interestingly there is only an increase of the radius of gyration R_g from 1.7 to 2.1 nm, which demonstrates that the structural morphology of the TAA and TAA-complexes is similar to the final CZTS powder. The determined Guinier prefactor G over temperature quantifies the qualitative behavior as expected from GIWAXS and in- and out-of-plane GISAXS and manifests the increase of the electron density contrast and particle numbers caused by the CZTS formation.

A more detailed analysis of the CZTS formation was recently published in Chemistry of Materials [4].

References:

- [1] K. Ito, T. Nakazawa; Electrical and optical properties of stannite-type quaternary semiconductor thin films; Jpn. J. Appl. Phys. 27, 2094-2097 (1988)
- [2] T. Todorov, M. Kita, J. Carda, P. Escribano; Cu₂ZnSnS₄ films deposited by a soft-chemistry method; Thin Solid Films 517, 2541-2544 (2009)
- [3] G. Beaucage; Approximations leading to a unified exponential/power-law approach to small-angle scattering; J. Appl. Crystallogr. 28, 717-728 (1995)
- [4] A. Fischereder, T. Rath, W. Haas, H. Amenitsch, J. Albering, D. Meischler, S. Larissegger, M. Edler, R. Saf, F. Hofer, G. Trimmel; Investigation of Cu₂ZnSnS₄ Formation from Metal Salts and Thioacetamide; Chem. Mater. 22, 3399-3406 (2010)

SELF-ASSEMBLY OF SHAPE CONTROLLED HIERARCHICAL POROUS THIN FILMS: MESOPORES AND NANOBXES

L. Malfatti¹, P. Falcaro², D. Marongiu¹, M. F. Casula³, H. Amenitsch⁴ and P. Innocenzi¹

- 1.) Laboratorio di Scienza dei Materiali e Nanotecnologie (LMNT), CR-INSTM, D.A.P., Università di Sassari, Palazzo Pou Salid, Piazza Duomo 6, 07041 Alghero SS, Italy
- 2.) CSIRO Materials Science & Engineering, Gate 5 Normanby Road, Clayton VIC 3168, Australia
- 3.) Dipartimento di Scienze Chimiche, Università di Cagliari, S.S. 554 bivio per Sestu, 09042 Monserrato CA, Italy
- 4.) Institute of Biophysics and Nanosystems Research, Austrian Academy of Sciences, Schmiedlstrasse 6, 8042, Graz, Austria

Self-assembly of materials through evaporation of a solvent is a versatile route to obtain different classes of organized matter at a nanoscale. On the ground of design of mesoporous materials, evaporation induced self-assembly (EISA) drives the formation and organization of micelles that act as the templates of mesopores. The final topology and organization of the pores is governed by the dimension and mesostructural order of the micelles; removal of the template leaves an ordered porous structure. A step ahead to the construction of complex materials is achieving hierarchical porosity, with the possibility to integrate different functions at the different length scales of the pores. Several strategies to fabricate hierarchical porous materials through self-assembly can be envisaged, but they basically rely on the capability of using templates of different dimensions which are able to organize during solvent evaporation. We have developed an alternative route to hierarchical nanoporous films through EISA and controlled crystallization of an inorganic salt. The idea is that the formation of salt nanocrystals acting as a porogen agent can be driven by evaporation of the solvent. The final material appears as a porous hierarchical film with two ranges of porosities, an ordered array of mesopores, and random distribution of cubic “nanoboxes” from the salt nanocrystals. The removal of the two types of templates can be obtained selectively; block copolymers are eliminated by thermal treatment and salt nanoboxes are removed by a simple water washing of the film.

Hybrid organic-inorganic silica mesostructured films have been deposited through EISA from a precursor sol containing methyltriethoxysilane (MTES) and tetraethoxysilane (TEOS) as the silica source alkoxides, following a protocol previously reported [1]. This sol allows preparing hybrid organic-inorganic films that exhibit a strong capability to form highly organized mesostructures using both ionic or block copolymer surfactants [1,2]. To form cubic-shaped templates during film deposition, an aqueous salt solution of NaCl and Na₂HPO₄ has been added to the MTES-TEOS sol. We have prepared a set of different samples changing the relative salt concentrations as reported in Table 1.

[NaCl]	[Na ₂ HPO ₄]	Pore shape
0.49	32·10 ⁻³	Mesopores
0.49	45.5·10 ⁻³	Mesopores
0.49	54·10 ⁻³	Mesopores
0.7	32·10 ⁻³	Mesopores
0.7	45.5·10 ⁻³	Mesopores + nanoboxes
0.7	54·10 ⁻³	Mesopores + nanoflakes
0.84	32·10 ⁻³	Mesopores and salt precipitates on film surface
0.84	45.5·10 ⁻³	Mesopores and salt precipitates on film surface
0.84	54·10 ⁻³	Mesopores + nanoboxes

Table 1. Summary of the films prepared with the different salt concentrations and the structures that have been observed.

GI-SAXS have been used to study the MTES-TEOS films after firing at 350°C; we have observed diffraction spots that have been attributed to the formation of an organized cubic mesophase. All the samples observed have shown the formation of ordered mesopores with similar mesophase symmetry; clearly the addition into the precursor sol of the salts does not interfere with the EISA process during the film deposition. The patterns have been assigned to a cubic symmetry mesostructure (body centered cubic, $Im\bar{3}m$ in the space group) with the (110) plane oriented perpendicular to the substrate (z direction), uniaxially distorted [3]. Following this attribution, the interplanar distances of the samples with 0.7 M NaCl and $45.5 \cdot 10^{-3}$ M Na_2HPO_4 , have been calculated to be $d_{1-10} = (16.7 \pm 1.8)$ nm and $d_{110} = (13.7 \pm 2)$ nm (Figure 1). Similar d -spacing values have been obtained from the other samples.

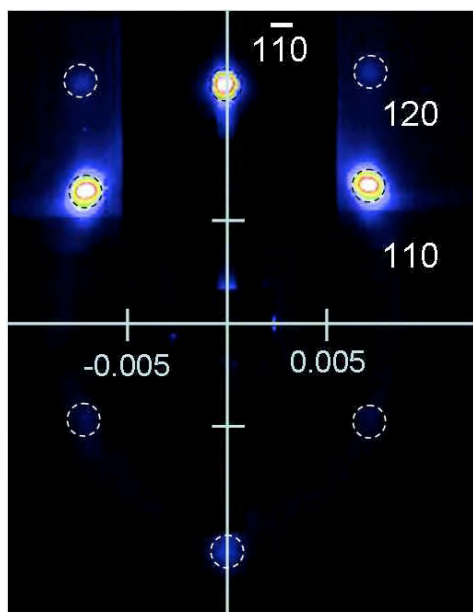


Figure 1. GISAXS pattern of a mesoporous hybrid thin film (sample 0.7 M NaCl – $45.5 \cdot 10^{-3}$ M Na_2HPO_4) after thermal treatment at 350°C. Indexation of the body centered cubic mesophase is shown in the figure.

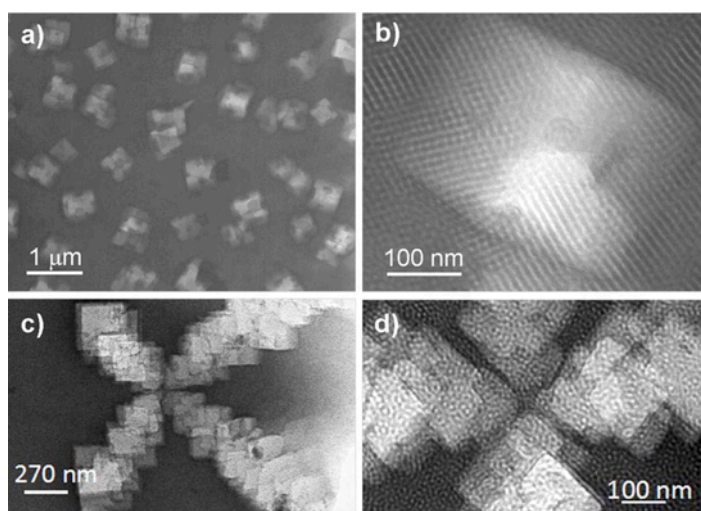


Figure 2. TEM images at different magnifications of the hierarchical porous films obtained with different salt concentrations in the sol: 0.7 M NaCl – $45.5 \cdot 10^{-3}$ M Na_2HPO_4 (a and b), 0.7 M NaCl – $54 \cdot 10^{-3}$ M Na_2HPO_4 (c and d).

TEM analysis on the samples fired at 350°C has revealed the presence of different types of nanoscale structures that appear spherical and cubic, as shown in Figures 2a and b.

The thermal calcination removes the templating organic micelle formed by the block copolymer leaving a porous organized structure with mesopores of spherical appearance and dimensions of (6.3 ± 0.6) nm; they self-organize into a cubic structure by EISA during film deposition. At the same time, the salts added in the precursor solutions allow forming another nanostructure which appears as a cubic “nanobox” of larger dimensions, in the range of 100 – 280 nm. XRD measurements have allowed to identify these structure as NaCl nanocrystals (not shown in Figures). Among those reported in Table 1, some specific compositions allow forming NaCl nanocrystals, while only in one case (sample 0.7 M NaCl – $54 \cdot 10^{-3}$ M Na_2HPO_4) a very peculiar “flake-like” nanostructure is obtained (Figures 2c and d). In the other samples, the formation of white salt precipitates on the film surface is observed.

The final material appears as a porous hierarchical film with two ranges of porosities, an ordered array of mesopores, and cubic nanoboxes from the salt nanocrystals. The samples

allow a selective functionalization of the nanopores through a controlled multistep process: in a first step the films can be fired in air at 350°C to remove the block copolymer template and therefore empty the mesopores; then, in a second step the films can be washed by water and then dried; this process allows eliminating the salt, leaving empty nanoboxes. The advantage of the presented procedure is given by the selective control of nanopore shaping and formation through film processing, this approach opens the route towards a new generation of hierarchical porous materials.

References:

- [1] P. Falcaro, S. Costacurta, G. Mattei, H. Amenitsch, A. Marcelli, M. Cestelli Guidi, M. Piccinini, A. Nucara, L. Malfatti, T. Kidchob and P. Innocenzi; *J. Am. Chem. Soc.*, 127, 3838-3846, (2005)
- [2] (a) De Theije, F. K.; Balkenende, A. R.; Verheijen, M. A.; Baklanov, M. R.; Mogilnikov, K. P.; Furukawa, Y. *J. Phys. Chem. B.* 2003, 107, 4280. (b) Balkenende, A. R.; de Theije, F. K.; Kriege, J. C. K. *Adv. Mater.* 2003, 15, 139
- [3] Innocenzi, P.; Malfatti, L.; Kidchob, T.; Falcaro, P.; Costacurta, S.; Guglielmi, M.; Mattei, G.; Amenitsch, H. *J. Synch. Rad.* 2005, 12, 734

SAXS STUDY OF CHROMONIC BEHAVIOUR OF COPPER-PHTHALOCYANINE DYE

A.Masters¹, M. Sinyureva¹, and G.J.T. Tiddy¹

School of Chemical Engineering and Analytical Science, the University of Manchester, Sackville Street, M60 1QD, Manchester, UK

Chromonic liquid crystals [1] are formed when compounds with disc-like or plank-like molecular shapes are dispersed in water. Even in dilute solutions they have a strong tendency to aggregate into stacks, which become ordered to give liquid crystals at higher concentrations. These liquid crystals occur widely in aqueous dispersions of many formulated products such as pharmaceuticals [2] and the dyes used in inkjet printing [3]. More generally, these liquid crystals occur with nucleic acids, and hence are of fundamental importance for biological systems. We propose a quantitative study to uncover the factors that determine the occurrence and properties of this class of mesophases in a combined experimental and theoretical investigation. The results are relevant to both the ink-jet and pharmaceutical industries, in which small structural differences often result in unwanted aggregation of the molecules, rendering promising new formulations useless.

Typically the compounds contain a central aromatic region surrounded by hydrophilic ionic or hydrogen-bonding solubilising groups. The driving force for aggregation is thought to be mainly enthalpic, resulting from strong attractive dispersion forces between the aromatic systems and also, in some case, from unlike charge attractions between ionic groups on the periphery. The phase behaviour is rich [1]. Both layer and columnar phases are known. In general, two chromonic phases are encountered for columnar aggregated structures: a fairly concentrated Col_h phase with its hexagonal array of molecular stacks, and a more dilute N_{col} (nematic) phase, which is a nematic array of aligned stacks with no positional ordering.

The stacks are reported to have various molecular arrangements, varying from single molecules to water-filled circular hollow chimneys, made out of a number of intertwined helical stacks [3]. For some systems there is a distinct first-order boundary between the N_{col} and Col_h phases, whilst for others the transition between them appears to be more gradual [1].

The aggregate structure of studied Cu-phthalocyanine dye was investigated using both small angle and wide angle X-ray scattering (SAXS and WAXS, respectively). Calculations from the XRD data along with the density measurements allow us to conclude that the column is comprised of unimolecular dye stacking.

The interesting observation is that the sharpness of the first order reflection gradually changes as the temperature is raised (Figure 1), which might be an indication of the gradual transition from hexagonal to nematic phase, i.e. weak first or second order rather than strongly first order.

Our attention was focused on the phase transition from hexagonal to nematic, which was investigated over the temperature range 5 - 21°C at 0.5°C intervals on heating. A potential hypothesis for the observed phenomenon could be accounted for by the transition from hexagonal to nematic in a sequence of at least two subsequent steps via a transitional phase. This intermediate phase occurs as pretransitional phenomenon at the hexagonal – nematic transition on heating, and is composed of the dye stacks connected locally, but not completely coalesced clusters. Therefore, the nematic phase on hexagonal – nematic transition can be

seen as fragmented hexagonal phases with long range nematic order of congregates with local hexagonal order, which results in a continuous structural transition from the hexagonal phase at lower temperatures to a nematic phase at higher temperature.

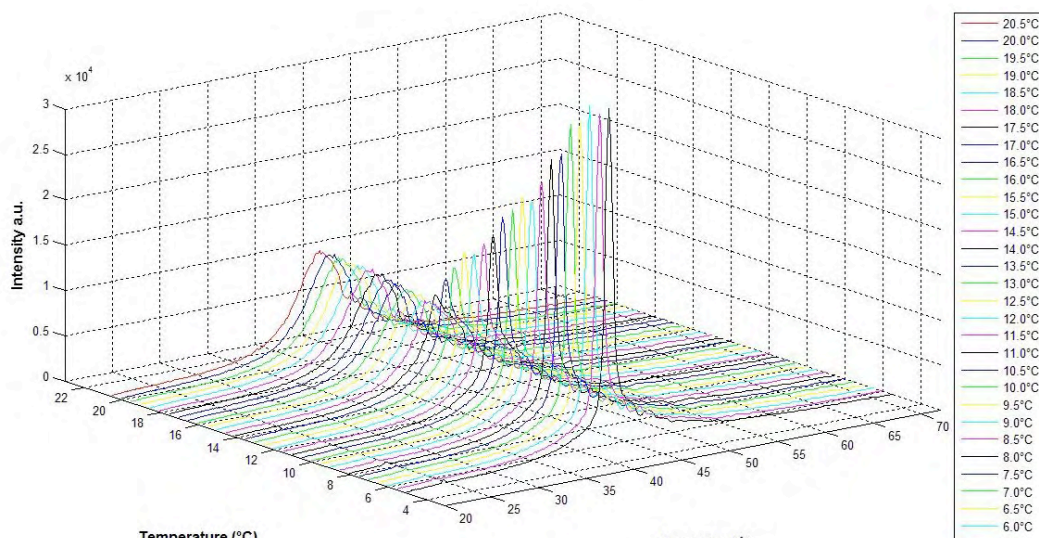


Figure 1. 3D Small-angle X-ray diffraction patterns for Cu-Phthalocyanine dye 29% wt/wt% at the range of temperatures 5 – 20.5°C at 0.5°C intervals.

References:

- [1] J. E. Lydon, Ch. 18, Handbook of Liquid Crystals, Vol. 2B, eds. D. Demus, J. Goodby, G. W. Gray, H.-W. Spiess and V. Vill, Wiley VCH, 1998. J. Lydon, *Curr. Opin. Colloid Interface* 1998, 3, 458. J. Lydon, *Curr. Opin. Colloid Interface* 2004, 8, 480
- [2] K. Mundy, J. C. Sleep and J. E. Lydon, *Liq. Cryst.* 1995, 19, 107
- [3] V. R. Horowitz, L. A. Janowitz, A. L. Modic, P. A. Heiney and P. J. Collings, *Phys. Rev. E* 2005, 72

REAL TIME STUDY OF THE FORMATION OF ZINC SULFIDE NANOPARTICLES

T. Rath^{1,2}, A. Pein^{1,2}, A. Fischereider^{1,2}, W. Haas^{2,3}, H. Amenitsch⁴, G. Trimmel^{1,2}

- 1.) Institute for Chemistry and Technology of Materials, Graz University of Technology, Stremayrgasse 9, 8010, Graz, Austria
- 2.) Christian Doppler Laboratory for Nanocomposite Solar Cells
- 3.) Institute for Electron Microscopy and Fine Structure Research, Graz University of Technology, Steyrergasse 17, 8010 Graz, Austria
- 4.) Institute of Biophysics and X-ray Structure Research, Austrian Academy of Sciences, Schmiedlstr. 6, A-8042 Graz, Austria

Nanocrystalline semiconductors are interesting for many scientists because of their unique size-dependent optical and electronic properties that differ significantly from their bulk characteristics. At the one hand, semiconductor nanoparticles provide the possibility to study fundamental properties of semiconducting nanoparticles and on the other hand, they have a high potential in many different technological applications, e.g. as photonic crystals or in optoelectronic devices. One versatile route for preparing nanoparticles of PbS, ZnS, CdS, and MnS was developed by Joo et al. using elemental sulfur, trioctylphosphine oxide (TOPO) and oleylamine as reagents [1,2]. This synthesis route yields nanoparticles in the range from 5 to 40 nm.

We investigated a colloidal synthesis route for zinc sulfide nanoparticles starting from a zinc salt and elemental sulfur dissolved in a long chained amine (oleylamine). The formation of the nanoparticles was induced by mild thermal treatment. In this regard we analyzed the nanoparticle growth with time resolved WAXS measurements. Especially influences of temperature, reaction time and concentration of the sulfur source were investigated.

The nanoparticle synthesis was done in a reaction vessel and a small amount of the reaction mixture (4.5 w% of nanoparticles in solution) was pumped through the measuring cell (flow through capillary) and back to the reaction vessel continuously [3] with a flow rate of 5 mL/min. So the WAXS-signals could be detected with a 1D gas detector with good time resolution.

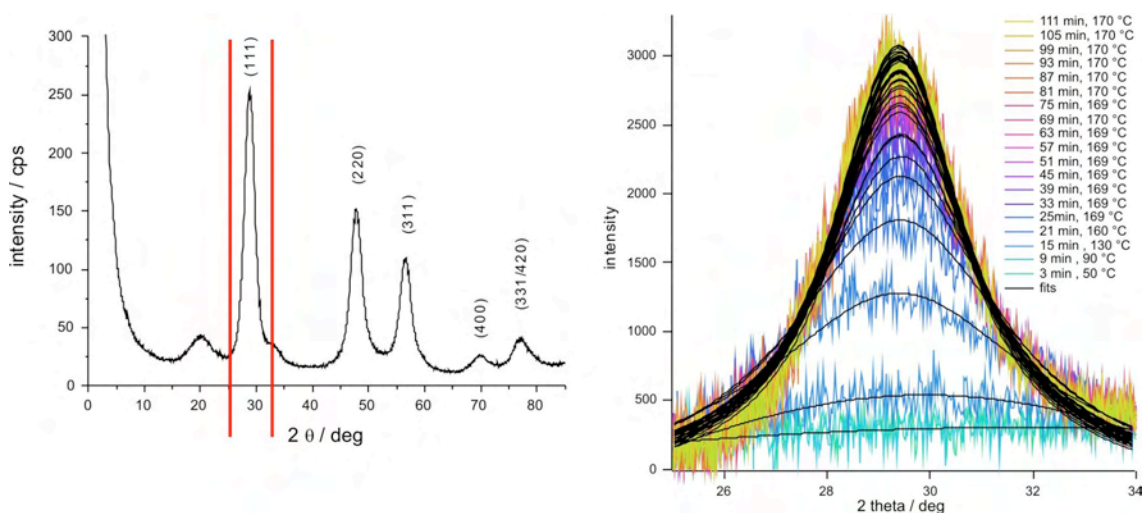


Figure 1. X-ray pattern of ZnS nanoparticles (left) and time resolved WAXS analysis of the evolution of the (111) peak

In Fig. 1 the X-ray diffraction pattern of ZnS nanoparticles and the time resolved WAXS analysis of the (111)- peak of the ZnS nanoparticles (reaction temperature 170°C, amount of sulfur source: 3 eq.) is presented. It can be clearly seen that the (111) - peak of ZnS at 28 ° 2θ starts to evolve after 15 min reaction time at about 130°C. We assume that the main part of

the material has cubic sphalerite structure but due to the fact that this peak is very broad ($26 - 31^\circ 2\theta$), it is difficult to analyze exactly if the prepared ZnS nanoparticles have cubic sphalerite or hexagonal wurtzite structure.

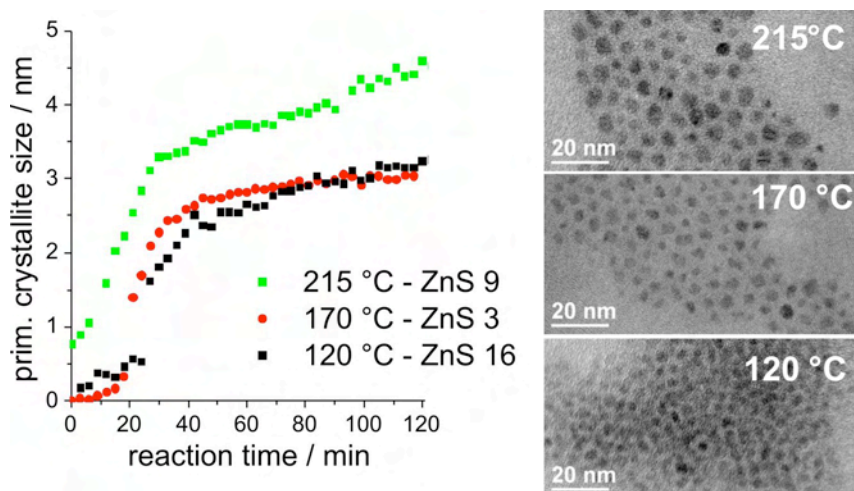


Figure 2. Primary crystallite size vs. reaction time at three different reaction temperatures (215 °C, 170 °C and 120 °C) and the corresponding TEM-images of the prepared nanoparticles after a reaction time of 120 min

Fitting of the WAXS-peaks with Lorentz function and estimation of the primary particle size with Scherrer equation shows that the growth of the nanoparticles follows a sigmoidal curve (see Figure 2). The growth starts after a reaction time of about 15 min (130°C), until a reaction time of about 30 - 40 min (approx. 170°C) the particles grow fast, and then the growth rate decreases. The nanoparticles prepared at 215 °C reach a particle size of about 4.5 nm which is significantly higher than the size of the nanoparticles prepared at 120 °C and 170°C, which is about 3 nm. This behavior is confirmed by TEM images (215°C: ~ 5 nm; 170°C: 3 - 3.5 nm; 120°C: 3 - 3.5 nm) which are also depicted in Figure 2.

References:

- [1] J. Joo, H.B. Na, T. Yu, J.H. Yu, Y.W. Kim, F.X. Wu, J.Z. Zhang, T. Hyeon; Generalized and facile synthesis of semiconducting metal sulfide nanocrystals; *J. Am. Chem. Soc.* 125, 11100-11105 (2003)
- [2] S. G. Kwon, T. Hyeon; Colloidal Chemical Synthesis and Formation Kinetics of Uniformly Sized Nanocrystals of Metals, Oxides, and Chalcogenides; *Acc. Chem. Res.* 41, 1696-1709 (2008)
- [3] P. Agren, M. Linden, J. B. Rosenholm, R. Schwarzenbacher, M. Kriechbaum, H. Amenitsch, P. Laggner, J. Blanchard, F. Schüth; Kinetics of Cosurfactant–Surfactant–Silicate Phase Behavior. 1. Short-Chain Alcohols; *J. Phys. Chem. B* 103, 5943-5948 (1999)

THERMALLY-INDUCED MESOSTRUCTURE FORMATION OF POLYMER RESIN-SURFACTANT COMPOSITES IN CONFINED ENVIRONMENTS

J. Schuster¹, R. Köhn¹, A. Keilbach¹, M. Döblinger¹, H. Amenitsch² and T. Bein¹

1.) Department of Chemistry and Biochemistry and Center for NanoScience (CeNS) University of Munich, Butenandtstraße 5-13 (E), 81377 Munich, Germany

2.) Institute of Biophysics and Nanosystems Research, Austrian Academy of Sciences Schmiedlstraße 6, 8042 Graz, Austria

Meng et al. [1] introduced a synthesis procedure for mesoporous carbon powders with variable structures and high surface areas. Recently, we were able to extend this approach to confined environments, as thin films [2] and in the channels of anodic alumina membranes. The mesostructured phases were obtained by evaporation-induced organic-organic self-assembly of a preformed resol precursor and the triblock copolymer templates Pluronic P123 and F127, followed by thermal treatments for thermopolymerization of the precursor, template removal and carbonization. Our in situ GISAXS measurements revealed that the structure formations occur during thermopolymerization and that the kinetics depend strongly on the processing temperatures. Structural changes during template removal and carbonization at temperatures up to 1100 °C in inert atmosphere could also be followed.

In-Situ GISAXS of Thin Films

2D-hexagonal (plane group, $p6mm$) mesoporous carbon thin films were obtained through evaporation-induced organic-organic self-assembly of a preformed oligomeric resol precursor and the triblock copolymer template pluronic P123 [1]. The carbon films were prepared on substrates by spin-coating a mixture of precursor and surfactant in ethanol. The thermopolymerization was followed in-situ during heating at variable temperatures of 90 °C to 180 °C. The thermally-induced structure formation at 100 °C is depicted in Figure 1.

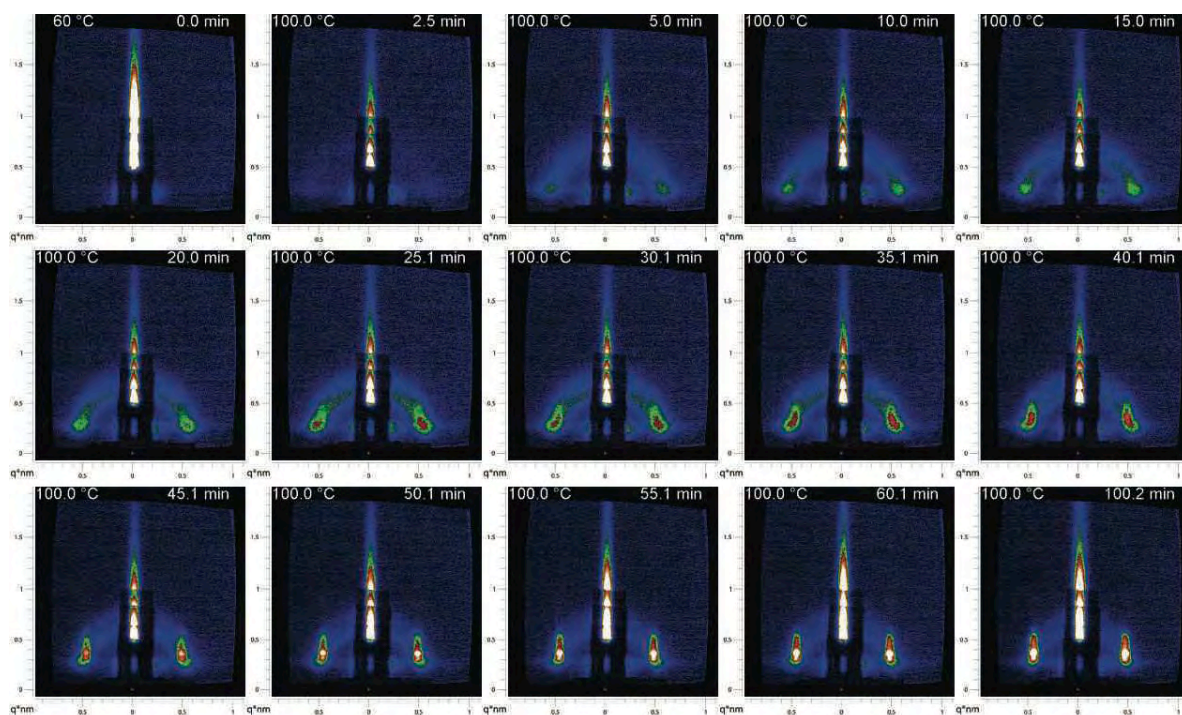


Figure 1. In-situ GISAXS measurement of the structure formation of a hexagonal thin film during heating at 100 °C.

Until 15 minutes after start only a diffuse ring and Yoneda peaks become visible, due to an evolving mesostructure, which is oriented randomly at that stage. During continued heating up to 40 min after start, the evolution of distinct peaks related to an oriented hexagonal mesostructure occurs. After 60 minutes, the peaks became more distinct and their intensity increased, but no further structural changes were visible.

In-Situ SAXS in Anodic Alumina Membranes

Cubic and circular hexagonal mesoporous carbon phases in the confined environment of anodic alumina membranes (AAM) pores were obtained by organic-organic self-assembly of a preformed oligomeric resin precursor and the triblock copolymer templates Pluronic F127 or P123, respectively. Casting and solvent-evaporation were followed by self-assembly and the formation of a condensed wall material by thermopolymerization of the precursor oligomers, resulting in mesostructured phenolic resin phases. The thermopolymerization could also be followed in-situ during heating at temperatures of 90°C to 180°C. The thermally-induced structure formation at 130°C of a circular hexagonal mesostructure is illustrated in Figure 2.

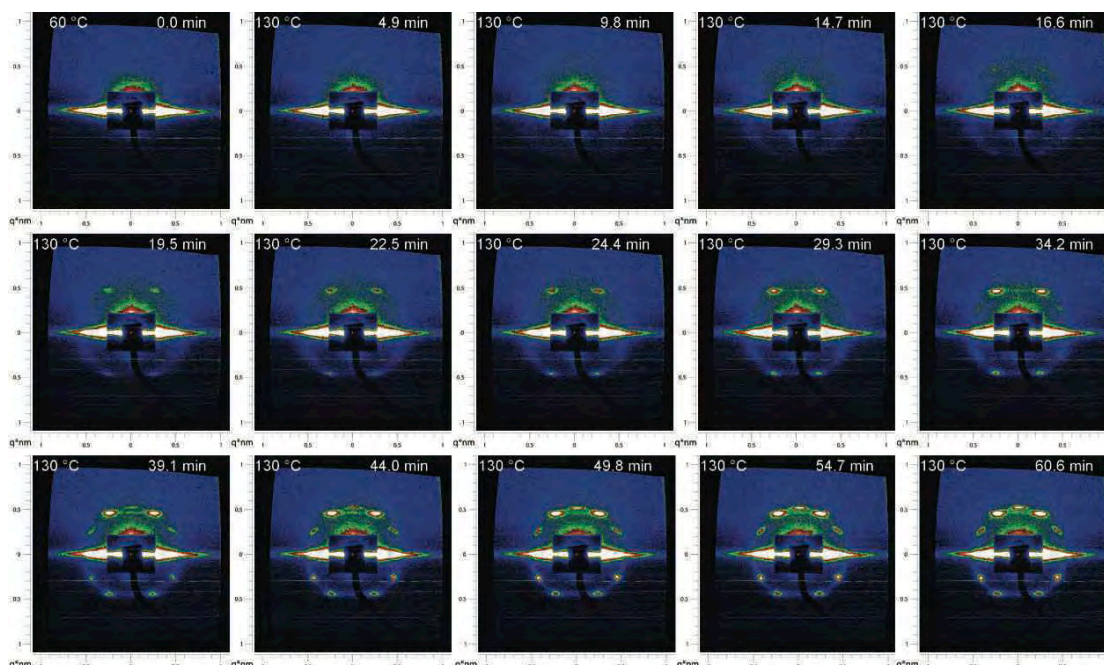


Figure 2. In-situ SAXS measurement of the structure formation of a circular hexagonal phase in an anodic alumina membrane during heating at 130°C

After 15 minutes the first peaks related to a circular hexagonal structure start to appear. A diffuse ring related to a random orientation is also visible, thus some parts are oriented randomly while others already show the final orientation. Upon further heating the intensity of the reflections increases, the structure is becoming completely circular hexagonal. Surprisingly some additional peaks appear after 39 min corresponding to a hexagonally ordered top-layer on the membrane. The delay of the structure formation of this top-layer in relation to the mesostructured phases in the membrane pores is not clear yet.

References:

- [1] Y. Meng, D. Gu, F. Zhang, Y. Shi, L. Cheng, D. Feng, Z. Wu, Z. Chen, Y. Wan, A. Stein and D. Zhao; A Family of Highly Ordered Mesoporous Polymer Resin and Carbon Structures from Organic-Organic Self-Assembly, *Chem. Mater.* 18 (18), 4447-4464 2006
- [2] J. Schuster, R. Köhn, A. Keilbach, M. Döblinger, H. Amenitsch and T. Bein; Two-Dimensional-Hexagonal Periodic Mesoporous Polymer Resin Thin Films by Soft Templating; *Chem. Mater* 21 (24), 5754-5762, 2009

SAXS ANALYSIS OF AN EFFICIENT WATER OXIDATION ELECTROCATALYTIC SYSTEM, BASED ON A CARBON NANOTUBES/ POLYOXOMETALATE COMPOSITE MATERIAL

F. M. Toma^{1,2}, A. Sartorel,³ M. Carraro³, H. Amenitsch⁴, T. Da Ros¹, L. Casalis^{2,5}, G. Scorrano³, G. Scoles², M. Prato¹, M. Bonchio³

- 1.) Center of Excellence for Nanostructured Materials (CENMAT), INSTM and Department of Pharmaceutical Sciences, University of Trieste, P.le Europa 1, 34127 Trieste, Italy
- 2.) SISSA-ELETTRA NanoInnovation Lab, SISSA-ISAS, Via Beirut 2-4, 34151 Trieste, Italy
- 3.) ITM-CNR and Department of Chemical Sciences, University of Padova, via Marzolo 1, 35131 Padova, Italy
- 4.) Institute of Biophysics and Nanosystems Research, Austrian Academy of Sciences, Schmiedlstr. 6, 8042-Graz, Austria
- 5.) Sincrotrone Trieste ScpA, SS14 Km 163,5 Area Science Park, Basovizza, 34149 Trieste, Italy

The dream-goal of energy research is to transpose the photosynthetic process into an artificial device, where the catalytic splitting of H₂O is finalized to the continuous production of oxygen (O₂), and hydrogen (H₂). Due to the high overpotential usually occurring, the crucial reaction to be efficiently carried out is the half-cell reaction $O_2 + 4 H^+ + 4 e^- \leftrightarrow 2 H_2O$ [1]. To this aim, very efficient and stable nano-structured, oxygen-evolving, anodes (OEAs) have been obtained by the assembly of a ruthenium-based catalyst with a conducting bed of multiwalled carbon nanotubes (MWCNTs) (Figure 1a). The catalyst is an inorganic and highly robust tetraruthenate cluster, stabilized by two polyoxometalate (POM) units, $M_{10}[Ru_4(H_2O)_4(\mu-O)_4(\mu-OH)_2(\gamma-SiW_{10}O_{36})_2]$ (M₁₀1, M = Cs, Li) [2,3], where the four Ru^{IV}-H₂O groups are able to mediate the $4e^-/4H^+$ overall process, through a sequential electron and proton loss in a relatively narrow potential range [4,5]. Our approach may improve the electrical contact between the redox active center and the surface of the electrode using MWCNTs. The latter serve as conductive nanowire scaffolds to provide heterogeneous support to **1** (controlling the morphology and increasing the surface area of the resulting nano-structured hybrid material) and to funnel the sequential electron-transfer to the electrode, favoring energy dispersion and relieving catalytic fatigue. To this purpose, water soluble MWCNTs decorated with polyamidoamine (PAMAM) ammonium dendrimers, (MWCNT-Dend) have been used to exploit ionic interaction with the polyanionic catalyst [6]. Nanostructured, doped Indium-Thin Oxide (ITO) anodes, obtained upon deposition of the hybrid composite **1**@MWCNT, perform water oxidation with a remarkably reduced overpotential. To get insights on its spectroscopic and morphological features, as well as on the composition and on the distribution of the catalytic domains, the hybrid composite **1**@MWCNT has been characterized by a variety of spectroscopy and microscopy techniques including: resonant Raman (rR), Scanning Transmission Electron Microscopy (STEM), X-ray Dispersive Energy Spectroscopy (XEDS) and high resolution Transmission Electron Microscopy (HRTEM), HiRes STEM.

By means of Small-Angle X-ray Scattering (SAXS), diffraction patterns have been obtained and analyzed for both MWCNT-Dend, and **1**@MWCNT (both at pH = 5.5, 0.5 mg/mL), and compared with the solution behavior of Li₁₀1 in water (pH = 5.5, 1 mg/mL). The scattering pattern observed in solution for Li₁₀1 (upper curve in Figure 1c) and the simulated curve are consistent with the geometry of the isolated POM molecule. The solution study gives a nearest neighbour distance of 6 nm at 50 mg/ml and no indication of aggregation phenomena. Comparison of the experimental curves registered for **1**@MWCNT (Figure 1c, middle trace) and MWCNT-Dend (Figure 1c, bottom trace) shows that, in the observed regime, scattering from **1** dominates with respect to the MWCNT walls. Accordingly, the inorganic oxo-clusters appear to be deposited on the MWCNT surface mainly as single entities (nearest neighbour distance is $d = 1.2$ nm), with a compact distribution driven by the positively charged, terminal

functions of the dendron moiety. This evidence has been confirmed by Z-contrast STEM images of **1**@MWCNT (Figure 1b), showing individually separated molecules of **1**, and it represents a key point to access single-site catalysis approaching the homogeneous behavior.

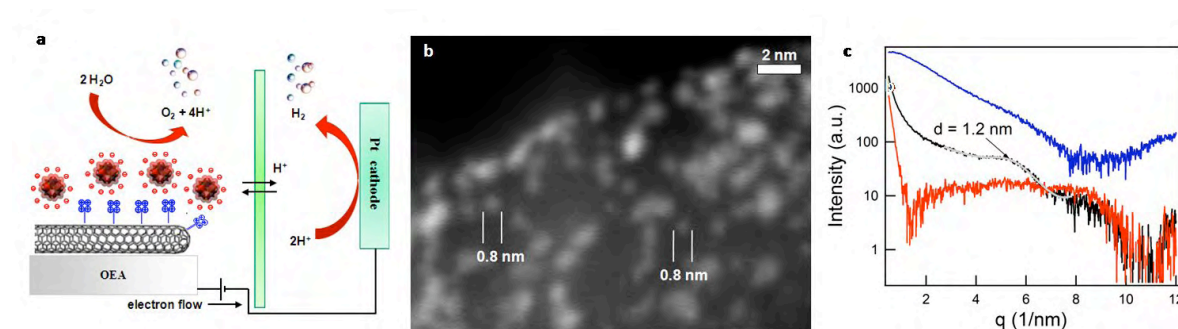


Figure 1. (a) scheme of the water splitting electrocatalytic cell integrating the nanostructured **1**@MWCNT. (b) Z-contrast STEM images where nano-domains (ca. 1 nm) ascribed to **1** yield a brighter contrast due to the presence of W and Ru. (c) SAXS measurements (H₂O, pH = 5.5) of **1**@MWCNT (black curve, 1 mg/mL) and fitting of correlation peak (grey curve) with a d-spacing of about 1.2 nm, MWCNT-Dend (red curve, 1 mg/mL) and **1** (blue curve, 0.5 mg/mL).

The simplest model to be consistent with the geometry of the molecules is a double ellipsoid form factor $F_{2\text{Ellip}}(q)$, in which the two ellipses have been rotated to each other by 90° , with the following dimensions (nm): Main Axis a 0.710 ± 0.001 ; Main Axis b 0.484 ± 0.001 ; Main Axis c 0.516 ± 0.001 ; Distance D 0.061 ± 0.002 .

Moreover, at low q a strong interparticle interference was observed, which has been taken into account using the PKY model for a hard sphere interaction potential as structure factor $S_{\text{HSph}}(q, R_{\text{HSph}}, P_{\text{HSph}})$ [7]. The two parameters describe the radius of the hard interaction potential R_{HSph} and the volume fraction of the scattering centers P_{HSph} . Additionally at very low q values a contribution of the scattering of larger scattering centers was visible, which was approximated by terms corresponding to a Porod slope with free exponent (described by c_{por} and p), as well as a constant background b_{ck} and an intensity scaling parameter I_0 . Therefore the measured intensity is described by the following equation:

$$I_{\text{exp}}(q) = I_0 \cdot S_{\text{HSph}}(q, R_{\text{HSph}}, P_{\text{HSph}}) \cdot |F_{2\text{ellip}}(q)|^2 + \frac{c_{\text{por}}}{q^p} + b_{\text{ck}} \quad (1)$$

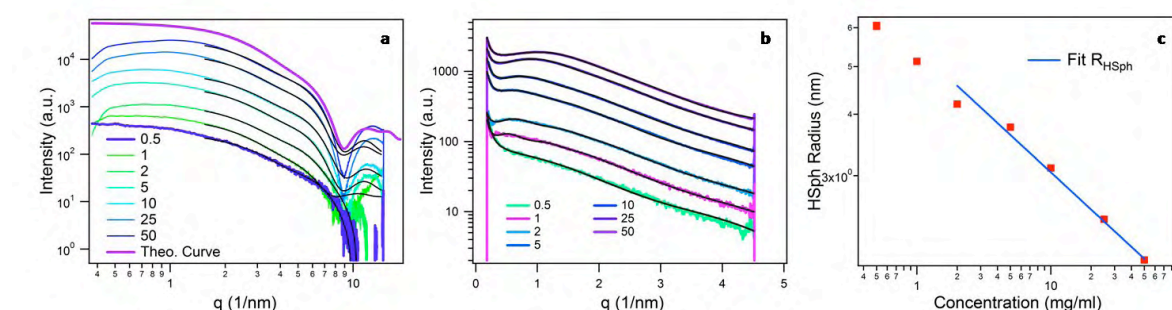


Figure 2. (a) Scattering data of **1** in the WAXS regime with full pattern refinement according to equation 1 only with the contribution of the double ellipsoid model. (b) Scattering data of **1** in the SAXS regime with full pattern refinement according to equation 1. Again the agreement of the fit with the data is remarkable. (c) Plot of the hard sphere interaction radius R_{HSph} vs. concentration c . The scaling law of the $R_{\text{HSph}} \propto c^\alpha$ with $\alpha = 0.25$. The expectation for non interacting molecules is $1/3$.

Further informations about this contribution are found in [8].

References:

- [1] V. Balzani, A. Credi, M. Venturi, *ChemSusChem* 1, 26-58 (2008)
- [2] A. Sartorel, M. Carraro, R. De Zorzi, S. Geremia, N.D. McDaniel, S. Bernhard, G. Scorrano, M. Bonchio, *J. Am. Chem. Soc.* 130, 5006-5007 (2008)
- [3] Y. V. Geletii, B. Botar, P. Kögerler, D. A. Hillesheim, D. G. Musaev, C. L. Hill, *Angew. Chem., Int. Ed.* 47, 3896- 3899 (2008)
- [4] A. Sartorel, P. Miró, E. Salvadori, S. Romain, M. Carraro, G. Scorrano, M. Di Valentin, A. Llobet, C. Bo, M. Bonchio, *J. Am. Chem. Soc.* 131, 16051-16053 (2009)
- [5] F. Liu, J. J. Concepcion, J. W. Jurss, T. Cardolaccia, J. L. Templeton, T. J. Meyer, *Inorg. Chem.* 47, 1727-1752 (2008)
- [6] M. A. Herrero, F. M. Toma, K. T. Al-Jamal, K. Kostarelos, A. Bianco, T. Da Ros, F. Bano, L. Casalis, G. Scoles, M. Prato *J. Am. Chem. Soc.*, 131, 9843-9848, (2009)
- [7] J. S. Pedersen, *Adv Colloid Interface Sci* 70, 171 (1997)
- [8] F. M. Toma, A. Sartorel, M. Iurlo, M. Carraro, P. Parisse, C. Maccato, S. Rapino, B. Rodriguez Gonzalez, H. Amenitsch, T. Da Ros, L. Casalis, A. Goldoni, M. Marcaccio, G. Scorrano, G. Scoles, F. Paolucci, M. Prato, M. Bonchio, *Nature Chem.* 2010, in press

GROWTH OF NANOCRYSTALS: PROBING THE MYTHS AND FACTS

R. Viswanatha,¹ S. Santra,¹ S. Sapra,¹ S. S. Datar,¹ D. D. Sarma,¹ H. Amenitsch,² Y. Zhou,³ S. K. Nayak,³ S. K. Kumar⁴

1.) Solid State and Structural Chemistry Unit, Indian Institute of Science, Bangalore-560012, India

2.) Institute of Biophysics and X-ray Structure Research, Austrian Academy of Sciences, Schmiedlstr. 6, 8042 Graz, Austria

3) Rensselaer Polytechnic Institute, Troy, New York 12180, USA.

4) Department of Chemical Engineering, Columbia University, New York, NY 10027, USA.

Solution growth of nanocrystals has been successfully applied to produce a large array of technologically important and fundamentally interesting systems. Study of growth mode controlling the size and size distribution of these nanocrystals has been the topic of recent interest in the scientific community. For example, recent studies of growth of Pt nanocrystals [1] using TEM have shown the presence of punctuated events like coalescence and other features not commonly considered in the classical growth models. In fact, the detailed studies of the growth of semiconductor and metal nanocrystals in recent times have shown that, in contrast to the common belief, growth of nanocrystals do not commonly occur through the celebrated “Ostwald ripening” process, controlled solely by the diffusion of the reacting species through the solvent.

Ostwald ripening (shown in Fig. 1) is defined as the growth of larger nanocrystals at the cost of smaller nanocrystals and is theoretically modeled using the Lifshitz-Slyozov-Wagner (LSW) theory. Until recently, one of the most extensively used expressions of LSW theory that has led to the misconception of diffusion limited growth is the cubic diameter dependence with time ($d^3 \sim t$). However, it has been shown recently that just $d^3 \propto t$ dependence cannot be used as a complete proof for the growth mechanism [2]. LSW theory not only predicts a dependence of average diameter on time but also the time dependence of the size distribution and the temperature dependence of the rate constant of the reaction. Though the Ostwald ripening is believed to be dominant mode of growth in nanocrystals in the quantum confined regime, there is a surprising dearth of convincing evidence studying the various dependencies to support this common belief.

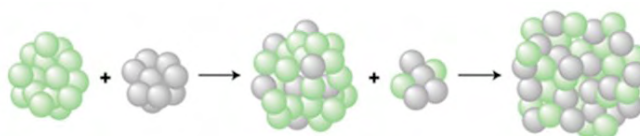


Figure 1. Typical Ostwald ripening behavior in crystal growth.

Recently, we studied the growth of CdS nanocrystals, formed by heating Cadmium acetate and thiourea in dimethyl formamide, using small angle X-ray scattering (SAXS) technique, using the SAXS beamline at Elettra. These data were further corroborated by transmission electron microscopy (TEM), X-ray diffraction studies and UV-absorption measurements. We find that along with a $d^3 \sim t$ dependence of the diameter (Fig. 2a), the slope K of the linear plot at different temperatures (T) follow $K \sim \exp(-E_a/k_B T)$ (Fig. 2b), E_a being the activation energy of the reaction, as predicted by the LSW theory. From this analysis, activation energy of 1.47 eV was obtained. Additionally we have also obtained the size distribution of the nanocrystals as a function of time using the SAXS analysis and shown in Fig. 2c. From these data, the time constants and their dependence on temperature (Fig. 2d) have been established as predicted by the LSW theory. Independent confirmation of the activation energy (1.55

eV) from the size distribution data establishes for the first time, a text-book like example of a pure diffusion dominated growth of nanocrystals with strict adherence to all the predictions of the LSW theory.

To understand the differences at a microscopic level in CdS and other systems like ZnO [2] where the reaction at the surface competed with the diffusion limited process, we carried out ab-initio calculations. These processes reveal the presence of an activated process in ZnO reaction and hence relatively important surface reaction term while CdS follows a non-activated process with the growth of nanocrystals being limited only by the diffusion process. The details of this work can be found in Ref [3].

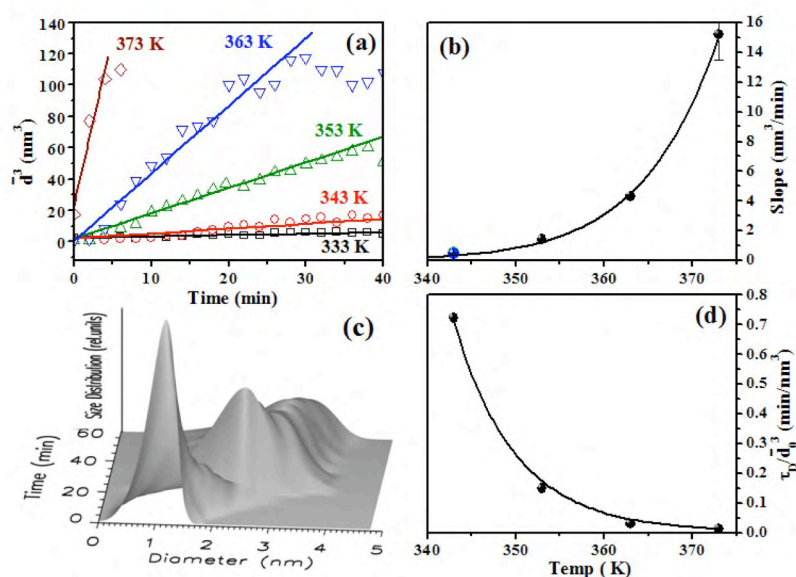


Figure 2. (a) Variation of the cube of diameter of the nanocrystals with time at different temperatures showing a linear dependence. (b) Variation of slope as a function of temperature, the solid line showing the fit obtained to these points. (c) Typical variation of size distribution as a function of time at 343 K. After 20 min, the distributions have been scaled by a factor of 10. (d) The dependence of τ_b/d_0^3 as a function of temperature is plotted.

References:

- [1] H. Zheng, R. K. Smith, Y. Jun, C. Kisielowski, U. Dahmen and A. P. Alivisatos, *Science*, 324 (2009), 1309
- [2] R. Viswanatha, P. K. Santra, C. Dasgupta and D. D. Sarma, *Physical Review Letters*, 98 (2007) 255501
- [3] R. Viswanatha, H. Amenitsch, S. Santra, S. Sapra, S. S. Datar, Y. Zhou, S. K. Nayak, S. K. Kumar and D. D. Sarma, *Journal of Physical Chemistry Letters*, 1 (2010) 304

Publications

Publications in Journals and Reviewed Proceedings 2009

P. Angerer, H. Simunkova, E. Schafner, M. B. Kerber, J. Wosik, G. E. Nauer
Structure and texture of electrochemically prepared nickel layers with co-deposited zirconia nanoparticles
Surf. Coat. Tech. 203, 1438-1443 (2009)

D. C. Arnold, J.M. O'Callaghan, A. Sexton, J.M. Tobin, H. Amenitsch, J.D. Holmes, M.A. Morris
The role of etched silicon channels on the pore ordering of mesoporous silica: The importance of film thickness on providing highly orientated and defect-free thin films
Applied Surface Science 255 (23), 9333-9342 (2009)

Z. Arsov, M. Rappolt, J. Grdadolnik
Weakened hydrogen bonds in water confined between lipid bilayers: The existence of a long-range attractive hydration force
ChemPhysChem 10 (9-10), pp. 1438-1441 (2009)

J. Baldrian, M. Steinhart, H. Amenitsch, S. Bernstorff
Disorder-order-crystalline state transitions of PEO-b-PPO-b-PEO copolymers and their blends: SAXS/WAXS/DSC study
Journal of Macromolecular Science, Part B, Volume 48 (Issue 1), pp. 174-184 (2009)

M. Buljan, I. Bogdanovic-Radovic, M. Karlušić, U. V. Desnica, G. Drazic, N. Radic, P. Dubcek, K. Salamon, S. Bernstorff and V. Holý
Formation of long-range ordered quantum dots arrays in amorphous matrix by ion beam irradiation
Applied Physics Letters 95, 063104-1 - 063104-3 (2009) and
Virtual Journal of Nanoscale Science & Technology, issue of August 24, 2009

M. Buljan, U. V. Desnica, M. Ivanda, N. Radić, and P. Dubček, G. Dražić, K. Salamon, S. Bernstorff, V. Holý
Formation of three-dimensional quantum-dot superlattices in amorphous systems: Experiments and Monte Carlo simulations
Physical Review B 79, art. no. 035310 (2009) and
Virtual Journal of Nanoscale Science & Technology, Volume 19, Issue 4, 2009))

M. Buljan, U. V. Desnica, G. Dražić, M. Ivanda, N. Radić, P. Dubček, K. Salamon, S. Bernstorff and V. Holý
The influence of deposition temperature on the correlation of Ge quantum dot positions in amorphous silica matrix
Nanotechnology 20 (8), art. no. 085612 (6 pages) (2009)

M. Buljan, S.R. C. Pinto, R.J. Kashtiban, A.G. Rolo, A. Chahboun, U. Bangert, S. Levichev, V. Holý, and M.J. M. Gomes
Size and spatial homogeneity of SiGe quantum dots in amorphous silica matrix
Journal of Applied Physics 106 (8), art. no. 084319 (2009)

G. Caracciolo, R. Caminiti, M. A. Digman, E. Gratton, S. Sanchez
Efficient escape from endosomes determines the superior efficiency of multicomponent lipoplexes
Journal of Physical Chemistry 113, 4995–4997 (2009)

- C. Chemin, J.M. Péan, C. Bourgaux, G. Pabst, P. Wüthrich, P. Couvreur, and M. Ollivon
Supramolecular organization of S12363-liposomes prepared with two different remote loading processes
Biochimica et biophysica acta 1788(5), 926-935 (2009)
- G. Cordoyiannis, A. Zidanšek, G. Lahajnar, Z. Kutnjak, H. Amenitsch, G. Nounesis, and S. Kralj
Influence of the Controlled-Pore Glass Confinement on the Layer Spacing of Smectic-A Liquid Crystals
Phys. Rev. E 79, art. no. 051703 (2009)
- V. Faivre, P.L. Bardonnet, P. Boullanger, H. Amenitsch, M., Ollivov, F. Falson
Self-Organization of synthetic cholesteryl oligoethyleneglycol glycosides in water
Langmuir 25 (16), pp. 9424-9431 (2009)
- P. Falcaro, L. Malfatti, T. Kidchob, G. Giannini, A. Falqui, M.F. Casula, H. Amenitsch, B. Marmiroli, G. Greci, P. Innocenzi
Hierarchical Porous Silica Films with Ultralow Refractive Index
Chemistry of Materials 21 (10), pp. 2055-2061 (2009)
- P. Falcaro, L. Malfatti, L. Vaccari, H. Amenitsch, B. Marmiroli, G. Greci, P. Innocenzi
Fabrication of Advanced Functional Devices Combining Soft Chemistry with X-ray Lithography in One Step
Advanced Materials 21 (48), Pages 4932 - 4936 (2009)
- D. Gracin, B. Etlinger, K. Juračić, A. Gajović, P. Dubček and S. Bernstorff
DC conductivity of amorphous-nano-crystalline silicon thin films
Vacuum, Volume 84, Issue 1, Pages 243-246 (2009)
- D. Grozdanić, R. Slunjski, B. Rakvin, P. Dubček, B. Pivac, N. Radić, S. Bernstorff
Structural analysis of amorphous Si films prepared by magnetron sputtering
Vacuum, Volume 84, Issue 1, Pages 126-129 (2009)
- M.R. Hammond, C. Li, C. Tsitsilianis and R. Mezzenga
Hierarchical self-organization in polyelectrolyte-surfactant complexes based on heteroarm star block copolyampholytes
Soft Matter 5, pp. 2371-2377 (2009)
- F. Häußler, J. Tritthart, H. Amenitsch, P. Laggner,
Time-resolved combined SAXS and WAXS studies on hydrating tricalcium silicate and cement
Advances in Cement Research 21 (3), pp. 101-111 (2009)
- A. Keilbach, M. Döblinger, R. Köhn, H. Amenitsch, T. Bein
Periodic Mesoporous Organosilica in Confined Environments
Chem. Eur. J., 15 (27), 6645-6650, 2009
- M.B. Kerber, E. Schafler, A.K. Wiczorek, G. Ribarik, S. Bernstorff, T. Ungar, M.J. Zehetbauer
Synchrotron X-ray line-profile analysis experiments for the in-situ microstructural characterisation of SPD nanometals during tensile deformation
Int. J. Mater. Res. (formerly Z. Metallk.) 100, 770-774 (2009)
- T. Lebold, L. A. Mühlstein, J. Blechinger, M. Riederer, H. Amenitsch, Ralf Köhn, K. Peneva, K. Müllen, J. Michaelis, C. Bräuchle, T. Bein
Tuning Single-Molecule Dynamics in Functionalized Mesoporous Silica
Chem. Eur. J., 15, 1661-1672, (2009)

- S. Lepoutre, J.-H. Småt, C. Laberty, H. Amenitsch, D. Grosso, M.. Lindén
Detailed study of the pore-filling processes during nanocasting of mesoporous films using SnO₂/SiO₂ as a model system
 Microporous and Mesoporous Materials 123 (1-3), 185–192 (2009)
- M. Lončarić, J. Sancho-Parramon, M. Pavlović, H. Zorc, P. Dubček, A. Turković, S. Bernstorff, G. Jakopic, A. Haase
Optical and structural characterization of silver islands films on glass substrates
 Vacuum, Volume 84, Issue 1, 188-192 (2009)
- L. Malfatti, S. Costacurta, T. Kidchob, P. Innocenzi, M. Casula, H. Amenitsch, D. Dattilo, M. Maggini
Mesostructured self-assembled silica films with reversible thermo-photochromic properties
 Microporous and Mesoporous Materials 120, 375–380 (2009)
- L. Malfatti, P. Falcaro, D. Marongiu, M. F. Casula, H. Amenitsch and P. Innocenzi
Self-assembly of shape controlled hierarchical porous thin films: Mesopores and nanoboxes
 Chemistry of Materials 21 (20), pp. 4846-4850 (2009)
- C. Marchini, M. Montani, A. Amici, H. Amenitsch, C. Marianecchi, D. Pozzi and G. Caracciolo
Structural stability and increase in size rationalize the efficiency of lipoplexes in serum *Langmuir* **25**, 3013-3021 (2009)
- P. Mariani, F. Spinozzi, F. Federiconi, H. Amenitsch, L. Spindler, I. Drevensek-Olenik
Small angle X-ray scattering analysis of deoxyguanosine 5'-monophosphate self-assembling in solution: Nucleation and growth of G-quadruplexes
 Journal of Physical Chemistry B 113 (22), pp. 7934-7944 (2009)
- B. Marmioli, G. Greci, F. Cacho-Nerin, B. Sartori, E. Ferrari, P. Laggner, L. Businaro, H. Amenitsch
Free jet micromixer to study fast chemical reactions by small angle X-ray scattering,
 Lab on a Chip, Vol. 9 - 14, pp. 2063-2069 (2009)
- M.G. Ortore, F. Spinozzi, P. Mariani, A. Paciaroni, L.R. S. Barbosa, H. Amenitsch, M. Steinhart, J. Ollivier and D. Russo
Combining structure and dynamics: non-denaturing high-pressure effect on lysozyme in solution
 Journal of the Royal Society Interface 6 (Suppl. 5), pp. S619-S634 (2009)
- G. Pabst, B. Boulgaropoulos, E. Gander, B.R. Sarangi, H. Amenitsch, V.A. Raghunathan, P. Laggner
Effect of ceramide on nonraft proteins
 Journal of Membrane Biology 231 (2-3), pp. 125-132 (2009)
- S. Perutková, M. Daniel, G. Dolinar, M. Rappolt, V. Kralj-Iglič, V., and A. Iglič
Stability of the Inverted Hexagonal Phase
 In: *Advances in Planar Lipid Bilayers and Liposomes*, Vol. 9, editors A. Leitmannova Liu and H.T. Tien, Academic Press (Burlington), pp. 237-278 (2009)
- B. Pili, C. Bourgaux, Florian Meneau, P. Couvreur, M. Ollivon
Interaction of an anticancer drug, Gemcitabine, with phospholipid bilayers
 J. Therm. Anal. Calorim. 98, 19–28 (2009)
- P. Pivette, V. Faivre, G. Daste, M. Ollivon and S. Lesieur
Rapid cooling of lipid in a prilling tower: Theoretical considerations and consequences on the structure of the microspheres
 Journal of Thermal Analysis and Calorimetry 98 (1), pp. 47-55 (2009)

B. Pivac, P. Dubcek, I. Capan, I. Zulim, T. Betti, H. Zorc, and S. Bernstorff
Nano Si Superlattices for the Next Generation Solar Cells
J. Nanosci. Nanotechnol. 9, 3853–3857 (2009)

D. Pozzi, G. Caracciolo, R. Caminiti, S. Candeloro De Sanctis, H. Amenitsch, C. Marchini, M. Montani and A. Amici
Toward the Rational Design of Lipid Gene Vectors: Shape Coupling between Lipoplex and Anionic Cellular Lipids Controls the Phase Evolution of Lipoplexes and the Efficiency of DNA Release
ACS Appl. Mater. Interfaces 1 (10), pp 2237–2249 (2009)

K. Salamon, O. Milat, M. Buljan, U.V. Desnica, N. Radić, P. Dubček and S. Bernstorff
Grazing incidence X-ray study of Ge-nanoparticle formation in (Ge:SiO₂)/SiO₂ multilayers
Thin Solid Films 517 (6), pp. 1899-1903 (2009)

J. Schuster, R. Köhn, A. Keilbach, M., Döblinger, H. Amenitsch, T. Bein
Two-Dimensional-Hexagonal Periodic Mesoporous Polymer Resin Thin Films by Soft Templatin
Chemistry of Materials 21 (24), pp. 5754-5762 (2009)

C. Sinturel, M. Vayer, R. Erre, H. Amenitsch
Thermal induced mobility of self-assembled platelets of polyethylene-block poly(ethylene oxide) in liquid precursors of unsaturated polyester thermoset
European Polymer Journal, Vol. 45 - 9, pp. 2505-2512 (September 2009)

L. Suber, G. Campi, A. Pifferi, P. Andreozzi, C. La Mesa, H. Amenitsch, R. Cocco, W. R. Plunkett
Polymer-Assisted Synthesis of Two-Dimensional Silver Meso-Structures
J. Phys. Chem. C, Vol. 113 - 26, pp. 11198-6 (2009)

A. Turković, M. Rakić, P. Dubček, M. Lučić-Lavčević, S. Bernstorff
SAXS/WAXS/DSC study of temperature evolution in nanopolymer electrolyte
Vacuum 84 (1), 68-71 (2009)

A Turković
Metal Oxide Nano-particles and Nano-composite Polymer Electrolytes - Electrodes and Electrolytes in Solar and Galvanic Cells of the Second Generation
ECS Transactions, Volume 19, Issue 27, pp. 153-161 (2009)

Publications January to August 2010

B. Alonso, F. Fayon, D. Massiot, H. Amenitsch, L. Malfatti, T. Kidchob, S. Costacurta and P. Innocenzi
Hybrid Organic-Inorganic Mesostructured Membranes: Interfaces and Organization at Different Length Scales
The Journal of Physical-Chemistry C **114**, 11730–11740, (2010)

L.R.S. Barbosa, M.G. Ortore, F. Spinozzi, P. Mariani, S. Bernstorff and R. Itri
The Importance of Protein-Protein Interactions on the pH-Induced Conformational Changes of Bovine Serum Albumin: A Small-Angle X-Ray Scattering Study
Biophysical Journal, Volume 98, Issue 1, 147-157, 6 January 2010

K. Brandenburg, J. Howe, S. Sánchez-Gómez, P. Garidel, M. Roessle, J. Andrä, R. Jerala, D., Zweytick, K. Lohner, M. Rappolt, S. Blondelle, I. Moriyon, G.M. De Tejada
Effective antimicrobial and anti-endotoxin activity of cationic peptides based on lactoferricin: A biophysical and microbiological study

Anti-Infective Agents in Medicinal Chemistry 9 (1), pp. 9-22 (2010)

M. Buljan, J. Grenzer, A. Keller, N. Radic, V. Vales, S. Bernstorff, T. Cornelius, H.T. Metzger and V. Holy

Growth of spatially ordered Ge nanoclusters in an amorphous matrix on rippled substrates

Physical Review B 82, 125316 (2010) and

Virtual Journal of Nanoscale Science & Technology -- September 20, 2010, Volume 22, Issue 13

G. Caracciolo, D. Pozzi, A. Amici, H. Amenitsch

Universality of DNA Adsorption Behavior on the Cationic Membranes of Nanolipoplexes

Journal of Physical Chemistry B 114 (5), pp. 2028-2032 (2010)

S. Costacurta, L. Malfatti, A. Patelli, P. Falcaro, H. Amenitsch, B. Marmioli, G. Greci, M. Picinini and P. Innocenzi

Deep X-ray Lithography for Direct Patterning of PECVD Films

Plasma Processes and Polymers 7, 459-465, (2010)

Y.-D. Dong, A.J. Tilley, I. Larson, M.J. Lawrence, H. Amenitsch, M. Rappolt, T. Hanley, B.J. Boyd

Non-equilibrium effects in self assembled mesophase materials - unexpected supercooling effects for cubosomes and hexosomes

Langmuir 26, 9000-9010 (2010)

A. Fischereder, T. Rath, W. Haas, H. Amenitsch, J. Albering, D. Meischler, S. Larissegger, M. Edler, R. Saf, F. Hofer, G. Trimmel

Investigation of Cu₂ZnSnS₄ formation from metal salts and thioacetamide

Chemistry of Materials 22 (11), pp. 3399-3406 (2010)

C. Fotakis, S. Gega, E. Siapi, C. Potamitis, K. Viras, P. Moutevelis-Minakakis, C.G. Kokotos, S. Durdagi, S. Golic Grdadolnik, B. Sartori, M. Rappolt, T. Mavromoustakos

Interactions at the bilayer interface and receptor site induced by the novel synthetic pyrrolidinone analog MMK3

Biochimica et Biophysica Acta - Biomembranes 1798 (3), pp. 422-432 (2010)

H. Jerabek, G. Pabst, M. Rappolt and T. Stockner

Membrane-mediated effect on ion channels induced by the anesthetic drug ketamine

J. Am. Chem. Soc. **132** (23), 7990-7997 (2010)

K. Juraić, D. Gracin, B. Šantić, D. Meljanac, N. Zorić, A. Gajović, P. Dubček, S. Bernstorff, M. Čeh

GISAXS and GIWAXS analysis of amorphous-nanocrystalline silicon thin films

Nuclear Instruments and Methods B 268, 259-262 (2010)

S. Lepoutre, B. Julián-López, C. Sanchez, H. Amenitsch, M. Linden, and D. Grosso

Nanocasted mesoporous nanocrystalline ZnO thin films

Journal of Materials Chemistry 20 (3), pp. 537-542 (2010) and

Vir. J. Nan. Sci. & Tech. 21 (2)

L. Malfatti, D. Marongiu, S. Costacurta, P. Falcaro, H. Amenitsch, B. Marmioli, G. Greci, M.F. Casula, P. Innocenzi

Writing Self-Assembled Mesoporous Films with In situ Formation of Gold Nanoparticles

Chemistry of Materials 22 (6), pp. 2132-2137 (2010)

P. Mariani, F. Spinozzi, F. Federiconi, M.G. Ortore, H. Amenitsch, L. Spindler, I. Drevensek-Olenik

Guanosine Quadruplexes in Solution: A Small-Angle X-ray Scattering Analysis of Temperature Effects on Self-Assembling

Journal of Nucleic Acids, Volume 2010, Article ID 472478, 10 (2010)

- B. Marmiroli, G. Greci, F. Cacho-Nerin, B. Sartori, P. Laggner, L. Businaro and H. Amenitsch
Experimental set-up for time resolved small angle x-ray scattering studies of nanoparticles formation using a free-jet micromixer
Nucl. Instrum. & Meth. B 268 (3-4), pp. 329-333 (2010)
- J.M. O'Callaghan, N. Petkov, M.P. Copley, D.C. Arnold, M.A. Morris, H. Amenitsch, J.D. Holmes
Time-resolved SAXS studies of periodic mesoporous organosilicas in anodic alumina membranes
Microporous and Mesoporous Materials 130 (1-3), pp. 203-207 (2010)
- M. G. Ortore, F. Spinozzi, P. Mariani, A. Paciaroni, L. R. S. Barbosa, H. Amenitsch, M. Steinhart, J. Ollivier, D. Russo
High-pressure simultaneously modifies structural and dynamical properties of lysozyme hydration shell
Scientific Highlights in ILL Annual Report 2009, pp. 60-61 (2010)
- B. Pili, C. Bourgaux, H. Amenitsch, G. Keller, S. Lepître-Mouelhi, D. Desmaële, P. Couvreur, M. Ollivon
Interaction of a new anticancer prodrug, gemcitabine-squalene, with a model membrane. Coupled DSC and XRD study
Biochimica et Biophysica Acta - Biomembranes 1798 (8), pp. 1522-1532 (2010)
- S.R.C. Pinto, R.J. Kashtiban, A.G. Rolo, M. Buljan, A. Chahboun, U. Bangert, N.P. Barradas, E. Alves, M.J.M. Gomes
Structural study of $Si_{1-x}Ge_x$ nanocrystals embedded in SiO_2 films
Thin Solid Films 518 (2010) 2569-2572
- S.R.C. Pinto, A.G. Rolo, A. Chahboun, M. Buljan, A. Khodorov, R.J. Kashtiban, U. Bangert, N.P. Barradas, E. Alves, S. Bernstorff and M.J.M. Gomes,
Multilayers of Ge nanocrystals embedded in Al_2O_3 matrix: Structural and electrical studies
Microelectronic Engineering 87, 2508-2512 (2010)
- D. Pozzi, H. Amenitsch, C. Marchini, G. Caracciolo
Phase diagram of 3β -[N-(N,N-dimethylaminoethane)-carbamoil]-cholesterol-dioleoylphosphatidyl-ethanolamine/DNA complexes suggests strategies for efficient lipoplex transfection
Applied Physics Letters 96 (18), art. no. 183703 (2010)
- Pozzi D, Caminiti R, Marianecchi C, Carafa M, Santucci E, De Sanctis SC, Caracciolo G.
Effect of cholesterol on the formation and hydration behavior of solid-supported niosomal membranes
Langmuir. 26(4), 2268-73 (2010)
- M. Rappolt
Bilayer thickness estimations with "poor" diffraction data
Journal of Applied Physics 107 (8), art. no. 084701 (2010)
- A.A. Rempel and A. Magerl
Non-periodicity in nanoparticles with closed-packed structures
Acta Cryst. A66, 479-483 (2010)
- J. Sancho-Parramon, V. Janicki, P. Dubček, M. Karlušić, D. Gracin, M. Jakšić, S. Bernstorff, D. Meljanac, K. Jurać
Optical and structural properties of silver nanoparticles in glass matrix formed by thermal annealing of field assisted film dissolution
Optical Materials 32, 510-514 (2010)

E. Schafler

Effects of releasing the hydrostatic pressure on the nanostructure after severe plastic deformation of Cu

Scripta Mater, Vol. 62 - 6, pp. 423-4 (2010)

W. Schmidt, P. Bussian, M. Lindén, H. Amenitsch, P. Agren, M. Tiemann, F. Schüth

Accessing ultrashort reaction times in particle formation with SAXS experiments: ZnS precipitation on the microsecond time scale

Journal of the American Chemical Society 132 (19), pp. 6822-6826 (2010)

F. Spieckermann, H. Wilhelma, M. Kerber, E. Schafler, G. Polt, S. Bernstorff, F. Addiego, M. Zehetbauer

Determination of lamella thickness distributions in isotactic polypropylene by

X-ray line profile analysis

Polymer 51 (2010) 4195-4199

F. Spieckermann, H. Wilhelm, E. Schafler, M. Kerber, S. Bernstorff and M.J. Zehetbauer

Plasticity and X-ray Line Profile Analysis of the Semicrystalline Polymer Poly(3-hydroxybutyrate)

Journal of Physics: Conference Series **240** (2010) 012146 (4 pages)

F. Spinozzi, L. Paccamiccio, P. Mariani, L. Q. Amaral

Melting regime of the anionic phospholipid DMPG: new Lamellar phase and porous bilayer model

Langmuir 26, 6484-6493 (2010)

C. V. Teixeira, H. Amenitsch, T. Fukushima, J. P. Hill, W. Jin, T. Aida, M. Hotokka and M. Lindén

Form factor of an N-layered helical tape and its application to nanotube formation of hexa-peri-hexabenzocoronene-based molecules

J. Appl. Cryst. (2010). 43, 850-857

R. Viswanatha, H. Amenitsch, S. Santra, S. Sapra, S.S. Datar, Y. Zhou, S.K. Nayak, S. Kumar, D.D. Sarma

Growth mechanism of cadmium sulfide nanocrystals

Journal of Physical Chemistry Letters 1 (1), pp. 304-308 (2010)

A. Yaghmur, M. Kriechbaum, H. Amenitsch, M. Steinhart, P. Laggner, M. Rappolt

Effects of pressure and temperature on the self-assembled fully hydrated nanostructures of monoolein-oil systems

Langmuir 26 (2), pp. 1177-1185 (2010)

A. Yaghmur, L. Paasonen, M. Yliperttula, A. Urtti, M. Rappolt

Structural elucidation of light activated vesicles

Journal of Physical Chemistry Letters 1 (6), pp. 962-966 (2010)

International Conferences and Workshops in 2009

H. Amenitsch

Grazing Incidence Small Angle Scattering

6th European Winter School (NESY 2009) on "Research with Neutron and Synchrotron Radiation", Sportheim Planneralm, Styria, Austria, 9.-11.3.2009 (invited lecture)

H. Amenitsch, P. Laggner, C. Riekell

Microfluidics

Saxier Meeting, Liverpool, UK, 16.02.2009 (lecture)

H. Amenitsch, L. Lechuga, M. Lazzarino, K. Jungnikl, B. Sartori, M. Rappolt
NanoScience Foundries and Fine Analysis Nano-Biolabs
NFFA Meeting, Bellaterra, Spain, 02. - 03.03.2009 (lecture)

H. Amenitsch, F. Cacho-Nerin, F. Schmid, B. Sartori, M. Rappolt, G. Holzapfel, A. Gerhard, P. Laggner
Nano-/micro-structural response of the collagen/matrix composite in human arterial adventitia links to mechanical properties
MRS Spring Meeting 2009, San Francisco, USA, 13. - 17.04.2009 (lecture)

H. Amenitsch, F. Cacho-Nerin, F. Schmid, B. Sartori, M. Rappolt, G. Holzapfel, A. Gerhard, P. Laggner
Collagen arrangement in human arterial adventitia explains macroscopic mechanical properties and reliability
E-MRS Spring Meeting 2009, Strasbourg, France, 08.06.2009 - 12.06.2009 (lecture)

H. Amenitsch, M. Rappolt, B. Sartori, B. Marmioli, P. Laggner, D. Cojoc, E. Ferrari, V. Garbin, S. Santucci, G. Greci, C. Riekel, M. Burghammer
Optical tweezers for advanced sample manipulation of micro-samples in SAS experiments
International Conference on Small-Angle Scattering SAS2009, Oxford, United Kingdom, 13. - 17.09.2009 (lecture)

Heinz Amenitsch
Self-Assembly of Mesoporous Materials on Surfaces
GISAXS Satellite Conference of SAS2009, Hamburg, Germany, 20.-23.9.2009 (talk)

H. Amenitsch
The Austrian SAXS beamline at Elettra: Status and Perspectives"
SAC Meeting, Trieste, Italy, 30.11.-1.12.2010 (talk)

H. Amenitsch, M. Rappolt, B. Sartori, B. Marmioli, P. Laggner, D. Cojoc, E. Ferrari, V. Garbin, S. Santucci, G. Greci, C. Riekel, M. Burghammer
What can be done with optical tweezers?
Coordination meeting optical tweezers, Grenoble, France. 12.10.2009 (lecture)

H. Amenitsch, P. Laggner, C. Riekel
Microfluidics for SAXS experiments
Final SAXIER Meeting, Hamburg, Germany, 27.11.2009 (lecture)

Z. Arsov, M. Rappolt, J. Grdadolnik, L. Quaroni
ATR-FTIR spectroscopy gives new insights into the lipid membranes in excess water 7th European Biophysics Congress, Genoa, Italy, 11.07.2009 - 15.07.2009 (lecture)

S. Bernstorff
Synchrotron sources and Instrumentation
6th European Winter School (NESY 2009) on "Research with Neutron And Synchrotron Radiation", Sporthelm Planneralm, Styria, Austria, 9.3.2009 (invited lecture)

S. Bernstorff, P. Dubcek, B. Pivac, S. Milosevic, N. Krstulovic, Z. Kregar
Pulsed Laser Deposition of Germanium using Nano-Pulse Lengths
GISAXS Satellite Conference of SAS2009, Hamburg, Germany, 20.-23.9.2009 (talk)

Sigrid Bernstorff, Mario Rakić, Aleksandra Turković and Pavo Dubček
SAXS/DSC/WAXD study of the effect of γ -radiation on nano-polymer electrolyte
14th International Conference on Small Angle Scattering, Oxford, UK, 13-18 September 2009 (poster)

S. Bernstorff, K. Juraić, D. Gracin, D. Meljanac, A. Gajović, P. Dubček, M. Ceh
Analysis of silicon amorphous/nanocrystalline multi-layers by GISAXS and GIWAXS
14th International Conference on Small Angle Scattering (SAS2009), Oxford, UK, 13-18 September
2009 (poster)

M. Bitenc, Z. Crnjak Orel, P. Podbršček, P. Dubček, S. Bernstorff, G. Dražić and M. Marinšek
Zinc oxide: morphology and growth
17th Conference on Materials and Technology, Portorož, Slovenia, 16-18.11.2009

B. Boulgaropoulos, E. Gander, Z. Arsov, B. Sarangi, V.A. Raghunathan, H.
Amenitsch, P. Laggner, G. Pabst
Structure and dynamics of apoptotic model membranes
7th Euro Fed Lipid Congress, Graz, Austria 18. - 21.10.2009 (lecture)

B. Boulgaropoulos, Z. Arsov, H. Amenitsch, P. Laggner, G. Pabst
How to Program Cell Death?
4th Christmas Biophysics Workshop, Leibnitz, Austria 14./ 15.12.2009 (lecture)

M. Buljan, U.V. Desnica, N. Radić, I. Bogdanović-Radović, M. Ivanda, G. Dražić, M. Karlušić, P.
Dubček, K. Salamon, S. Bernstorff, V. Holy
Strukturna svojstva poluvodičkih nanočestica
6. Znanstveni sastanak Hrvatskog fizikalnog društva, Primošten, Croatia 8-11. 10. 2009

M. Buljan, U.V. Desnica, N. Radić, M. Ivanda, G. Dražić, P. Dubček, K. Salamon, S. Bernstorff, V.
Holy
Formation of three-dimensional quantum dot superlattices in amorphous systems
Seminar; Braga, Portugal, 11.05.2009 (invited talk)

F. Cacho-Nerin, F. Schmid, B. Sartori, M. Rappolt, G. Holzapfel, P. Laggner, H. Amenitsch
*New Insights into the Mechanical Properties of the Human Adventitia from its Nano/microstructural
Response*
International Conference on Small-Angle Scattering SAS2009, Oxford, United
Kingdom, 13. - 17.09.2009 (poster)

C. Camerani
Application of SAXS in the colloidal industry
Sixth Nordic Workshop on Scattering from Soft Matter, University of Aarhus, Aarhus, Denmark, 28 -
29 January 2009 (invited lecture)

G. Campi, A. Mari and L. Suber
*In situ and ex-situ XAS and XRD study of Silver particles formation in a template of a polynaphthalene
polymer in acidic aqueous solutions*
Workshop GILDA '09, Palermo, Italy, 3-4 December 2009

I. Capan, P. Dubček, M. Buljan, U. Desnica, R. Slunjski, N. Krstulović, Z. Kregar, S. Milošević, N.
Radić, H. Zorc, T. Betti, I. Zulim, B. Pivac
Nanostructures for the next generation of semiconductor devices
Croatian-Japanese Workshop on Advanced Materials Science, Zagreb, Croatia, 29-30 June 2009

G. Caracciolo, R. Caminiti, D. Pozzi, M. A. Digman, E. Gratton, S. Sanchez, C. Marchini, M.
Montani, A. Amici and H. Amenitsch
Efficient escape from endosomes determines the superior efficiency of multicomponent lipoplexes
7th European Biophysics Congress, July 11th-15th 2009, Genova, Italy (poster)

G. Cordoyiannis, A. Zidanšek, G. Lahajnar, Z. Kutnjak, H. Amenitsch, D. Jesenek, G. Nounesis, and S. Kralj

Influence of the Controlled-Pore Glass Confinement on the Layer Spacing of Smectic-A Liquid Crystals

10th European Conference on Liquid Crystals / Colmar - France, April 19-24 (2009)

U.V. Desnica, M. Buljan, K. Salamon, K. Dubcek, M. Ivanda, N. Radic, Z. Siketic, I. Bogdanovic-Radovic, I.D. Desnica-Frankovic, S. Bernstorff

Germanium nanocrystals in SiO₂ matrix produced by magnetron sputtering and subsequent thermal treatment

14th International Conference on Small Angle Scattering, Oxford, UK, 13-18 September 2009 (talk)

U. Desnica, M. Buljan, K. Salamon, N. Radić, P. Dubček, Z. Siketić, I. Bogdanović-Radović, M. Ivanda, S. Bernstorff

Germanijske kvantne točke u amorfnoj SiO₂ matrici

Knjiga sažetaka, Zagreb, Croatia, 2009 (poster)

P. Dubček, B. Pivac, N. Radić, S. Bernstorff

Strukturna istraživanja tankih filmova amorfnog silicija

Zbornik sažetaka 6. Znanstvenog sastanka HFDA, Zagreb, Croatia, 2009 (poster)

P. Dubček

Small angle probe into thin film

18th Croatian-Slovenian Crystallographic Meeting, Varaždin, Croatia, June 17 - 21, 2009, (plenary lecture)

P. Falcaro

X-Rays & Sol-Gel: an external source to tune material properties

XVth International Sol-Gel Conference, August 23-27 2009, Porto de Galinhas, Brazil

M.C.A. Fantini C.V. Teixeira, T.S. Martins, J.R. Matos, H. Amenitsch

Growth kinetics of cubic mesoporous silica

International Conference on Small-Angle Scattering SAS2009, Oxford, United Kingdom, 13. - 17.09.2009 (poster)

S. Ibrahimkutty, M. Rappolt, B. Sartori, Peter L. and H. Amenitsch

Characterization of Mesostructured Si-Particles by Comparison of Gas Phase and Powder Deposit Studies

International Conference on Small-Angle Scattering SAS2009, Oxford, United Kingdom, 13. - 17.09.2009 (oral presentation)

S. Ibrahimkutty, K. Jungnikl, M. Rappolt, B. Sartori, P. Laggner, H. Amenitsch

In-situ SAXS gas-phase study on the initial mesophase formation of Silica aerosols - the influence of temperature and humidity

International Conference on Small-Angle Scattering SAS2009, Oxford, United Kingdom, 13. - 17.09.2009 (poster)

P. Innocenzi

Fabrication of mesoporous functionalized arrays by integrating deep X-ray lithography with dip-pen writing

Ist "Hybrid Materials: International Conference on Multifunctional, Hybrid and Nanomaterials", Tours, France, 15-19.3.2009

A-C. Johnson, Z. Abbas, S. Wall and C. Camerani

Aggregation of colloidal silica: combined SAXS and electrospray analysis

European Student Colloid Conference, University of Almeria, Spain, July 15-18, 2009

K. Jungnikl, I. Shyjumon, M. Rappolt, B. Sartori, P. Laggner, H. Amenitsch
In-situ SAXS gas-phase study on the initial mesophase formation of Silica aerosols – the influence of temperature and humidity

BioAmorPhys - The Max Plank Summer School on Amorphous Solids in Physics and Biology, Berlin, Germany, 1.- 3.06.2009

K. Jungnikl

The Macromolecular Structure of Wood Cell Walls and its Biomechanical Significance

Sit and Relax Session (SAXS), Trieste, Italy, 22.06.2009 - 22.06.2009 (lecture)

K. Juraić, D. Gracin, D. Meljanac, A. Gajović, P. Dubček, B. Šantić, S. Bernstorff, M. Čeh

GISAXS and GIWAXS analysis of amorphous-nanocrystalline silicon thin films

EMRS Spring Meeting, Strasbourg, France, June 8-12, 2009

A. Keilbach, J. Schuster, B. Platschek, N. Petkov, T. Bein

TP B8 –Ultradünne funktionale Nanodrähte für elektronische und optische Anwendungen

Summarizing Workshop SFB 486 "Nanoman - Ten Years in a Nutshell" Venice, Italy, 16.-19.09.2009

M.B. Kerber, E. Schafler, L. Balogh, S. Scheriau, T. Ungar, M.J. Zehetbauer

X-ray line-profile analysis of HPT-deformed nickel

2nd International Symposium on Bulk Nanostructured Materials, Ufa, Russia, September 2009

A. Khodorov, S. Levichev, A. Chahboun, A.G. Rolo, N. P. Barradas, E. Alves, M.J.M. Gomes

Growth and characterization of Mn- doped ZnO/TiO₂ multilayered nanostructures grown by pulsed laser deposition

10th International Conference Trends in Nanotechnology, Barcelona, Spain, September 10-13, 2009

P. Laggner

Bridging the Gap to Synchrotrons: New High-Brilliance SAXS Techniques for the Laboratory

ACA 2009 Annual Meeting, Toronto, Canada, 25. - 30.07.2009 (lecture)

P. Laggner, M. Kriechbaum, H. Amenitsch, P. Hernegger, A. Hodzic, M. Schmuck, M. Kalinina

Bridging the Gap to Synchrotrons: New High-Brilliance SAXS Techniques for the Laboratory

International Conference on Small-Angle Scattering SAS2009, Oxford, United

Kingdom, 13. - 17.09.2009 (oral)

V.Lughi

Bio- and Nanomaterials in Photovoltaics

CBM seminar, Trieste, Italy, March 31st, 2009

V.Lughi

Approcci chimici alla fabbricazione di materiali fotovoltaici nanostrutturati

"I giovani e la chimica in Friuli - Venezia Giulia", 24.9.2009

L. Malfatti

Photoinduced Formation of Wrinkled Microstructures with Long-Range Order in Thin Oxide Films

IX national AUSI congress on "Nanophase Materials", Montepioni, Iglesias, June 3-5 2009

L. Malfatti, T. Kidchob, D. Aiello, R. Aiello, P. Innocenzi

Aggregation States of Rhodamine 6G in Mesoporous Silica Films

I International Conference on Multifunctional, Hybrid and Nanomaterials, Tours, France, March 15-19 2009

B. Marmiroli, G. Greci, H. Amenitsch, B. Sartori, F. Cacho Nerin, P. Laggner, L. Businaro
Jet micromixer for studying ultrafast chemical reactions by Small Angle X-Ray Scattering
MRS Spring Meeting, San Francisco (USA), 13/04/2009 (lecture)

B. Marmiroli, G. Greci, F. Cacho-Nerin, B. Sartori, E. Ferrari, P. Laggner, L. Businaro, H. Amenitsch
Free jet micromixer to study fast chemical reactions by small angle X-ray scattering
BioAmorPhys - The Max Plank Summer School on Amorphous Solids in Physics and Biology, Berlin, Germany, 01.06.2009 - 03.06.2009

B. Marmiroli, G. Greci, F. Cacho-Nerin, B. Sartori, P. Laggner, L. Businaro, H. Amenitsch
Experimental set-up for time resolved small angle x-ray scattering studies of nanoparticles formation using a free -jet micromixer
E-MRS Spring Meeting 2009, Strasbourg, France, 08.06.2009 - 12.06.2009 (lecture)

B. Marmiroli G. Greci, F. Cacho-Nerin, B. Sartori, P.Laggner, L. Businaro, H. Amenitsch
Sub millisecond time-resolved SAXS studies of Calcium Carbonate formation
International Conference on Small-Angle Scattering SAS2009, Oxford, United Kingdom, 13. - 17.09.2009 (poster)

B. Marmiroli, H. Amenitsch
Microfluidics for nanoanalytic techniques using synchrotron radiation
ICS UNIDO conference on "Advanced diagnostics and drug-delivery at the nanoscale: state of the art and possible applications to orphan diseases", Trieste, Italy, 13.- 15.10.2009 (lecture)

G.R. Mitchell
Nano-structured polymers
PACCON 2009 Pure and Applied Chemistry International Conference 2009, Naresuan University, Phitsanulok, Thailand, January 14-16, 2009

G.R. Mitchell
Extracting quantitative data from SAXS/SANS data for anisotropic systems
SAS2009, Oxford, UK, September 2009

G.R. Mitchell, S. Wangsoub, F.J. Davis and R.H. Olley
Directing the crystallisation of polymers using self-assembling nanoparticles
SAS2009, Oxford, UK, September 2009

G. Pabst
Membrane physics matters ?
Canadian Neutron Center Seminar, Chalk River, Canada, 24.02.2009 (lecture)

G. Pabst
Effect of sphingomyelinase on physical properties of biomimetic membranes
Canadian Neutron Center Seminar, Chalk River, 26.02.2009 (lecture)

G. Pabst
What to learn on membrane physics by SAXS
Institute of Physics Seminar, Zagreb, Croatia, 18.06.2009 (lecture)

S. Perutkova, M. Daniel, T. Mares, A. Perne, G. Dolinar, M. Rappolt, V. Kralj-Iglic, A. Iglic
Role of Phospholipid Asymmetry in Stability of Inverted Hexagonal Mesoscopic Phases
53rd Biophysical Society Meeting, Boston, USA, 28.02.- 04.03.2009

S. Perutkova, M. Daniel, M. Rappolt, V. Kralj-Iglic, I. Iglic
Mathematical model of inverted hexagonal phase in biomembranes influenced by anisotropic constituents

20th International Symposium on Bioelectrochemistry and Bioenergetics, Sibiu, Romania, 10. - 14.05.2009 (lecture)

S. Perutkova, M. Danie, G. Dolinar, V. Kralj-Iglic, M. Rappolt, A. Iglic
Stability of inverted hexagonal mesoscopic phase affected by phospholipid anisotropy
7th European Biophysics Congress, Genoa, Italy, 11. - 15.07.2009

S. R. C. Pinto, M. Buljan, R. J. Kashtiban, A. G. Rolo, A. Chahboun, U. Bangert, and M. J. M. Gomes
Structural study of $Si_{1-x}Ge_x$ nanocrystals embedded in SiO_2 films
EMRS 2009 Spring Meeting, Symposium I, Strasbourg, France June 8-12, 2009

S. R. C. Pinto, R. J. Kashtiban, M. Buljan, A. G. Rolo, A. Chahboun, S. Levichev, A. Khodorov, U. Bangert, and M. J. M. Gomes
Structural study of Ge nanocrystals embedded in Al_2O_3 films
25th International Conference on Defects in Semiconductors, St. Petersburg, Russia, July 20-24, 2009

S. R. C. Pinto, R. J. Kashtiban, A. G. Rolo, A. Chahboun, E. Alves, U. Banger, and M. J. M. Gomes
Multilayers of Ge nanocrystals embedded in Al_2O_3 matrix: vibrational and structural studies
23rd International Conference on Amorphous and Nanocrystalline Semiconductors (ICANS 23), Utrecht, Holland, August 23-28, 2009

D. Pozzi, G. Carraciolo, R. Caminiti, C. Marianecchi, M. Carafa, E. Santucci
Effect of cholesterol on the structure of phospholipid and non-phospholipid membranes
7th European Biophysics Congress, July 11th-15th 2009, Genova, Italy (poster)
In: European Biophysics Journal. Genova, 11-15 Luglio 2009, vol. 38 (Suppl. 1), p. S193

N. Radić, Z. Siketić, I. Bogdanović-Radović, M. Buljan, U.V. Desnica, Uroš, R. Slunjski, B. Pivac
 SiO_x thin films prepared by magnetron sputtering
16th International Scientific Meeting on Vacuum Science and Technique (2009)

N. Radić, Z. Siketić, I. Bogdanović-Radović, M. Buljan, U.V. Desnica, R. Slunjski, B. Pivac, H. Zorc
Tanki filmovi SiO_x pripravljeni magnetronskim rasprašenjem
Zbornik sažetaka 6. Znanstvenog sastanka HFDA, Zagreb, Croatia 2009 (poster)

M. Rappolt
Micelles, your cells
Sit and Relax Session (SAXS), Trieste, Italy, 11.02.2009 (lecture)

M. Rappolt
The biologically relevant mesophases as „seen“ by X-rays
Neutrons and X-rays meet biology, Berlin, Germany, 25. - 27.02.2009 (lecture)

M. Rappolt
Glycolipid Membranes as „Seen“ by SAXS
(Glyco)lipids, Structures, Functions, and Interactions Meeting, Hamburg, Germany, 12.06.2009 (lecture)

M. Rappolt, P. Laggner, B. Sartori, M. Almgren, A. Yaghmur
Synchrotron Light for Characterizing Curved Membrane Systems Mimicking Fusion Processes
7th Euro Fed Lipid Congress, Graz, Austria, 18.10.2009 - 21.10.2009 (lecture)

M. Rappolt

Micelles, your cells

4th Christmas Biophysics Workshop, Leibnitz, Austria, 14.- 15.12.2009 (lecture)

T. Rath, S. Larissegger, C. Fradler, H. Amenitsch, G. Trimmel

A time resolved X-ray scattering study of the thermal formation process of thin nanocrystalline metal sulfide layers

E-MRS 2009, Strasbourg, France, June 9, 2009 (poster)

T. Rath, E. Maier, M. Edler, A. Fischereder, S. Larissegger, A. Pein, W. Haas, G. Mauthner, F. Hofer, E. List, G. Trimmel

Organic-inorganic semiconductor blends for photovoltaic applications

Nano and Photonics 2009, Mauterndorf, Austria, March 11, 2009 (poster)

T. Rath, E. Maier, A. Fischereder, M. Edler, W. Haas, C. Fradler, S. Moscher, S. Larissegger, A. Santis-Alvarez, R. Saf, G. Mauthner, E. J.W. List, F. Hofer, G. Trimmel

Application of Nanocomposite Layers consisting of Electroactive Polymers and Sulfidic Nanoparticles in Hybrid Photovoltaics

SloNano2009, Ljubljana, Slovenia, 19–21 October, 2009 (talk)

T. Rath, E. Maier, S. Larissegger, A. Fischereder, M. Edler, W. Haas, C. Fradler, S. Moscher, A. Santis Alvarez, R. Saf, G. Mauthner, E.J.W. List, F. Hofer, G. Trimmel

Application of Nanocomposite Layers of Sulfidic Nanoparticles and Electroactive Polymers in Hybrid Photovoltaics

European Polymer Congress 2009 (EPF09). Graz Austria, July 12, 2009 (talk)

E. Schafner

Dislocation density and vacancy concentration in severely deformed metals from line profiles

Workshop: X-ray line profile analysis: a training course from basics to practice, Dep. Materials Physics, Eötvös Lorand University Budapest, Hungary, April 2009 (invited)

J. Schuster, A. Keilbach, M. Döblinger, R. Köhn, T. Bein

Ordered Mesoporous Carbon in Confined Environments through Soft-Templating: Thin Films and Tubular Hosts

21. Deutsche Zeolith-Tagung, Kiel, Germany, 04.-06.03.2009

R. Schuster and M. Kerber

Microstructural parameters of fcc and bcc nanomaterials as investigated by means of in-situ deformation synchrotron Bragg peak analysis

Seminar Uni Vienna, Austria, 12.11.2009

S. Shao, M. Dimitrov, R. Köhn

Synthesis and Characterization of Highly Organized Mesoporous Palladium Doped Tin Dioxide Thin Films for Gas Sensing

21. Deutsche Zeolith-Tagung, Kiel, Germany, 04.-06.03.2009

F. Spieckermann, H. Wilhelm, E.Schafner, M. Kerber, S. Bernstorff and M.J. Zehetbauer

Plasticity and X-ray Line Profile Analysis of Poly(3-hydroxybutyrate)

15th International Conference on the Strength of Materials (ICSMA 15), Dresden, Germany, August 16-21, 2009

C.V. Teixeira, H. Amenitsch, T. Fukushima, J.P. Hill, W. Jin, T. Aida, M. Hotokka, M. Linden

Formation of hexagonally ordered nanotubes via helical intermediate

XIV Conference on Small-Angle Scattering, Oxford, UK, 13/09/2009

G. Trimmel

Formation of Sulfidic Nanoparticles in Semiconducting Polymers for Hybrid Photovoltaics
Nano and Photonics Mauterndorf 2009, Mauterndorf, Austria, March 12, 2009 (talk)

A. Turković

Metal oksidne nano-čestice i nano-kompozitni polimerni elektroliti, - elektrode i elektroliti u solarnim i galvanskim ćelijama druge generacije

Knjiga Sažetaka, 1. Radionica sekcije za industrijsku i primjenjenu fiziku hrvatskog fizikalnog društva, Zagreb, Croatia, 2009 (invited lecture)

A. Turkovic, P. Dubcek, M. Rakic, M. Loncaric and S. Bernstorff

SAXS Studies of TiO₂ Nanoparticles in Polymer Electrolytes and Nanophased Films

216th ECS Meeting, Vienna, Austria, 4 -9 October, 2009 (Oral)

A. Turkovic

Metal Oxide Nano-particles and Nano-composite Polymer Electrolytes - Electrodes and Electrolytes in Solar and Galvanic Cells of the Second Generation

215th ECS Meeting, San Francisco, CA, May 24-29, 2009

S. Wangsoub, F.J. Davis, G.R. Mitchell and R.H. Olley

Controlled preparation of nanofibrils from low molar compounds in a polymer matrix

Euromat 2009, Glasgow, UK, September 2009

S. Wangsoub, F.J. Davis, P.J.F. Harris, G.R. Mitchell and R.H. Olley

Nanofibrils and gels formed from the self-organisation of sorbitol derivatives

Biological and Soft Matter Institute of Physics Conference, University of Warwick, UK, April 2009

H. Wilhelm, F. Spieckermann, M. Kerber, E. Schafner, S. Bernstorff, M. Zehetbauer

Phase-specific mechanisms of plasticity in polymorphic polypropylene

15th International Conference on the Strength of Materials, Dresden, Germany, August 16-21, 2009

A. Zargham, Th. Schmidt, J. I. Flege, T. Laurus, E. Piskorska-Hommel, R. Hildebrand, S. Röhe, M. Bäumer and J. Falta

Multi-scale structural characterization of colloidal nanoparticle films

European Materials Research Society Spring Meeting 2009, Strasbourg, France, 8–12 June 2009 (oral)

ELETTRA Highlights 2008-2009

J.I. Flege, B. Gehl, V. Aleksandrovic, Th. Schmidt, A. Frömsdorf, A. Pretorius, S. Bernstorff, A. Rosenauer, H. Weller, J. Falta, M. Bäumer

Structural and chemical effects of plasma treatment on close-packed colloidal nanoparticle layers

Elettra Research Highlight, pp. 20-21 (2009)

A. Keilbach, M. Döblinger, R. Köhn, H. Amenitsch, T. Bein

Periodic mesoporous organosilica in confined environments

Elettra Research Highlight, pp. 38-39 (2009)

P. Mariani, F. Spinozzi, F. Federiconi, H. Amenitsch, L. Spindler, I. Drevensek-Olenik

Nucleation and growth of Deoxyguanosine 5'-Monophosphate quadruplexes in dilute solution studied by SAXS

Elettra Research Highlight, pp. 100-101 (2009)

B. Marmioli, G. Greci, F. Cacho-Nerin, B. Sartori, E. Ferrari, P. Laggner, L. Businaro, H. Amenitsch
Free jet micromixer to study fast chemical and biological reactions by Small Angle X-Ray Scattering
Elettra Research Highlight, pp. 118-119 (2009)

PhD Thesis / Doktorarbeiten 2009

Yao Da (Charlie) Dong
Investigation of nanostructured liquid crystal particles as novel agrochemical delivery agents
Monash University, 2009

Berhard Gehl
University of Bremen, Germany, 11.6.2009

Kresimir Salamon
Rasprsenje x-zracenja s površina pri malom upadnom kutu: istraživanje nanostrukture i morfologije površinskih tankih heterogenih slojeva
Zagreb, 2009

Master Theses (Tesi di Laurea, Diplomarbeit) 2009

M.M. Suchanova
Fluorescence properties of glass with 2.0 wt.% of CdS
Ural Federal University, Ekaterinburg, Russia
Diplom 2009

M. Battiston
Films of semiconductor nanocrystals: a SAXS characterization
Laurea Thesis, University of Trieste, Italy

Maria Teresa Silvi
Tecniche di diffusione a piccolo angolo dei raggi X e dei neutroni per la determinazione strutturale di proteine in soluzione
Università Politecnica delle Marche, Ancona

Authors Index

AMENITSCH, H.	52, 58, 67, 73, 80, 82, 85, 87, 90, 94, 112, 115, 117, 122, 124, 126, 129
ANTONIOLLI, F.	40
BALDASSARRI, E.	102
BATTISTON, M.	40
BAEUMER, M.	71
BEIN, T.	124
BENETTI, F.	80
BERNSTORFF, S.	40, 43, 45, 47, 49, 54, 56, 60, 63, 65, 69, 71, 76, 77
BOGDANOVIC-RADOVIC, I.	43
BONCHIO, M.	126
BOULGAROPOULOS, B.	82
BOYD, B.	94
BRADSHAW, J.P.	99
BRANDENBURG, K.	84
BROWN, C.P.	85
BULJAN, M.	43, 77
BURATTINI, D.D.	102
CACHO-NERIN, F.	58, 85
CAMPI, G.	109
CARACCILOLO, G.	87, 90
CARRARO, M.	126
CASALIS, L.	126
CASULA, M.F.	117
CEH, M.	49
CHABOUN, A.	77
CHATZIGEORGIOU, P.	93
CONDE, O.	77
COZZARINI, L.	40
DA ROS, T.	126
DATAR, S.S.	129
DAVIS, F.	63
DESNICA, U.	43
DOEBLINGER, M.	124
DONG, YAO-DA	94
DRAZIC, G.	43
DUBCEK, P.	43, 45, 47, 49, 54, 56, 65, 76
DURACCIO, D.	60
EDLER, M.	115
FALCARO, P.	117
FALTA, J.	71
FAUSTINI, M.	112
FISCHEREDER, A.	115, 122
GAJOVIC, A.	49
GOMES, M.J.M.	77
GRACIN, D.	49
GRENCI, G.	58
GROSSO, D.	112

GUTSMANN, T.	84
HAAS, W.	122
HOLY, V.	43
HOWE, J.	84
IGLIC, A.	107
INNOCENCI, P.	117
JERABEK, H.	105
JERCINOVIC, M.	65
JOHNSON, C.	97
JOZIC, D.	56
JUNGNIKL, K.	52
JURAIC, K.	49, 76
KACONIS, Y.	84
KARLUSIC, M.	43
KE, L.J.	99
KEILBACH, A.	124
KERBER, M.B.	69
KOEHN, R.	124
KREGAR, Z.	45, 47
KRSTULOVIC, N.	45, 47
KUMAR, S.K.	129
LAGGNER, P.	58, 82
LAKEY, J.	97
LEGNAME, G.	80
LEVICHEV, S.	77
LICCOCIA, S.	85
LONCARIC, M.	54
LUCIC LAVCEVIC, M.	56
LUGHI V.	40
MACLEOD, J.	85
MAGERL, A.	67
MALFATTI, L.	117
MARI, A.	109
MARIANI, P.	102
MARMIROLI, B.	58, 112
MARONGIU, D.	117
MASTERS, A.	122
MAVROMOUSTAKOS, T.	93
MILAT, O.	65
MILOSEVIC, S.	45, 47
MITCHELL, G.	60, 63
NAYAK, S.K.	129
OLLEY, R.H.	63
PABST, G.	82, 105
PEIN, A.	122
PERUTKOVA, S.	107
PEZZUTO, M.	60
PIFFERI, A.	109
PINTO, S.R.C.	77
PIVAC, B.	45, 47
POZZI, D.	87, 90
PRATO, M.	126
RADIC, N.	43, 65

RADIVO, A.	40
RAPPOLT, M.	84, 93, 94, 99, 105, 107
RATH, T.	115, 122
REMPEL, A.	67
RIDLEY, H.	97
ROEHE, S.	71
ROLO, A.G.	77
ROSEI, F.	85
SA'ADEDIN, F.	99
SALAMON, K.	65
SANCHO-PARRAMON, J.	54
SANTRA, S.	129
SAPRA, S.	129
SARMA, D.D.	129
SARTOREL, A.	126
SARTORI, B.	58
SCHAFLER, E.	69
SCHMIDT, TH.	71
SCHMIDT, W.	73
SCHUSTER, J.	124
SCHUSTER, R.	69
SCOLES, G.	126
SCORRANO, G.	126
SILVESTRE, C.	60
SINTUREL, C.	112
SINTYUREVA, M.	120
SOLOVYOVA, A.	97
SPIECKERMANN, F.	69
SPINOZZI, F.	102
STOCKNER, T.	105
SUBER, L.	109
TIDDY, G.J.T.	120
TILLEY, A.	94
TOMA, F.	126
TRAVERSA, E.	85
TRIMMEL, G.	115, 122
TURKOVIC, A.	76
VAYER, M.	112
VIEIRA, E.M.F.	77
VISWANATHA, R.	129
VITTORINI ORGEAS, A.	85
WANGSOUB, S.A.	63
ZARGHAM, A.	71
ZEHETBAUER, M.	69
ZHOU, Y.	129
ZORC, H.	54